frontiers | Research Topics

Variability in the solar wind and its impact on the coupled magnetosphere-ionosphere-thermosphere system

Edited by
Yi Wang, Boyi Wang, Andrey Samsonov, Nithin Sivadas, Yulia Bogdanova and Guram Kervalishvili

Published in
Frontiers in Astronomy and Space Sciences
Frontiers in Physics

FRONTIERS EBOOK COPYRIGHT STATEMENT

The copyright in the text of individual articles in this ebook is the property of their respective authors or their respective institutions or funders. The copyright in graphics and images within each article may be subject to copyright of other parties. In both cases this is subject to a license granted to Frontiers.

The compilation of articles constituting this ebook is the property of Frontiers.

Each article within this ebook, and the ebook itself, are published under the most recent version of the Creative Commons CC-BY licence. The version current at the date of publication of this ebook is CC-BY 4.0. If the CC-BY licence is updated, the licence granted by Frontiers is automatically updated to the new version.

When exercising any right under the CC-BY licence, Frontiers must be attributed as the original publisher of the article or ebook, as applicable.

Authors have the responsibility of ensuring that any graphics or other materials which are the property of others may be included in the CC-BY licence, but this should be checked before relying on the CC-BY licence to reproduce those materials. Any copyright notices relating to those materials must be complied with.

Copyright and source acknowledgement notices may not be removed and must be displayed in any copy, derivative work or partial copy which includes the elements in question.

All copyright, and all rights therein, are protected by national and international copyright laws. The above represents a summary only. For further information please read Frontiers' Conditions for Website Use and Copyright Statement, and the applicable CC-BY licence.

ISSN 1664-8714
ISBN 978-2-8325-6673-2
DOI 10.3389/978-2-8325-6673-2

Generative AI statement
Any alternative text (Alt text) provided alongside figures in the articles in this ebook has been generated by Frontiers with the support of artificial intelligence and reasonable efforts have been made to ensure accuracy, including review by the authors wherever possible. If you identify any issues, please contact us.

About Frontiers

Frontiers is more than just an open access publisher of scholarly articles: it is a pioneering approach to the world of academia, radically improving the way scholarly research is managed. The grand vision of Frontiers is a world where all people have an equal opportunity to seek, share and generate knowledge. Frontiers provides immediate and permanent online open access to all its publications, but this alone is not enough to realize our grand goals.

Frontiers journal series

The Frontiers journal series is a multi-tier and interdisciplinary set of open-access, online journals, promising a paradigm shift from the current review, selection and dissemination processes in academic publishing. All Frontiers journals are driven by researchers for researchers; therefore, they constitute a service to the scholarly community. At the same time, the *Frontiers journal series* operates on a revolutionary invention, the tiered publishing system, initially addressing specific communities of scholars, and gradually climbing up to broader public understanding, thus serving the interests of the lay society, too.

Dedication to quality

Each Frontiers article is a landmark of the highest quality, thanks to genuinely collaborative interactions between authors and review editors, who include some of the world's best academicians. Research must be certified by peers before entering a stream of knowledge that may eventually reach the public - and shape society; therefore, Frontiers only applies the most rigorous and unbiased reviews. Frontiers revolutionizes research publishing by freely delivering the most outstanding research, evaluated with no bias from both the academic and social point of view. By applying the most advanced information technologies, Frontiers is catapulting scholarly publishing into a new generation.

What are Frontiers Research Topics?

Frontiers Research Topics are very popular trademarks of the *Frontiers journals series*: they are collections of at least ten articles, all centered on a particular subject. With their unique mix of varied contributions from Original Research to Review Articles, Frontiers Research Topics unify the most influential researchers, the latest key findings and historical advances in a hot research area.

Find out more on how to host your own Frontiers Research Topic or contribute to one as an author by contacting the Frontiers editorial office: frontiersin.org/about/contact

Variability in the solar wind and its impact on the coupled magnetosphere-ionosphere-thermosphere system

Topic editors

Yi Wang — Harbin Institute of Technology, Shenzhen, China
Boyi Wang — Harbin Institute of Technology, Shenzhen, China
Andrey Samsonov — University College London, United Kingdom
Nithin Sivadas — Goddard Space Flight Center, National Aeronautics and Space Administration, United States
Yulia Bogdanova — Rutherford Appleton Laboratory, United Kingdom
Guram Kervalishvili — GFZ Helmholtz Centre for Geosciences, Germany

Citation

Wang, Y., Wang, B., Samsonov, A., Sivadas, N., Bogdanova, Y., Kervalishvili, G., eds. (2025). *Variability in the solar wind and its impact on the coupled magnetosphere-ionosphere-thermosphere system*. Lausanne: Frontiers Media SA. doi: 10.3389/978-2-8325-6673-2

Table of contents

frontiers | Frontiers in Physics

TYPE Editorial
PUBLISHED 22 July 2025
DOI 10.3389/fphy.2025.1658092

Check for updates

OPEN ACCESS

EDITED AND REVIEWED BY
Joseph E. Borovsky,
Space Science Institute (SSI), United States

*CORRESPONDENCE
Yi Wang,
wingwy@mail.ustc.edu.cn
Boyi Wang,
bywang08@gmail.com

RECEIVED 02 July 2025
ACCEPTED 14 July 2025
PUBLISHED 22 July 2025

CITATION
Wang Y, Wang B, Samsonov A, Sivadas N, Bogdanova Y and Kervalishvili G (2025) Editorial: Variability in the solar wind and its impact on the coupled magnetosphere-ionosphere-thermosphere system.
Front. Phys. 13:1658092.
doi: 10.3389/fphy.2025.1658092

COPYRIGHT
© 2025 Wang, Wang, Samsonov, Sivadas, Bogdanova and Kervalishvili. This is an open-access article distributed under the terms of the Creative Commons Attribution License (CC BY). The use, distribution or reproduction in other forums is permitted, provided the original author(s) and the copyright owner(s) are credited and that the original publication in this journal is cited, in accordance with accepted academic practice. No use, distribution or reproduction is permitted which does not comply with these terms.

Editorial: Variability in the solar wind and its impact on the coupled magnetosphere-ionosphere-thermosphere system

Yi Wang[1,2]*, Boyi Wang[1,2]*, Andrey Samsonov[3], Nithin Sivadas[4], Yulia Bogdanova[5] and Guram Kervalishvili[6]

[1]State Key Laboratory of Solar Activity and Space Weather, School of Aerospace, Harbin Institute of Technology, Shenzhen, China, [2]Shenzhen Key Laboratory of Numerical Prediction for Space Storm, School of Aerospace, Harbin Institute of Technology, Shenzhen, China, [3]Mullard Space Science Laboratory, University College London, Dorking, United Kingdom, [4]Goddard Space Flight Center, National Aeronautics and Space Administration, Greenbelt, United States, [5]RAL Space, Science and Technology Facilities Council, United Kingdom Research and Innovation, Rutherford Appleton Laboratory, Didcot, United Kingdom, [6]GFZ Helmholtz Centre for Geosciences, Potsdam, Germany

KEYWORDS

solar wind, magnetosphere-ionosphere-thermosphere, space weather, solar wind variability, solar wind - magnetosphere interaction, solar wind - magnetosphere - ionosphere coupling

Editorial on the Research Topic
Variability in the solar wind and its impact on the coupled magnetosphere-ionosphere-thermosphere system

Introduction

The inherent variability of the solar wind, from large-scale structures to kinetic-scale fluctuations, drives a cascade of energy transfer and plasma processes throughout the coupled Magnetosphere-Ionosphere-Thermosphere (M-I-T) system. Understanding these multiscale interactions is critical not only for advancing fundamental heliophysics but also for developing effective mitigation strategies against the hazards space weather poses to our technologically dependent society. This Research Topic confronts this grand challenge by integrating *in situ* observations, theoretical analysis, and numerical modeling to elucidate the causal chain that links microscopic plasma mechanisms to their large-scale terrestrial consequences. By consolidating findings across four complementary areas of study, this Research Topic aims to contribute to a more predictive, physics-based understanding, laying a stronger foundation for enhancing forecasting capabilities.

Solar wind and magnetosheath dynamics

Some space plasma and magnetic field structures hitting the magnetosphere result from the interaction between the Interplanetary Magnetic Field (IMF) discontinuities

and the bow shock. Lu et al. studies an event in which they identified both a hot flow anomaly [1] and a foreshock bubble [2] using THEMIS and MMS data near the subsolar bow shock. Their observations confirm the previously published hybrid simulation results, which show that these two phenomena can coexist. The authors emphasize the importance of multiple spacecraft observations to reveal the full scope of foreshock transients.

Madanian et al. presents another interesting event in which a density structure within the magnetic cloud impacted the Earth and caused significant variations in the magnetopause and bow shock locations. The most interesting feature of the event is a sunward flow [3] in the inner magnetosheath near the subsolar point following the solar wind dynamic pressure decrease. The authors find that the sunward flow is formed due to magnetosheath expansion and is driven by the magnetic pressure gradient force.

Chen et al. presents a theoretical investigation into the fundamental problem of three-dimensional, time-dependent magnetic reconnection. Its principal contribution is the first-ever analytical demonstration that steady-state plasma outflows can theoretically exist within a time-varying magnetic field, resolving an apparent contradiction between observations of quasi-steady reconnection in turbulent environments [4] and the intuition that a dynamic field should drive a dynamic flow.

Villante comments on the analysis of solar wind density fluctuations (0.45–4.65 mHz) by Di Matteo et al. [5]. The author refers to the previous papers [6], which showed only 50% agreement between frequencies of fluctuations observed by two spacecraft in the solar wind. They point out that these results suggest compressional solar wind modes may drive magnetospheric fluctuations. However, there are analysis challenges due to spatial variability and methodological differences that may alter the results of the data analysis.

Magnetospheric phenomena

Chen et al. analyzes an interplanetary shock event that reveals two simultaneous electron acceleration processes in Earth's radiation belts. They find that shock-induced impulsive electric fields instantly energized relativistic electrons near dusk, creating energy-dependent drift echoes. The authors emphasize the important role of the modulations by an azimuthally confined ultralow frequency [7] wave in this energization process.

The review by Archer et al. examines magnetopause MHD surface waves [8] as a critical mediator of the solar wind-magnetosphere interaction. The authors highlight how the magnetopause can act as a dynamic resonator, forming standing eigenmodes whose frequencies are directly governed by upstream solar wind conditions. This mechanism effectively filters, accumulates, and guides turbulent solar wind energy into geospace. The paper concludes that overcoming current theoretical challenges is essential for understanding this global energy transfer and for interpreting data from future space missions.

Xie et al. presents the first report of electron cyclotron harmonic waves [9] responding to an interplanetary shock. They find that shock compression boosted >0.1 keV electron fluxes by 30%–50%, providing free energy for wave growth. This confirms a direct solar wind-magnetosphere coupling pathway where shock-induced electron injections drive wave instability within minutes.

Leveraging high-resolution MMS data, Wei et al. investigates the electron firehose instability [10] in the magnetotail, revealing that this phenomenon, typically associated with reconnection outflows and depolarization fronts, can also arise in the pristine plasma sheet. Their analysis further implicates this instability as a potential driver for magnetotail flapping motions and the generation of associated sub-ion scale Alfvénic fluctuations.

Ionospheric and thermospheric responses

Davidson et al. examines the delay in the response time of ion-neutral wind in the high-latitude ionosphere to substorm onsets [11]. Using data from Scanning Doppler Imagers (SDI) and the Poker Flat Incoherent Scatter Radar (PFISR) of 23 substorms, they find the average neutral wind response time to be 16 min. Their analysis shows that a southward turning of IMF 1.5 h before the substorm onset and large electron densities in the ionosphere lead to faster response time.

Li et al. conducts a simulation-based study comparing the ionospheric total electron content (TEC) between the South Atlantic Anomaly (SAA) and the Indian Ocean (IO) at solar maximum. The authors apply the empirical orthogonal function (EOF) method to analyze the spatial and temporal variations in both regions. The results show clear differences in the structure and behavior of the equatorial ionization anomaly (EIA) between the two areas, influenced by geomagnetic field deviations and tidal effects.

Space weather impacts

The impact of the extreme geomagnetic storm [12] of May 2024 on the re-entry of a Starlink satellite from very low-Earth orbit is studied in Oliveira et al. In comparison with the previous observations of the satellites' re-entries during a variety of geomagnetic conditions, it is shown that a sharp altitude decay starts at the start of the storm main phase, and that severity of the storm increases a speed of the satellite altitude decay and the time difference between the predicted and observed re-entry dates. The physical reasons behind the enhanced drag effects during the increased geomagnetic conditions have been discussed, as well as a need for a more detailed investigation of the causal relationship between storm occurrence and satellite orbital decay.

Li et al. studies an interplanetary coronal mass ejection [13] that triggered intense geomagnetic activity, severely degraded GNSS positioning performance in low-latitude Hong Kong. The study reveals that magnetospheric compression during the storm's initial phase caused more pronounced ionospheric scintillation [14] than that during the main phase. They also examines the accuracies of different GNSS positioning techniques. Overall, the authors attempt to establish a chain from solar wind dynamics to ionospheric turbulence and GNSS degradation, which contributes to enhancing space weather monitoring.

Space radiation poses a serious risk to crewed missions, especially to future missions to Mars, with the Galactic Cosmic

Rays (GCR) being a main contributor to the radiation dose on those missions [15]. Song et al. developed the Space-Dependent Energetic cosmic ray Modulation using MAgnetic spectrometer (SDEMMA) model, which models Galactic Cosmic Ray dynamic beyond 1.0 AU, covering the inner heliosphere between Earth and Mars. This novel model explicitly resolves radial gradients under diverse heliospheric conditions. The application of the model in the calculation of the dose equivalent rate is demonstrated.

The perspective by Wang et al. presents a paradigm-shifting argument that fundamentally reframes the role of space weather in aviation science [16]. In a critical departure from decades of research that treated space weather impacts as isolated phenomena largely confined to specific risks in polar regions, this work provides a systemic, global link between space weather events and widespread flight delays and cancellations. The authors are the first to quantitatively establish that space weather is not merely a technical concern but a significant and previously underestimated contributor to the performance degradation of the entire air transportation network.

Author contributions

YW: Writing – review and editing, Writing – original draft. BW: Writing – review and editing, Writing – original draft. AS: Writing – review and editing, Writing – original draft. NS: Writing – review and editing, Writing – original draft. YB: Writing – original draft, Writing – review and editing. GK: Writing – review and editing, Writing – original draft.

Funding

The author(s) declare that financial support was received for the research and/or publication of this article. YW and BW acknowledge support from National Natural Science Foundation of China 42174199 and 42030204, the National Key R & D Program of China (Grant No. 2022YFF0503900), the Specialized Research Fund for State Key Laboratory of Solar Activity and Space Weather, Guangdong Basic and Applied Basic Research Foundation 2023B1515040021 and 2024A1515011442, Shenzhen Technology Project (GXWD20220817152453003, JCYJ20240813104927037 and RCJC20210609104422048), and Shenzhen Key Laboratory Launching Project (No. ZDSYS20210702140800001); AS acknowledges support from the UK Space Agency under Grant ST/T002964/1; NS was supported by the NASA Cooperative Agreement 80NSSC21M0180G and NASA grant 80NSSC23K0446; YB was supported by STFC RAL Space In House Research award ST/M001083/1.

Conflict of interest

The authors declare that the research was conducted in the absence of any commercial or financial relationships that could be construed as a potential conflict of interest.

Generative AI statement

The author(s) declare that no Generative AI was used in the creation of this manuscript.

Publisher's note

All claims expressed in this article are solely those of the authors and do not necessarily represent those of their affiliated organizations, or those of the publisher, the editors and the reviewers. Any product that may be evaluated in this article, or claim that may be made by its manufacturer, is not guaranteed or endorsed by the publisher.

References

1. Zhang H, Sibeck DG, Zong Q-G, Gary SP, McFadden JP, Larson D, et al. Time history of events and macroscale interactions during substorms observations of a series of hot flow anomaly events. *J Geophys Res Space Phys* (2010) 115(A12). doi:10.1029/2009JA015180

2. Omidi N, Eastwood JP, Sibeck DG. Foreshock bubbles and their global magnetospheric impacts. *J Geophys Res Space Phys* (2010) 115(A6). doi:10.1029/2009JA014828

3. Siscoe GL, Crooker NU, Belcher JW. Sunward flow in Jupiter's magnetosheath. *Geophys Res Lett* (1980) 7(1):25–8. doi:10.1029/GL007i001p00025

4. Gosling JT, Skoug RM, McComas DJ, Smith CW. Direct evidence for magnetic reconnection in the solar wind near 1 AU. *J Geophys Res* (2005) 110(A1):A01107. doi:10.1029/2004ja010809

5. Di Matteo S, Katsavrias C, Kepko L, Viall NM. Azimuthal size scales of solar wind periodic density structures. *The Astrophysical J* (2024) 969(1):67. doi:10.3847/1538-4357/ad479e

6. Di Matteo S, Villante U. The identification of solar wind waves at discrete frequencies and the role of the spectral analysis techniques. *J Geophys Res Space Phys* (2017) 122(5):4905–20. doi:10.1002/2017JA023936

7. Southwood DJ, Kivelson MG. Charged particle behavior in low-frequency geomagnetic pulsations 1. Transverse waves. *J Geophys Res Space Phys* (1981) 86(A7):5643–55. doi:10.1029/JA086iA07p05643

8. Kivelson MG, Etcheto J, Trotignon JG. Global compressional oscillations of the terrestrial magnetosphere: the evidence and a model. *J Geophys Res Space Phys* (1984) 89(A11):9851–6. doi:10.1029/JA089iA11p09851

9. Shaw RR, Gurnett DA. Electrostatic noise bands associated with the electron gyrofrequency and plasma frequency in the outer magnetosphere. *J Geophys Res (1896-1977)* (1975) 80(31):4259–71. doi:10.1029/JA080i031p04259

10. Quest KB, Shapiro VD. Evolution of the fire-hose instability: Linear theory and wave-wave coupling. *J Geophys Res Space Phys* (1996) 101(A11):24457–69. doi:10.1029/96JA01534

11. Rostoker G, Akasofu S-I, Foster J, Greenwald RA, Kamide Y, Kawasaki K, et al. Magnetospheric substorms—definition and signatures. *J Geophys Res Space Phys* (1980) 85(A4):1663–8. doi:10.1029/JA085iA04p01663

12. Gonzalez WD, Joselyn JA, Kamide Y, Kroehl HW, Rostoker G, Tsurutani BT, et al. What is a geomagnetic storm? *J Geophys Res Space Phys* (1994) 99(A4):5771–92. doi:10.1029/93JA02867

13. Richardson IG, Cane HV. Near-earth interplanetary coronal mass ejections during solar cycle 23 (1996 – 2009): catalog and summary of properties. *Solar Phys* (2010) 264(1):189–237. doi:10.1007/s11207-010-9568-6

14. Kintner PM, Ledvina BM, de Paula ER. GPS and ionospheric scintillations. *Space Weather-the Int J Res Appl* (2007) 5(9). doi:10.1029/2006SW000260

15. Durante M, Cucinotta FA. Physical basis of radiation protection in space travel. *Rev Mod Phys* (2011) 83(4):1245–81. doi:10.1103/RevModPhys.83.1245

16. Wang Y, Xu XH, Wei FS, Feng XS, Bo MH, Tang HW, et al. Additional flight delays and magnetospheric–ionospheric disturbances during solar storms. *Scientific Rep* (2023) 13(1):3246. doi:10.1038/s41598-023-30424-2

frontiers | Frontiers in Physics

TYPE Original Research
PUBLISHED 07 February 2024
DOI 10.3389/fphy.2024.1334531

Check for updates

OPEN ACCESS

EDITED BY
Boyi Wang,
Harbin Institute of Technology, Shenzhen, China

REVIEWED BY
Xiaochen Shen,
Boston University, United States
Xochitl Blanco-Cano,
National Autonomous University of Mexico, Mexico

*CORRESPONDENCE
Nigang Liu,
liung5@mail.sysu.edu.cn
Zhenpeng Su,
szpe@mail.ustc.edu.cn

RECEIVED 07 November 2023
ACCEPTED 25 January 2024
PUBLISHED 07 February 2024

CITATION
Xie Y, Liu N, Su Z, Yi S, He Z, Yu J, Li K, Chen Z and Cui J (2024), Interplanetary shock induced intensification of electron cyclotron harmonic waves in the Earth's inner magnetosphere. *Front. Phys.* 12:1334531. doi: 10.3389/fphy.2024.1334531

COPYRIGHT
© 2024 Xie, Liu, Su, Yi, He, Yu, Li, Chen and Cui. This is an open-access article distributed under the terms of the Creative Commons Attribution License (CC BY). The use, distribution or reproduction in other forums is permitted, provided the original author(s) and the copyright owner(s) are credited and that the original publication in this journal is cited, in accordance with accepted academic practice. No use, distribution or reproduction is permitted which does not comply with these terms.

Interplanetary shock induced intensification of electron cyclotron harmonic waves in the Earth's inner magnetosphere

Yi Xie[1,2], Nigang Liu[1,2]*, Zhenpeng Su[3,4,5]*, Siyang Yi[1,2], Zhaoguo He[1,2], Jiang Yu[1,2], Kun Li[1,2], Zuzheng Chen[1,2] and Jun Cui[1,2]

[1]Planetary Environmental and Astrobiological Research Laboratory (PEARL), School of Atmospheric Sciences, Sun Yat-Sen University, Zhuhai, China, [2]Key Laboratory of Tropical Atmosphere-Ocean System, Sun Yat-Sen University, Ministry of Education, Zhuhai, China, [3]CAS Center for Excellence in Comparative Planetology, CAS Key Laboratory of Geospace Environment, Mengcheng National Geophysical Observatory, University of Science and Technology of China, Hefei, China, [4]Deep Space Exploration Laboratory, School of Earth and Space Sciences, University of Science and Technology of China, Hefei, China, [5]Collaborative Innovation Center of Astronautical Science and Technology, Hefei, China

Electron cyclotron harmonic (ECH) waves are electrostatic emissions frequently observed in the Earth's magnetosphere. By precipitating magnetospheric hot electrons into the ionosphere, ECH waves play a critical role in the formation of diffuse aurora. Previous research has extensively investigated the strong dependence of ECH waves on the geomagnetic activities. In this study, we present the first report of the prompt response of ECH waves to an interplanetary shock on the basis of WIND and Van Allen Probes observations. Our observations and analyses demonstrate that the interplanetary shock compression can increase >0.1 keV hot electron fluxes in the dayside inner magnetosphere, consequently leading to the prompt intensification of ECH waves by promoting the wave instability. These findings expand our comprehension of the impacts of solar wind disturbances on magnetospheric plasma waves and offer fresh insights into solar wind-magnetosphere-ionosphere coupling.

KEYWORDS

interplanetary shock, electron cyclotron harmonic wave, solar wind-magnetosphere-ionosphere coupling, inner magnetosphere, plasma wave instability

1 Introduction

Electron cyclotron harmonic (ECH) waves are electrostatic emissions [1] that typically appear in thermal plasmas in the Earth's magnetosphere [2–6]. They are usually observed as harmonic wave bands at frequencies between multiples of electron gyrofrequency (f_{ce}) [7–9]. Through cyclotron resonance, ECH waves are able to efficiently precipitate keV electrons from the magnetosphere to the ionosphere, contributing to the formation of diffuse aurora [10–16]. Therefore, a comprehensive understanding of the spatiotemporal distribution of ECH waves is required to forecast space weather [17–22].

The generation of ECH waves is proposed to be associated with Bernstein-mode instability driven by hot electron loss cone distributions [23,24]. These emissions with quasi-perpendicular wave vectors are confined near their source regions [24]. While

extensive event and statistical studies have focused on the strong dependence of ECH waves on geomagnetic activities [3,25–27], none have directly established a link between ECH waves and solar wind disturbances. Interplanetary shocks, a subset of solar wind discontinuities frequently observed during active days [28–31], are highly geoeffective [32–35]. Numerous works have reported the immediate impacts of interplanetary shocks on magnetospheric plasma waves, including ultra low frequency waves, whistler-mode waves, magnetosonic waves, and EMIC waves [36–44]. Thus, the questions that naturally arise are whether and how an interplanetary shock can abruptly influence magnetospheric ECH waves.

In this study, using observations from the WIND [45] and Van Allen Probes missions [46], we present a representative ECH wave event during an interplanetary shock. The observations and analyses show that a shock compression can increase > 0.1 keV hot electron fluxes in the Earth's dayside inner magnetosphere, thus leading to the prompt intensification of ECH waves by promoting the wave instability.

2 Observation

Here we utilize the combined observations of WIND and Van Allen Probes to monitor the prompt response of ECH wave to an interplanetary shock. The Wind satellite operated in a halo orbit near the L1 Lagrange point. The Solar Wind Experiment (SWE) [47], the Magnetic Fields Investigation (MFI) [48], and the Three-Dimensional Plasma and Energetic Particle Investigation (3DP) [49] onboard WIND measured the solar wind parameters. The Van Allen Probes mission, comprising two identical probes (termed as RBSP-A and RBSP-B), orbited near the equator with perigees of approximately 0.1 R_E and apogees of approximately 6 R_E [46]. In this work, we mainly used the High Frequency Receiver (HFR) of the Electric and Magnetic Field Instrument Suite and Integrated Science (EMFISIS) instrument [50] to observe ECH waves. The HFR provided electric spectral intensities in the frequency range of 10–400 kHz in survey mode. Note the Waveform Frequency Receiver (WFR) of EMFISIS can provide electric spectral intensities at frequencies ranging from 10 Hz to 12 kHz. However, the WFR electric spectral data had been contaminated seriously above 5 kHz during the event in this work, and did not allow the clear observation of ECH waves. Following the method in Kurth et al. [51], we can derive the background plasma density N_e from the upper hybrid resonance frequency. The fluxgate magnetometer (MAG) of EMFISIS and the Electric Field and Waves (EFW) [52] instrument captured the background electromagnetic field. The Helium Oxygen Proton Electron (HOPE) Mass Spectrometer [53] of the Energetic particle, Composition and the Thermal (ECT) plasma suite [54] provided the electron flux data from several eV to ~ 50 keV. The geomagnetic indices were obtained from the OMNI database.

Figures 1A–G plot the solar wind parameters observed by WIND from 07 June 2014 to 11 June 2014. At 16:12 UT on 07 June 2014, a fast forward interplanetary shock was monitored, marked by abrupt increases in magnetic field strength, velocity, density, temperature, and dynamic pressure. According to the list by Chi et al. [55], there was an interplanetary coronal mass ejection (ICME) between approximately 19:00 UT on 08 June 2014 and 10:00 UT on 10 June 2014. This ICME exhibited typical features, including a declining velocity profile, low proton temperature, and bidirectional streaming of suprathermal electrons [56,57]. In a statistical sense, ICMEs [c1]might be the major driver of shocks [c2]during solar maximum, but shocks exist during solar minimum even if few ICMEs are present [58]. The large time lapse between the shock and the ICME front makes it uncertain to determine their relations. Whether this shock was driven by the ICME or a fast solar wind stream requires detailed studies in future and beyond the scope of this work. Approximately 41 min after its arrival in WIND data, the interplanetary shock with a drastic increase in solar wind dynamic pressure from 1 nPa to 6 nPa, compressed the Earth's magnetosphere. This compression caused an increase of SYM-H index from −5 nT to 23 nT. Figure 1H shows the response of inner magnetospheric ECH waves to the interplanetary shock as observed by RBSP-A on 07 June 2014. Around the shock arrival, RBSP-A operated in the northern hemisphere (MLAT~ 15°) of dayside magnetosphere (L~ 6, MLT~ 9 hr) under relatively quiet conditions (SYM-H > -10 nT and AE < 350 nT). Before the shock arrival, RBSP-A received faint and intermittent ECH wave signals ($P_E < 1 \times 10^{-10}$ mV^{2}m^{-2}Hz^{-1}) appearing as harmonic bands below the upper hybrid resonance frequency f_{UHR}. Note the WFR observations were too noisy to identify ECH waves below 10 kHz. As marked by the vertical dashed lines (16:53 UT), the shock compression caused a sudden and significant intensification of ECH wave power, increasing by approximately one order of magnitude to $P_E \sim 1 \times 10^{-9}$ mV^{2}m^{-2}Hz^{-1}. Compared with the ECH waves typically confined in the near equatorial region, this ECH wave event was observed at relatively higher latitudes (MLAT~ 15°) with a weak intensity. This is consistent with the statistical characteristics of ECH waves showed in previous studies [25,59,60]. It should also be mentioned that this ECH wave intensification was not a manifestation of the spatial variation of waves but a temporal behavior. During the inbound pass before the shock arrival, RBSP-A only observed weak or no ECH waves in larger L-shells with comparable MLT (as shown in Figure 1H). The inward movement of these weak ECH waves triggered by shock compression could not explain the wave intensification. Thus, the ECH wave intensification should be related to variations in plasma environment triggered by the shock compression, which will be further investigated in the following section.

3 Physical explanations

Figure 2 presents the temporal evolutions of background electromagnetic fields and plasmas measured by RBSP-A during the event. Corresponding to the shock compression at 16:53 UT (marked by the vertical dashed line in Figure 2), the background magnetic field intensity increased from 200 nT to 223 nT. In contrast, the background plasma density N_e in the low-density plasma trough remained consistently below 10 cm^{-3} (which is dominant by the cold plasma) with no systematic variations after the shock. The interplanetary shock also induced ultralow-frequency waves with impulsive electric field amplitudes of 5 mV/m, subsequently resulting in a significant acceleration of hot electron fluxes above 0.1 keV. It is noteworthy that the similar responses of

10.3389/fphy.2024.1334531

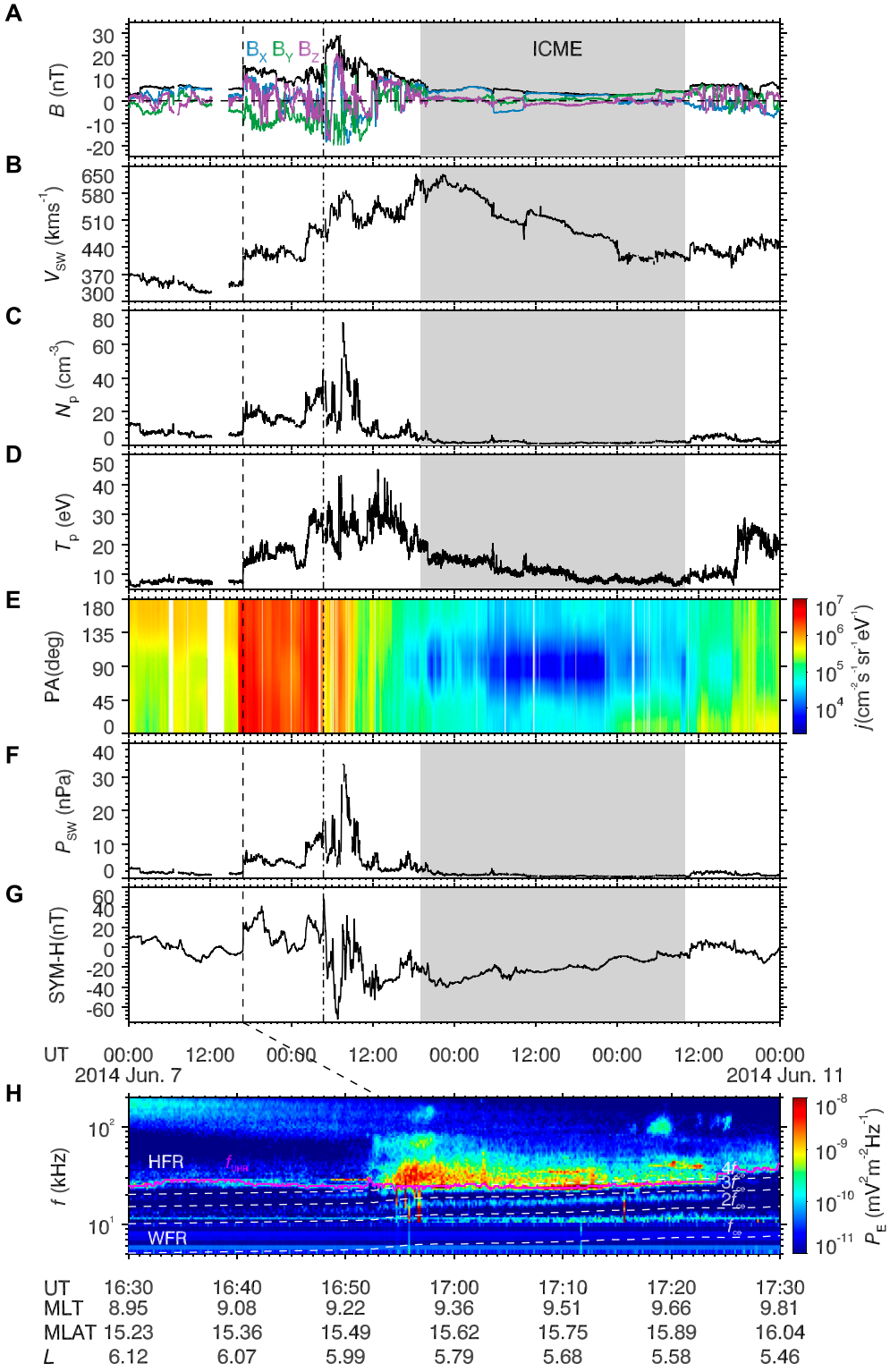

FIGURE 1
Overview of the ECH wave event on 07 June 2014: **(A)** Magnetic field magnitude B_t and components (B_X, B_Y, B_Z) in the geocentric solar magnetospheric (GSM) coordinate. **(B)** Bulk velocity V_{sw}. **(C)** Proton density N_p. **(D)** Proton temperature T_p. **(E)** suprathermal electron flux j. **(F)** Solar wind dynamic pressure P_{sw}. **(G)** Geomagnetic SYM-H index. **(H)** Zoom-in figure of Wave electric power spectra P_E with overplotted electron gyrofrequency (f_{ce}) harmonics and upper hybrid resonance frequency (f_{UHR}). The solar wind measurements by Wind satellite at ~ 1.26 × 10^6 km from Earth have been shifted 41 min according to the SYM-H measurements. The shadowed areas mark an ICME. The vertical dashed lines in each panel mark the arrival of interplanetary shock.

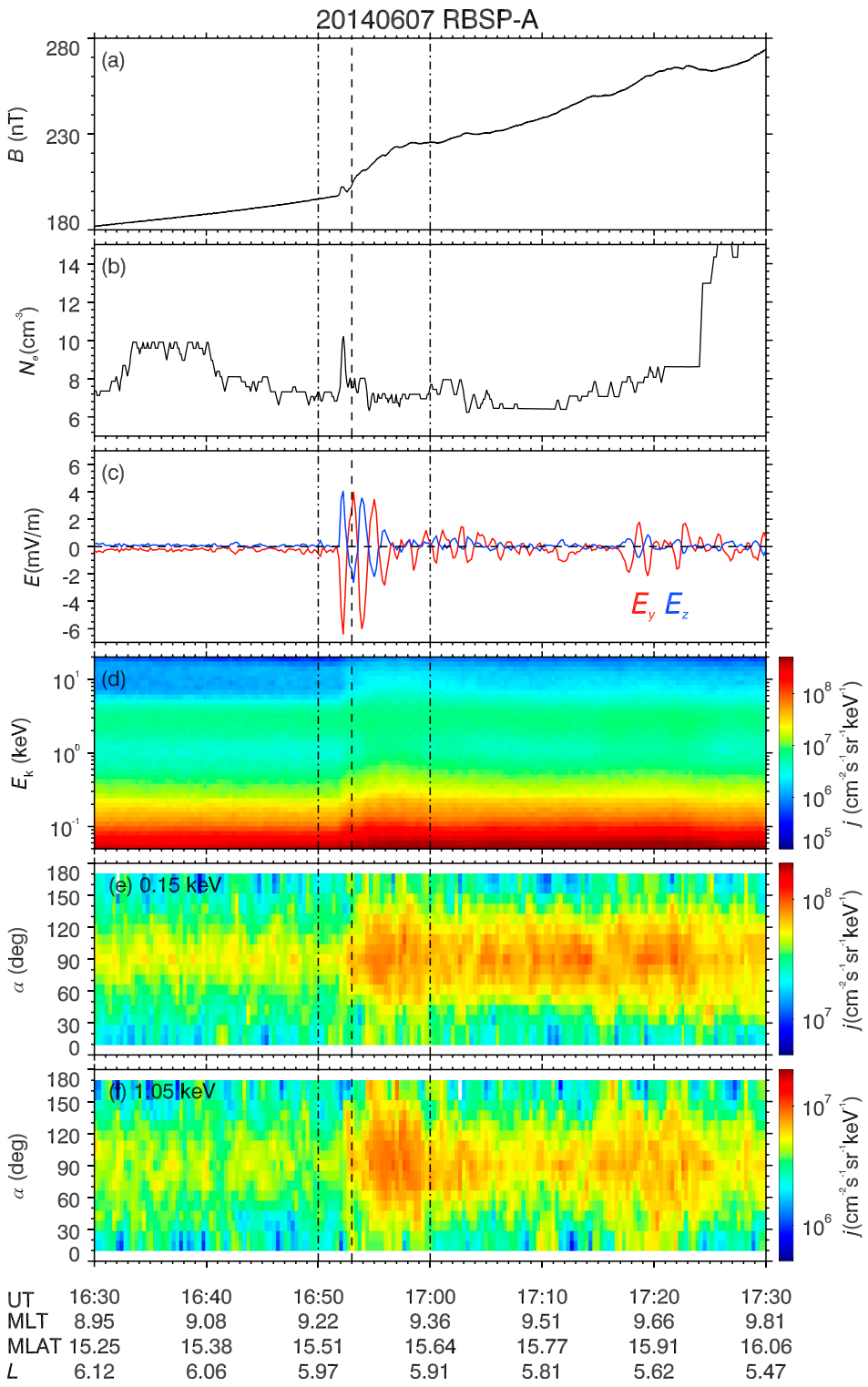

FIGURE 2
Temporal evolution of background fields and plasmas of 07 June 2014 event: **(A)** background magnetic field strength B. **(B)** Background plasma density N_e. **(C)** Electric field components in the modified geocentric solar ecliptic (mGSE) coordinate system. **(D)** electron spin-averaged differential flux j. **(E,F)** differential electron fluxes j at specific energies. The vertical dashed line mark the arrival of interplanetary shock, and the vertical dash-dotted lines mark the pre-shock and post-shock moments for the growth rate calculation.

magnetospheric electron fluxes ranging from low energy to relativistic energy to interplanetary shocks have been reported by numerous studies [37,61–65]. However, the modulation of hot electron fluxes by the ULF wave can not be clearly observed in Figures 2D–F. Possible explanations for this could be the following: 1) rapid relaxation by magnetospheric plasma waves (ECH waves

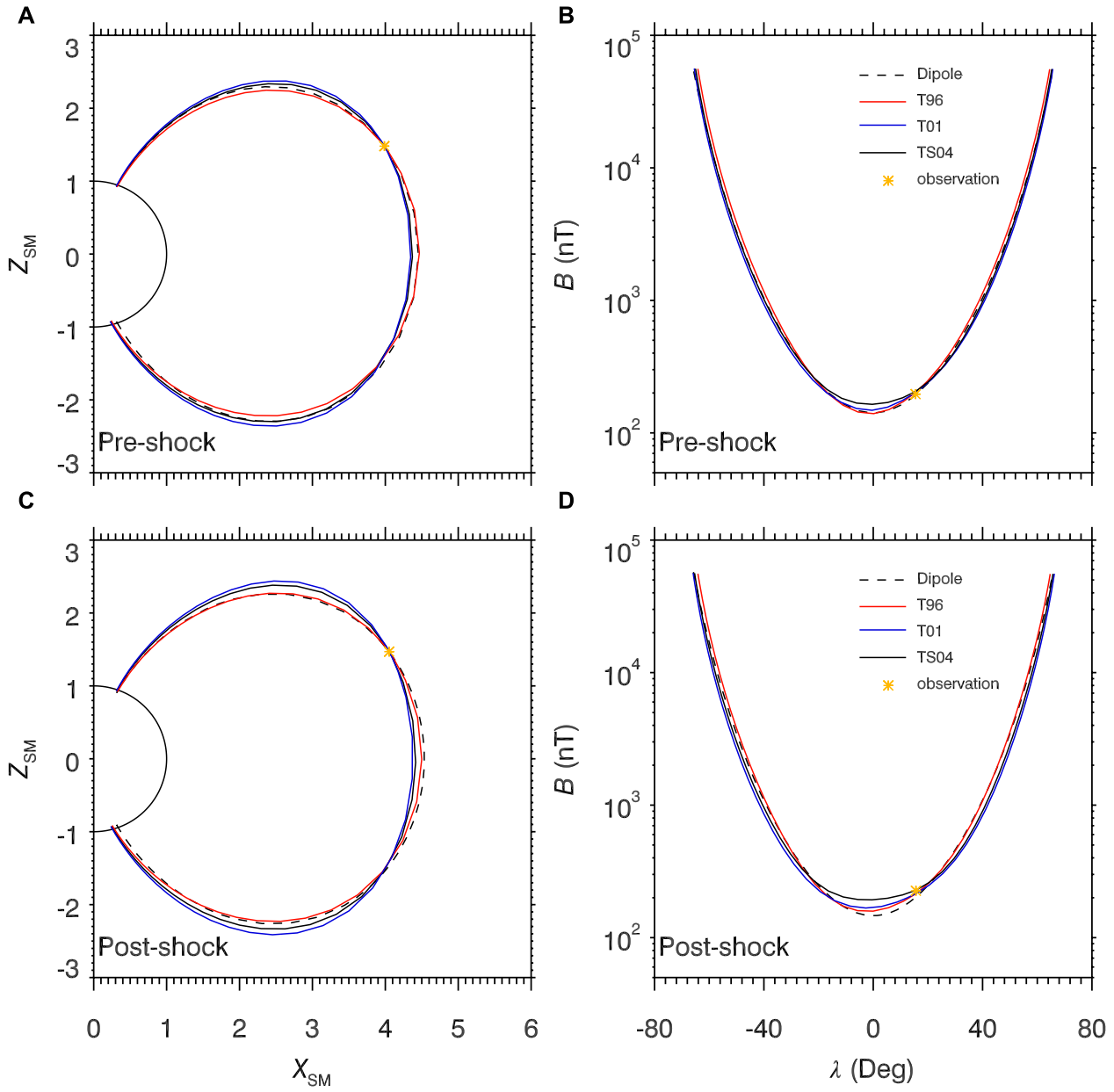

FIGURE 3
Comparison between different geomagnetic models at the pre-shock and post-shock moments on 07 June 2014: **(A,C)** Modeled magnetic field configurations in the SM X-Z plane along the field lines traced from the RBSP-A location and **(B,D)** corresponding field intensities as a function of magnetic latitude for dipole (black dashed lines), T96 (red solid lines), T01 (blue solid lines), and TS04 (black solid lines) geomagnetic models. The orange asterisks represent the locations of RBSP-A and observed magnetic field intensities at specific moments.

and chorus); 2) the comparable cadence (~21 s) of HOPE instrument to ULF wave period (~1–2 min). As reported by previous theoretical studies [23,24], the enhancement of hot electron fluxes could promote the wave instability by providing more free energy, and then lead to the wave intensification.

To further determine the influence of shock compression on the generation of ECH waves, we use the BO code [66] to calculate the linear dispersion relations and wave growth rates. The inputs of the code include the background magnetic field intensity and electron phase space density F. The observed electron PSD is fitted by a total of N bi-Maxwellian components.

$$F(v_\perp, v_\parallel) = \sum_{i=1}^{N} F_i, \tag{1}$$

$$F_i = \frac{n_i}{\pi^{3/2} V_{\parallel th_i} V_{\perp th_i}^2} \exp\left[-\frac{(v_\parallel - V_{dz_i})^2}{V_{\parallel th_i}^2}\right] \times \left\{\frac{r_{a_i}}{A_{a_i}} \exp\left[-\frac{(v_\perp - V_{dr_i})^2}{V_{\perp th_i}^2}\right] + \frac{r_{b_i}}{\alpha_i A_{b_i}} \exp\left[-\frac{(v_\perp - V_{dr_i})^2}{\alpha_i V_{\perp th_i}^2}\right]\right\}, \tag{2}$$

where $r_{a_i} = \frac{1-\alpha_i\Delta_i}{1-\alpha_i}$, $r_{b_i} = \frac{-\alpha_i+\alpha_i\Delta_i}{1-\alpha_i}$. For the ith plasma component, n_i is the density; $V_{\parallel th_i}$, $V_{\perp th_i}$, V_{dz_i}, and V_{dr_i} are the parallel thermal

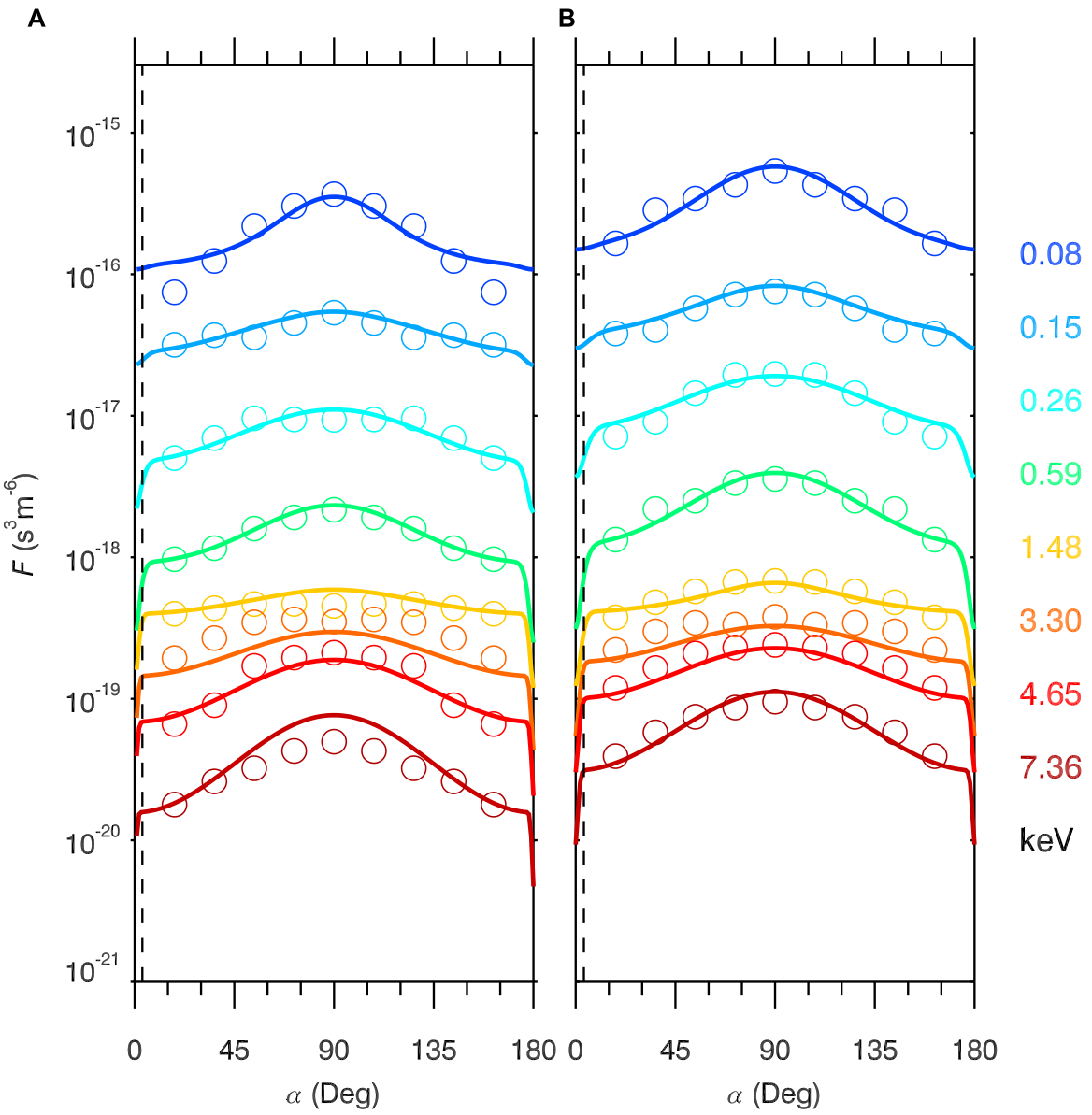

FIGURE 4
Electron phase space densities in pitch angle-energy space at pre-shock **(A)** and post-shock **(B)** moments on 07 June 2014. The solid lines and circles represent modeled and observed electron phase space densities, and the black vertical dashed lines represent the modeled loss cone angles.

velocity, perpendicular thermal velocity, parallel drift velocity, and perpendicular ring beam velocity; expressions $A_{a_i} = A_{b_i} = 1$ when $V_{dr_i} = 0$; α_i and Δ_i characterize the size and the depth of the loss cone. According to previous numerical studies [24,67,68], we set the background cold electrons as the 1 eV component for calculation. Note the sum of each component density n_i is equal to the background plasma density N_e.

As the ECH wave powers (Figure 1H) and background plasma conditions (Figure 2) exhibited systematic variations following the interplanetary shock, we selected two specific times for analyses (marked by the vertical dash-dotted lines in Figure 2): 1) pre-shock moment at 16:50 UT; 2) post-shock moment at 17:00 UT. The satellite data provide direct measurements of background magnetic field intensity and plasma density for the growth rate calculation. However, because of the instrumentation constraints and data quality, electron flux data from HOPE are unavailable in small pitch angles ($< 18°$) during this event. Theoretically, the local loss cone angle α_{loss} of bounced electrons can be determined by the following expression [69]:

$$\sin \alpha_{\text{loss}}{}^2 = \frac{B_0}{B_{\text{loss}}} \tag{3}$$

where B_0 and B_{loss} are the magnetic field intensities at the satellite position and low altitude mirror point where electrons get lost. Here we assume the mirror point locates at 100 km height. Because of the absence of measurements for B_{loss}, we rely on geomagnetic models to derive the ratio $\frac{B_0}{B_{\text{loss}}}$. Figure 3 shows comparisons between different Tsyganenko geomagnetic models [70–72] around the interplanetary shock. Since the satellite was located in the inner magnetosphere, the field line configurations of the Tsyganenko models closely resemble

TABLE 1 The fitting parameters of electron phase space densities for the 07 June 2014 event.

Groups	Components	n_i (m^{-3})	$T_{\parallel th_i}$ (keV)	$T_{\perp th_i}$ (keV)	α_i	Δ_i	V_{dz_i}	V_{dr_i}
pre-shock (16:50 UT)	1	4.00×10^6	0.001	0.001	1.0	1.0	0	0
	2	3.00×10^6	0.0082	0.0150	1.0	1.0	0	0
	3	3.00×10^5	0.0411	0.0501	1.0	1.0	0	0
	4	6.00×10^4	0.1393	0.2406	0.01	0.2	0	0
	5	1.30×10^5	1.7769	2.9112	0.0016	0.3	0	0
post-shock (17:00 UT)	1	4.00×10^6	0.001	0.001	1.0	1.0	0	0
	2	3.00×10^6	0.0125	0.0192	1.0	1.0	0	0
	3	3.00×10^5	0.0478	0.0601	1.0	1.0	0	0
	4	1.10×10^5	0.1557	0.2730	0.011	0.2	0	0
	5	1.60×10^5	2.2289	3.6845	0.0018	0.3	0	0

those of the dipole field. Different with the situation in larger L-shells, there was no off-equatorial magnetic field minimum on the field lines of this event, which has been suggested to explain the latitudinal extension of ECH waves. However, even in the inner magnetosphere ($5 < L < 6.6$) usually with the absence of off-equatorial magnetic field minimums, ECH waves can extend to MLAT > 15° with decreasing amplitudes according to MMS observations (as shown in Figure 3 of Lou et al. [59]). Further understanding of the high-latitude ECH waves requires detailed investigations in the future. Comparing with the T96 and T01 models, the magnetic field strengths derived from TS04 model align more closely with the observation values after the shock compression. Therefore, we use TS04 geomagnetic model [72] to estimate the loss cone size. Based on Eq. 3, the modeled loss cone angles α_{loss} are 3.49° and 3.68° at the pre-shock and post-shock moments. These approximations suggest that the interplanetary shock may not trigger significant changes in the electron loss cone through adiabatic processes during this event. Taking into account the estimated loss cone sizes, Figure 4 plots the modeled and observed electron phase space densities at the pre-shock and post-shock moments. To reduce the intense fluctuations of electron flux data (as shown in Figures 2E, F), we smoothed the data over 8 adjacent time points (~168 s) and symmetrized the data with respect to the 90° pitch angle. The detailed fitting parameters of bi-Maxwellian components are given in Table 1. Generally speaking, the modeled electron phase space densities are in reasonable agreement with the observations.

Figures 5A, D illustrate the ECH wave linear growth rates calculated by the BO code within $87° < \theta < 90°$ at the pre-shock and post-shock moments. Based on the observations (Figure 1H), we focus on the first three harmonic bands below the upper hybrid resonance frequency. It is evident that the modeled growth rates roughly share the similar frequency distributions with the observed ECH wave intensities, indicating the electron phase space density fittings reasonably reflect the real conditions. In comparison to the pre-shock moment, the modeled growth rates at the post-shock moment increase by approximately threefold, qualitatively explaining the intensification of ECH waves after the interplanetary shock. Figures 5B, E show the wave frequency ω/Ω_e as a function of normalized wave vector $k\rho_e$ at $\theta = 89°$ (ω is the wave angular frequency, Ω_e is the electron angular gyrofrequency, and ρ_e is the gyroradius). These dispersion relations enable the calculation of the wave minimum resonant energy E_{min}, which can be determined as follows.

$$E_{min} = \frac{1}{2} m_e v_\parallel^2, \tag{4}$$

$$v_\parallel = \frac{\omega - n\Omega_e}{k_\parallel}, \tag{5}$$

here $v\parallel$ is the electron parallel velocity, $k\parallel = k\cos\theta$ is the wave parallel vector, n is the resonance order, and m_e is the electron rest mass. Based on Figures 5B, C, E, F show the minimum resonant energy E_{min} of different harmonic bands (each with a specific resonance order) as a function of wave frequency ω/Ω_e at $\theta = 89°$. Combined with the wave growth rates shown in Figures 5A, D, the corresponding E_{min} for the frequencies with positive growth rates predominantly falls within the range of 0.1 keV–1 keV. These calculations indicate the ECH wave intensification is highly associated with the shock-induced enhancement of > 0.1 keV hot electrons, which enlarges the free energy for ECH wave excitation.

4 Discussion and conclusion

In contrast to previous studies focusing on the dependence of ECH waves on geomagnetic activities [3,25,26,59], here we present the first report of the prompt response of ECH waves to an interplanetary shock based on the WIND and Van Allen Probes observations. A fast forward interplanetary shock with a drastic increase in solar wind dynamic pressure (from 1 nPa to 6 nPa) compressed the Earth's magnetosphere, causing the prompt intensification of dayside inner magnetospheric ECH waves. The observations and analyses suggest that the shock-induced enhancement of > 0.1 keV hot electron enlarges the free energy for the ECH wave excitation, consequently leading to the intensification of ECH waves by promoting the wave instability. Another intriguing phenomenon is the impact of a solar wind disturbance on ECH waves on 08 June 2014. As marked by the

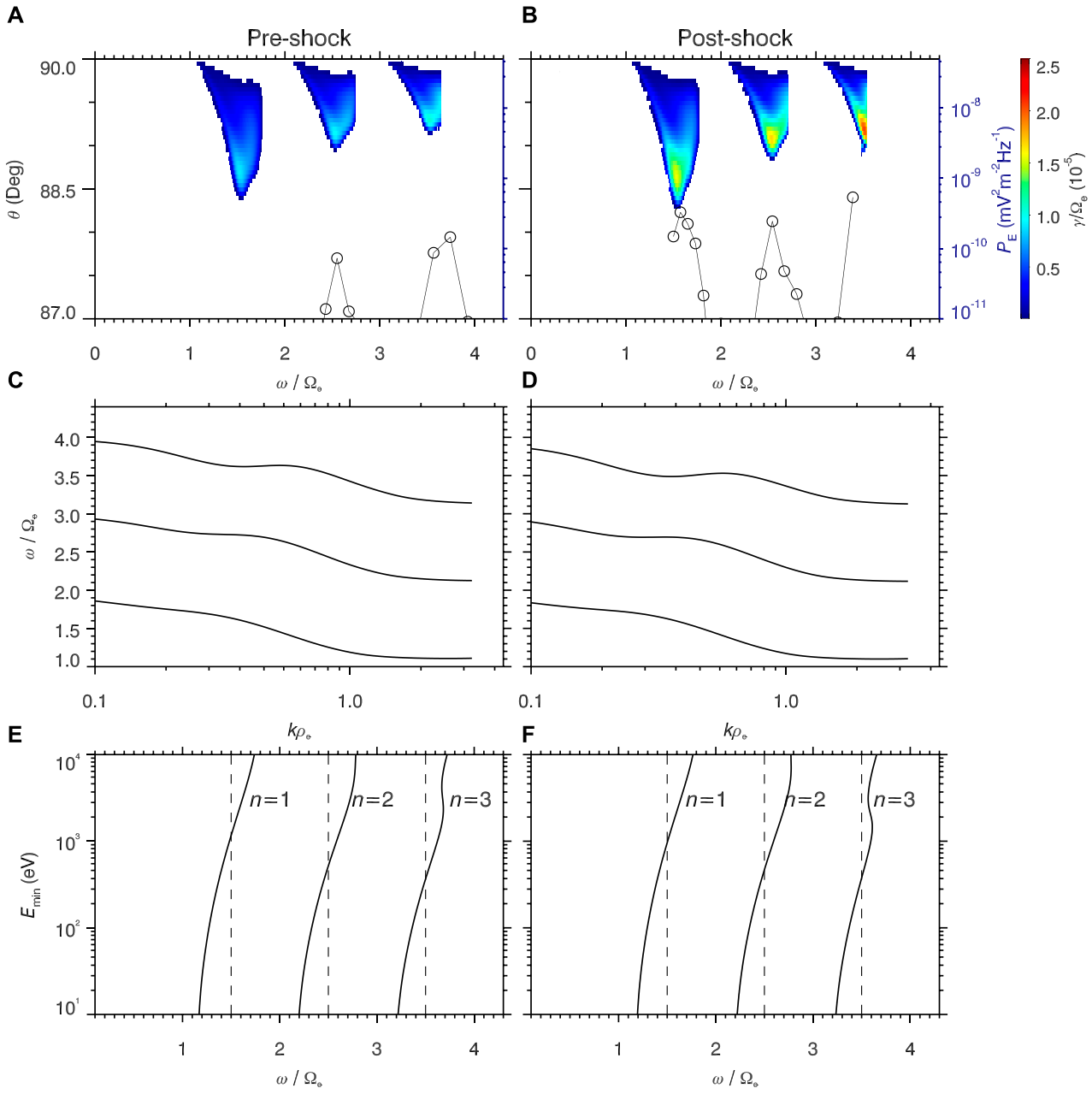

FIGURE 5
ECH wave growth rates, dispersion relations, and minimum resonant energy of first three harmonic bands at pre-shock and post-shock moments. **(A,D)** linear wave growth rates γ/Ω_e as a function of frequency ω/Ω_e and wave normal angle θ with overplotted electric power intensity P_E of ECH waves from HFR data; **(B,E)** wave frequency ω/Ω_e as a function of normalized wave vector $k\rho_e$ (ρ_e is the gyroradius) at $\theta = 89^\circ$; **(C,F)** minimum resonant energy E_{min} of different harmonic bands (with specific resonance order) as a function of wave frequency ω/Ω_e at $\theta = 89^\circ$.

vertical dash-dotted line in Figures 1A–G, there were increases in solar wind magnetic field and dynamic pressure at ~04:44 UT on 08 June 2014. Different with the event on 07 June 2014, this structure was not an interplanetary shock. Figure 6 shows ECH wave observations measured by the twin Van Allen Probes satellites on 08 June 2014. Corresponding to the arrival of the solar wind disturbance (marked by the vertical dash-dotted line in Figure 6), RBSP-A near the perigee was unable to receive ECH wave signals, while RBSP-B in the dayside magnetosphere ($L \sim 5.8$) observed the prompt intensification of ECH waves. In addition to the prompt impacts, the solar wind compressions in magnetosheath on 07 and 08 June 2014 could increase the dayside reconnection rate and lead to the strong convection in the magnetosphere [73]. Probably because of the associated hot electron injections and plasmasphere erosions, both satellites observed the enhanced occurrences of ECH waves on 08 June 2014. A comprehensive understanding of the dependence of ECH waves on solar winds requires further investigation in the future.

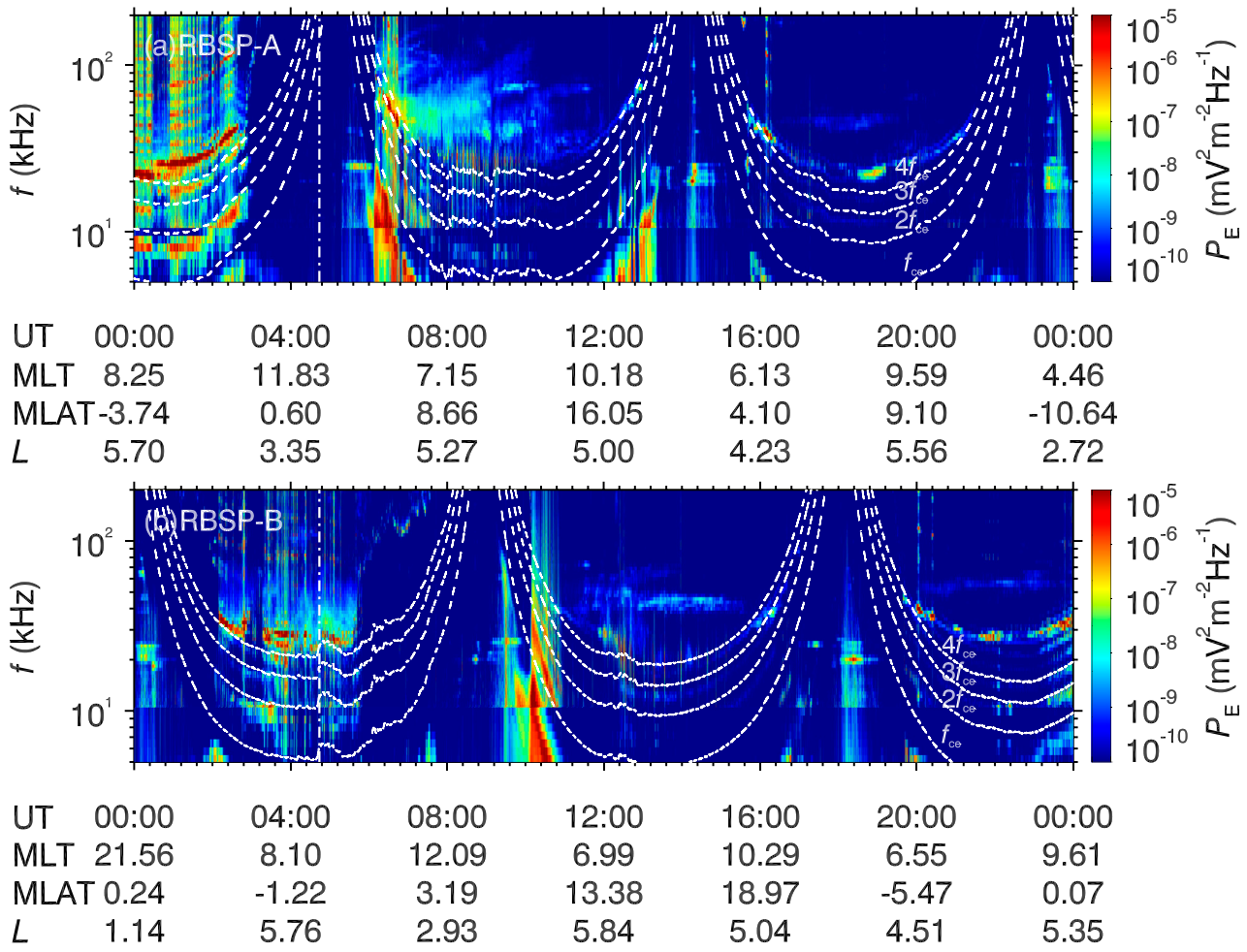

FIGURE 6
Wave electric power spectra P_E observed by **(A)** RBSP-A and **(B)** RBSP-B on 08 June 2014. The vertical dash-dotted line in **(A,B)** marks the same moment as the dash-dotted line in Figures 1A–G.

In this work, we employ the BO code to compute the linear wave dispersion relation and growth rate of ECH waves. The calculations are based on the hot electron flux data measured by HOPE. However, as shown in Figure 4, the electron flux data exhibit irregular fluctuations over pitch angles and are notably absent within the loss cone, and the bi-Maxwellian fittings of electron fluxes are unable to capture all the subtle changes. Because of these data and technical limitations, the BO modeling here only provides a qualitative understanding of the observed wave evolutions following the interplanetary shock. In the future, detailed numerical studies are required to evaluate the results obtained in this work.

The prompt responses of magnetospheric waves to solar wind disturbances have attracted increasing interests. Recent works have reported the immediate effects of solar wind disturbances on chorus, hiss, magnetosonic waves, and electromagnetic ion cyclotron waves [36–44,74]. Owing to the important roles of these plasma waves in magnetosphere dynamics, solar wind disturbances could lead to non-negligible changes in space weather by affecting the spatiotemporal distribution of plasma waves. For instance, the ECH wave intensification event reported in this work might contribute to the formation of shock diffuse aurora, attributed to ECH waves' capacity to scatter keV electrons [75]. Our present findings, in conjunction with previous research, have brought new insights into the solar wind-magnetosphere-ionosphere coupling and highlighted the dependence of magnetospheric waves on the solar wind disturbances.

Data availability statement

The original contributions presented in the study are included in the article/supplementary material, further inquiries can be directed to the corresponding authors.

Author contributions

YX: Data curation, Formal Analysis, Visualization, Writing–review and editing. NL: Data curation, Formal Analysis, Investigation, Methodology, Project administration, Visualization, Writing–original draft. ZS: Funding acquisition, Project

administration, Writing–review and editing. SY: Writing–review and editing. ZH: Writing–review and editing. JY: Writing–review and editing. KL: Writing–review and editing. ZC: Writing–review and editing. JC: Writing–review and editing.

Funding

The author(s) declare financial support was received for the research, authorship, and/or publication of this article. This work was supported by the National Natural Science Foundation of China grants 42004140, 42130204, 42188101, and 42274198, the Strategic Priority Research Program of Chinese Academy of Sciences grant XDB 41000000, and the Key Research Program of the Chinese Academy of Sciences grant ZDRE-KT-2021-3.

Conflict of interest

The authors declare that the research was conducted in the absence of any commercial or financial relationships that could be construed as a potential conflict of interest.

Publisher's note

All claims expressed in this article are solely those of the authors and do not necessarily represent those of their affiliated organizations, or those of the publisher, the editors and the reviewers. Any product that may be evaluated in this article, or claim that may be made by its manufacturer, is not guaranteed or endorsed by the publisher.

References

1. Shaw RR, Gurnett DA. Electrostatic noise bands associated with the electron gyrofrequency and plasma frequency in the outer magnetosphere. *J Geophys Res* (1975) 80:4259–71. doi:10.1029/JA080i031p04259

2. Roeder JL, Koons HC. A survey of electron cyclotron waves in the magnetosphere and the diffuse auroral electron precipitation. *J Geophys Res* (1989) 94:2529–41. doi:10.1029/JA094iA03p02529

3. Meredith NP, Horne RB, Thorne RM, Anderson RR. Survey of upper band chorus and ECH waves: implications for the diffuse aurora. *J Geophys Res (Space Physics)* (2009) 114:A07218. doi:10.1029/2009JA014230

4. Ni B, Thorne R, Liang J, Angelopoulos V, Cully C, Li W, et al. Global distribution of electrostatic electron cyclotron harmonic waves observed on THEMIS. *Geophys Res Lett* (2011) 38:L17105. doi:10.1029/2011GL048793

5. Liu X, Chen L, Engel MA, Jordanova VK. Global simulation of electron cyclotron harmonic wave instability in a storm-time magnetosphere. *Geophys Res Lett* (2020) 47:e86368. doi:10.1029/2019GL086368

6. Gao Z, Zuo P, Feng X, Wang Y, Jiang C, Wei F. Evidence of nonlinear interactions between magnetospheric electron cyclotron harmonic waves. *Geophys Res Lett* (2020) 47:e88452. doi:10.1029/2020GL088452

7. Kennel CF, Scarf FL, Fredricks RW, McGehee JH, Coroniti FV. VLF electric field observations in the magnetosphere. *J Geophys Res* (1970) 75:6136–52. doi:10.1029/JA075i031p06136

8. Fredricks RW, Scarf FL. Recent studies of magnetospheric electric field emissions above the electron gyrofrequency. *J Geophys Res* (1973) 78:310–4. doi:10.1029/JA078i001p00310

9. Gurnett DA, Anderson RR, Tsurutani BT, Smith EJ, Paschmann G, Haerendel G, et al. Plasma wave turbulence at the magnetopause: observations from ISEE 1 and 2. *J Geophys Res* (1979) 84:7043–58. doi:10.1029/JA084iA12p07043

10. Lyons LR. Electron diffusion driven by magnetospheric electrostatic waves. *J Geophys Res* (1974) 79:575–80. doi:10.1029/JA079i004p00575

11. Horne RB, Thorne RM. Electron pitch angle diffusion by electrostatic electron cyclotron harmonic waves: the origin of pancake distributions. *J Geophys Res* (2000) 105:5391–402. doi:10.1029/1999JA900447

12. Horne RB, Thorne RM, Meredith NP, Anderson RR. Diffuse auroral electron scattering by electron cyclotron harmonic and whistler mode waves during an isolated substorm. *J Geophys Res* (2003) 108:1290. doi:10.1029/2002JA009736

13. Ni B, Thorne RM, Horne RB, Meredith NP, Shprits YY, Chen L, et al. Resonant scattering of plasma sheet electrons leading to diffuse auroral precipitation: 1. Evaluation for electrostatic electron cyclotron harmonic waves. *J Geophys Res* (2011) 116:A04218. doi:10.1029/2010JA016232

14. Tao X, Thorne RM, Li W, Ni B, Meredith NP, Horne RB. Evolution of electron pitch angle distributions following injection from the plasma sheet. *J Geophys Res* (2011) 116:A04229. doi:10.1029/2010ja016245

15. Zhang X, Angelopoulos V, Ni B, Thorne RM, Horne RB. Quasi-steady, marginally unstable electron cyclotron harmonic wave amplitudes. *J Geophys Res (Space Physics)* (2013) 118:3165–72. doi:10.1002/jgra.50319

16. Yang Q, Liu S, Yang H, Zhang S, Tang J, Xiao F, et al. Efficient scattering loss of energetic electrons by enhanced higher-band ECH waves observed by van allen probes. *Geophys Res Lett* (2023) 50:e2023GL103927. doi:10.1029/2023GL103927

17. Shprits YY, Subbotin D, Ni B. Evolution of electron fluxes in the outer radiation belt computed with the VERB code. *J Geophys Res* (2009) 114:A11209. doi:10.1029/2008JA013784

18. Su Z, Xiao F, Zheng H, Wang S. STEERB: a three-dimensional code for storm-time evolution of electron radiation belt. *J Geophys Res* (2010) 115:A09208. doi:10.1029/2009JA015210

19. Su Z, Xiao F, Zheng H, Wang S. CRRES observation and STEERB simulation of the 9 October 1990 electron radiation belt dropout event. *Geophys Res Lett* (2011) 38:L06106. doi:10.1029/2011GL046873

20. Tu W, Cunningham GS, Chen Y, Henderson MG, Camporeale E, Reeves GD. Modeling radiation belt electron dynamics during GEM challenge intervals with the DREAM3D diffusion model. *J Geophys Res* (2013) 118:6197–211. doi:10.1002/jgra.50560

21. Glauert SA, Horne RB, Meredith NP. Three-dimensional electron radiation belt simulations using the BAS Radiation Belt Model with new diffusion models for chorus, plasmaspheric hiss, and lightning-generated whistlers. *J Geophys Res* (2014) 119:268–89. doi:10.1002/2013JA019281

22. Ni B, Thorne RM, Zhang X, Bortnik J, Pu Z, Xie L, et al. Origins of the Earth's diffuse auroral precipitation. *Space Sci Rev* (2016) 200:205–59. doi:10.1007/s11214-016-0234-7

23. Ashour-Abdalla M, Kennel C. Nonconvective and convective electron cyclotron harmonic instabilities. *J Geophys Res* (1978) 83:1531–43. doi:10.1029/JA083iA04p01531

24. Horne RB. Path-integrated growth of electrostatic waves: the generation of terrestrial myriametric radiation. *J Geophys Res* (1989) 94:8895–909. doi:10.1029/JA094iA07p08895

25. Ni B, Gu X, Fu S, Xiang Z, Lou Y. A statistical survey of electrostatic electron cyclotron harmonic waves based on THEMIS FFF wave data. *J Geophys Res (Space Physics)* (2017) 122:3342–53. doi:10.1002/2016JA023433

26. Liu X, Chen L, Xia Z. The relation between electron cyclotron harmonic waves and plasmapause: case and statistical studies. *Geophys Res Lett* (2020) 47:e2020GL087365. doi:10.1029/2020GL087365

27. Liu S, Chen Y, Yang Q, Yang H, Xiao F, Wang B, et al. Statistical study on spatial distribution of frequency-chirping ech elements by van allen probes. *Geophys Res Lett* (2023) 50:e2023GL106371. doi:10.1029/2023GL106371

28. Colburn DS, Sonett CP. Discontinuities in the solar wind. *Space Sci Rev* (1966) 5:439–506. doi:10.1007/BF00240575

29. Hudson PD. Discontinuities in an anisotropic plasma and their identification in the solar wind. *Planet Space Sci* (1970) 18:1611–22. doi:10.1016/0032-0633(70)90036-X

30. Greco A, Perri S, Servidio S, Yordanova E, Veltri P. The complex structure of magnetic field discontinuities in the turbulent solar wind. *Astrophys J Lett* (2016) 823:L39. doi:10.3847/2041-8205/823/2/L39

31. Artemyev AV, Angelopoulos V, Vasko IY, Runov A, Avanov LA, Giles BL, et al. On the kinetic nature of solar wind discontinuities. *Geophys Res Lett* (2019) 46:1185–94. doi:10.1029/2018GL079906

32. Russell CT, Ginskey M, Petrinec SM. Sudden impulses at low-latitude stations: steady state response for northward interplanetary magnetic field. *J Geophys Res* (1994) 99:253–61. doi:10.1029/93JA02288

33. Borodkova NL, Zastenker GN, Sibeck DG. A case and statistical study of transient magnetic field events at geosynchronous orbit and their solar wind origin. *J Geophys Res* (1995) 100:5643–56. doi:10.1029/94JA03144

34. Lyon JG. The solar wind-magnetosphere-ionosphere system. *Science* (2000) 288:1987–91. doi:10.1126/science.288.5473.1987

35. Zuo P, Feng X, Xie Y, Wang Y, Li H, Xu X. Automatic detection algorithm of dynamic pressure pulses in the solar wind. *Astrophysical J* (2015) 803:94. doi:10.1088/0004-637X/803/2/94

36. Fu HS, Cao JB, Mozer FS, Lu HY, Yang B. Chorus intensification in response to interplanetary shock. *J Geophys Res* (2012) 117:A01203. doi:10.1029/2011JA016913

37. Su Z, Zhu H, Xiao F, Zheng H, Wang Y, Shen C, et al. Disappearance of plasmaspheric hiss following interplanetary shock. *Geophys Res Lett* (2015) 42:3129–40. doi:10.1002/2015GL063906

38. Liu N, Su Z, Gao Z, Reeves GD, Zheng H, Wang Y, et al. Shock-induced disappearance and subsequent recovery of plasmaspheric hiss: coordinated observations of RBSP, THEMIS, and POES satellites. *J Geophys Res (Space Physics)* (2017) 122:10. doi:10.1002/2017JA024470

39. Liu N, Su Z, Zheng H, Wang Y, Wang S. Prompt disappearance and emergence of radiation belt magnetosonic waves induced by solar wind dynamic pressure variations. *Geophys Res Lett* (2018) 45:585–94. doi:10.1002/2017GL076382

40. Zhou C, Li W, Thorne RM, Bortnik J, Ma Q, An X, et al. Excitation of dayside chorus waves due to magnetic field line compression in response to interplanetary shocks. *J Geophys Res (Space Physics)* (2015) 120:8327–38. doi:10.1002/2015JA021530

41. Yue C, Chen L, Bortnik J, Ma Q, Thorne RM, Angelopoulos V, et al. The characteristic response of whistler mode waves to interplanetary shocks. *J Geophys Res (Space Physics)* (2017) 122(10). 047057. doi:10.1002/2017JA024574

42. Fu H, Yue C, Ma Q, Kang N, Bortnik J, Zong Q-g., et al. Frequency-dependent responses of plasmaspheric hiss to the impact of an interplanetary shock. *Geophys Res Lett* (2021) 48:e2021GL094810. doi:10.1029/2021GL094810

43. Jin Y, Liu N, Su Z, Zheng H, Wang Y, Wang S. Immediate impact of solar wind dynamic pressure pulses on whistler-mode chorus waves in the inner magnetosphere. *Geophys Res Lett* (2022) 49:e2022GL097941. doi:10.1029/2022GL097941

44. Liu N, Su Z. Prompt responses of magnetospheric whistler-mode waves to solar wind dynamic pressure pulses. *Front Astron Space Sci* (2023) 10. doi:10.3389/fspas.2023.1193600

45. Ogilvie K, Desch M. The wind spacecraft and its early scientific results. *Adv Space Res* (1997) 20:559–68. doi:10.1016/s0273-1177(97)00439-0

46. Mauk BH, Fox NJ, Kanekal SG, Kessel RL, Sibeck DG, Ukhorskiy A. Science objectives and rationale for the radiation belt storm probes mission. *Space Sci Rev* (2013) 179:3–27. doi:10.1007/s11214-012-9908-y

47. Ogilvie KW, Chornay DJ, Fritzenreiter RJ, Hunsaker F, Keller J, Lobell J, et al. SWE, A comprehensive plasma instrument for the wind spacecraft. *Space Sci Rev* (1995) 71:55–77. doi:10.1007/BF00751326

48. Lepping RP, Acũna MH, Burlaga LF, Farrell WM, Slavin JA, Schatten KH, et al. The wind magnetic field investigation. *Space Sci Rev* (1995) 71:207–29. doi:10.1007/BF00751330

49. Lin RP, Anderson KA, Ashford S, Carlson C, Curtis D, Ergun R, et al. A three-dimensional plasma and energetic particle investigation for the wind spacecraft. *Space Sci Rev* (1995) 71:125–53. doi:10.1007/BF00751328

50. Kletzing CA, Kurth WS, Acuna M, MacDowall RJ, Torbert RB, Averkamp T, et al. The electric and magnetic field instrument suite and integrated science (EMFISIS) on RBSP. *Space Sci Rev* (2013) 179:127–81. doi:10.1007/s11214-013-9993-6

51. Kurth WS, Pascuale SD, Faden JB, Kletzing CA, Hospodarsky GB, Thaller S, et al. Electron densities inferred from plasma wave spectra obtained by the waves instrument on van allen probes. *J Geophys Res* (2014) 120:904–14. doi:10.1002/2014JA020857

52. Wygant J, Bonnell J, Goetz K, Ergun R, Mozer F, Bale S, et al. The electric field and waves instruments on the radiation belt storm probes mission. *Space Sci Rev* (2013) 179:183–220. doi:10.1007/s11214-013-0013-7

53. Funsten HO, Skoug RM, Guthrie AA, MacDonald EA, Baldonado JR, Harper RW, et al. Helium, oxygen, proton, and electron (HOPE) mass spectrometer for the radiation belt storm probes mission. *Space Sci Rev* (2013) 179:423–84. doi:10.1007/s11214-013-9968-7

54. Spence HE, Reeves GD, Baker DN, Blake JB, Bolton M, Bourdarie S, et al. Science goals and overview of the energetic particle, composition, and thermal plasma (ECT) suite on NASA's Radiation Belt Storm Probes (RBSP) mission. *Space Sci Rev* (2013) 179:311–36. doi:10.1007/s11214-013-0007-5

55. Chi Y, Shen C, Wang Y, Xu M, Ye P, Wang S. Statistical study of the interplanetary coronal mass ejections from 1995 to 2015. *Solar Phys* (2016) 291:2419–39. doi:10.1007/s11207-016-0971-5

56. Zurbuchen TH, Richardson IG. In-situ solar wind and magnetic field signatures of interplanetary coronal mass ejections. *Space Sci Rev* (2006) 123:31–43. doi:10.1007/s11214-006-9010-4

57. Wu C-C, Lepping RP. Statistical comparison of magnetic clouds with interplanetary coronal mass ejections for solar cycle 23. *Solar Phys* (2011) 269:141–53. doi:10.1007/s11207-010-9684-3

58. Kilpua EKJ, Lumme E, Andreeova K, Isavnin A, Koskinen HEJ. Properties and drivers of fast interplanetary shocks near the orbit of the Earth (1995-2013). *J Geophys Res (Space Physics)* (2015) 120:4112–25. doi:10.1002/2015JA021138

59. Lou Y, Gu X, Summers D, Ni B, Liu K, Fu S, et al. Statistical distributions of dayside ECH waves observed by MMS. *Geophys Res Lett* (2018) 45(12):738. 730–12. doi:10.1029/2018GL080125

60. Yu J, Wang J, Chen Z, Ren A, Liu X, Liu N, et al. Statistical evidence for off-equatorial minimum-B-pocket as a source region of electron cyclotron harmonic waves in the dayside outer magnetosphere. *Geophys Res Lett* (2023) 50:e2022GL102583. doi:10.1029/2022GL102583

61. Zong Q, Zhou X, Wang YF, Li X, Song P, Baker DN, et al. Energetic electron response to ULF waves induced by interplanetary shocks in the outer radiation belt. *J Geophys Res* (2009) 114:A10204. doi:10.1029/2009JA014393

62. Foster JC, Wygant JR, Hudson MK, Boyd AJ, Baker DN, Erickson PJ, et al. Shock-induced prompt relativistic electron acceleration in the inner magnetosphere. *J Geophys Res Accepted* (2015) 120:1661–74. doi:10.1002/2014JA020642

63. Ren J, Zong QG, Miyoshi Y, Zhou XZ, Wang YF, Rankin R, et al. Low-energy (<200 eV) electron acceleration by ULF waves in the plasmaspheric boundary layer: van allen probes observation. *J Geophys Res (Space Physics)* (2017) 122:9969–82. doi:10.1002/2017JA024316

64. Ren J, Zong QG, Zhou XZ, Spence HE, Funsten HO, Wygant JR, et al. Cold plasmaspheric electrons affected by ULF waves in the inner magnetosphere: a van allen probes statistical study. *J Geophys Res (Space Physics)* (2019) 124:7954–65. doi:10.1029/2019JA027009

65. Ma X, Tian AM, Shi QQ, Bai SC, Yao ST, Shen XC, et al. Electron pitch angle distributions in compressional Pc5 waves by THEMIS-A observations. *Geophys Res Lett* (2021) 48:e95730. doi:10.1029/2021GL095730

66. Xie H, Xiao Y. PDRK: a general kinetic dispersion relation solver for magnetized plasma. *Plasma Sci Tech* (2016) 18:97–107. doi:10.1088/1009-0630/18/2/01

67. Zhou Q, Xiao F, Yang C, Liu S, He Y, Baker DN, et al. Generation of lower and upper bands of electrostatic electron cyclotron harmonic waves in the Van Allen radiation belts. *Geophys Res Lett* (2017) 44:5251–8. doi:10.1002/2017GL073051

68. Lou Y, Cao X, Ni B, Tu W, Gu X, Fu S, et al. Diffuse auroral electron scattering by electrostatic electron cyclotron harmonic waves in the dayside magnetosphere. *Geophys Res Lett* (2021) 48:e92208. doi:10.1029/2020GL092208

69. Roederer JG, Zhang H. *Dynamics of magnetically trapped particles*. Berlin: Springer (2016).

70. Tsyganenko NA, Stern DP. Modeling the global magnetic field of the large-scale Birkeland current systems. *J Geophys Res* (1996) 101:27187–98. doi:10.1029/96JA02735

71. Tsyganenko NA. A model of the near magnetosphere with a dawn-dusk asymmetry 1. mathematical structure. *J Geophys Res Space Phys* (2002) 107. SMP 12–1–SMP 12–15. doi:10.1029/2001JA000219

72. Tsyganenko NA, Sitnov MI. Modeling the dynamics of the inner magnetosphere during strong geomagnetic storms. *J Geophys Res* (2005) 110:A03208. doi:10.1029/2004JA010798

73. Boudouridis A, Lyons LR, Zesta E, Ruohoniemi JM. Dayside reconnection enhancement resulting from a solar wind dynamic pressure increase. *J Geophys Res (Space Physics)* (2007) 112:A06201. doi:10.1029/2006JA012141

74. Liu N, Su Z, Gao Z, Zheng H, Wang Y, Wang S. Can solar wind decompressive discontinuities suppress magnetospheric electromagnetic ion cyclotron waves associated with fresh proton injections? *Geophys Res Lett* (2020) 47:e90296. doi:10.1029/2020GL090296

75. Zhou XY, Strangeway RJ, Anderson PC, Sibeck DG, Tsurutani BT, Haerendel G, et al. Shock aurora: FAST and DMSP observations. *J Geophys Res (Space Physics)* (2003) 108:8019. doi:10.1029/2002JA009701

frontiers | Frontiers in Physics

TYPE Original Research
PUBLISHED 21 March 2024
DOI 10.3389/fphy.2024.1368166

Check for updates

OPEN ACCESS

EDITED BY
Boyi Wang,
Harbin Institute of Technology, Shenzhen, China

REVIEWED BY
Kedeng Zhang,
Wuhan University, China
Ercha Aa,
Massachusetts Institute of Technology, United States

*CORRESPONDENCE
Zheng Li,
zli@nuist.edu.cn

RECEIVED 10 January 2024
ACCEPTED 13 March 2024
PUBLISHED 21 March 2024

CITATION
Li Z, Wang Y, Shao J, Wang L, Li J, Zhang H, Xu X and Gu C (2024), A comparison of ionospheric TEC between the South Atlantic anomaly region and the Indian Ocean region based on TIEGCM simulations in 2002.
Front. Phys. 12:1368166.
doi: 10.3389/fphy.2024.1368166

COPYRIGHT
© 2024 Li, Wang, Shao, Wang, Li, Zhang, Xu and Gu. This is an open-access article distributed under the terms of the Creative Commons Attribution License (CC BY). The use, distribution or reproduction in other forums is permitted, provided the original author(s) and the copyright owner(s) are credited and that the original publication in this journal is cited, in accordance with accepted academic practice. No use, distribution or reproduction is permitted which does not comply with these terms.

A comparison of ionospheric TEC between the South Atlantic anomaly region and the Indian Ocean region based on TIEGCM simulations in 2002

Zheng Li[1,2]*, Yan Wang[1], Jingjing Shao[3], Luyao Wang[3], Jingyuan Li[1], Hua Zhang[1], Xiaojun Xu[2] and Chunli Gu[4]

[1]Institute of Space Weather, Nanjing University of Information Science and Technology, Nanjing, China, [2]State Key Laboratory of Lunar and Planetary Science, Macau University of Science and Technology, Taipa, Macao SAR, China, [3]School of Mathematics and Statistics, Nanjing University of Information Science and Technology, Nanjing, China, [4]Beijing Institute of Applied Meteorology, Beijing, China

Using the Thermosphere-Ionosphere-Electrodynamic General Circulation Model (TIEGCM), a comparison of the ionospheric total electron content (TEC) between the South Atlantic anomaly (SAA) and the Indian Ocean (IO) at solar maximum is performed in this study. The results show that the average total electron content in the SAA is greater than that in the Indian Ocean in general. In order to further analyze the difference between the two regions, the empirical orthogonal function (EOF) are used to investigate the temporal and spatial characteristics of TEC. The empirical orthogonal function method separate part of the global four-peak structure (an equatorial ionization anomaly structure, distributed in Southeast Asia, South America, Africa, and central Pacific) and spatial variations in both regions. Moreover, the first mode of EOF shows the different distribution of Equatorial ionization anomaly in South America and central Pacific caused by deviation of geomagnetic field and tides between two regions, and the enhancement of TEC in SAA region at dusk is emphasized, but the enhancement of TEC in IO region at dawn is emphasized. The second mode performs the distribution of EIA in Africa related to solar radiation and $E \times B$ drift. The third mode indicates the similar spatiotemporal variations from the geomagnetic field. Besides, the correlation between TEC and Dst in two regions indicate that there are some deficiencies in simulation to the specificity of SAA, and the deficiencies are likely caused by the model's inaccurate simulation of the magnetic field and particle deposition in the SAA region.

KEYWORDS

South Atlantic anomaly, geomagnetic field, ionosphere, total electron content, empirical orthogonal function

1 Introduction

The ionosphere is greatly affected by solar EUV radiation and geomagnetic activity, and shows many spatiotemporal variations, such as latitudinal variations, seasonal variations, diurnal variations, South Atlantic anomaly (SAA) and Weddell Sea anomaly (WSA) [1]. The ionosphere plays an important role in space weather, and there is a strong coupling process between it and the upper and lower regions. At high altitudes, the particle in

ionosphere interacts with plasma in the magnetosphere, which allows high-energy particles and electrodynamic energy to enter the Earth, while at low altitudes, the ionosphere is regulated by tropospheric weather and surface topology [2,3]. On either side of the Earth's magnetic equator, there is a very important phenomenon in the ionosphere called Equatorial ionization anomaly (EIA) [4]. In the past few decades, numerous research had been done on EIA. [5] theoretically investigated the daily variation of this latitudinal distribution of EIA, in which production, loss, and transport of ionization were taken into account. With the Sheffield University plasmasphere-ionosphere model (SUPIM), [6] researched the characteristic of ionosphere, and the F region electrodynamic drift generates the plasma fountain and the anomaly, which was symmetric with respect to the magnetic equator. Furthermore, by analyzing the ROCSAT-1 satellite data and SAMI2 model simulations, [7] investigated the formation of plasma density structure in the low-latitude F region, and the result showed that the formation of four-peaks structure can be explained by the longitudinal variation of the daytime vertical $E \times B$ drift.

Meanwhile, empirical orthogonal function (EOF) method has been widely used in ionospheric studies and achieved fruitful results. With EOF method, [8] developed an empirical model of ionospheric total electron content (TEC) over Wuhan, some experiments had been done to improve the external driver of the model, and the EOF model had higher precision compared with International Reference Ionosphere 2000 (IRI-2000). [9] constructed an empirical ionospheric model of the TEC over North America (20°–60°N, 40° to 140°W) from GPS TEC data collected by Massachusetts Institute of Technology (MIT) Haystack Observatory during the years 2001–2012, and the temporal variations were expressed analytically in terms of local time, season, solar activity, and the spatial variations by cubic-spline functions, and this model could reflect the majority of the quiet time monthly means and the characteristic temporal-spatial variations in the North America. In terms of magnetic storm, [10] performed a TEC model during storm conditions with the combination of EOF and regression analyses techniques, and the hour of the day, the day number of the year, F10.7p and A indices, were chosen as inputs for the modeling techniques to take into account diurnal and seasonal variation of TEC, solar, and geomagnetic activities, respectively, and this model performed well for storms with nonsignificant ionospheric TEC response and storms that occurred during period of low solar activity. Besides, [11] used the EOF analysis technique to construct a parameterized time-varying global Az model, and their results demonstrated the effectiveness of the combined data ingestion and EOF modeling technique in improving the specifications of ionospheric density variations. [12] investigated spatial and temporal TEC variations in GNSS observable through EOF model and substantiated their findings against existing empirical International Reference Ionosphere 2016 (IRI-2016) and NeQuick-2 models, and EOF model had superior performance compared to other regional and global models in terms of temporal-spatial composition and percentage deviation and correlation plots.

The SAA is a magnetic anomaly region on the Earth, the magnetic field strength of the SAA is 30%–50% weaker compared to other regions at the same latitude [13], and the larger magnetic declination here results in an anomaly in the four-peak structure of EIA [14]. Therefore, in the SAA region, the inner radiation belts are closer to the Earth, and more particles from outer space arrive closer to the Earth's surface [15,16]. The morphology of equatorial F region irregularity (EFI) in the SAA longitude sector could be affected by seasonally ionospheric responses to the energetic particle precipitation in SAA, and sunset equatorial electrodynamics plays a key role in controlling the seasonal and longitudinal occurrences of the quiet time EFI [17]. In addition, the ionosphere of SAA has attracted some attentions. [18] modeled the ionizing effect of ~45 TECU and ~23 TECU in the topside ionosphere at middle and low latitudes, including a near-equatorial forbidden zone outside of the SAA, and the important basis of the long duration and wide latitudinal extension of the positive ionospheric storm was obtained, and they suggested there was a good correlation between the increase of TEC and the extension of high-energy electrons. [19] utilized the Global Self-consistent Model of the Thermosphere, Ionosphere and Protonosphere (GSM TIP) to predict the main and recovery phases of ionospheric storms in the SAA region. [20] made a theoretical study of the upper and lower boundaries of the ionospheric generator region in the SAA on the basis of the models of Mass Spectrometer Incoherent Scatter Model (NRLMSISE-00) and IRI-2016.

In general, there are few works to analyse the regional specificity of ionosphere TEC in the SAA obtained from TIEGCM. Recently, [21] used TIEGCM simulations to compare ionosphere TEC distributions between 2002 and 2008 in the SAA. They focused on the difference of TEC between solar maximum and minimum conditions, but they did not mention the difference of model TEC between SAA and other areas. Therefore, this paper chose another region to compare with SAA to study the characteristic of TEC in the SAA region, and this study focused on the spatiotemporal variations of ionospheric TEC in two regions within 1 year. Meanwhile, it is necessary to mention the Macau Scientific Satellite-1 (MSS-1), which is the first scientific satellite to use a low inclination orbit to monitor the geomagnetic field and space environment in the South Atlantic Anomaly (SAA) near the equator, and one of the objectives of MSS-1 is to study the specificity of SAA region. Therefore, this paper is also the preliminary work for the follow-up study of the measurements obtained from MSS-1. Besides, a comparison of geomagnetic indices Dst and TEC was performed to test the response of regional TEC to geomagnetic activities in the SAA and IO regions. To analyze the differences between TEC in SAA region and TEC in other regions, this paper compared the distribution characteristics of ionospheric TEC between SAA region (10°N to 60°S, 100°W to 20°E) and Indian Ocean (IO) region (10°N to 60°S, 20°E to 140°E) in 2002, and the EOF method was used to explain these differences in detail. In this study, TIEGCM was used to simulate hourly TEC value of 2002 in the SAA region and the IO region. In addition, the EOF analysis was performed to compare the temporal-spatial variations. Section 2 introduces the TIEGCM and EOF methodology. Section 3 gives the main results and discussion. The summary is given in Section 4.

2 Data and methods

2.1 TIEGCM

TIEGCM is a global 3D time-varying numerical model developed by the National Center for Atmospheric Research

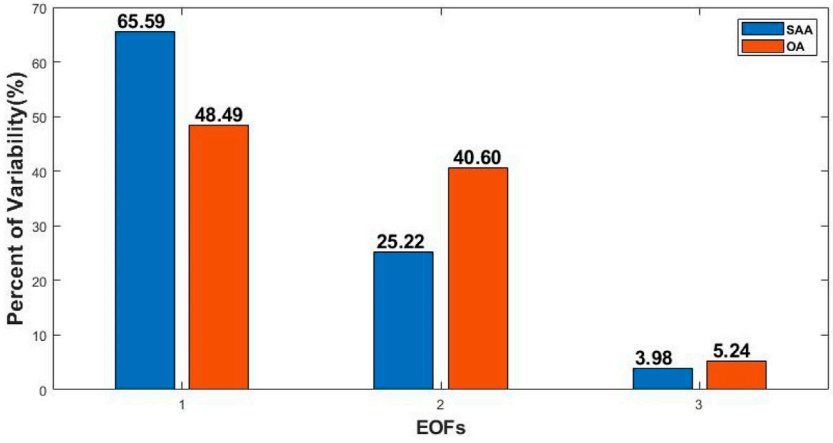

FIGURE 1
Percentage of variability explained by the first three EOFs obtained from the TIEGCM simulations in the SAA and IO regions.

(NCAR) [22–24]. By using the finite difference method, the self-consistent solutions of the dynamics equation, thermodynamic equation and continuity equation of the neutral component and some charged particles in the thermosphere atmosphere are obtained. The input parameters include the solar radiation index F10.7, the 81-day average F10.7a of F10.7 and the geomagnetic index Kp. The lower boundary of the model is driven by tidal climatology based on the Global Scale wave model (SGWM). TIEGCM has been used to carry out many researches in the field of space weather, and has achieved numerous results [25–32]. The TIEGCM V2.0 is used in this work and it has a horizontal resolution of 2.5 longitude ×2.5 latitude, 57 pressure surfaces from ~97km to ~500 km with a vertical resolution of 1/4 scale height.

2.2 EOF analysis method

EOF analysis, also known as principal component analysis (PCA), is a data decomposition technique in which the original data is represented by orthogonal basis functions and principal component sets. The EOF function is determined by the data itself by calculating the eigenvector of the covariance matrix of the data or by singular value decomposition. The raw data is divided into several patterns to fully represent its properties. The key point is to preserve the changes presented in the data set as much as possible while reducing the dimension of the data set. It can be summed up as a spatiotemporal field dimension reduction method [33–35]. From the perspective of spatial variations, EOF method can be regarded as the decomposition of main spatial distribution. From the perspective of temporal variations, EOF method can be understood as an analysis method to extract the main oscillation signal types of variable field, and decompose a field sequence with a complex oscillation system into several relatively single oscillation component systems [36].

EOF method has been widely used in the research of space weather [21,37–41]. In this paper, we arrange the TEC grid data (28 longitude ×49 latitude, time resolution 1 h) simulated by TIEGCM in the selected area, and got a grid of 1,372 × 8,736. 8,736 is the data of 24 h 1 day in the first 364 days of 2002, and the EOF method is applied to these data. Besides, the distribution of space and time is separated and decomposed into time function and space function, as shown below Eq. 1 (Yu et al., 2023):

$$TEC(\theta,\varphi,t) = \sum_{i=1}^{n} EOF_i(\theta,\varphi)T_i(t) \quad (1)$$

As shown in Figure 1, the first three modes are selected to explain the spatial (EOF_i) and temporal (T_i) distribution of TEC. The three modes accounts for 65.59%, 25.22% and 3.98% for the SAA region, and 48.49%, 40.60% and 5.24% for the IO region. The total percentage of variability are 94.79% in the SAA region and 94.33% in the IO regions, and thus can reflect the contribution of the mechanism in this mode to the variation of TEC.

3 Results and discussion

In this section, the ionospheric MEAN TEC field and the first three modes of variability (EOFi, Ti) in the SAA and IO regions obtained from TIEGCM in 2002 are compared and discussed. Moreover, the correlation coefficient between TEC and Dst is performed in the SAA and IO regions.

3.1 MEAN TEC field

Figure 2A shows the plots of the mean TEC in the SAA region. The MEAN TEC is the result of average treatment to TEC throughout 1 year in the SAA region, and it is the same treatment in the IO region. The most obvious is the peak regions of 100°W to 75W°, which correspond to the peak EIA in South America. It is one of the four peaks of the global EIA distribution. From 100°W to 75°W, the mean TEC presents two maximum area, which are symmetric in general. It can be seen that another maximum area appears near the equator in 30°W to 20°E. Furthermore, the TEC decreases as latitude increases in general. Figure 2B shows the plots of the mean TEC in the IO region. From

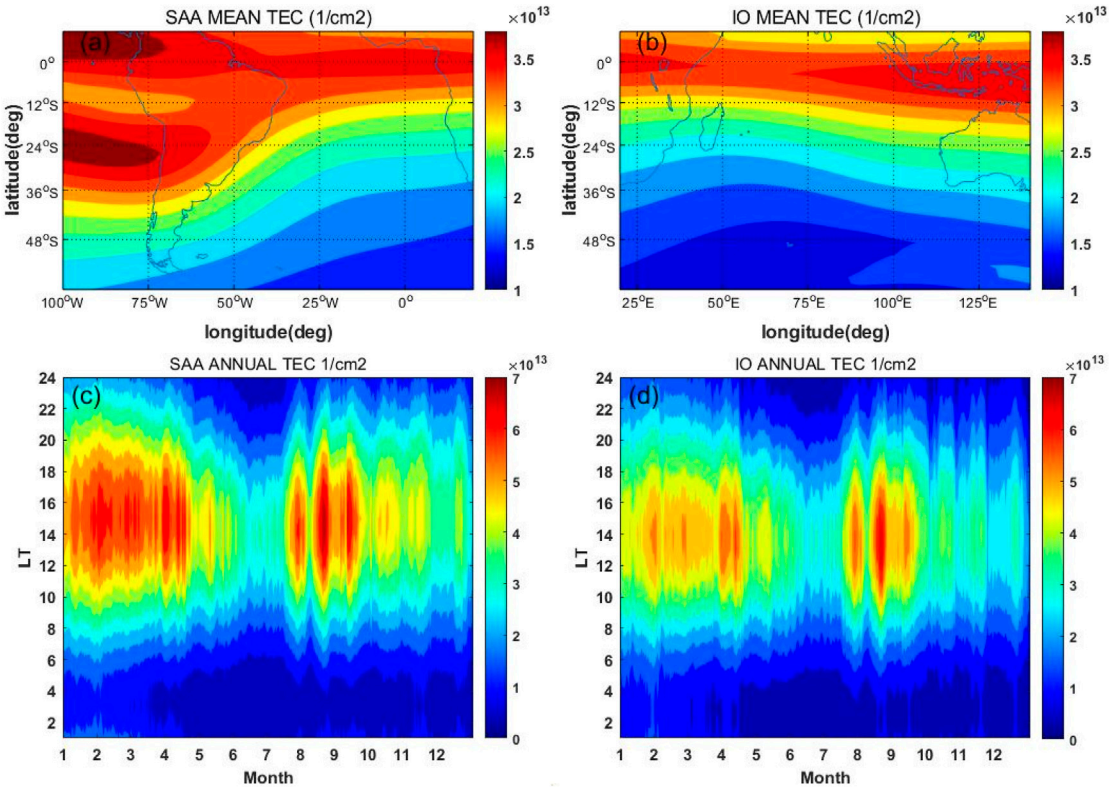

FIGURE 2
(A) TEC time-averaged maps (1/cm^2) derived from the TIEGCM simulations of SAA region. **(B)** TEC time-averaged maps (1/cm^2) derived from the TIEGCM simulations of IO region. **(C)** The diurnal and seasonal variations of TEC in the SAA region. **(D)** The diurnal and seasonal variations of TEC in the IO region.

Figure 2B, there is a maximum distribution of TEC at low latitudes. Besides, TEC shows a change of strength in the latitudinal direction with two peaks at 25°E and 125°E. The maximum areas in Figures 2A, B located in the South America and the Africa, which are parts of the global four-peak structure. Figure 2C shows the diurnal and seasonal variations of TEC in the SAA region in 2002. The ANNUAL TEC is the result of average treatment to TEC throughout whole area in the SAA region, and it is the same treatment in the IO region. From Figure 2C we can see that the mean TEC has significant diurnal variations. Taking the variations in April as an example, the TEC rise at about 5:00LT and reached the maximum at about 14:00LT, and the value of TEC decline at about 16:00LT and reached its minimum at about 3:00LT. In addition, seasonal variations can also be seen. The seasonal variation presents a double-peak structure, with a main peak in August to October, the secondary peak in February to April, a main valley in June and July, and the secondary valley in November and December. Figure 2D shows the diurnal and seasonal variations of TEC in the IO region in 2002. As Figure 2D shows, the TEC in the IO region has similar variations with the SAA region. However, it is noticeable the peaks duration is shorter and the peak intensity is less in the IO region than that in the SAA region.

The distributions of MEAN TEC in the SAA and IO regions shown in Figures 2A, B were similar to the result of Oh et al. [7]. Due to the presence of magnetic anomaly in the SAA region, the deviations between geomagnetic and geographic equator produced longitudinal and hemispheric variations in the neutral meridional winds, and then affected EIA distribution [42]. Lin et al. (2017) and [43] suggested that the field-aligned plasma was transported from the summer to winter hemispheres in the morning by neutral winds, and this effect became less around noon. Meanwhile, this created a stronger equatorial fountain effect in the southern hemisphere than that in the northern hemisphere, with more $E \times B$ drift through longitudinally dependent dynamo process occurring south of the equator [44–46]. For the diurnal variations shown in Figures 2C, D, [47] considered that this variation was the result of the equatorial particle fountain (EPF) effect during the day and the $E \times B$ drift velocity during the night. The seasonal variations appeared in the SAA and IO regions, which indicated the TEC was dependent on the seasons. The characteristics were consistent with the results of [21].

3.2 First mode

Figure 3A presents the EOF1 in the SAA regions. The two maximum area are distributed around 100°W, 10°N and 26°S, and the phenomenon of EIA only exists between 100°W and 50°W. The peak regions of 100°W to 75°W still exist, and they distributed on both sides of 12°S, which reflects the symmetrical distribution of EIA in South America. Besides, EOF1 appears to decrease from south to north between 50°W and 20°E. Figure 3B displays the EOF in the IO

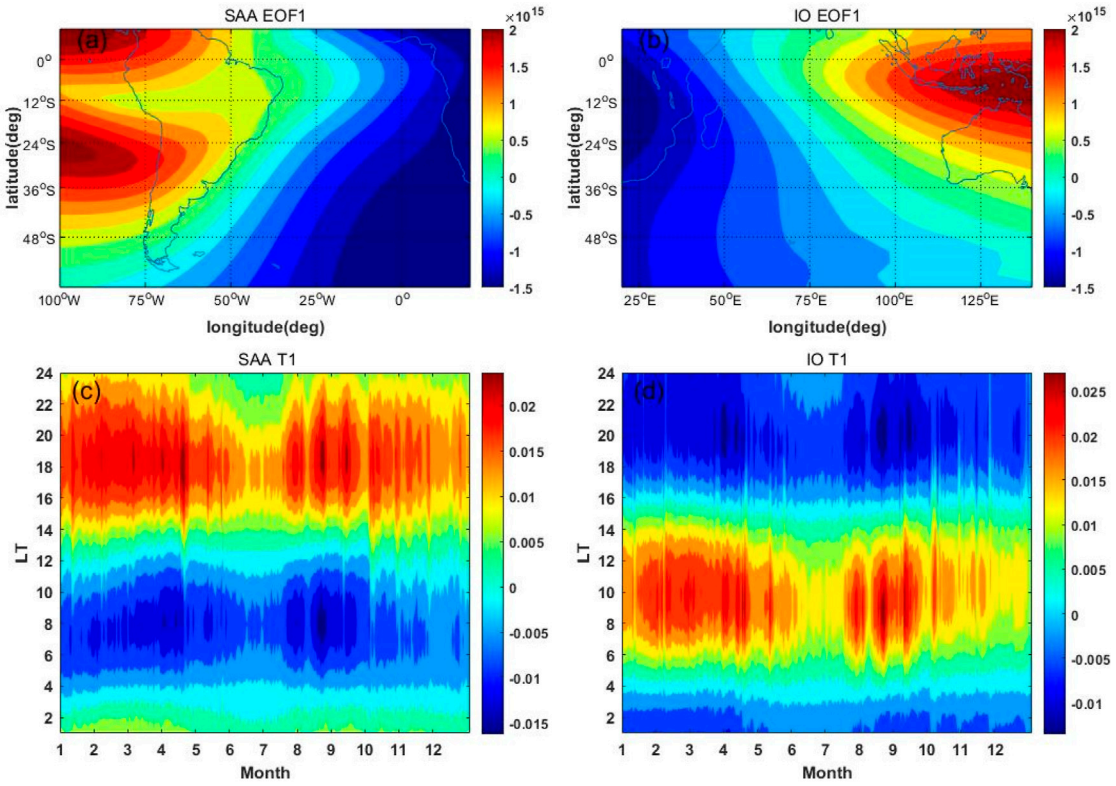

FIGURE 3
(A) EOF1 derived from the TIEGCM simulations in the SAA region. **(B)** EOF1 derived from the TIEGCM simulations in the IO region. **(C)** T1 derived from the TIEGCM simulations in the SAA region. **(D)** T1 derived from the TIEGCM simulations in the IO region.

region. As Figure 3B shows, there is a peak around 135°E and 10°S. Moreover, the EOF decreases from north to south between 100°E and 140°E, and the maximum in the IO region is one peak, which reflects the distribution of EIA in central Pacific. There is a decrease in the zonal direction in EOF1 in the SAA and IO region, which is also consistent with the characteristics in MEAN TEC, and the combined analysis of the two graphs shows that the minimum region of EOF1 is between 25°W and 75°E. As shown in Figures 3C, D, the result of Ti is divided into two dimensions, with the vertical axis representing 24 h and the horizontal axis representing 364 days. The maximum of T1 occurs at 18:00LT, and minimum of T1 occurs at 4:00LT in the SAA region. While the maximum of T1 occurs at 10:00LT, and minimum occurs at 16:00LT in the IO region. For the seasonal variation, T1 is less in June, July and December than in other months in the SAA and IO regions.

Compared with MEAN TEC, EOF1 highlighted the maximums of four-peak structure, the bimodal structure in the SAA region accords with the distribution of EIA, as the research of [44]. The $E \times B$ drift produced the EPF effect with particles settling on both sides of the equator. Besides, this variation in the zonal direction might be related to the change of the lower tide, namely, the dynamo effect in region E [48]. Due to the deviation of the geomagnetic field, the maximum in the SAA region tended to be south of the equator, while the maximum in the IO region occurred near the equator. There were zonal variations of EOF1 in the SAA and IO regions, which had been attributed to variations in tides. [49] thought the tides would act on variations at E-layer because of the heat exchange and radiative absorption, which caused the zonal variation in the SAA and IO regions. In the research of [50], the thermospheric zonal wind also shows a similar variation. Furthermore, the seasonal variation shown in Figures 3C, D was consistent with the study by [21]. However, the T1 maximum occurred at dusk in the SAA region, but at dawn in the IO region. Annual variations in solar activity affected the variations in the ionosphere over 1 year, and the intensity of the EPF effect determines the variation of ionospheric intensity, and the EOF method highlighted it.

3.3 Second mode

Figures 4A, B present the EOF2 in the SAA and IO regions. EOF2 focuses on the peak in Africa and ignores the peak located in South America in the SAA regions, and EOF2 have a single center rather than a bimodal structure like EOF1. It shows decrease from north to south in middle latitude in the SAA region. There is a peak at 10°E around equator in the SAA region, and it exists a decrease from east to west. Besides, the maximum located at 30°E around equator in the IO region, and it exist a decrease from west to east and from north to south. Moreover, the maximum area in the SAA region is smaller than that in the IO region. Figures 4C, D present the T2 in the SAA and IO regions. The maximum of T2 occurs at 11:00LT in the SAA region, and the minimum occurs at 0:00LT, and T2 is less in June and July in the SAA region. The maximum of

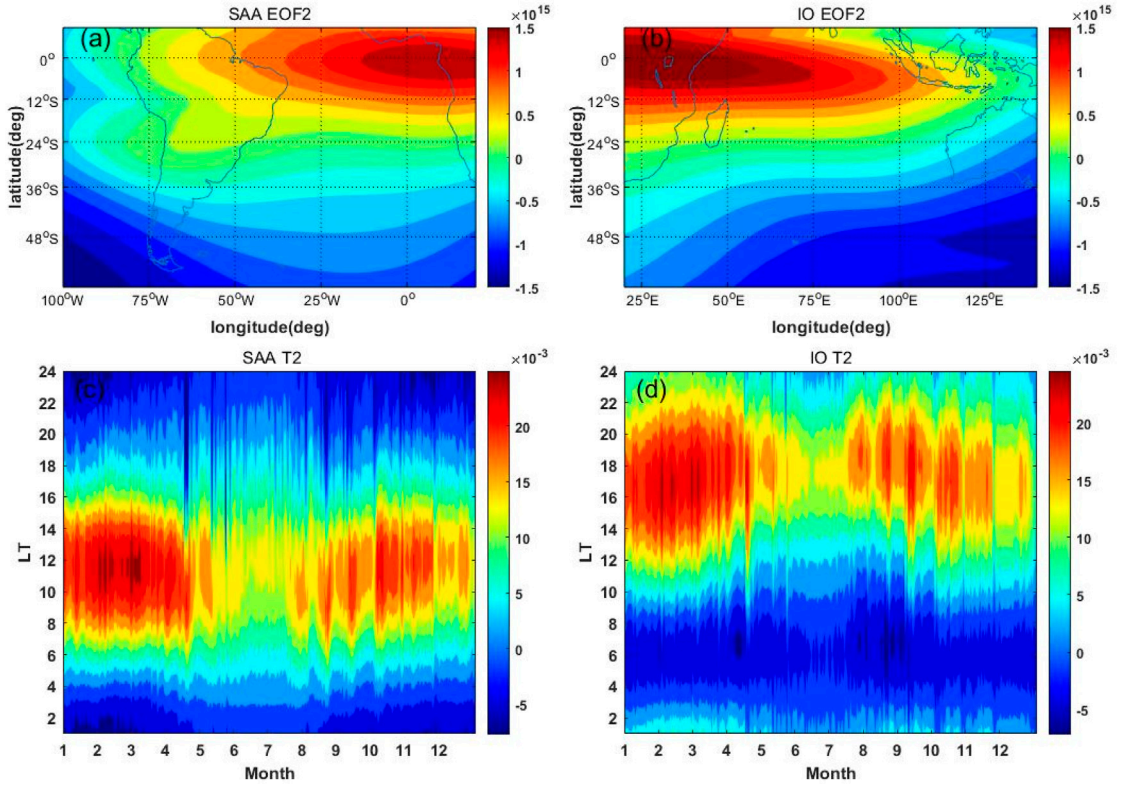

FIGURE 4
(A) EOF2 derived from the TIEGCM simulations in the SAA region. **(B)** EOF2 derived from the TIEGCM simulations in the IO region. **(C)** T2 derived from the TIEGCM simulations in the SAA. **(D)** T2 derived from the TIEGCM simulations in the IO region.

T2 occurs at 18:00LT in the IO region, and the minimum occurs at 6:00LT, and T2 is also less in June and July.

This EOF mode focused on the peak located in Africa. Consistent with the first mode, the zonal variation was influenced by the lower tides. Moreover, [48] made a comparison between the electron density simulated by TIEGCM and the electron density observed by IMAGE-FUV, which explained the four-peaked longitudinal variation by the effects of an eastward propagating zonal wavenumber-3 diurnal tide (DE3). Besides, the longitudinal variations were relative with solar radiation, and as the latitude increases, the particle deposition decreases. Combined with T1 of the first mode, the maximum of time distribution was mainly at noon and dusk, while the daytime $E \times B$ drift and nighttime downward drift was obvious. Furthermore, the various events of the vertical $E \times B$ drift velocity variations at magnetic equator and the resultant ionospheric featured at low and mid latitudes were researched, [47] revealed the practical consequences of these $E \times B$ events on the equatorial radio signal propagation and the good agreement found with the results of SUPIM. In the second mode, the EOF results showed that the results in the SAA region are more related to the daytime, while the results in the IO region were more related to the nighttime. This result was related to the characteristic of EOF method. When combined with T1, it could be seen that both daytime and nighttime $E \times B$ drift had an impact on Ti in the SAA and IO regions, but the extent of the effect was different. SAA was more affected at dawn, and IO was more affected at dusk.

3.4 Third mode

Figures 5A, B present the EOF3 in the SAA and IO regions. Figure 5A shows EOF3 in the SAA region, and it shows zonal variation in low and middle latitudes. There are two minimum areas, which occur around at 45°W,36°S and 50°W,10°N, and the maximum of EOF3 exist near the low latitudes of 100°W and 20°E. Besides, EOF3 increases from 50°W to 100°W and from 40°W to 20°E. Figure 5B shows EOF3 in the IO region. The minimum is around at 85°E and 10°S, and the maximum is around 23°E and 140°E. The decline of EOF3 from north to south can also be seen in the IO region. Figures 5C, D present the T3 in the SAA and IO regions. Both figures have distinct seasonal and diurnal features. The maximum of T3 occurs around 8:00LT in the SAA region, and the minimum occurs around 18:00LT. The maximum of T3 occurs around 5:00LT in the IO region, and minimum occurs at 15:00LT. There is 3-h lag in the SAA region. Moreover, there are similar characteristic in the SAA and IO regions. The minimum occurs in June and July in the SAA and IO regions, and the dawn-dusk variation appears in both regions.

As shown in Figures 5A, B, the zonal variations occurred. The maximum areas near 23°E in the two figures corresponded to each other, which could be seen as the four-peak structure is a prominent feature of EIA structure. Although the third mode in the EOF method had a small proportion of variability (3.98% and 5.24%), it still had a clear distribution feature. The maximum were the South America and Africa parts of the four-peak structure.

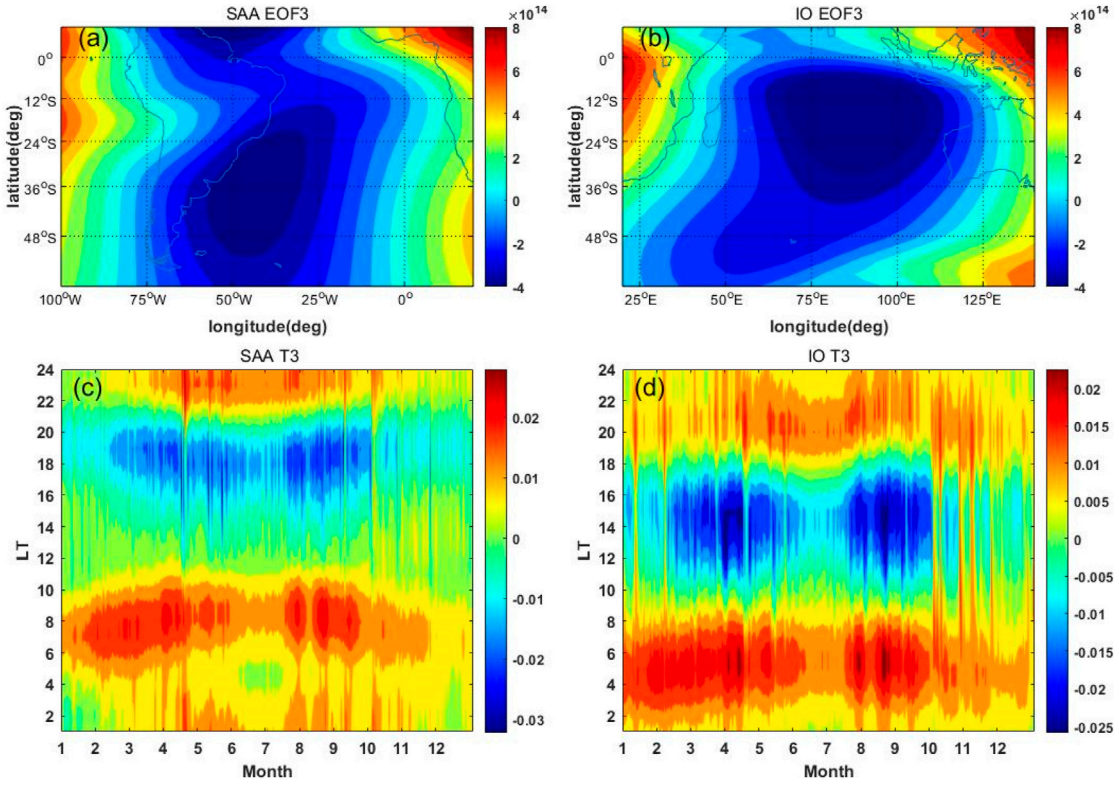

FIGURE 5
(A) EOF3 derived from the TIEGCM simulations in the SAA region. **(B)** EOF3 derived from the TIEGCM simulations in the IO region. **(C)** T3 derived from the TIEGCM simulations in the SAA region. **(D)** T3 derived from the TIEGCM simulations in the IO region.

Similar to the first two modes, the solar activity was the main reason for the seasonal variation, and the low tides determined the zonal variation.

3.5 Correlation analysis

Figure 6A shows monthly average TEC in two regions. TEC in the SAA region is higher than that in IO throughout the year particularly from January to April and October to December This might be because there is more particle deposition in the SAA region than that in the IO region [15,16]. Besides, TEC from June to August in the two regions are similar. TEC differ markedly in other months, with less values in the IO region. To compare the influence to ionosphere TEC from geomagnetic field and particle deposition in two regions, the correlation analysis is performed between TEC and Dst. Figure 6B show the hourly TEC in the SAA region and the Dst index during 2002. Figure 6C show the hourly TEC in the IO region and the Dst index during 2002. The correlation coefficient between TEC and Dst is −0.0248 in the SAA region and 0.0534 in the IO region. However, some research show TEC should be related with geomagnetic activities. [51–53], and the result is contrary to expectations. Therefore, there is reason to believe that the TIEGCM is flawed in the impact of geomagnetic activities, and this flaw may be caused by inadequate simulations of the geomagnetic field and particle deposition in the SAA region.

4 Conclusion

In this paper, the ionospheric TEC distribution was simulated by TIEGCM model in the SAA and IO regions in 2002, and EOF method is carried out on these data, and the spatiotemporal variables are separated. The three modes account for 94.7% and 94.3% respectively in the SAA and IO, which represent the basic characteristics of the spatial and temporal characteristic of TEC. In addition, a comparison of TEC between SAA and IO region is performed. Besides, the correlation coefficient between TEC and Dst is done in the SAA and IO regions.

According to the MEAN TEC of the SAA and IO regions, the existence of EIA four-peak structure can be seen. EIA in the SAA region is distributed on both sides of 12°S, while EIA in IO region is distributed on both sides of the equator. Both meridional and zonal variations exist in the MEAN TEC, which may because of the larger magnetic inclination in the SAA region. The first mode accounts for 65.59% and 48.49% of the data variability in the SAA and IO regions respectively. EOF1 reflects the zonal distribution of TEC and the main part of four-peak structure, which is considered to be caused by the difference of geomagnetic field and atmospheric tide, and the enhancement of TEC in SAA region at dusk is emphasized, but the enhancement of TEC in IO region at dawn is emphasized in the first mode. The second mode accounts for 25.22% and 40.60% of the data variability in the SAA and IO regions. EOF2 reflects the zonal and meridian variations, which is closely related to solar radiation and EPF effect. In

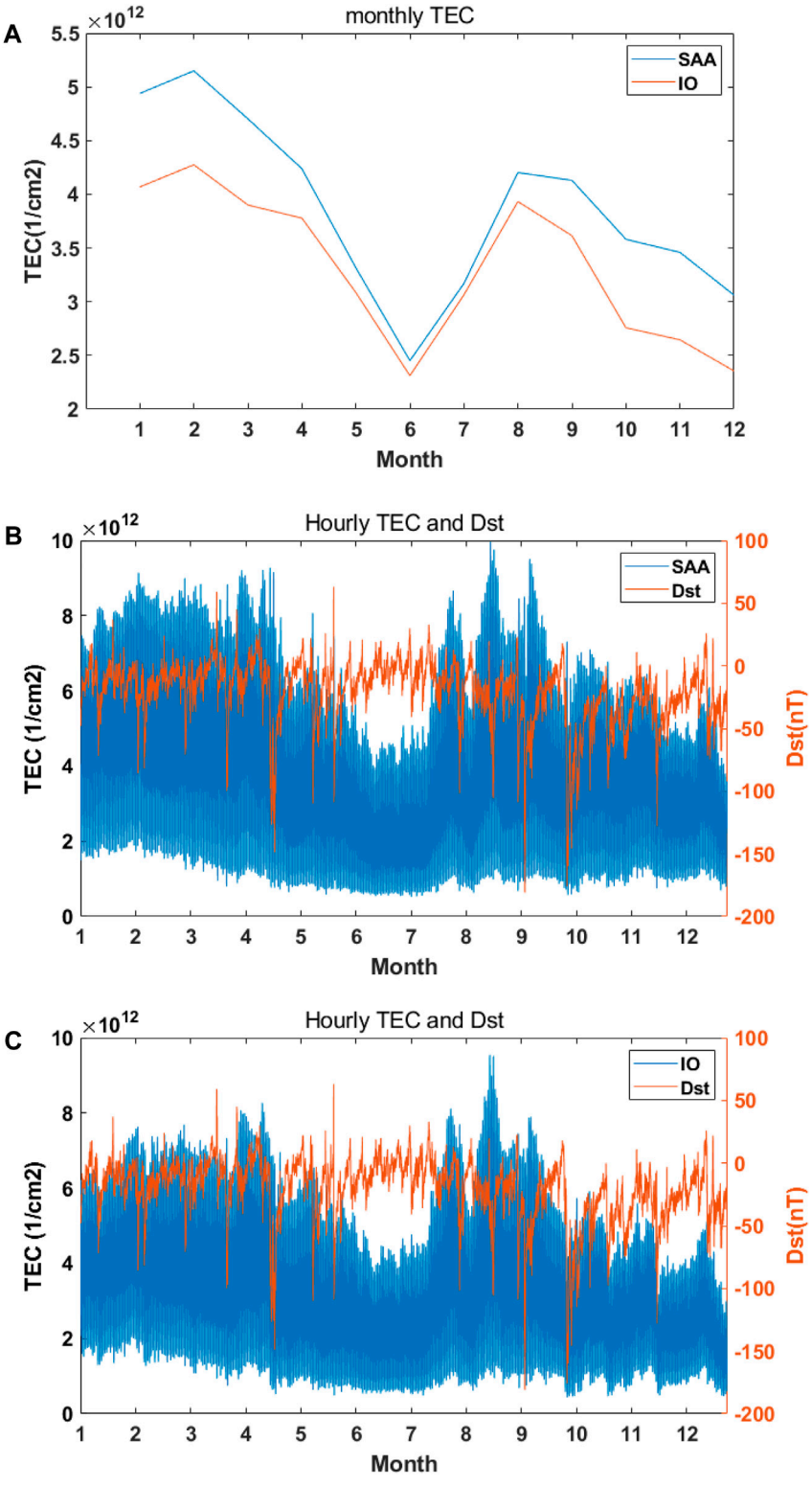

FIGURE 6
(A) Monthly average TEC in the SAA and IO regions in 2002. **(B)** Hourly TEC in the SAA region and Dst index in 2002. **(C)** Hourly TEC in the IO region and Dst index in 2002.

combination with the two modes, the SAA region is susceptible to the related physical processes during the day, and the IO region is susceptible to the processes at night. The third mode accounts for 3.98% and 5.24% of the data variability in the SAA and IO regions. EOF3 reflects the strong-weak-strong structure of TEC varying with longitude.

As for the temporal variations, the variation of ionospheric TEC shows obvious diurnal and seasonal variations in the SAA and IO regions. TEC value in spring and autumn are lower than those in summer and winter in the southern hemisphere, particularly from January to April and October to December. The EOF methods can separate the dawn-dust variations of TEC. Besides, by comparing the correlation of TEC and Dst between SAA and IO region, we found the difference is not significant. This result indicates that there are some deficiencies in simulation to the specificity of SAA, and the deficiencies are likely caused by the model's inaccurate simulation of the magnetic field and particle deposition in the SAA region.

Data availability statement

The datasets presented in this study can be found in online repositories. The names of the repository/repositories and accession number(s) can be found in the article/Supplementary Material.

Author contributions

ZL: Conceptualization, Data curation, Funding acquisition, Investigation, Methodology, Project administration, Resources, Supervision, Validation, Writing–review and editing. YW: Conceptualization, Data curation, Formal Analysis, Investigation, Methodology, Software, Visualization, Writing–original draft, Writing–review and editing. JS: Formal Analysis, Writing–review and editing. LW: Formal Analysis, Writing–review and editing. JL: Supervision, Writing–review and editing. HZ: Writing–review and editing. XX: Project administration, Writing–review and editing. CG: Writing–review and editing.

Funding

The author(s) declare that financial support was received for the research, authorship, and/or publication of this article. This research was funded by the National Natural Science Foundation of China (grant numbers 42074183) and the Open Project Program of State Key Laboratory of Lunar and Planetary Sciences (Macau University of Science and Technology) (Macau FDCT grant no. SKL-LPS(MUST)-2021-2023).

Conflict of interest

The authors declare that the research was conducted in the absence of any commercial or financial relationships that could be construed as a potential conflict of interest.

Publisher's note

All claims expressed in this article are solely those of the authors and do not necessarily represent those of their affiliated organizations, or those of the publisher, the editors and the reviewers. Any product that may be evaluated in this article, or claim that may be made by its manufacturer, is not guaranteed or endorsed by the publisher.

References

1. Forbes JM, Palo SE, Zhang X. Variability of the ionosphere. *J Atmos Solar-Terrestrial Phys* (2000) 62(8):685–93. doi:10.1016/s1364-6826(00)00029-8

2. Clilverd MA, Smith AJ, Thomson NR. The annual variation in quiet time plasmaspheric electron density, determined from whistler mode group delays. *Planet Space Sci* (1991) 39(7):1059–67. doi:10.1016/0032-0633(91)90113-o

3. Rishbeth H, Mendillo M. Patterns of F2-layer variability. *J Atmos Solar-Terrestrial Phys* (2001) 63(15):1661–80. doi:10.1016/s1364-6826(01)00036-0

4. Appleton EV. Two anomalies in the ionosphere. *Nature* (1946) 157(3995):691. doi:10.1038/157691a0

5. Anderson DN. A theoretical study of the ionospheric F region equatorial anomaly—I. Theory. *Theory(j) Planet Space Sci* (1973) 21(3):409–19. doi:10.1016/0032-0633(73)90040-8

6. Balan N, Bailey GJ. Equatorial plasma fountain and its effects: possibility of an additional layer. *J Geophys Res* (1995) 100(21):21421–32. doi:10.1029/95ja01555

7. Oh SJ, Kil H, Kim WT, Paxton LJ, Kim YH. The role of the vertical <I><B>E</B>×<I><B>B</B></I> drift for the formation of the longitudinal plasma density structure in the low-latitude F region. *Gottingen, Germany: Copernicus Publications* (2008) 26(7):2061–7. doi:10.5194/angeo-26-2061-2008

8. Mao T, Wan WX, Liu LB. An EOF based empirical model of TEC over wuhan. *Chin J Geophys* (2005) 48(4):827–34. doi:10.1002/cjg2.720

9. Chen Z, Zhang SR, Coster AJ, Fang G. EOF analysis and modeling of GPS TEC climatology over North America. *J Geophys Res Space Phys* (2015) 120(4):3118–29. doi:10.1002/2014ja020837

10. Uwamahoro JC, Habarulema JB. Modelling total electron content during geomagnetic storm conditions using empirical orthogonal functions and neural networks. *J Geophys Res Space Phys* (2015) 120(12):000–11. doi:10.1002/2015ja021961

11. Aa E, Ridley AJ, Huang W, Zou S, Liu S, Coster AJ, et al. An ionosphere specification technique based on data ingestion algorithm and empirical orthogonal function analysis method. *Space Weather* (2018) 16:1410–23. doi:10.1029/2018SW001987

12. Ansari K, Park KD, Panda SK. Empirical Orthogonal Function analysis and modeling of ionospheric TEC over South Korean region. *Acta Astronautica* (2019) 161:313–24. doi:10.1016/j.actaastro.2019.05.044

13. Mandea M, Purucker M. The varying core magnetic field from a space weather perspective(J). *Space Sci Rev* (2018) 214:1–20. doi:10.1007/s11214-017-0443-8

14. Lin CH, Wang W, Hagan ME, Hsiao CC, Immel TJ, Hsu ML, et al. Plausible effect of atmospheric tides on the equatorial ionosphere observed by the FORMOSAT-3/COSMIC: three-dimensional electron density structures. *Geophys Res Lett* (2007) 34(11). doi:10.1029/2007gl029265

15. Domingos J, Jault D, Pais MA, Mandea M. The South atlantic anomaly throughout the solar cycle. *Earth Planet Sci Lett* (2017) 473:154–63. doi:10.1016/j.epsl.2017.06.004

16. Dachev TP. South-atlantic anomaly magnetic storms effects as observed outside the international space station in 2008–2016. *J Atmos Solar-Terrestrial Phys* (2018) 179:251–60. doi:10.1016/j.jastp.2018.08.009

17. Ko CP, Yeh HC. COSMIC/FORMOSAT-3 observations of equatorial F region irregularities in the SAA longitude sector. *J Geophys Res Space Phys* (2010) 115(A11). doi:10.1029/2010ja015618

18. Suvorova AV, Huang CM, Dmitriev AV, Kunitsyn VE, Andreeva ES, Nesterov IA, et al. Effects of ionizing energetic electrons and plasma transport in the ionosphere during the initial phase of the December 2006 magnetic storm. *J Geophys Res Space Phys* (2016) 121(6):5880–96. doi:10.1002/2016ja022622

19. Dmitriev AV, Suvorova AV, Klimenko MV, Ratovsky KG, Rakhmatulin RA, et al. Predictable and unpredictable ionospheric disturbances during St. Patrick's Day magnetic storms of 2013 and 2015 and on 8–9 March 2008. *J Geophys Res Space Phys* (2017) 122(2):2398–423. doi:10.1002/2016ja023260

20. Yi SQ, Xu XJ, Zhou ZL, Chang Q, Wang X, Luo L, et al. Theoretical study of the ionospheric dynamo region inside the South Atlantic Anomaly. *Earth Planet Phys* (2023) 7(1):84–92. doi:10.26464/epp2023015

21. Yu J, Li Z, Wang Y, Shao J, et al. An empirical orthogonal function study of the ionospheric TEC predicted using the TIEGCM model over the South Atlantic anomaly in 2002 and 2008. *J Universe* (2023) 9(2):102. doi:10.3390/universe9020102

22. Roble RG, Ridley EC, Richmond AD, Dickinson RE. A coupled thermosphere/ionosphere general circulation model. *Geophys Res Lett* (1988) 15(12):1325–8. doi:10.1029/gl015i012p01325

23. Richmond AD, Ridley EC, Roble RG. A thermosphere/ionosphere general circulation model with coupled electrodynamics. *Geophys Res Lett* (1992) 19(6):601–4. doi:10.1029/92gl00401

24. Qian L, Burns AG, Emery BA, et al. The NCAR TIE-GCM: a community model of the coupled thermosphere/ionosphere system. *Model ionosphere–thermosphere Syst* (2014) 73–83. doi:10.1002/9781118704417.ch7

25. Chang LC, Lin CH, Liu JY, Balan N, Yue J, Lin J. Seasonal and local time variation of ionospheric migrating tides in 2007–2011 FORMOSAT-3/COSMIC and TIE-GCM total electron content. *J Geophys Res Space Phys* (2013) 118(5):2545–64. doi:10.1002/jgra.50268

26. Maute A, Richmond AD. Examining the magnetic signal due to gravity and plasma pressure gradient current with the TIE-GCM. *J Geophys Res Space Phys* (2017) 122(12):486–12. doi:10.1002/2017ja024841

27. Li Z, Knipp D, Wang W, Sheng C, Qian L, Flynn S. A comparison study of NO cooling between TIMED/SABER measurements and TIEGCM simulations. *J Geophys Res Space Phys* (2018) 123(10):8714–29. doi:10.1029/2018ja025831

28. Li Z, Knipp D, Wang W. Understanding the behaviors of thermospheric nitric oxide cooling during the 15 May 2005 geomagnetic storm. *J Geophys Res Space Phys* (2019) 124:2113–26. doi:10.1029/2018JA026247

29. Li Z, Sun M, Li J, Zhang K, Zhang H, Xu X, et al. Significant variations of thermospheric nitric oxide cooling during the minor geomagnetic storm on 6 may 2015. *Universe* (2022) 8:236. doi:10.3390/universe8040236

30. Rao SS, Chakraborty M, Kumar S, Singh AK. Low-latitude ionospheric response from GPS, IRI and TIE-GCM TEC to solar cycle 24. *Astrophysics Space Sci* (2019) 364:216–4. doi:10.1007/s10509-019-3701-2

31. Zhang KD, Wang H, Wang WB, Liu J, Zhang S, Sheng C. Nighttime meridional neutral wind responses to SAPS simulated by the TIEGCM: a universal time effect. *Earth Planet Phys* (2021) 5(1):1–11. doi:10.26464/epp2021004

32. Wang H, Lühr H, Zhang KD. Longitudinal variation in the thermospheric superrotation: CHAMP observation and TIE-GCM simulation. *Geophys Res Lett* (2021) 48(18):e2021GL095439. doi:10.1029/2021gl095439

33. Björnsson H, Venegas SA. A manual for EOF and SVD analyses of climatic data. *CCGCR Rep* (1997) 97(1):112–34.

34. Wilks DS. Principal component (EOF) analysis. *Int Geophys* (2011) 100:519–62. Academic Press. doi:10.1016/b978-0-12-385022-5.00012-9

35. Bro R, Smilde AK. Principal component analysis. *Anal Methods* (2014) 6(9):2812–31. doi:10.1039/c3ay41907j

36. Ding YG, Liang JY, Liu JF. New research on diagnoses of meteorological variable fields using EOF/PCA(J). *Chin J Atmos Sci* (2005) 29(2):307–13.

37. Lei J, Dou X, Burns A, Wang W, Luan X, Zeng Z, et al. Annual asymmetry in thermospheric density: observations and simulations. *J Geophys Res Space Phys* (2013) 118(5):2503–10. doi:10.1002/jgra.50253

38. Talaat ER, Zhu X. Spatial and temporal variation of total electron content as revealed by principal component analysis. *Gottingen, Germany: Copernicus Publications* (2016) 34(12):1109–17. doi:10.5194/angeo-34-1109-2016

39. Ruan H, Lei J, Dou X, Liu S, Aa E. An exospheric temperature model based on CHAMP observations and TIEGCM simulations. *Space Weather* (2018) 16(2):147–56. doi:10.1002/2017sw001759

40. Flynn S, Knipp DJ, Matsuo T, Mlynczak M, Hunt L. Understanding the global variability in thermospheric nitric oxide flux using empirical orthogonal functions (EOFs). *J Geophys Res Space Phys* (2018) 123(5):4150–70. doi:10.1029/2018ja025353

41. Li Z, Knipp D, Wang W, Shi Y, Wang M, Su Y, et al. An EOFs study of thermospheric nitric oxide flux based on TIEGCM simulations. *J Geophys Res Space Phys* (2019) 124(11):9695–708. doi:10.1029/2019ja027004

42. Balan N, Rajesh PK, Sripathi S, Tulasiram S, Liu J, Bailey G. Modeling and observations of the north–south ionospheric asymmetry at low latitudes at long deep solar minimum. *Adv Space Res* (2013) 52(3):375–82. doi:10.1016/j.asr.2013.04.003

43. Tulasi Ram S, Su SY, Liu CH. FORMOSAT-3/COSMIC observations of seasonal and longitudinal variations of equatorial ionization anomaly and its interhemispheric asymmetry during the solar minimum period. *J Geophys Res Space Phys* (2009) 114(A6). doi:10.1029/2008ja013880

44. Deminov MG, Kochenova NA, Sitnov YS. Longitudinal variations of the electric field in the dayside equatorial ionosphere. *Geomagn Aeron* (1988) 28:57–60.

45. Batista IS, De Medeiros RT, Abdu MA, de Souza JR, Bailey GJ, de Paula ER. Equatorial ionospheric vertical plasma drift model over the Brazilian region. *J Geophys Res Space Phys* (1996) 101(A5):10887–92. doi:10.1029/95ja03833

46. Ren Z, Wan W, Liu L, Heelis RA, Zhao B, Wei Y, et al. Influences of geomagnetic fields on longitudinal variations of vertical plasma drifts in the presunset equatorial topside ionosphere. *J Geophys Res Space Phys* (2009) 114(A3). doi:10.1029/2008ja013675

47. Horvath I, Essex EA. Vertical <i>E</i> × <i>B</i> drift velocity variations and associated low-latitude ionospheric irregularities investigated with the TOPEX and GPS satellite data. *Gottingen, Germany: Copernicus Publications* (2003) 21(4):1017–30. doi:10.5194/angeo-21-1017-2003

48. Hagan ME, Maute A, Roble RG, Richmond AD, Immel TJ, England SL. Connections between deep tropical clouds and the Earth's ionosphere. *Geophys Res Lett* (2007) 34(20). doi:10.1029/2007gl030142

49. Hagan ME, Forbes JM. Migrating and nonmigrating diurnal tides in the middle and upper atmosphere excited by tropospheric latent heat release. *J Geophys Res Atmospheres* (2002) 107(D24). ACL 6-1-ACL 6-15. doi:10.1029/2001jd001236

50. Zhang K, Wang W, Wang H, Dang T, Liu J, Wu Q. The longitudinal variations of upper thermospheric zonal winds observed by the CHAMP satellite at low and midlatitudes. *J Geophys Res Space Phys* (2018) 123(11):9652–68. doi:10.1029/2018ja025463

51. Sergeeva MA, Maltseva OA, Gonzalez-Esparza JA, Mejia-Ambriz JC, De la Luz V, Corona-Romero P, et al. TEC behavior over the Mexican region. *Ann Geophys* (2018) 61(1):GM104. doi:10.4401/ag-7465

52. Sunardi B, Muslim B, Sakya AE, Rohadi S, Sulastri S, Murjaya J. Ionospheric earthquake effects detection based on total electron content (TEC) GPS correlation[C]// IOP conference series: Earth and environmental science. *IOP Publishing* (2018) 132(1):012014. doi:10.1088/1755-1315/132/1/012014

53. Zhang K, Wang H, Yamazaki Y. Effects of subauroral polarization streams on the equatorial electrojet during the geomagnetic storm on 1 June 2013: 2. The temporal variations. *J Geophys Res Space Phys* (2022) 127(2):e2021JA030180. doi:10.1029/2021ja030180

frontiers | Frontiers in Astronomy and Space Sciences

TYPE Mini Review
PUBLISHED 30 May 2024
DOI 10.3389/fspas.2024.1407172

Check for updates

OPEN ACCESS

EDITED BY
Andrey Samsonov,
University College London, United Kingdom

REVIEWED BY
Alexei V. Dmitriev,
Lomonosov Moscow State University, Russia
Zhongwei Yang,
Chinese Academy of Sciences (CAS), China

*CORRESPONDENCE
Martin O. Archer,
m.archer10@imperial.ac.uk

RECEIVED 26 March 2024
ACCEPTED 30 April 2024
PUBLISHED 30 May 2024

CITATION
Archer MO, Pilipenko VA, Li B, Sorathia K, Nakariakov VM, Elsden T and Nykyri K (2024), Magnetopause MHD surface wave theory: progress & challenges.
Front. Astron. Space Sci. 11:1407172.
doi: 10.3389/fspas.2024.1407172

COPYRIGHT
© 2024 Archer, Pilipenko, Li, Sorathia, Nakariakov, Elsden and Nykyri. This is an open-access article distributed under the terms of the Creative Commons Attribution License (CC BY). The use, distribution or reproduction in other forums is permitted, provided the original author(s) and the copyright owner(s) are credited and that the original publication in this journal is cited, in accordance with accepted academic practice. No use, distribution or reproduction is permitted which does not comply with these terms.

Magnetopause MHD surface wave theory: progress & challenges

Martin O. Archer[1]*, Vyacheslav A. Pilipenko[2], Bo Li[3], Kareem Sorathia[4], Valery M. Nakariakov[5], Tom Elsden[6] and Katariina Nykyri[7]

[1]Space, Plasma, and Climate Community, Department of Physics, Imperial College London, London, United Kingdom, [2]Space Research Institute, Russian Academy of Sciences, Moscow, Russia, [3]Institute of Space Sciences, Shandong University, Weihai, China, [4]Applied Physics Laboratory, Johns Hopkins University, Laurel, MD, United States, [5]Centre for Fusion, Space and Astrophysics, Department of Physics, University of Warwick, Coventry, United Kingdom, [6]School of Mathematics and Statistics, University of St Andrews, St. Andrews, United Kingdom, [7]NASA-Goddard Space Flight Center, Greenbelt, MD, United States

Sharp boundaries are a key feature of space plasma environments universally, with their wave-like motion (driven by pressure variations or flow shears) playing a key role in mass, momentum, and energy transfer. This review summarises magnetohydrodynamic surface wave theory with particular reference to Earth's magnetopause, due to its mediation of the solar-terrestrial interaction. Basic analytic theory of propagating and standing surface waves within simple models are presented, highlighting many of the typically-used assumptions. We raise several conceptual challenges to understanding the nature of surface waves within a complex environment such as a magnetosphere, including the effects of magnetic topology and curvilinear geometry, plasma inhomogeneity, finite boundary width, the presence of multiple boundaries, turbulent driving, and wave nonlinearity. Approaches to gain physical insight into these challenges are suggested. We also discuss how global simulations have proven a fruitful tool in studying surface waves in more representative environments than analytic theory allows. Finally, we highlight strong interdisciplinary links with solar physics which might help the magnetospheric community. Ultimately several upcoming missions provide motivation for advancing magnetopause surface wave theory towards understanding their global role in filtering, accumulating, and guiding turbulent solar wind driving.

KEYWORDS

magnetohydrodynamics, MHD theory discontinuities, MHD waves, surface waves, surface eigenmode, magnetosphere, magnetopause, global simulation

1 Introduction

The plasma Universe hosts a wide variety of different environments. Since over large scales plasmas from different sources cannot mix, these systems tend to be bounded by sharp discontinuities—typically large-scale sheets of electrical currents. Figure 1A illustrates several of these environments and discontinuities across the heliosphere. Akin to waves on water or the membrane of a drum, space plasma boundaries are observed to be in almost continual wave-like motion, including (but not limited to): coronal loops (Nakariakov et al., 2016;

Wang, 2016); coronal mass ejections (Nykyri and Foullon, 2013); the heliospheric current sheet (Smith, 2001); termination shock/heliopause (Zirnstein et al., 2022); and the planetary magnetospheres of Earth (Plaschke et al., 2009a; Plaschke et al., 2009b; He et al., 2020), Mercury (Boardsen et al., 2010; Sundberg et al., 2012), Mars (Wang et al., 2023), Saturn (Masters et al., 2009; Ma et al., 2015), and Jupiter (Volwerk et al., 2013; Montgomery et al., 2023). These surface waves, driven by pressure variations and/or velocity shears, play a key role in mass, momentum, and energy transfer across boundaries (Kivelson and Chen, 1995), meaning they have a major impact on their environment's energy budget.

A prime example is Earth's magnetopause, the interface of the solar-terrestrial interaction that leads to space weather's impacts on vital infrastructure. Magnetopause dynamics have wide-ranging consequences throughout geospace—both directly and through the magnetospheric ultra-low frequency (ULF) waves they generate—affecting radiation belts, magnetotail plasmasheet, auroral oval, mid-latitude ionosphere, and geomagnetic/geoelectric fields (e.g., Elkington, 2006; Summers et al., 2013; Hwang and Sibeck, 2016). These impacts make magnetopause dynamics a cornerstone of solar-terrestrial physics research.

This review concerns magnetohydrodynamic (MHD) surface wave theory through the lens of Earth's magnetopause. Basic theory is briefly discussed (see Plaschke, 2016, for more and relation to observations) though we focus on current challenges, posing suggestions of how to advance progress.

2 MHD theory

2.1 Surface waves

Like body MHD waves able to propagate through the bulk plasma, surface waves at the interface of two media can be derived from wave solutions in displacement

$$\boldsymbol{\xi}(\mathbf{r},t) = \boldsymbol{\xi}(\mathbf{k},\omega)\, e^{i(\mathbf{k}\cdot\mathbf{r}-\omega t)}$$

about equilibrium (subscript 0's) in the linearised Ideal MHD equation

$$\rho_0 \frac{\partial^2 \boldsymbol{\xi}}{\partial t^2} = \nabla\left(\boldsymbol{\xi}\cdot\nabla p_0 + \gamma p_0 \nabla\cdot\boldsymbol{\xi}\right) + \frac{1}{\mu_0}(\nabla\times\mathbf{B}_0)\times\left[\nabla\times(\boldsymbol{\xi}\times\mathbf{B}_0)\right] + \frac{1}{\mu_0}\left[\nabla\times\nabla\times(\boldsymbol{\xi}\times\mathbf{B}_0)\right]\times\mathbf{B}_0,$$

which has corresponding density ρ, pressure p, and magnetic field $\mathbf{B}$ perturbations

$$\delta\rho = -\rho_0\nabla\cdot\boldsymbol{\xi} - \boldsymbol{\xi}\cdot\nabla\rho_0$$

$$\delta p = -\gamma p_0\nabla\cdot\boldsymbol{\xi} - \boldsymbol{\xi}\cdot\nabla p_0$$

$$\delta\mathbf{B} = \nabla\times(\boldsymbol{\xi}\times\mathbf{B}_0),$$

with γ being the adiabatic index.

Often surface waves are considered at discontinuities with the most studied being unbounded tangential discontinuities (TDs; Kruskal and Schwartzschild, 1954; Sen, 1963; Southwood, 1968; Goedbloed, 1971; Walker, 1981; Pu and Kivelson, 1983a; Pu and Kivelson, 1983b), pressure balanced surfaces with no threaded mass/magnetic flux—a reasonable approximation to the magnetopause in the absence of reconnection. Surface waves are, however, also supported by the other MHD discontinuities and shocks (Lubchich and Pudovkin, 1999; Lubchich and Despirak, 2005; Ruderman et al., 2018), as well as transition layers (Chen and Hasegawa, 1974; Lee and Roberts, 1986; Uberoi, 1989; De Keyser et al., 1999).

Figure 1B demonstrates the key features of a surface wave on a planar TD with uniform half-spaces. They are collective modes of vortical plasma motions, mathematically constructed from magnetosonic waves on each side independently obeying dispersion relation

$$k_{n,a}^2 = -k_t^2 + \frac{\omega_a^4}{v_{\mathrm{A},a}^2\omega_a^2 + c_{\mathrm{S},a}^2\left[\omega_a^2 - (\mathbf{k}_t\cdot\mathbf{v}_{\mathrm{A},a})^2\right]}, \tag{1}$$

where a represents one half-space (magnetosphere/magnetosheath), n and t denote normal and tangential directions, v_A and c_S are the Alfvén and sound speeds, and ω_a is the rest frame angular frequency. If the plasma has velocity $\mathbf{u}_{0,a}$ in the local frame, the Doppler shift gives $\omega = \omega_a + \mathbf{k}_t\cdot\mathbf{u}_{0,a}$.

Surface waves are necessarily localised to their discontinuity, hence exhibit evanescence normal to the boundary, i.e., $\mathrm{Re}(k_{n,a}^2) < 0$. Fluctuations' decay scale depends on plasma conditions, thus can be different on either side. Amplitudes peak at the discontinuity, necessitating a reversal of polarisation across the boundary (Southwood, 1974).

The two wave solutions are tied together through boundary conditions: the tangential wave vector $\mathbf{k}_t$ and wave frequency ω are the same on both sides, and the normal displacement ξ_n (or equivalently velocity) and total pressure perturbation $\delta p_{tot} = \delta p + \mathbf{B}_0\cdot\delta\mathbf{B}/\mu_0$ are continuous. This leads to general surface wave dispersion relation applied to the magnetopause.

$$\frac{k_{n,\mathrm{msh}}}{\rho_{0,\mathrm{msh}}\left[\omega_{\mathrm{msh}}^2 - (\mathbf{k}_t\cdot\mathbf{v}_{\mathrm{A,msh}})^2\right]} = \frac{k_{n,\mathrm{msp}}}{\rho_{0,\mathrm{msp}}\left[\omega_{\mathrm{msp}}^2 - (\mathbf{k}_t\cdot\mathbf{v}_{\mathrm{A,msp}})^2\right]}, \tag{2}$$

where subscripts msh and msp represent the magnetosheath and magnetosphere sides, respectively. Eq. 2 must be solved numerically and yields quasi-fast and quasi-slow modes (Pu and Kivelson, 1983a). It can be simplified assuming incompressibility ($c_\mathrm{S}\to\infty$), where $k_n^2 = -k_t^2$ on both sides and Eq. 2 becomes.

$$\omega = \frac{\mathbf{k}_t\cdot\left(\rho_{0,\mathrm{msh}}\mathbf{u}_{0,\mathrm{msh}} + \rho_{0,\mathrm{msp}}\mathbf{u}_{0,\mathrm{msp}}\right)}{\rho_{0,\mathrm{msh}} + \rho_{0,\mathrm{msp}}} \pm \sqrt{\frac{\rho_{0,\mathrm{msh}}(\mathbf{k}_t\cdot\mathbf{v}_{\mathrm{A,msh}})^2 + \rho_{0,\mathrm{msp}}(\mathbf{k}_t\cdot\mathbf{v}_{\mathrm{A,msp}})^2}{\rho_{0,\mathrm{msh}} + \rho_{0,\mathrm{msp}}} - \frac{\rho_{0,\mathrm{msh}}\rho_{0,\mathrm{msp}}}{\left(\rho_{0,\mathrm{msh}} + \rho_{0,\mathrm{msp}}\right)^2}\left[\mathbf{k}_t\cdot\left(\mathbf{u}_{0,\mathrm{msh}} - \mathbf{u}_{0,\mathrm{msp}}\right)\right]^2}.$$

This has forward and backward propagating solutions with respect to $\mathbf{k}_t$, though as the flow shear increases one is reversed

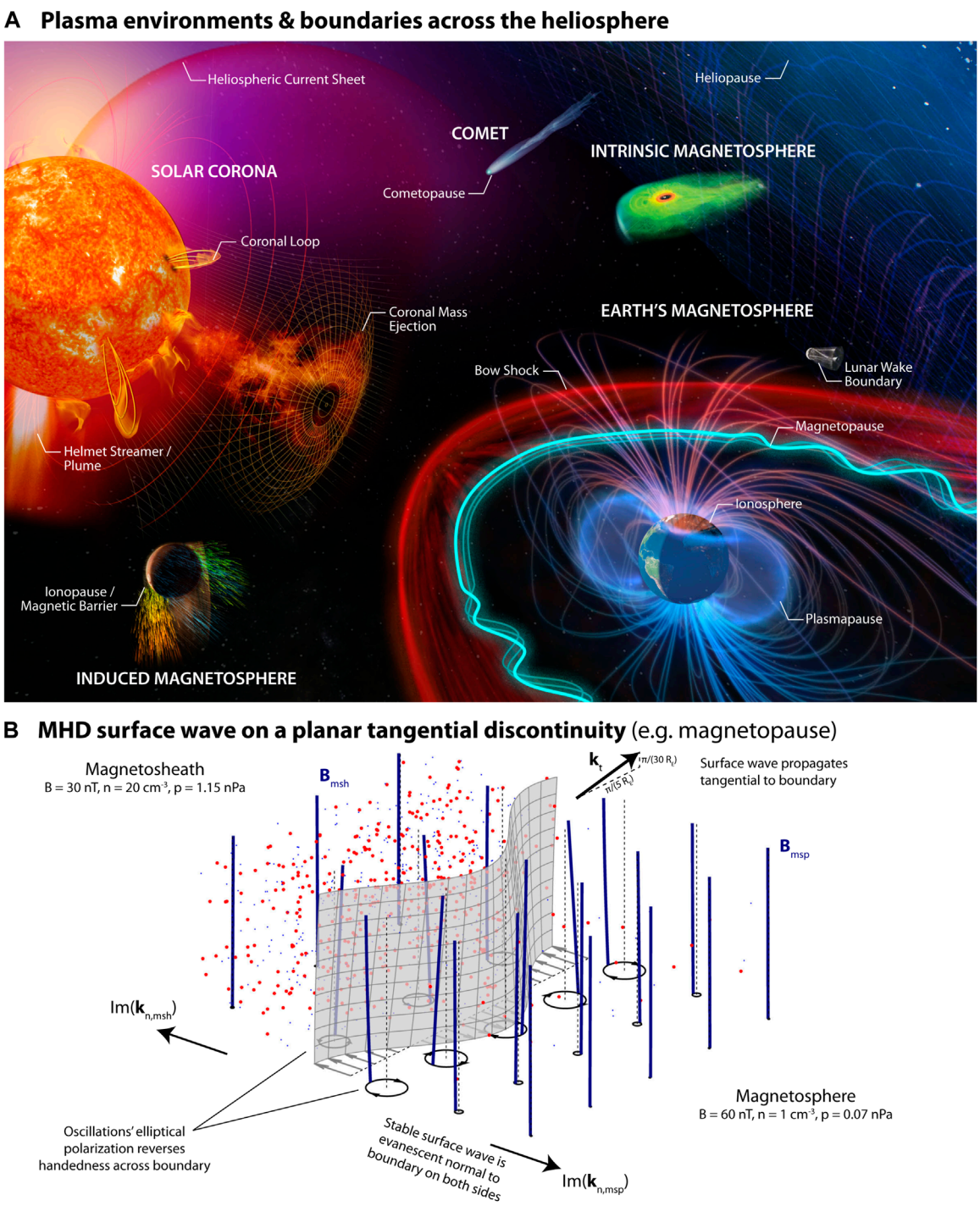

FIGURE 1
(A) Illustration across the heliosphere of different plasma environments and their boundaries which support surface waves (adapted from images by NASA and Emmanuel Masongsong). **(B)** Diagram of a surface wave on a tangential discontinuity, such as the magnetopause. Displayed are the discontinuity (grey), magnetic field lines (navy), and relative numbers of ions (red) and electrons (blue). An animated version can be found in the Supplementary Material.

becoming a "negative energy" wave (e.g., Mann et al., 1999). Increasing the shear further results in exponential growth in time, corresponding to the classical criterion for the Kelvin-Helmholtz Instability (KHI, Chandrasekhar, 1961). While intimately related to surface waves, we shall not discuss KHI further here (see instead review Masson and Nykyri, 2018). At the magnetopause typically $u_{0,\mathrm{msh}} \gg u_{0,\mathrm{msp}}$, $\rho_{0,\mathrm{msh}} \gg \rho_{0,\mathrm{msp}}$ and $B_{0,\mathrm{msh}} \ll B_{0,\mathrm{msp}}$, hence the approximate relation

$$\omega \approx \mathbf{k}_t \cdot \mathbf{u}_{0,\mathrm{msh}} \pm \omega_0$$

$$\omega_0 = \sqrt{\frac{\left(\mathbf{k}_t \cdot \mathbf{B}_{0,\mathrm{msp}}\right)^2 + \left(\mathbf{k}_t \cdot \mathbf{B}_{0,\mathrm{msh}}\right)^2}{\mu_0\left(\rho_{0,\mathrm{msp}} + \rho_{0,\mathrm{msh}}\right)}} \approx \frac{\mathbf{k}_t \cdot \mathbf{B}_{0,\mathrm{msp}}}{\sqrt{\mu_0 \rho_{0,\mathrm{msh}}}} \tag{3}$$

holds for $\left(\mathbf{k}_t \cdot \mathbf{u}_{0,\mathrm{msh}}\right)^2 \rho_{0,\mathrm{msp}}/\rho_{0,\mathrm{msh}} \ll \omega_0^2$, consisting of a natural frequency ω_0 for no flow shear (Chen and Hasegawa, 1974; Plaschke and Glassmeier, 2011) along with an advective Doppler shift.

In reality the magnetopause has finite thickness ~100–2500 km (Berchem and Russell, 1982; Paschmann et al., 2005), whereas the above theory treated it as infinitesimally thin. While this limit is valid for wavelengths much larger than the thickness, a finite-width boundary has been considered through either a continuously-varying transition (Chen and Hasegawa, 1974; De Keyser et al., 1999) or uniform layer bounded by two discontinuities (Lee et al., 1981). Finite thickness introduces inner and outer surface modes, and can allow waves to propagate inside the layer due to the presence of turning points. Surface waves may resonantly convert to Alfvén or slow magnetosonic waves if their resonance conditions, $\omega^2 = \left(\mathbf{k}_t \cdot \mathbf{v}_A\right)^2$ or $\omega^2 = \left(\mathbf{k}_t \cdot \mathbf{v}_A\right)^2 c_S^2/\left(v_A^2 + c_S^2\right)$, become locally fulfilled within the transition. This irreversible mode conversion leads to damping of the surface mode, even in the absence of any dissipation in the system (Chen and Hasegawa, 1974; Lee and Roberts, 1986; Uberoi, 1989). Damping (or conversely growth) of surface waves results, through Eq. 1, in the evanescent magnetosonic waves exhibiting phase motion along the normal direction (Pu and Kivelson, 1983a; Archer et al., 2021).

2.2 Surface eigenmodes

The theory presented in Section 2.1 holds for unbounded TDs, whereas magnetospheric field lines are necessarily terminated at their intersection with the ionosphere, as displayed in Figures 2A, B for simple box and cylindrical magnetospheric models (e.g., Southwood, 1974; Kivelson et al., 1984). The ionospheric boundary conditions are highly reflecting for magnetosonic modes, even more than for Alfvén waves (Kivelson and Southwood, 1988), meaning standing surface waves might form between conjugate ionospheres, known as surface eigenmodes (Chen and Hasegawa, 1974; Plaschke and Glassmeier, 2011). These modes have been considered on either the magnetopause or plasmapause, with quantization condition

$$\frac{\mathbf{k}_t \cdot \mathbf{B}_{0,\mathrm{msp}}}{B_{0,\mathrm{msp}}} = \pm\frac{j\pi}{S}, \tag{4}$$

where $j \in \mathbb{N}$ and S is the field line length. Surface eigenmodes have conceptual similarities to field line resonances, Alfvén waves locally standing on field lines due to ionospheric reflection (e.g., Southwood, 1974). They are, however, rather different from cavity (for a closed magnetosphere with quantized azimuthal wavenumbers; Kivelson et al., 1984; Kivelson and Southwood, 1985) and waveguide (for an open-ended magnetotail with a spectrum of azimuthal wavenumbers; Samson et al., 1992; Wright, 1994) modes. These eigenmodes instead consist of propagating, rather than evanescent, magnetosonic waves that form approximately radially standing structure from reflection by boundaries or turning points. See Archer et al. (2022) for further comparison.

Magnetopause surface eigenmodes (MSEs) are typically considered around the subsolar meridian, where flow shears are low. Its eigenfrequency in an incompressible box model is thus given by Eq. 3, making it the lowest frequency magnetospheric normal mode and highly penetrating into the magnetosphere due to expected low azimuthal wavenumbers (Plaschke et al., 2009b; Plaschke and Glassmeier, 2011; Archer and Plaschke, 2015). The frequency has an approximately linear dependence on solar wind speed—via balance of magnetospheric magnetic and solar wind dynamic pressures, proportionality of magnetosheath and solar wind densities, and "stiffness" of the magnetosphere (Chen and Hasegawa, 1974; Archer et al., 2013a; Archer and Plaschke, 2015; Nenovski, 2021). Compressibility should modify this only slightly (Pu and Kivelson, 1983a).

It had been suggested fast solar wind might inhibit MSE, as meridional magnetosheath flow could reverse one of the counter-propagating surface waves (Plaschke and Glassmeier, 2011). Later this was considered important only for large dipole tilts, based on time-of-flight calculations within empirical models (Archer and Plaschke, 2015). Away from the subsolar meridian it was thought MSE would be advected tailward by the magnetosheath. However, it was shown theoretically (as well as in observations and simulations) that MSE can stand stationary against the flow across a wide local time range on the dayside, trapping wave energy locally (Archer et al., 2021).

In box models MSE currents flow only within the magnetopause, forming field-aligned currents at low altitudes which close via ionospheric Pedersen currents (Plaschke and Glassmeier, 2011). Whether surface modes directly have significant effects on the ionosphere or ground, and where these might map to, has been debated (Kivelson and Southwood, 1988; Southwood and Kivelson, 1990; Southwood and Kivelson, 1991; Kozyreva et al., 2019; Archer et al., 2023a).

2.3 Theoretical challenges

Numerous fundamental conceptual challenges concerning magnetopause surface waves remain, even in the linear theory. These are due to standard box/cylindrical models (Figures 2A, B) being oversimplifications of the magnetospheric environment, neglecting aspects of the full physics.

Standard models feature straight equilibrium field lines, however, field line curvature significantly affects MHD waves. To account for this one requires a magnetic (field-aligned) coordinate system with corresponding metric tensor (Stern, 1970; Stern, 1976; D'haeseleer et al., 1991). Note an orthogonal system may not exist, e.g., in the case of background field-aligned currents (Salat and Tataronis, 2000; Rankin et al., 2006). Such methods applied to the magnetospheric Alfvén continuum have shown eigenfrequencies differ from time-of-flight estimates typically by ~20–75% and vary with polarisation (Singer et al., 1981; Rankin et al., 2006; Elsden and Wright, 2020). The problem is more complex for surface waves, since solutions in each half-space, with likely different magnetic coordinate systems, must be tied together. Nonetheless, a simple

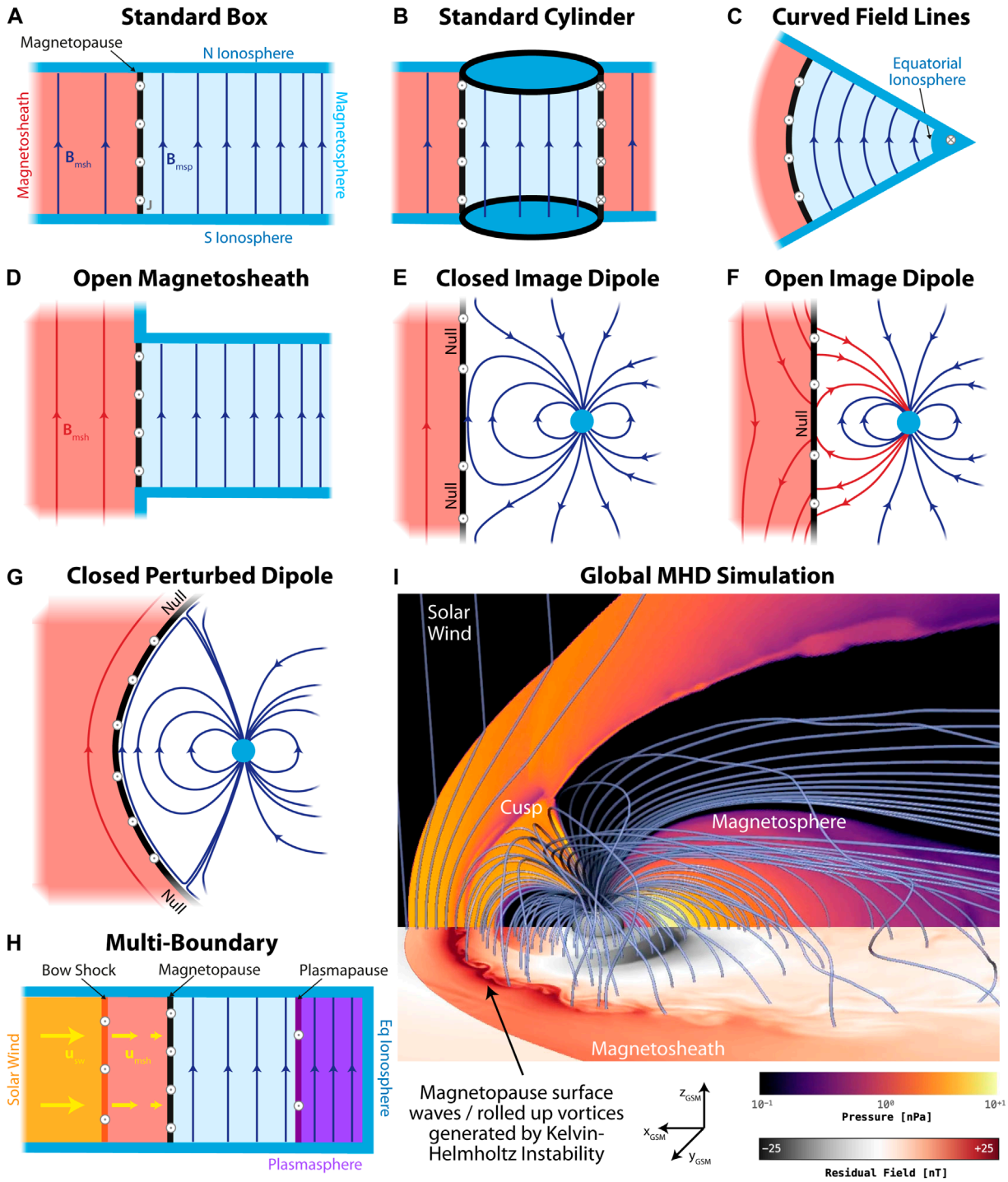

FIGURE 2
Diagrams of analytic MHD magnetosphere models that have been applied to magnetopause surface wave theory **(A, B)**, and model setups which could advance current challenges to this theory **(C–H)**. These may be complemented by global MHD simulations of the magnetosphere **(I)**, such as GAMERA (Zhang et al., 2019). Depicted is a northward IMF run exhibiting KHI waves/vortices at the magnetopause, with equatorial plane showing residual magnetic field from a dipole, and meridional plane showing thermal pressure.

model to determine surface waves' sensitivity to field line curvature is the hydromagnetic wedge (Radoski, 1970) depicted in Figure 2C. Here cylindrical coordinates describe axial field lines, each with a constant radius of curvature (their radial coordinate), confined between two angles of azimuth corresponding to ionospheric boundaries.

Field lines are terminated in the ionosphere on both sides of the discontinuity in standard models. While this is valid for the

plasmapause, at the magnetopause field lines in the magnetosheath should be open (Kozyreva et al., 2019). A modified box model with open magnetosheath flux is illustrated in Figure 2D. While the quantization condition on closed magnetospheric field lines (Eq. 4) should be unaffected, continuity of normal displacement across the boundary (Walker, 1981; Plaschke and Glassmeier, 2011) requires zero perturbation above/below the intersection of the magnetopause with the ionosphere, i.e., $\xi_x(x=0,y,z,t) = \mathrm{rect}(\pi z/S)\cos(k_z z)\exp\left(i\left[k_y y-\omega t\right]\right)$. The Fourier decomposition of this boundary condition introduces additional magnetosheath wavenumbers. These must also follow the magnetosonic dispersion relation (Eq. 1), hence may consist of propagating components in addition to evanescent waves. The overall effect would be a form of diffraction into the magnetosheath.

The magnetic field models presented have still been highly simplified. Close to Earth the field is reasonably approximated by a dipole, but differs substantially from this in the outer magnetosphere. Dipole equilibrium magnetic field models have been used to explore surface modes due to velocity shears (Leonovich and Kozlov, 2019), though by definition these models cannot include background currents or thermal pressure gradients. Placing an image dipole in the solar wind gives an analytic closed magnetosphere with planar infinitely conducting magnetopause and two magnetic null points at the cusps, as shown in Figure 2E (Chapman and Bartels, 1940). More representative closed magnetosphere models, like in Figure 2G, can be constructed by perturbing a dipole. Introducing (just two) spherical harmonic corrections to dipole Euler potentials produces a reasonable magnetosphere (Stern, 1967), though how to describe magnetosheath field lines in this framework is unclear. Alternatively, expressing the field as a scalar potential in parabolic harmonics with contributions from the dipole and magnetopause currents allows one to confine the geomagnetic field within a paraboloidal magnetopause (Stern, 1985), though magnetic coordinates must be determined numerically (Degeling et al., 2010).

In closed magnetosphere models the magnetopause is a TD. While it is often stated the magnetopause may be treated as a rotational discontinuity for an open magnetosphere (e.g., Sonnerup and Ledley, 1974), this neglects any density/pressure gradients present between the two media. Therefore, for an open magnetosphere the magnetopause must consist of both compressional and rotational boundaries (Dorville et al., 2014). The image dipole model (Figure 2E) can be simply extended to represent an open magnetosphere, as shown in Figure 2F (Kan and Akasofu, 1974). Constructing a realistic open magnetosphere model analytically remains an outstanding challenge (Zaharia and Birn, 2005).

These more representative models (Figures 2E–G) may help understanding effects of the polar cusps. Alfvén wave propagation is significantly affected by local variations in magnetic field strength and/or curvature when wavelengths are comparable to inhomogeneity scales (Pilipenko et al., 1999; Pilipenko et al., 2005), leading to reflection up to ~80–90%. If similar holds for surface waves, surface eigenmodes might stand between reflection points in conjugate cusps rather than ionospheres. Another benefit to these models would be in probing non-resonant wave coupling. While Alfvén and magnetosonic modes are independent in uniform media, when inhomogeneities are introduced waves necessarily have mixed properties (Radoski, 1971; Goossens et al., 2019). Understanding the partial, irreversible conversion of surface waves' compressional energy into Alfvén waves could help determine potential impacts of surface waves on the system and any filtering/processing the magnetosphere imposes upon them (cf. Pilipenko et al., 1999).

Thus far surface waves on a single boundary have been considered. However, it is clear from Figure 1A numerous boundaries exist within the magnetosphere. Given the large-scale nature of surface eigenmodes across the magnetic field, they cannot exist in isolation. This motivates a multi-boundary approach, such as in Figure 2H. Some progress towards this has considered eigenmodes of the outer magnetosphere, modeled as a slab or annular cylinder bounded by magnetopause and plasmapause (Nenovski et al., 2007; Nenovski, 2021). How the surface eigenmodes of individual boundaries are modified by, and couple to, the existence of another boundary has yet to be explored. Furthermore, introduction of the bow shock and equatorial ionospheric boundaries is required for a more complete description.

Resonant absorption for a finite-width boundary has been poorly explored outside of standard models. Where (either inside or outside) the transition layer mode conversion occurs and how this varies with surface mode harmonics is not well understood in more realistic setups. Since mode conversion provides a means for field-aligned current generation from a purely compressional wave (Southwood and Kivelson, 1990; Itonaga et al., 2000; Plaschke and Glassmeier, 2011) it is an important topic relevant to the ionospheric and ground-based impacts of surface modes (Kivelson and Southwood, 1988; Archer et al., 2023a).

Linear surface wave theory typically solves either initial value (where the boundary is perturbed and allowed to evolve) or eigenvalue problems (where normal modes are sought). Under these approaches it is not possible to self consistently consider variable solar wind forcing. However, solar wind and magnetosheath plasmas are highly turbulent, modifying conditions present adjacent to the magnetopause over timescales comparable to (or shorter than) surface wave periodicities. It has been suggested, by analogy with a driven harmonic oscillator with stochastically varying eigenfrequency, magnetosheath turbulence might suppress the surface mode (Pilipenko et al., 2017). The potential damping factor in such a toy model using representative turbulent amplitudes/spectra have not yet been estimated. Expanding this approach to self-consistently treat turbulent driving in addition to its effect on the eigenfrequency is required to more realistically formulate this problem.

It is finally worth noting only linear wave theory has been discussed. Nonlinear effects have been investigated analytically on planar TDs (cf. Figure 1B) for incompressible plasmas (Hollweg, 1987; Alì and Hunter, 2003). While this is of greatest relevance to a KH-unstable boundary, even in the marginally stable and weakly nonlinear regimes surface waves undergo wave steepening, crest/trough sharpening, and non-local self-interactions, leading to their breakdown in finite time. There is certainly more scope to explore this topic.

Many of these current challenges simply cannot be realistically treated by analytic theory. Nonetheless, modifications to simple models will likely provide insight into the physics. However, to more representatively model them in a complex

environment like the magnetosphere necessitates numerical simulations.

3 Global simulations

Global simulations (mostly MHD, as shown in Figure 2I) have become a valuable tool in studying geospace, though correctly interpreting their results requires understanding the underlying physics and numerics (Raeder, 2003; Zhang et al., 2019; Raeder et al., 2021). The choice of grid, resolution, algorithms, and solver order have implications on whether boundary layers are resolved/smeared, in turn affecting surface wave growth/damping rates and wavelengths (Hartinger et al., 2015; Sorathia et al., 2017; Michael et al., 2021).

Magnetopause dynamics driven by upstream pressure changes (e.g., Børve et al., 2011; Desai et al., 2021; Horaites et al., 2023) and KHI (e.g., Slinker et al., 2003; Collado-Vega et al., 2007; Fairfield et al., 2007) have been explored in global simulations. These have included reproducing impulsively-excited MSE, showing this eigenmode can be sustained in a realistic magnetosphere (Hartinger et al., 2015; Archer et al., 2021).

Distinct inner and outer surface modes for continuous transition layers have been demonstrated. Results vary on whether their local frequencies are the same (Claudepierre et al., 2008; Archer et al., 2022; Archer et al., 2023a) or slightly different (Li et al., 2012), but agree these modes have different local wavelengths. Similarly, even just for intrinsic KHI-generated waves, differences are reported on whether surface wave frequencies are global (Claudepierre et al., 2008; Guo et al., 2010) or locally varying (Merkin et al., 2013; Archer et al., 2021), though their wavelengths clearly vary with local time from noon (Guo et al., 2010; Li et al., 2012; Merkin et al., 2013; Archer et al., 2021). Surface wave frequencies appear correlated with solar wind speed (Claudepierre et al., 2008; Li et al., 2012). Dayside MSE have been demonstrated seeding tailward-travelling surface waves that subsequently amplify via KHI despite not being at the instability's intrinsic frequency (Hartinger et al., 2015; Archer et al., 2021), highlighting different driving mechanisms can be coupled thus may not always be as simple as often assumed.

The mixed properties of MHD waves from non-resonant wave coupling of the surface mode in a realistic plasma environment have been reported. These lead to field-aligned current generation throughout the magnetosphere, peaking at the inner edge of the boundary layer rather than the Open-Closed Boundary (Archer et al., 2023a). They also affect velocity polarisations, exhibiting axes aligned to the local (highly distorted) geomagnetic field (Li et al., 2013) and orientations perpendicular to amplitude gradients (Archer et al., 2023a), more akin to Alfvénic modes (Southwood and Kivelson, 1984). Resonant coupling of surface waves to Alfvén and cavity/waveguide body eigenmodes has been demonstrated in regions where frequencies match (Merkin et al., 2013; Archer et al., 2021; Archer et al., 2022).

Simulation results suggest the cusps do not reflect surface modes, but do introduce additional magnetic field nodes/antinodes and polarisation reversals compared to the velocity (Archer et al., 2022). They have also demonstrated standing structure and plasma inhomogeneities can alter the standard magnetosonic plasma–magnetic field correlation (Archer et al., 2023b). Finally, simulations have provided insight into potential impacts of surface waves on energetic particles (Claudepierre et al., 2008; Sorathia et al., 2017) and the ionosphere/ground (Archer et al., 2023a).

Global simulations have, therefore, provided valuable insight to some of the theoretical challenges raised in section 2.3, though further work in resolving inconclusive results and addressing outstanding questions remains.

4 Discussion

Boundary processes are key to the global dynamics and energetics of space plasma systems. Indeed it has been appreciated that the magnetopause may act as a (slow roll-off) low-pass filter (Smit, 1968; Freeman et al., 1995; Børve et al., 2011; Archer et al., 2013b; Desai et al., 2021), with surface waves contributing by processing, accumulating, and guiding upstream disturbances. Given magnetopause surface waves have natural frequencies (dependent on plasma conditions, Chen and Hasegawa, 1974; Miura and Pritchett, 1982; Archer and Plaschke, 2015), they may act as a magnetospheric resonator providing an efficient mechanism for frequency-dependent absorption of turbulent driving. Further theoretical/modelling work addressing the challenges raised in this review are required to assess this prospect. We have only considered MHD theory; extensions include kinetic surface wave theory (Lee, 2019) and/or coupling to Kinetic Alfvén Waves within the magnetopause (Hasegawa, 1976; Lee et al., 1994).

The connection between magnetospheric and solar waves has long been recognized (Nakariakov et al., 2016). For example, the best observed solar collective motions—transverse fundamental kink modes of coronal loops (Nakariakov et al., 2021)—can be strikingly well understood in terms of surface waves supported by interfaces of vanishing (Goossens et al., 2009) or finite widths (Hollweg and Yang, 1988) in models similar to Figure 2B. Though historically classified as "body modes" (Edwin and Roberts, 1983), in the long-wavelength linear limit kink modes are relatively insensitive to the details of the MHD environment (Goossens et al., 2009) and their dispersion relation reduces to exactly that of the surface eigenmode (Eq. 3). While theoretical understanding of their resonant interplay with the Alfvén continuum benefitted considerably from magnetospheric studies (Pascoe et al., 2011), their remotely-sensed nature have enabled effects like field line curvature (Van Doorsselaere et al., 2004; van Doorsselaere et al., 2009) and the localization of wave exciters (Nakariakov et al., 2004) to be addressed. Concepts such as wave packets have been elucidated by the stationary phase method (Guo et al., 2022; Li et al., 2023), addressing effects of waveguide dispersion (Kolotkov et al., 2021). These advancements from the solar environment could aid current challenges in the magnetospheric context.

Overall, advancing magnetopause surface wave theory will provide vital underpinning in interpreting data from upcoming missions. These include SMILE, which aims to uncover the fundamental modes of the dayside solar wind–magnetosphere

interaction through soft X-ray imaging (Wang and Branduardi-Raymont, 2022), and HelioSwarm, which among its objectives is to assess the impact of solar wind turbulence on the magnetosphere (Klein et al., 2023).

Author contributions

MA: Funding acquisition, Project administration, Visualization, Writing–original draft. VP: Conceptualization, Writing–review and editing. BL: Writing–review and editing. KS: Visualization, Writing–review and editing. VN: Writing–review and editing. TE: Writing–review and editing. KN: Funding acquisition, Writing–review and editing.

Funding

The author(s) declare that financial support was received for the research, authorship, and/or publication of this article. This review was supported by the International Space Science Institute (ISSI) in Bern, through ISSI International Team project #546 "Magnetohydrodynamic Surface Waves at Earth's Magnetosphere (and Beyond)". MOA was supported by UKRI (STFC/EPSRC) Stephen Hawking Fellowship EP/T01735X/1 and UKRI Future Leaders Fellowship MR/X034704/1.

Acknowledgments

We thank Ferdinand Plaschke, Anatoly Leonovich, and Harley M. Kelly for helpful discussions. For the purpose of open access, the author(s) has applied a Creative Commons attribution (CC BY) licence to any Author Accepted Manuscript version arising.

Conflict of interest

The authors declare that the research was conducted in the absence of any commercial or financial relationships that could be construed as a potential conflict of interest.

The author(s) declared that they were an editorial board member of Frontiers, at the time of submission. This had no impact on the peer review process and the final decision.

Publisher's note

All claims expressed in this article are solely those of the authors and do not necessarily represent those of their affiliated organizations, or those of the publisher, the editors and the reviewers. Any product that may be evaluated in this article, or claim that may be made by its manufacturer, is not guaranteed or endorsed by the publisher.

Supplementary material

The Supplementary Material for this article can be found online at: https://www.frontiersin.org/articles/10.3389/fspas.2024.1407172/full#supplementary-material

References

Alì, G., and Hunter, J. K. (2003). Nonlinear surface waves on a tangential discontinuity in magnetohydrodynamics. *Q. Appl. Math.* 61, 451–474. doi:10.1090/qam/1999831

Archer, M. O., Hartinger, M. D., and Horbury, T. S. (2013a). Magnetospheric "magic" frequencies as magnetopause surface eigenmodes. *Geophys. Res. Lett.* 40, 5003–5008. doi:10.1002/grl.50979

Archer, M. O., Hartinger, M. D., Plaschke, F., Southwood, D. J., and Rastaetter, L. (2021). Magnetopause ripples going against the flow form azimuthally stationary surface waves. *Nat. Commun.* 12, 5697. doi:10.1038/s41467-021-25923-7

Archer, M. O., Hartinger, M. D., Rastaetter, L., Southwood, D. J., Heyns, M., Eggington, J. W. B., et al. (2023a). Auroral, ionospheric and ground magnetic signatures of magnetopause surface modes. *J. Geophys. Res. Space Phys.* 128, e2022JA031081. doi:10.1029/2022JA031081

Archer, M. O., Horbury, T. S., Eastwood, J. P., Weygand, J. M., and Yeoman, T. K. (2013b). Magnetospheric response to magnetosheath pressure pulses: a low pass filter effect. *J. Geophys. Res. Space Phys.* 118, 5454–5466. doi:10.1002/jgra.50519

Archer, M. O., and Plaschke, F. (2015). What frequencies of standing surface waves can the subsolar magnetopause support? *J. Geophys Res. Space Phys.* 120, 3632–3646. doi:10.1002/2014JA020545

Archer, M. O., Southwood, D. J., Hartinger, M. D., Rastaetter, L., and Wright, A. N. (2022). How a realistic magnetosphere alters the polarizations of surface, fast magnetosonic, and alfvén waves. *J. Geophys. Res. Space Phys.* 127, e2021JA030032. doi:10.1029/2021JA030032

Archer, M. O., Southwood, D. J., Rastaetter, L., and Nykyri, K. (2023b). Magnetosonic ULF waves with anomalous plasma–magnetic field correlations: standing waves and inhomogeneous plasmas. *Geophys. Res. Lett.* 50, e2023GL104762. doi:10.1029/2023GL104762

Berchem, J., and Russell, C. T. (1982). The thickness of the magnetopause current layer: ISEE 1 and 2 observations. *J. Geophys. Res.* 87, 2108–2114. doi:10.1029/JA087iA04p02108

Boardsen, S. A., Sundberg, T., Slavin, J. A., Anderson, B. J., orth, H., Solomon, S. C., et al. (2010). Observations of Kelvin-Helmholtz waves along the dusk-side boundary of Mercury's magnetosphere during MESSENGER's third flyby. *Gephys. Res. Lett.* 37, L12101. doi:10.1029/2010GL043606

Børve, S., Sato, H., Pécseli, H. L., and Trulsen, J. K. (2011). Minute-scale period oscillations of the magnetosphere. *Ann. Geophys.* 29, 663–671. doi:10.5194/angeo-29-663-2011

Chandrasekhar, S. (1961) *Hydrodynamic and hydromagnetic stability*. Oxford, UK: Oxford University Press.

Chapman, S., and Bartels, J. (1940) *Geomagnetism*. Oxford, UK: Oxford University Press.

Chen, L., and Hasegawa, A. (1974). A theory of long-period magnetic pulsations: 2. impulse excitation of surface eigenmode. *J. Geophys. Res.* 79, 1033–1037. doi:10.1029/JA079i007p01033

Claudepierre, S. G., Elkington, S. R., and Wiltberger, M. (2008). Solar wind driving of magnetospheric ULF waves: pulsations driven by velocity shear at the magnetopause. *J. Geophys. Res. Space Phys.* 113, A05218. doi:10.1029/2007JA012890

Collado-Vega, Y. M., Kessel, R. L., Shao, X., and Boller, R. A. (2007). MHD flow visualization of magnetopause boundary region vortices observed during high-speed streams. *J. Geophys. Res. Space Phys.* 112, A06213. doi:10.1029/2006JA012104

Degeling, A. W., Rankin, R., Kabin, K., Rae, I. J., and Fenrich, F. R. (2010). Modeling ULF waves in a compressed dipole magnetic field. *J. Geophys. Res.* 115, A10212. doi:10.1029/2010JA015410

De Keyser, J., Roth, M., Reberac, F., Rezeau, L., and Belmont, G. (1999). Resonant amplification of MHD waves in realistic subsolar magnetopause configurations. *J. Geophys. Res. Space Phys.* 104, 2399–2409. doi:10.1029/1998JA900060

Desai, R. T., Freeman, M. P., Eastwood, J. P., Eggington, J. W. B., Archer, M. O., Shprits, Y. Y., et al. (2021). Interplanetary shock-induced magnetopause motion: comparison

between theory and global magnetohydrodynamic simulations. *Geophys. Res. Lett.* 48, e2021GL092554. doi:10.1029/2021GL092554

D'haeseleer, W. D., Hitchon, W. N. G., Callen, J. D., and Shohet, J. L. (1991) *Flux coordinates and magnetic field structure: a guide to a fundamental tool of plasma theory*. Berlin, Germany: Springer. doi:10.1007/978-3-642-75595-8

Dorville, N., Belmont, G., Rezeau, L., Grappin, R., and Retinó, A. (2014). Rotational/compressional nature of the magnetopause: application of the bv technique on a magnetopause case study. *J. Geophys. Res. Space Phys.* 119, 1898–1908. doi:10.1002/2013JA018927

Edwin, P. M., and Roberts, B. (1983). Wave propagation in a magnetic cylinder. *Sol. Phys.* 88, 179–191. doi:10.1007/BF00196186

Elkington, S. R. (2006). "A review of ULF interactions with radiation belt electrons," in *Magnetospheric ULF waves: synthesis and new directions*. Editors K. Takahashi, P. J. Chi, R. E. Denton, and R. L. Lysak (United States: John Wiley and Sons). 169 of *Geophysical Monograph Series*. doi:10.1029/169GM06

Elsden, T., and Wright, A. (2020). Evolution of high-*m* poloidal alfvén waves in a dipole magnetic field. *J. Geophys. Res. Space Phys.* 125, e2020JA028187. doi:10.1029/2020JA028187

Fairfield, D. H., Kuznetsova, M. M., Mukai, T., Nagai, T., Gombosi, T. I., and Ridley, A. J. (2007). Waves on the dusk flank boundary layer during very northward interplanetary magnetic field conditions: observations and simulation. *J. Geophys. Res. Space Phys.* 112, A08206. doi:10.1029/2006JA012052

Freeman, M. P., Freeman, N. C., and Farrugia, C. J. (1995). A linear perturbation analysis of magnetopause motion in the Newton-Busemann limit. *Ann. Geophys.* 13, 907–918. doi:10.1007/s00585-995-0907-0

Goedbloed, J. P. (1971). Stabilization of magnetohydrodynamic instabilities by force-free magnetic fields: I. plane plasma layer. *Physica* 53, 412–444. doi:10.1016/0031-8914(71)90127-3

Goossens, M., Terradas, J., Andries, J., Arregui, I., and Ballester, J. L. (2009). On the nature of kink MHD waves in magnetic flux tubes. *A&A* 503, 213–223. doi:10.1051/0004-6361/200912399

Goossens, M. L., Arregui, I., and Van Doorsselaere, T. (2019). Mixed properties of MHD waves in non-uniform plasmas. *Front. Astron. Space Sci.* 6, 20. doi:10.3389/fspas.2019.00020

Guo, M., Li, B., Van Doorsselaere, T., and Shi, M. (2022). Impulsively generated kink wave trains in solar coronal slabs. *MNRAS* 515, 4055–4064. doi:10.1093/mnras/stac2006

Guo, X. C., Wang, C., and Hu, Y. Q. (2010). Global MHD simulation of the Kelvin-Helmholtz instability at the magnetopause for northward interplanetary magnetic field. *J. Geophys. Res. Space Phys.* 115, A10218. doi:10.1029/2009JA015193

Hartinger, M. D., Plaschke, F., Archer, M. O., Welling, D. T., Moldwin, M. B., and Ridley, A. (2015). The global structure and time evolution of dayside magnetopause surface eigenmodes. *Geophys. Res. Lett.* 42, 2594–2602. doi:10.1002/2015GL063623

Hasegawa, A. (1976). Particle acceleration by MHD surface wave and formation of aurora. *J. Geophys. Res.* 81, 5083–5090. doi:10.1029/JA081i028p05083

He, F., Guo, R.-L., Dunn, W. R., Yao, Z.-H., Zhang, H.-S., Hao, Y.-X., et al. (2020). Plasmapause surface wave oscillates the magnetosphere and diffuse aurora. *Nat. Commun.* 11, 1668. doi:10.1038/s41467-020-15506-3

Hollweg, J. V. (1987). Incompressible magnetohydrodynamic surface waves: nonlinear aspects. *ApJ* 317, 918–925. doi:10.1086/165341

Hollweg, J. V., and Yang, G. (1988). Resonance absorption of compressible magnetohydrodynamic waves at thin "surfaces". *J. Geophys. Res. Space Phys.* 93, 5423–5436. doi:10.1029/JA093iA06p05423

Horaites, K., Rintamäki, E., Zaitsev, I., Turc, L., Grandin, M., Cozzani, G., et al. (2023). Magnetospheric response to a pressure pulse in a three-dimensional hybrid-vlasov simulation. *J. Geophys. Res. Space Phys.* 128, e2023JA031374. doi:10.1029/2023JA031374

Hwang, K.-J., and Sibeck, D. G. (2016) *Low-frequency waves in space plasmas*. Washington DC, USA: American Geophysical Union, 213–239. doi:10.1002/9781119055006.ch13

Itonaga, M., Yoshikawa, A., and Fujita, S. (2000). A wave equation describing the generation of field-aligned current in the magnetosphere. *Earth Planet Sp.* 52, 503–507. doi:10.1186/BF03351654

Kan, J. R., and Akasofu, S.-I. (1974). A model of the open magnetosphere. *J. Geophys. Res.* 79, 1379–1384. doi:10.1029/JA079i010p01379

Kivelson, M. G., and Chen, S.-H. (1995). The magnetopause: surface waves and instabilities and their possible dynamical consequences. *Geophys. Monogr. Ser.*, 257–268. doi:10.1029/GM090p0257

Kivelson, M. G., Etcheto, J., and Trotignon, J. G. (1984). Global compressional oscillations of the terrestrial magnetosphere: the evidence and a model. *J. Geophys Res.* 89, 9851–9856. doi:10.1029/JA089iA11p09851

Kivelson, M. G., and Southwood, D. J. (1985). Resonant ULF waves: a new interpretation. *Geophys. Res. Lett.* 12, 49–52. doi:10.1029/GL012i001p00049

Kivelson, M. G., and Southwood, D. J. (1988). Hydromagnetic waves and the ionosphere. *Geophys. Res. Lett.* 15, 1271–1274. doi:10.1029/GL015i011p01271

Klein, K. G., Spence, H., Alexandrova, O., Argall, M., Arzamasskiy, L., Bookbinder, J., et al. (2023). Helioswarm: a multipoint, multiscale mission to characterize turbulence. *Space Sci. Rev.* 219, 74. doi:10.1007/s11214-023-01019-0

Kolotkov, D. Y., Nakariakov, V. M., Moss, G., and Shellard, P. (2021). Fast magnetoacoustic wave trains: from tadpoles to boomerangs. *MNRAS* 505, 3505–3513. doi:10.1093/mnras/stab1587

Kozyreva, O., Pilipenko, V., Lorentzen, D., Baddeley, L., and Hartinger, M. (2019). Transient oscillations near the dayside open-closed boundary: evidence of magnetopause surface mode? *J. Geophys. Res. Space Phys.* 124, 9058–9074. doi:10.1029/2018JA025684

Kruskal, M., and Schwartzschild, M. (1954). Some instabilities of a completely ionized plasma. *Proc. R. Soc. Lond. Ser. A* 223, 348–360. doi:10.1098/rspa.1954.0120

Lee, H. J. (2019) *Fundamentals of theoretical plasma physics: mathematical description of plasma waves*. Singapore: World Scientific Publishing. doi:10.1142/11168

Lee, L. C., Albano, R. K., and Kan, J. R. (1981). Kelvin-Helmholtz Instability in the magnetopause-boundary layer region. *J. Geophys. Res. Space Phys.* 86, 54–58. doi:10.1029/JA086iA01p00054

Lee, L. C., Johnson, J. R., and Ma, Z. W. (1994). Kinetic alfvén waves as a source of plasma transport at the dayside magnetopause. *J. Geophys. Res. Space Phyiscs* 99, 17405–17411. doi:10.1029/94JA01095

Lee, M. A., and Roberts, B. (1986). On the behavior of hydromagnetic surface waves. *Astrophysical J.* 30, 430–439. doi:10.1086/163911

Leonovich, A., and Kozlov, D. A. (2019). Kelvin-helmholtz instability in a dipole magnetosphere: the magnetopause as a tangential discontinuity. *J. Geophys. Res. Space Phys.* 124, 7936–7953. doi:10.1029/2019JA026842

Li, B., Guo, M., Yu, H., Chen, S.-X., and Shi, M. (2023). Three-dimensional propagation of kink wave trains in solar coronal slabs. *MNRAS* 518, L57–L62. doi:10.1093/mnrasl/slac139

Li, W., Wang, C., Tang, B., Guo, X., and Lin, D. (2013). Global features of Kelvin-Helmholtz waves at the magnetopause for northward interplanetary magnetic field. *J. Geophys. Res. Space Phys.* 118, 5118–5126. doi:10.1002/jgra.50498

Li, W. Y., Guo, X. C., and Wang, C. (2012). Spatial distribution of Kelvin-Helmholtz instability at low-latitude boundary layer under different solar wind speed conditions. *J. Geophys. Res. Space Phys.* 117, A08230. doi:10.1029/2012JA017780

Lubchich, A. A., and Despirak, I. V. (2005). Magnetohydrodynamic waves within the medium separated by the plane shock wave or rotational discontinuity. *Ann. Geophys.* 23, 1889–1908. doi:10.5194/angeo-23-1889-2005

Lubchich, A. A., and Pudovkin, M. I. (1999). "Transmission of fast magnetosonic wave through rotational discontinuity," in Conference: XXII Annual seminar Physics of Auroral Phenomena, March 14 to March 18, 2022.

Ma, X., Stauffer, B., Delamere, P. A., and Otto, A. (2015). Asymmetric Kelvin-Helmholtz propagation at Saturn's dayside magnetopause. *J. Geophys. Res. Space Phys.* 120, 1867–1875. doi:10.1002/2014JA020746

Mann, I. R., Wright, A. N., Mills, K. J., and Nakariakov, V. M. (1999). Excitation of magnetospheric waveguide modes by magnetosheath flows. *J. Geophys Res. Space Phys.* 104, 333–353. doi:10.1029/1998JA900026

Masson, A., and Nykyri, K. (2018). Kelvin-Helmholtz instability: lessons learned and ways forward. *Space Sci. Rev.* 214, 71. doi:10.1007/s11214-018-0505-6

Masters, A., Achilleos, N., Bertucci, C., Dougherty, M. K., Kanani, S. J., Arridge, C. S., et al. (2009). Surface waves on Saturn's dawn flank magnetopause driven by the Kelvin–Helmholtz instability. *Planet. Space Sci.* 57, 1769–1778. doi:10.1016/j.pss.2009.02.010

Merkin, V. G., Lyon, J. G., and Clausepierre, S. G. (2013). Kelvin-Helmholtz instability of the magnetospheric boundary in a three-dimensional global MHD simulation during northward IMF conditions. *J. Geophys. Res. Space Phys.* 118, 5478–5496. doi:10.1002/jgra.50520

Michael, A. T., Sorathia, K. A., Merkin, V. G., Nykyri, K., Burkholder, B., Ma, X., et al. (2021). Modeling Kelvin-Helmholtz instability at the high-latitude boundary layer in a global magnetosphere simulation. *Geophys. Res. Lett.* 48, e2021GL094002. doi:10.1029/2021GL094002

Miura, A., and Pritchett, P. L. (1982). Nonlocal stability analysis of the MHD Kelvin-Helmholtz instability in a compressible plasma. *J. Geophys. Res. Space Phys.* 87, 7431–7444. doi:10.1029/JA087iA09p07431

Montgomery, J., Ebert, R. W., Allegrini, F., Bagenal, F., Bolton, S. J., DiBraccio, G. A., et al. (2023). Investigating the occurrence of Kelvin-Helmholtz instabilities at Jupiter's dawn magnetopause. *Geophys. Res. Lett.* 50, e2023GL102921. doi:10.1029/2023GL102921

Nakariakov, V. M., Anfinogentov, S. A., Antolin, P., Jain, R., Kolotkov, D. Y., Kupriyanova, E. G., et al. (2021). Kink oscillations of coronal loops. *Space Sci. Rev.* 217, 73. doi:10.1007/s11214-021-00847-2

Nakariakov, V. M., Arber, T. D., Ault, C. E., Katsiyannis, A. C., Williams, D. R., and Keenan, F. P. (2004). Time signatures of impulsively generated coronal fast wave trains. *MNRAS* 349, 705–709. doi:10.1111/j.1365-2966.2004.07537.x

Nakariakov, V. M., Pilipenko, V., Heilig, B., Jelínek, P., Karlický, M., Klimushkin, D. Y., et al. (2016). Magnetohydrodynamic oscillations in the solar corona and Earth's magnetosphere: towards consolidated understanding. *Space Sci. Rev.* 200, 75–203. doi:10.1007/s11214-015-0233-0

Nenovski, P. (2021). MHD surface waves - a source of global magnetospheric modes (resonances)? *Adv. Space Res.* 67, 731–738. doi:10.1016/j.asr.2020.09.039

Nenovski, P., Villante, U., Francia, P., Vellante, M., and Bochev, A. (2007). Do we need a surface wave approach to the magnetospheric resonances? *Planet. Space Sci.* 55, 680–693. doi:10.1016/j.pss.2006.04.038

Nykyri, K., and Foullon, C. (2013). First magnetic seismology of the CME reconnection outflow layer in the low corona with 2.5-D MHD simulations of the Kelvin-Helmholtz instability. *Geophys. Res. Lett.* 40, 4154–4159. doi:10.1002/grl.50807

Paschmann, G., Haaland, S., Sonnerup, B. U. O., Hasegawa, H., Georgescu, E., Klecker, B., et al. (2005). Characteristics of the near-tail dawn magnetopause and boundary layer. *Ann. Geophys.* 23, 1481–1497. doi:10.5194/angeo-23-1481-2005

Pascoe, D. J., Wright, A. N., and De Moortel, I. (2011). Propagating coupled alfvén and kink oscillations in an arbitrary inhomogeneous corona. *ApJ* 731, 73. doi:10.1088/0004-637X/731/1/73

Pilipenko, V., Federov, E., Mazur, N. G., Engebretson, M. J., and Hughes, W. J. (1999). Magnetohydrodynamic waveguide/resonator for pc3 ULF pulsations at cusp latitudes. *Earth Planets Space* 51, 441–448. doi:10.1186/BF03352248

Pilipenko, V. A., Kozyreva, O., Baddeley, L., Lorentzen, D. A., and Belakhovsky, V. B. (2017). Suppression of the dayside magnetopause surface modes. *Sol.-Terr. Phys.* 3, 17–25. doi:10.12737/stp-34201702

Pilipenko, V. A., Mazur, N. G., Federov, E. N., Engebretson, M. J., and Murr, D. L. (2005). Alfvén wave reflection in a curvilinear magnetic field and formation of alfvénic resonators on open field lines. *J. Geophys. Res. Space Phys.* 110, A10S05. doi:10.1029/2004JA010755

Plaschke, F. (2016) *Low-frequency waves in space plasmas*. Washington DC, USA: AGU, 193–212. doi:10.1002/9781119055006.ch12

Plaschke, F., and Glassmeier, K. H. (2011). Properties of standing Kruskal-Schwarzschild-modes at the magnetopause. *Ann. Geophys.* 29, 1793–1807. doi:10.5194/angeo-29-1793-2011

Plaschke, F., Glassmeier, K.-H., Auster, H. U., Angelopoulos, V., Constantinescu, O. D., Fornaçon, K.-H., et al. (2009a). Statistical study of the magnetopause motion: first results from THEMIS. *J. Geophys. Res. Space Phys.* 114, A00C10. doi:10.1029/2008JA013423

Plaschke, F., Glassmeier, K.-H., Auster, H. U., Constantinescu, O. D., Magnes, W., Angelopoulos, V., et al. (2009b). Standing Alfvén waves at the magnetopause. *Geophys. Res. Lett.* 36, L02104. doi:10.1029/2008GL036411

Pu, Z.-Y., and Kivelson, M. G. (1983a). Kelvin-Helmholtz Instability at the magnetopause: solution for compressible plasmas. *J. Geophys. Res. Space Phys.* 88, 841–852. doi:10.1029/JA088iA02p00841

Pu, Z.-Y., and Kivelson, M. G. (1983b). Kelvin-Helmholtz Instability at the magnetopause: energy flux into the magnetosphere. *J. Geophys. Res. Space Phys.* 88, 853–861. doi:10.1029/JA088iA02p00853

Radoski, H. R. (1970). The resonance barrier theory of hydromagnetic waves. *J. Geomag. Geoelec.* 22, 361–379. doi:10.5636/jgg.22.361

Radoski, H. R. (1971). A note on the problem of hydromagnetic resonances in the magnetosphere. *Planet. Space Sci.* 19, 1012–1013. doi:10.1016/0032-0633(71)90152-8

Raeder, J. (2003) *Space plasma simulation*. Berlin, Heidelberg, Germany: Springer.

Raeder, J., Germaschewski, K., Cramer, W. D., and Lyon, J. (2021). *Magnetospheres in the Solar System* (Washington DC, USA: AGU), chap. Global simulations. *Geophys. Monogr. Ser.*, 595–606. doi:10.1002/9781119815624.ch37

Rankin, R., Kabin, K., and Marchand, R. (2006). Alfvénic field line resonances in arbitrary magnetic field topology. *Adv. Space Res.* 38, 1720–1729. doi:10.1016/j.asr.2005.09.034

Ruderman, M. S., Vickers, E., Ballai, I., and Erdelyi, R. (2018). Propagation of leaky surface waves on contact magnetohydrodynamic discontinuities in incompressible plasmas. *Phys. Plasmas* 25, 122107. doi:10.1063/1.5050591

Salat, A., and Tataronis, J. A. (2000). Conditions for existence of orthogonal coordinate systems oriented by magnetic field lines. *J. Geophys. Res.* 105, 13055–13062. doi:10.1029/1999JA000221

Samson, J. C., Harrold, B. G., Ruohoniemi, J. M., Greenwald, R. A., and Walker, A. D. M. (1992). Field line resonances associated with MHD waveguides in the magnetosphere. *Geophys. Res. Lett.* 19, 441–444. doi:10.1029/92GL00116

Sen, A. K. (1963). Stability of hydromagnetic kelvin-helmholtz discontinuity. *Phys. Fluids* 6, 1154–1163. doi:10.1063/1.1706875

Singer, H. J., Southwood, D. J., Walker, R. J., and Kivelson, M. G. (1981). Alfvén wave resonances in a realistic magnetospheric magnetic field geometry. *J. Geophys. Res.* 86, 4589–4596. doi:10.1029/JA086iA06p04589

Slinker, S. P., Fedder, J. A., Sibeck, D. G., Lyon, J. G., Frank, L. A., and Mukai, T. (2003). Simulation of magnetopause oscillations observed january 9, 1996. *Geophys. Res. Lett.* 30, 1569. doi:10.1029/2003GL017063

Smit, G. R. (1968). Oscillatory motion of the nose region of the magnetopause. *J. Geophys. Res.* 73, 4990–4993. doi:10.1029/JA073i015p04990

Smith, E. J. (2001). The heliospheric current sheet. *J. Geophys. Res. Space Phys.* 106, 15819–15831. doi:10.1029/2000JA000120

Sonnerup, B. U. O., and Ledley, B. G. (1974). Magnetopause rotational forms. *J. Geophys. Res.* 79, 4309–4314. doi:10.1029/JA079i028p04309

Sorathia, K. A., Merkin, V. G., Ukhorskiy, A. Y., Mauk, B. H., and Sibeck, D. G. (2017). Energetic particle loss through the magnetopause: a combined global mhd and test-particle study. *J. Geophys. Res. Space Phys.* 122, 9329–9343. doi:10.1002/2017JA024268

Southwood, D. J. (1968). The hydromagnetic stability of the magnetospheric boundary. *Planet. Space Sci.* 16, 587–605. doi:10.1016/0032-0633(68)90100-1

Southwood, D. J. (1974). Some features of field line resonances in the magnetosphere. *Planet. Space Sci.* 22, 483–491. doi:10.1016/0032-0633(74)90078-6

Southwood, D. J., and Kivelson, M. G. (1984). Relations between polarization and the structure of ULF waves in the magnetosphere. *J. Geophys. Res.* 89, 5523–5529. doi:10.1029/JA089iA07p05523

Southwood, D. J., and Kivelson, M. G. (1990). The magnetohydrodynamic response of the magnetospheric cavity to changes in solar wind pressure. *J. Geophys. Res. Space Phys.* 95, 2301–2309. doi:10.1029/JA095iA03p02301

Southwood, D. J., and Kivelson, M. G. (1991). An approximate description of field-aligned currents in a planetary magnetic field. *J. Geophys. Res. Space Phys.* 96, 67–75. doi:10.1029/90JA01806

Stern, D. (1967). Geomagnetic euler potentials. *J. Geophys. Res.* 72, 3995–4005. doi:10.1029/JZ072i015p03995

Stern, D. P. (1970). Euler potentials. *Am. J. Phys.* 35, 494–501. doi:10.1119/1.1976373

Stern, D. P. (1976). Representation of magnetic fields in space. *Rev. Geophys.* 14, 199–214. doi:10.1029/RG014i002p00199

Stern, D. P. (1985). Parabolic harmonics in magnetospheric modeling: the main dipole and the ring current. *J. Geophys. Res. Space Phys.* 90, 10851–10863. doi:10.1029/JA090iA11p10851

Summers, D., Mann, I. R., Baker, D. N., and Schulz, M. (2013). *Dynamics of the Earth's radiation belts and inner magnetosphere* (Washington, D.C., United States: American Geophysical Union). doi:10.1029/GM199

Sundberg, T., Boardsen, S. A., Slavin, J. A., Anderson, B. J., amd, T. H., Zurbuchen, H. K., et al. (2012). MESSENGER orbital observations of large-amplitude Kelvin-Helmholtz waves at Mercury's magnetopause. *J. Geophys. Res. Space Phys.* 117, A04216. doi:10.1029/2011JA017268

Uberoi, C. (1989). Resonant absorption of Alfvén compressional surface waves. *J. Geophys. Res.* 94, 6941–6944. doi:10.1029/JA094iA06p06941

Van Doorsselaere, T., Debosscher, A., Andries, J., and Poedts, S. (2004). The effect of curvature on quasi-modes in coronal loops. *A&A* 424, 1065–1074. doi:10.1051/0004-6361:20041239

van Doorsselaere, T., Verwichte, E., and Terradas, J. (2009). The effect of loop curvature on coronal loop kink oscillations. *Space Sci. Rev.* 149, 299–324. doi:10.1007/s11214-009-9530-9

Volwerk, M., Jia, X., Paranicas, C., Kurth, W. S., Kivelson, M. G., and Khurana, K. K. (2013). Ulf waves in Ganymede's upstream magnetosphere. *Ann. Geophys.* 31, 45–59. doi:10.5194/angeo-31-45-2013

Walker, A. D. M. (1981). The Kelvin-Helmholtz instability in the low-latitude boundary layer. *Planet. Space Sci.* 29, 1119–1133. doi:10.1016/0032-0633(81)90011-8

Wang, C., and Branduardi-Raymont, G. (2022). Progress of solar wind magnetosphere ionosphere link explorer (SMILE) mission. *Chin. J. Space Sci.* 38, 657–661. doi:10.11728/cjss2018.05.657

Wang, L., Huang, C., Du, A., Ge, Y., Chen, G., Yang, Z., et al. (2023). Kelvin–Helmholtz instability at mars: *in situ* observations and kinetic simulations. *ApJ* 947, 51. doi:10.3847/1538-4357/acc655

Wang, T. J. (2016). "*Low-frequency Waves in space plasmas* (Washington DC, USA: AGU), chap. Waves," in *Solar coronal loops*, 395–418. doi:10.1002/9781119055006.ch23

Wright, A. N. (1994). Dispersion and wave coupling in inhomogeneous MHD waveguides. *J. Geophys. Res. Space Phys.* 99, 159–167. doi:10.1029/93JA02206

Zaharia, S., Birn, J., and Cheng, C. Z. (2005). Toward a global magnetospheric equilibrium model. *J. Geophys. Res. Space Phys.* 110, A09228. doi:10.1029/2005JA011101

Zhang, B., Sorathia, K. A., Lyon, J. G., Merkin, V. G., Garretson, J. S., and Wiltberger, M. (2019). GAMERA: a three-dimensional finite-volume MHD solver for non-orthogonal curvilinear geometries. *ApJ* 244, 20. doi:10.3847/1538-4365/ab3a4c

Zirnstein, E. J., Shrestha, B. L., McComas, D. J., Dayeh, M. A., Heerikhuisen, J., Reisenfeld, D. B., et al. (2022). Oblique and rippled heliosphere structures from the interstellar boundary explorer. *Nat. Astron.* 6, 1398–1413. doi:10.1038/s41550-022-01798-6

frontiers | Frontiers in Astronomy and Space Sciences

TYPE Original Research
PUBLISHED 05 August 2024
DOI 10.3389/fspas.2024.1431611

Check for updates

OPEN ACCESS

EDITED BY
Guram Kervalishvili,
GFZ German Research Centre for Geosciences, Germany

REVIEWED BY
Zhonghua Xu,
Virginia Tech, United States
Iwona Stanislawska,
Polish Academy of Sciences, Poland

*CORRESPONDENCE
Pingbing Zuo,
pbzuo@hit.edu.cn

RECEIVED 12 May 2024
ACCEPTED 11 July 2024
PUBLISHED 05 August 2024

CITATION
Li W, Liu T, Zuo P, Zou Z, Ruan M and Wei J (2024), Low-latitude ionospheric responses and positioning performance of ground GNSS associated with the geomagnetic storm on March 13–14, 2022.
Front. Astron. Space Sci. 11:1431611.
doi: 10.3389/fspas.2024.1431611

COPYRIGHT
© 2024 Li, Liu, Zuo, Zou, Ruan and Wei. This is an open-access article distributed under the terms of the Creative Commons Attribution License (CC BY). The use, distribution or reproduction in other forums is permitted, provided the original author(s) and the copyright owner(s) are credited and that the original publication in this journal is cited, in accordance with accepted academic practice. No use, distribution or reproduction is permitted which does not comply with these terms.

Low-latitude ionospheric responses and positioning performance of ground GNSS associated with the geomagnetic storm on March 13–14, 2022

Wenrui Li[1,2], Tong Liu[3], Pingbing Zuo[1,2]*, Zhengyang Zou[4], Mengsi Ruan[1,2] and Jiayun Wei[1,2]

[1]Shenzhen Key Laboratory of Numerical Prediction for Space Storm, Institute of Space Science and Applied Technology, Harbin Institute of Technology, Shenzhen, China, [2]Key Laboratory of Solar Activity and Space Weather, National Space Science Center, Chinese Academy of Sciences, Beijing, China, [3]Department of Land Surveying and Geo-Informatics, The Hong Kong Polytechnic University, Kowloon, Hong Kong SAR, China, [4]State Key Laboratory of Lunar and Planetary Sciences, Macau University of Science and Technology, Taipa, Hong Kong SAR, China

Interplanetary coronal mass ejections (ICMEs) and the driven geomagnetic storms have a profound influence on the ionosphere, potentially leading to a degradation in positioning performance. In this study, we made a comprehensive analysis of the entire process of the impact of a typical ICME and its driven geomagnetic storm on the low-latitude ionosphere during March 13–14, 2022 (π-day storm) and the positioning performance of Global Navigation Satellite System (GNSS). During the passage of the ICME event, significant ionospheric scintillation, and TEC (total electron content) disturbances were observed in the low-latitude Hong Kong region. The ICME sheath region intensively compressed the magnetosphere via solar wind dynamic pressure enhancement and subsequently drove the storm main phase. It is found that both the magnetospheric compression that formed the storm initial phase and the storm main phase caused ionospheric scintillation. In comparison, the intensity of the ionospheric scintillation caused by the intense magnetospheric compression just before the storm main phase is even more pronounced. We also analyzed the impact of storms on standard point positioning (SPP), precise point positioning (PPP) and real-time kinematic (RTK) techniques. The positioning accuracies of single-frequency SPP and PPP experienced the most severe decline, and there was a noticeable increase in the initialization time for dual-frequency static PPP and RTK during the event. RTK demonstrated a shorter convergence time and higher accuracy during this event, but it was limited to short-baseline RTK (<30 km).

KEYWORDS

geomagnetic storm, GNSS, ionosphere, ICME, data analysis

1 Introduction

Geomagnetic storms are major disturbance of the Earth's magnetosphere caused by the solar wind-magnetosphere couplings. The geomagnetic storms are generally caused by interplanetary coronal mass ejection (ICME), the corotating interaction region (CIR), and

high-speed streams. In particular, intense storms (Dst_{min} < −100 nT) are usually driven by ICMEs with sustaining strong southward magnetic fields in sheath regions (Zhang et al., 2007). The geomagnetic storm can induce global disruptions in the ionospheric, commonly known as ionospheric storms (Buonsanto, 1999; Balan et al., 2010). As a result, the positioning performance of Global Navigation Satellite Systems (GNSSs) could be degraded due to ionospheric refraction and diffraction effects amplified by geomagnetic storms (Yang et al., 2020).

When traversing the ionosphere, electromagnetic waves refract, with a reduced propagation speed. The refraction effects include the following three points: 1) Degraded positioning performance of single-frequency standard point positioning (SPP) and precise point positioning (PPP). The refraction on single-frequency signals can be corrected using various ionospheric models, such as the Klobuchar model (Klobuchar, 1987) for GPS, the NeQuick model (Nava et al., 2008) for Galileo, and the BeiDou global ionospheric delay correction model (BDGIM) (Yuan et al., 2019). However, even the best-performing BDGIM model can correct only up to 80% of the ionospheric delay. An overall increase in global positioning errors due to the reduced effectiveness of global ionospheric models could still occur during geomagnetic storms (Yang et al., 2020; Nie et al., 2022a; Luo et al., 2023). 2) Reduced accuracy of real-time kinematic (RTK) data. Amplified local disturbances during storms cause greater local ionospheric gradients, thereby affecting the accuracy of real-time kinematic (RTK) data. Wielgosz et al. (2005) found that under severe ionospheric conditions, the remote RTK instantaneous ambiguity resolution (AR) located in Ohio was no longer effective during the 2003 Halloween geomagnetic storm. At the same time, it also hindered on-the-fly (OTF) AR. For the Halloween storm event, Bergeot et al. (2011) found that the RTK positioning performance decreased during the storm, especially at stations in northern Europe. It is noteworthy that these events were all driven by ICMEs, and the research on RTK effects has mostly focused on mid- or high-latitude regions. Studies of the storm-induced effects on positioning performance in low-latitude areas near the equator are still relatively scarce. 3) Reduced convergence speed of PPP. Besides final accuracy, fast convergence speeds for positioning are also required for PPP users. Many studies have focused on reducing the initialization time of PPP and improving its accuracy (Collins et al., 2010; Ge et al., 2008; Geng et al., 2010; Li et al., 2011). However, although regional ionospheric modeling can be used to ameliorate the slow convergence rate caused by ionospheric delay, this approach may be less effective during geomagnetic storms (Yao et al., 2013).

Diffraction occurs when GNSS signals pass through ionospheric irregularities. During storms, widespread irregularities in the ionosphere cause rapid and random fluctuations in the amplitude and phase of GNSS signals, known as ionospheric scintillation (Kintner et al., 2007). It can result in signal loss (Lovati et al., 2023), cycle slips (Li et al., 2023; Xiang et al., 2022), and a reduction in the number of visible satellites (Yang and Morton, 2020), ultimately leading to sudden increases of positioning errors. Compared with the errors caused by refraction, the positioning errors induced by ionospheric scintillation are more unstable, significant, and challenging to correct. This is especially obvious in the equatorial belt regions where scintillation is enhanced due to the small-scale irregularities formed by the ascent of plasma bubbles (Moraes et al., 2018; Zakharenkova and Cherniak, 2021).

Understanding the specific causes and impacts of space weather events on GNSS positioning accuracy is crucial. Numerous attempts have been made to study the positioning degeneration caused by intense geomagnetic storms triggered by ICMEs, such as the Halloween storm on 30 October 2003 (Wielgosz et al., 2005; Bergeot et al., 2011) and St. Patrick's Day geomagnetic storm in 2015 (Lu et al., 2020; Poniatowski and Nykiel, 2020; Yang et al., 2020; Nie et al., 2022b). Paziewski et al. (2022) and Luo et al. (2018) compared and analyzed the positioning performances of RTK and PPP receivers, respectively, during three geomagnetic storm events. Unfortunately, they only roughly analyzed the observed degradation in positioning over the entire storm event, and from an engineering perspective, attributed it to anomalous changes in the ionosphere or signal anomalies without analyzing the space weather causal chain. Jacobsen and Andalsvik (2016); Jacobsen and Schäfer (2012) found a close correlation between ionospheric disturbances and auroral electrojet currents and attempted to use predictions of auroral electrojet to aid in forecasting disturbances in GNSS positioning. The impact of ICMEs and their consequent geomagnetic storms and magnetospheric compression on positioning degeneration and the specific impact mechanisms are still not well understood. Overall, previous studies have barely investigated the background physical process between the GNSS-based positioning performance and the ICMEs event as well as the geomagnetic storms in detail. In this study, to address this problem, we comprehensively explored the entire chain from the ICME event on March 13–14, 2022 to GNSS positioning performance. Specifically, the commencement of the π-day geomagnetic storm induced by the ICME, the following response of the ionosphere, and the succeeded disturbances of GNSS signals are quantitatively investigated in detail. Moreover, we identified the distinctive impact of the enhanced dynamic pressure structure within ICMEs sheath on both the ionosphere and positioning errors. The present work provides a new insight on the effects of space weather on the GNSS. In Section 2, the data sources and processing methods are presented. In Section 3 and Section 4, the observations and data analyses are presented. Section 5 provides a summary.

2 Data and processing method

2.1 Data

The solar wind plasma and magnetic field data, including the solar wind magnetic field, the solar wind speed, proton density, proton temperature, proton number density (with a 1-min time resolution) and the SymH index (with a 1-min time resolution), were downloaded from https://omniweb.gsfc.nasa.gov/ow_min.html. The GOES X-ray fluxes are available at https://www.ngdc.noaa.gov/stp/satellite/goes-r.html.

Five stations of the Hong Kong continuous operational reference system are selected: HKLM, HKKS, HKTK, HKCL, and HKST. The location of each station is shown in Figure 1, and the longitude, latitude, receiver, and antenna type information is listed in Table 1. The observational data was downloaded from https://www.geodetic.gov.hk/sc/rinex/DOWNV.ASPX. The precision clock files and

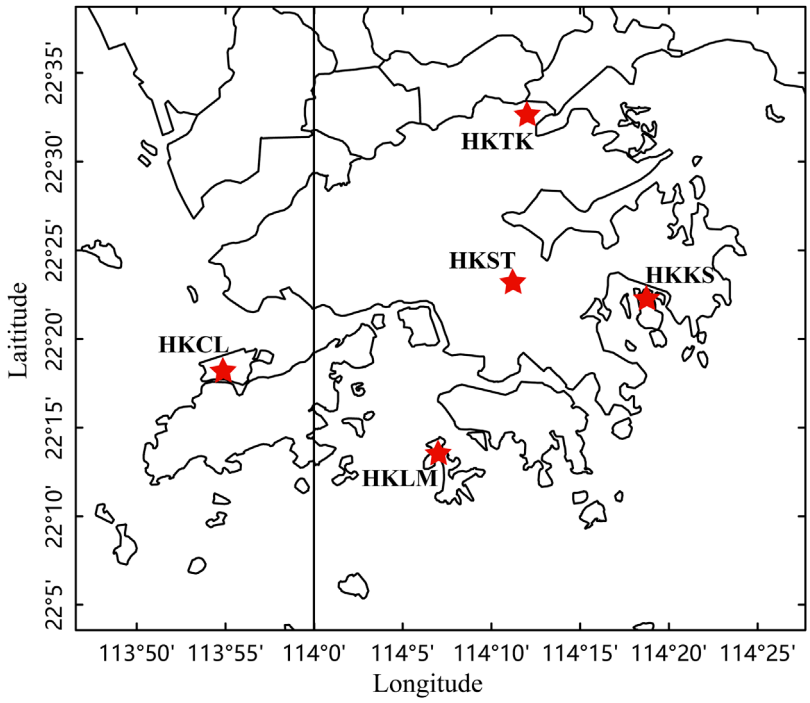

FIGURE 1
The locations of the five low-latitude GNSS stations in Hong Kong are marked by red stars.

TABLE 1 Position and equipment information of the five GNSS stations in Hong Kong.

Stations	Longitude	Latitude	Receiver	Antenna
HKKS	114°18′42.96″	22°22′4.43″	Leica GR50	Trimble 59800.00 + SCIS
HKLM	114°7′12.21″	22°13′8.25″	Leica GR50	Trimble 59800.00 + SCIS
HKTK	114°13′23.80″	22°32′47.65″	Leica GR50	Trimble 59800.00 + SCIS
HKCL	113°54′27.79″	22°17′45.03″	Trimble NetR9	Trimble 59800.00 + SCIT
HKST	114°11′3.27″	22°23′42.97″	Leica GR50	Leica AR25.R4 + LEIT

precision ephemeris files are downloaded from https://cddis.nasa.gov/archive/gnss/products/. The antenna files are downloaded from https://files.igs.org/pub/station/general/.

2.2 Processing methodology

2.2.1 Ionospheric parameter calculations from GNSS

The total electron content (TEC) is calculated by the carrier smoothing pseudorange method using ground-based GNSS data. GNSS geodetic receivers generally have at least 2 frequencies. Since the ionosphere causes different delays for different frequency code observations, this feature can be used to calculate the TEC of the slant signal path of the ionosphere. If the numerical frequency is known, the TEC is proportional to the delay, expressed as Eq. 1:

$$I_k = \alpha \cdot \frac{STEC}{f_k^2} \tag{1}$$

where I_k denotes the delay in meters of the L_k band of the GPS, $STEC$ denotes the TEC on the slant signal path, α is the constant value to link the TECU (1 TEC unit = 10^{16} electrons/m^2) and length units, and f is the frequency. Then, from the carrier phase raw observation L1 and L2 from the ground GNSS receivers, a new observation named L4 can be formed, which keeps the ionospheric delay expressed as Eq. 2:

$$L_4 = L_1 - L_2 = I + b_{r,21} + b^s_{21} + (\lambda_1 N_1 - \lambda_2 N_2) + \varepsilon_{L4} \tag{2}$$

Where L_f is the carrier phase measurements at frequency f (m), $b_{r,21,}$ and $b^s{}_{21}$ are the errors introduced by the differential phase bias (DPB) of the receiver and satellite, respectively; λ_f is the wavelength (m) and N_f is the integer ambiguity at frequency f (cycle); and ε_{L4} is the residuals.

TABLE 2 The main calculation data processing models and methods of SPP, PPP and RTK.

Item	Models and methods		
	SPP	PPP	RTK
GNSS satellite selection	GPS	GPS	GPS
Sampling interval	5s	5s	5s
Elevation mask angle	15°	15°	-
Satellite orbit	-	IGS final products (15min interval)	-
Satellite clock	-	IGS final clock products (5min interval)	-
Filter type	Forward processing	Forward processing	-
Tides correction	Off	On	-
Ionosphere correction	Broadcast/IF	Broadcast/IF	-
Troposphere correction	Saastamoninen	Estimate ZTD	-
Receiver kinematics	-	Static/Kinematic	-

Similarly, geometry-free combinations based on the pseudorange can be deduced. Afterward, the carrier-to-code levelling method (Zhang et al., 2019) is used to address the ambiguity problem to obtain the *STEC*, with the accuracy of the carrier and without carrier ambiguity. The detailed data processes are the same as those in Ciraolo et al. (2007) and Nie et al. (2018).

In addition, the remaining disturbance terms after removing the long-term trends, the rate of total TEC change index (ROTI), and S4 are also calculated to explore the regional ionospheric state during the disturbance or scintillation stage.

2.2.2 Positioning model

The RTKLIB 2.4.2 open source program package for standard and precise positioning with GNSS is used for SPP/PPP and RTK solutions. This study uses the console application on Linux to run rnx2rtkp in parallel with RTKLIB. Detailed information about the RTKLIB can be found on the RTKLIB website (https://www.rtklib.com/). Table 2 provides the primary processing models and methods used in the SPP and PPP solutions.

In the RTK positioning model, the kinematic positioning of the postprocessing function is selected. HKST is chosen as the reference station. The average baseline length is 20.47 km, while the shortest baseline is between the HKKS and HKST, with a length of 13.5 km.

3 Solar wind and X-ray flare observations

Figure 2 shows the solar wind magnetic field and plasma data from WIND at around L1 point (shifted by 44 min) and the geomagnetic SymH index on 2022 March 10-17th. Between 22:40 UT on March 13th and 19:00 UT on March 15th, a typical ICME was observed by WIND (see the shifted region between two vertical red lines in Figure 2). The ICME was identified based on several magnetic field and plasma characteristics, including strong magnetic fields (panel (a)), smooth field rotation (panel (c)) and low plasma β values (panel (i)) (this ICME was also identified by Ian Richardson and Hilary Cane; see the ICME list at https://izw1.caltech.edu/ACE/ASC/DATA/level3/icmetable2.htm). At 10:04 UT (10:48 UT after shifted) on March 13th, an interplanetary shock driven by this ICME was detected (labeled "S"). Across the shock front, there was a significant sharp increase in the magnetic field magnitude, proton temperature, number density, solar wind dynamic pressure, and plasma bulk velocity. This ICME-driven shock caused the storm sudden commencement (SSC, see the blue vertical line in panel (j)). The solar wind data were shifted by 44 min, which is the difference between the time when the shock wave reaches the L1 point and the SSC, to represent the solar wind conditions just outside the magnetosphere and indicate the correspondence between the solar wind disturbance and the magnetic storm phases.

Between the shock and ICME body, the ICME sheath region formed from 10:04 UT to 22:40 UT on March 13th (WIND observation). The characteristics of the ICME sheath region are as follows: 1) the intensity of the turbulent magnetic field increases with a strong southward magnetic field, and there are several reversals in the magnetic field direction (the first southward magnetic field lasts for 160 min, reaching a minimum of −12.09 nT; the last southward magnetic field lasts for 110 min, reaching a minimum of −23.46 nT). 2) The plasma temperature, velocity, dynamic pressure, and number density remain consistently high in this region. An increase in the number density also indicates an increase in the solar wind dynamic pressure, which suggests that the magnetosphere will experience strong compression. 3) The onset and main phase of the storm were driven by the ICME sheath region owing to the persistent strong southward magnetic field.

Due to the compression of the shock, the magnetopause current was enhanced, and the geomagnetic field was also significantly

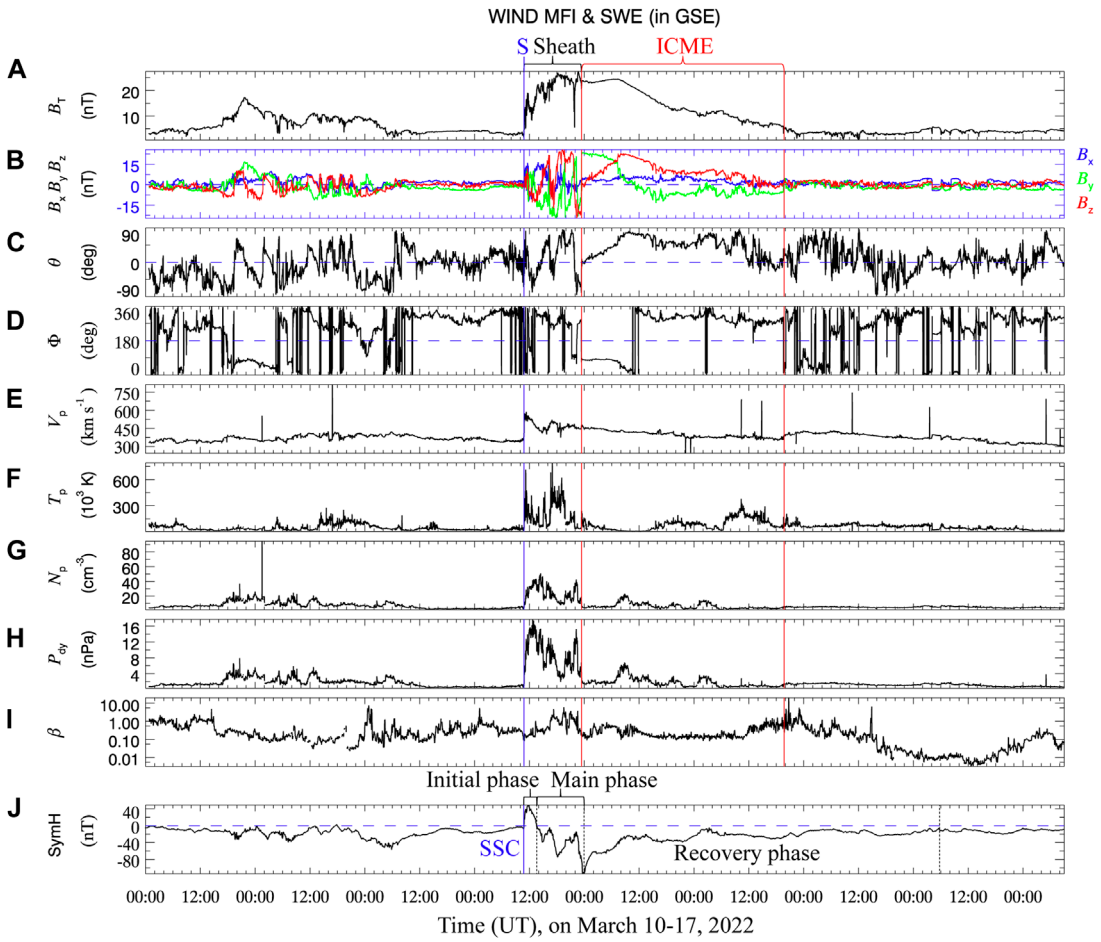

FIGURE 2
Shifted solar wind magnetic field, plasma data and SymH index from March 10 to 17 March 2022. **(A)** magnetic field intensity and **(B)** its three components (in GSE coordinate), **(C)** latitudinal angle, **(D)** longitudinal angle, **(E)** plasma bulk velocity, **(F)** proton temperature, **(G)** number density, **(H)** solar wind dynamic pressure, **(I)** plasma beta, and **(J)** SymH index. The "S" marked with the blue vertical line represents the interplanetary shock driven by the ICME, and the two red vertical lines enclose the ICME body. In panel **(J)**, the "SSC" marked with the blue vertical line represents the storm sudden commencement.

enhanced, triggering the relatively momentary initial phase of the magnetic storm, from 10:48 UT to 13:33 UT. The magnetic field is generally negative during a storm due to the cancellation effect, and the short increase in the SymH index in the initial phase is caused by the compression of the magnetosphere by the sheath region. From 13:33 to 23:40 UT on March 13th (black lines in panel (j)) was the main phase of the geomagnetic storm, where the SymH index continuously decreased to a minimum of −114 nT, which indicates an intense storm. After 23:40 UT, the SymH index began to increase and gradually recovered to near zero throughout the following days from March 14th to March 17th. Notably, there were also three minor to moderate geomagnetic storms on the 10th, 11th and 12th before this π-day storm event, with minimum SymH indices of −33 nT, −39 nT and −56 nT, respectively (see the SymH index before the arrival of the ICME-driven shock). From panel b, it can be inferred that these three magnetic storms were induced by persistent interplanetary southward magnetic fields from weak solar wind disturbances.

Figure 3 presents the soft X-ray flux observations by GOES-16 during 2022 March 7–16, which are used to track solar activity and solar flares. An M-class flare occurred 2 days before the π day storm event at 22:34 UT on Mar. 11th. One M-class flare occurred at 8:38 UT on Mar. 14th, and two other M-class flares occurred at 12:43 UT and 22:46 UT on Mar. 15th. However, from the SSC (the vertical blue line) until the end of the main phase of the geomagnetic storm (the second vertical dashed black line), no M-class or X-class solar flares appeared.

4 Ionospheric responses at low-latitude stations in Hong Kong

The standard deviation of the VTEC for all satellites at the HKCL GNSS station was counted, as shown in Figure 4. The location of the ionospheric piercing point is different for each satellite, so the standard deviation actually indicates the magnitude of the difference

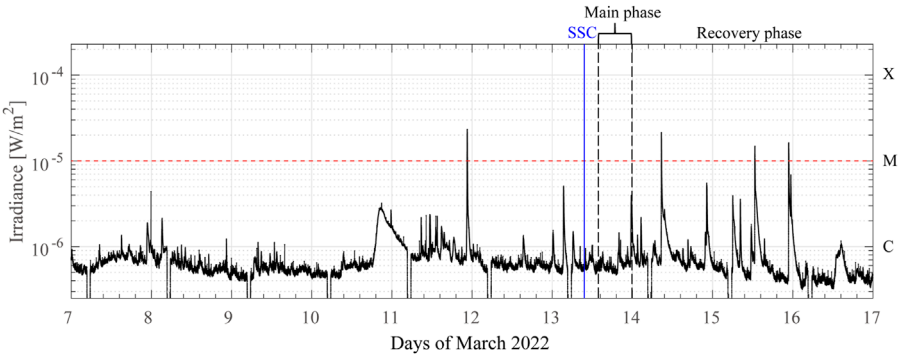

FIGURE 3
Soft 1-s X-ray fluxes on 2022 March 7–16 detected by GOES-16. The "SSC" marked with the blue vertical line represents the timing of the storm sudden commencement, the two black dashed vertical lines enclose the main phase of the storm.

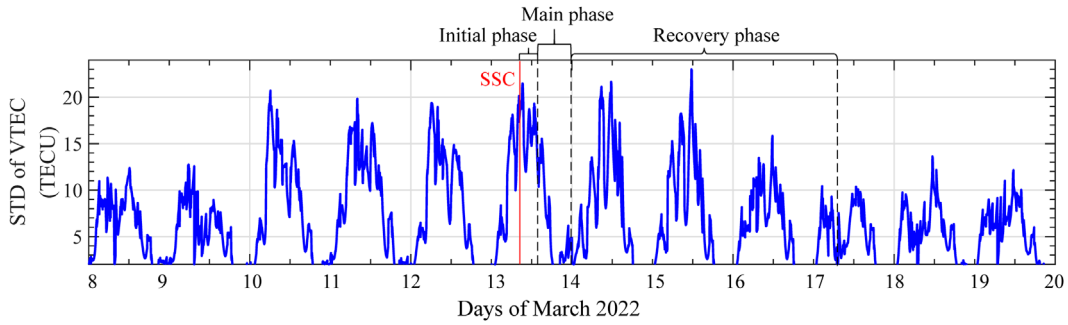

FIGURE 4
The standard deviation of VTEC for all satellites at the HKCL GNSS station.

in the spatial gradient of the ionosphere over Hong Kong. In general, both flares and magnetic storms can cause ionospheric disturbances, which can change the observed TEC (Foster and Rideout, 2005; Lu et al., 2020). As analyzed in Section 3, during the period from March 10th to March 12th, three weak to moderate geomagnetic storms occurred. From March 13th to March 15th, the intense π-day storm was driven by the sheath and the body of the ICME (see the analysis of the three storm phases in Section 3). On the other hand, on March 11th and March 14th, one M-class flare occurred separately, and on March 15th, there were two M-class flares, with the standard deviation of the VTEC reaching its maximum. These space weather events are responsible for the abnormally large peak in the standard deviation of the VTEC during the period of ionospheric disturbances from March 10th to March 15th.

The TEC, the ROTI, which characterizes the short-term variations in the ionosphere, and S4, which characterizes the intensity of the scintillation at each GNSS station, are presented in Figure 5. From March 10th to March 12th and from March 14th to March 15th, ROTI and S4 are very small, indicating no significant ionospheric scintillation over Hong Kong during these periods. There was pronounced and sustained ionospheric scintillation during the period from 12:00–18:00 UT on March 13th (from 20:00 on March 13th to 2:00 on March 14th in local time for the HKCL station). The maximum ROTI reached 3.35 TECU/min, and the maximum S4 index was 1.12, which indicated very strong ionospheric scintillation.

This ionospheric scintillation included three parts in terms of S4 and ROTI. The first part is obviously stronger than the other two parts. Figure 6 shows the shifted solar wind dynamic pressure, SymH index, ROTI and S4 index on March 13th. The gray area represents the period before the start of the storm main phase. During this period, the solar wind dynamic pressure increased from less than 1 nPa–17.67 nPa. The magnetosphere was intensively compressed by the sheath region of the ICME, which resulted in the storm initial phase. The first part of this ionospheric scintillation index S4 reaches a maximum of 1.12, which indicted a super strong scintillation. It may be caused by plasma bubbles or a more complex prereversal enhancement (PRE) generated by magnetospheric compression. The other two parts of the ionospheric scintillation are caused by the storm main phase. The maximum values of indices S4 are 0.86 (strong scintillation) and 0.41 (medium scintillation), respectively.

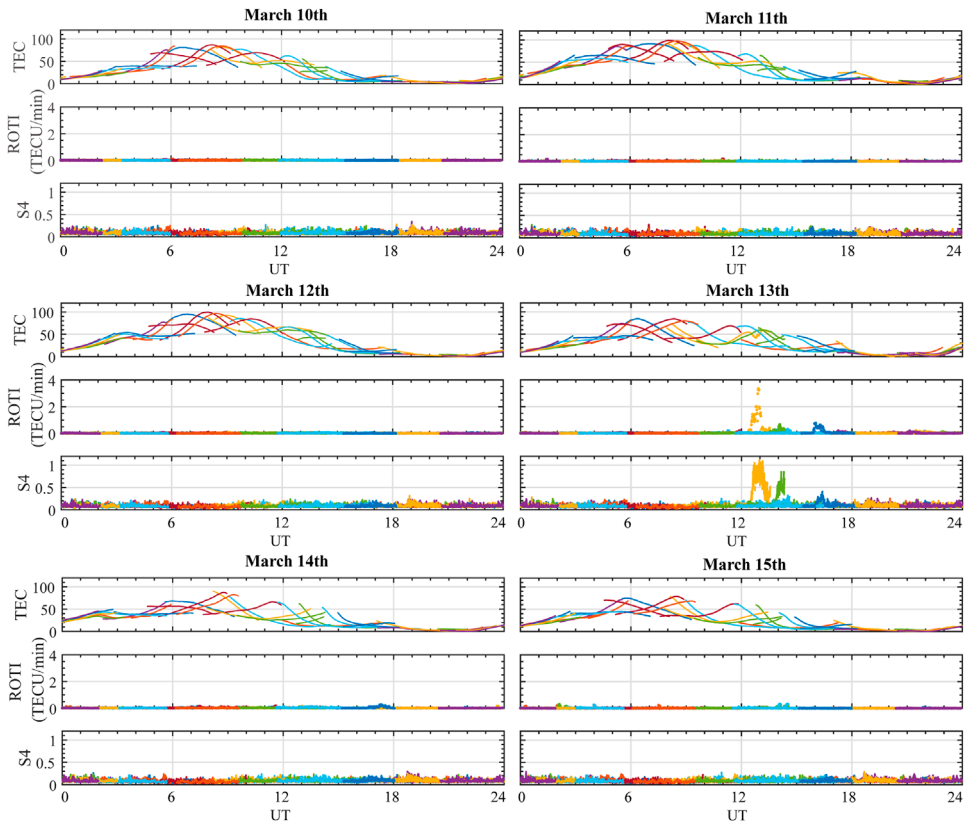

FIGURE 5
The ionospheric response of the HKCL from March 10 to 15. Each subplot shows, from top to bottom, the variation of ionospheric TEC, the ROTI, and the S4 index for all satellites.

5 GNSS-based positioning performance analysis

5.1 SPP and PPP performance

The positioning errors for the three stations, HKKS, HKLM, and HKTK, from March 8th to 16th, 2022, were calculated using RTKLIB. Figure 7 shows the results of single-frequency SPP and PPP with broadcast ionospheric corrections. The SPP and PPP errors increased from March 12th to March 14th. Compared with the RMS errors in 3D for the following days when the error was stable, the errors for SPP and PPP increased by approximately 151.79 cm and 3.32 cm, respectively, from the 12th to the 14th of March. At the same time, the North and East errors for the single-frequency SPP are in the meter range, and the Up component and 3D errors are greater than 10 m, which is significantly greater than the single-frequency PPP results. In this experiment, the low-latitude single-frequency PPP achieved decimeter-to centimeter-level accuracy.

As discussed in the above section, just before the SSC of the π-day storm, there was a moderate geomagnetic storm with a minimum SymH value of −56 nT occurring on March 12th. This moderate storm also affected the positioning accuracy. Hence, the positioning error started to increase from Mar12th. The direct impact of flares on positioning accuracy is typically momentary (Yasyukevich et al., 2018). Nie et al. (2022a) indicated that flares with a magnitude lower than the X-level or flares with a relatively low X-level have a minimal impact on positioning errors. Although there were two M-class flares on the 11th and 14th days, the direct impact of flares on positioning errors during these days was not substantial. Therefore, the initial phase and main phase of the π-day storm resulted in an increase in the positioning error from March 13th to March 14th. The deterioration of single-point positioning accuracy may be generated by specific effects of magnetic storms on the equatorial ionosphere, such as equatorial ionization anomalies (EIAs) and equatorial plasma bubbles (EPBs) (Aa et al., 2023).

Figure 8 shows the RMS errors of dual-frequency SPP and dual-frequency PPP with ionospheric correction of the ionosphere-free linear combination for the HKKS, HKLM, and HKTK stations from Mar 8th to 17th, 2022. Compared with single-frequency positioning, there is a significant improvement in overall accuracy. Additionally, utilizing dual-frequency combinations can mitigate the impact of geomagnetic storms to a great extent. To examine the daily variations in error, we plotted the data for single-frequency kinematic PPP for each epoch over these 10 days in Figure 9. Additionally, Table 3 provides the convergence times for dual-frequency dynamic and static PPP positioning on the March 13th and 14th, compared with

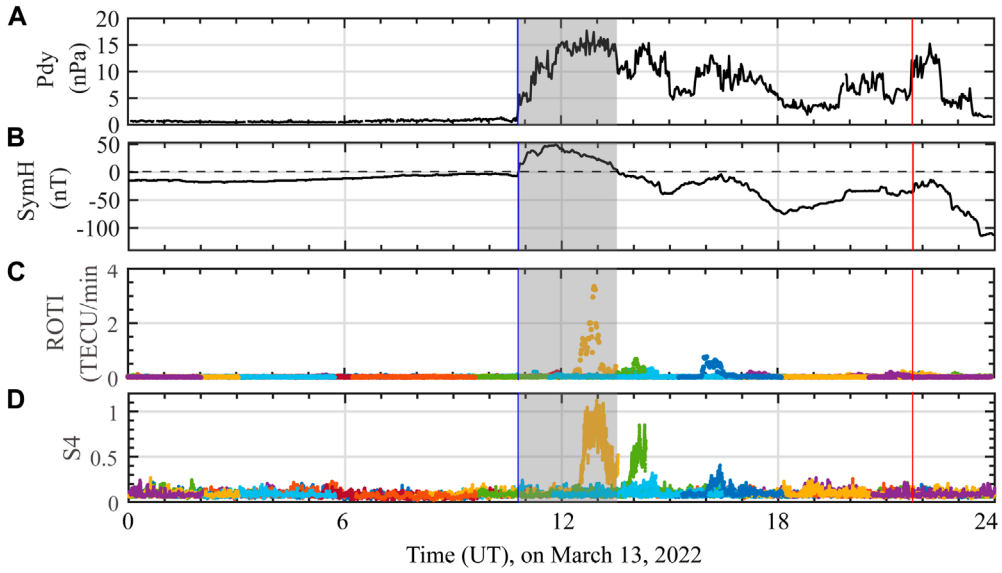

FIGURE 6
The solar wind, ionosphere, and positioning errors on the entire day of the 13th. **(A)** Shifted solar wind dynamic pressure; **(B)** SymH index; **(C)** ROTI; **(D)** Scintillation index S4.

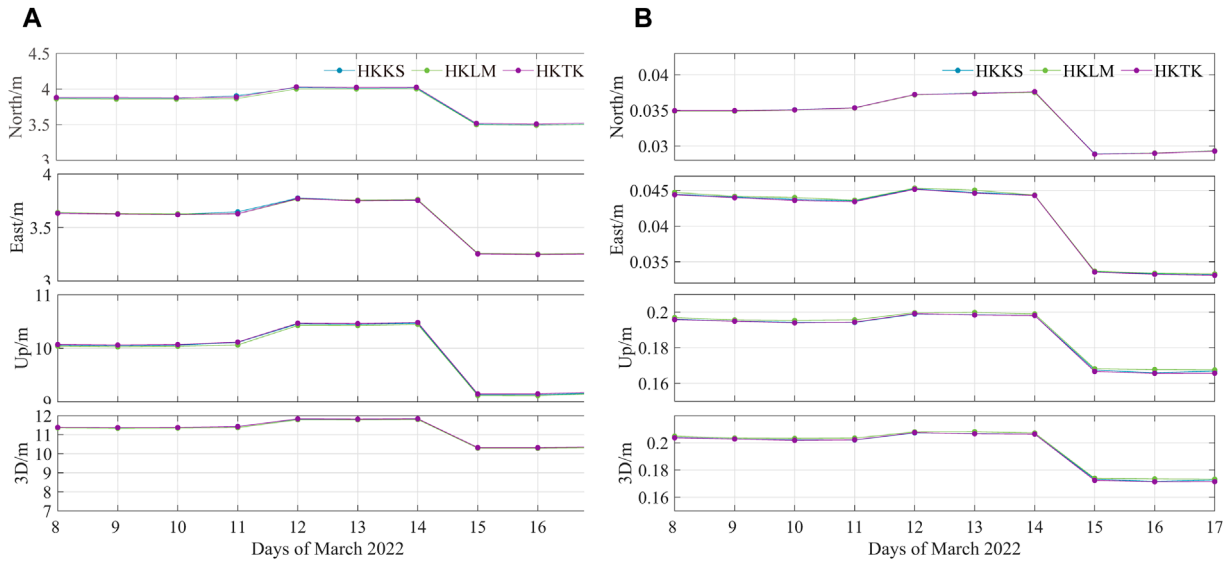

FIGURE 7
The RMS error of **(A)** SPP with a single frequency and **(B)** PPP with a single frequency for the HKKS, HKLM, and HKTK stations from March 8th to 17th, 2022. (The convergence time is set to 30 min for PPP).

that for magnetic quiet days (here, we select the days on Feb. 15–16 representing the magnetic quiet days).

Figure 9 illustrates the daily error variations for single-frequency dynamic PPP. It can be seen that: 1) The errors are larger in the morning and gradually decrease at night, showing a positive correlation with the TEC (see the first panel in Figure 5). 2) The waveforms on the 12th, 13th, and 14th days show a slight increase and are more pronounced than those on the 15th and 16th days, as shown in Figure 7B. 3) The maximum positioning errors during the 3 days of the magnetic storm period also increase. Additionally, no positioning error anomalies were found near the times of the flare events marked in Figure 2.

Table 3 presents the convergence times during magnetic quiet days and magnetic storm days for kinematic and static PPP. The

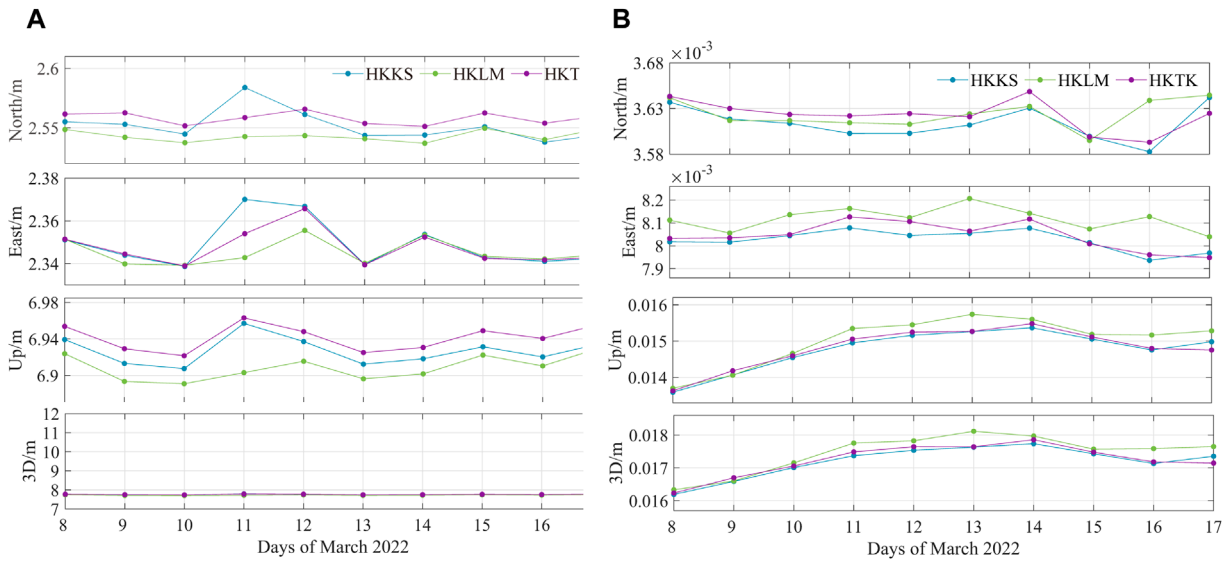

FIGURE 8
The RMS errors of **(A)** SPP with dual frequency and **(B)** PPP with dual frequency for the HKKS, HKLM, and HKTK stations from March 8th to 17th, 2022. (The convergence time is set to 30 min for PPP).

convergence time of dynamic PPP shows no significant difference between magnetic quiet and magnetic storm days. For static PPP, there is an extended convergence time on the 13th and 14th days during the intense magnetic storm, with an additional 30 min compared with that on the magnetic quiet days.

5.2 RTK performance analyses

Figure 10 displays the daily RMS errors for RTK positioning for the five GNSS stations. Notably, the errors at the HKCL station exhibit anomalies over several days, potentially due to its long baseline with the reference station. As outlined in Section 2.3.2, only the baseline for the HKCL exceeds 30 km. Disregarding this station, we magnified the vertical axis to analyze the error variation trends for other stations. Due to being a reference station, the error at HKST remains consistent at its minimum value. It is evident that the RTK accuracy was hardly affected by the magnetic storm, except for a small peak in the Up component on March 13th. Furthermore, in addition to the HKCL site, the RTK positioning accuracy is slightly better than that of the PPP site, reaching the centimeter level. Jacobsen and Andalsvik (2016) and Paziewski et al. (2022) analyzed Norwegian stations during St. Patrick's storm day and revealed that the PPP accuracy was better than that of the RTK. We believe that such differences arise due to the short baselines selected for our RTK stations, averaging 20.47 km, whereas they chose a reference station that was far from other stations (over 180 km), leading to significant ionospheric spatial gradients.

In addition to the positioning accuracy, the convergence time is also an important indicator of RTK positioning performance. Table 4 provides the convergence times of the three components for RTK positioning during both magnetic quiet and magnetic storm days. A convergence threshold of 0.03 m is set. It is evident that the solution durations for each station on March 14th significantly increased. The convergence of the error solution starts at 00:00 UT on March 14th, when the SymH index is the lowest. Additionally, the HKCL experiences longer convergence times on the 13th to 14th centuries, possibly due to the longer baseline, as it is the farthest station from the reference station HKST.

6 Summary

It is known that geomagnetic storms cause various disturbances in the ionosphere, and these disturbances could affect GNSS positioning performance because of signal propagation effects. This study investigated the changes in the low-latitude ionosphere and GNSS-based positioning performance with the passage of a typical ICME on March 2022 and driven π-day geomagnetic storms, with a focus on the causal chain from solar wind disturbance to magnetospheric and ionospheric responses and on the effects of GNSS positioning techniques.

For the ionospheric parameters, the VTEC standard deviation is well correlated with magnetic storms and flares. From March 10th to 15th, the VTEC standard deviation increased significantly. It can be explained by the sequential occurrence of several M-class flares and magnetic storms, including intense π-day storms on these days. The ROTI and S4 indices showed significant disturbances after the arrival of the sheath region driven by the body of the ICME. The ICME sheath region intensively compressed the magnetosphere due to dramatically enhanced solar wind dynamic pressure, which contributed to the initial storm phase and subsequently drove the main storm phase due to the structure with persistent strong southward magnetic fields. Both

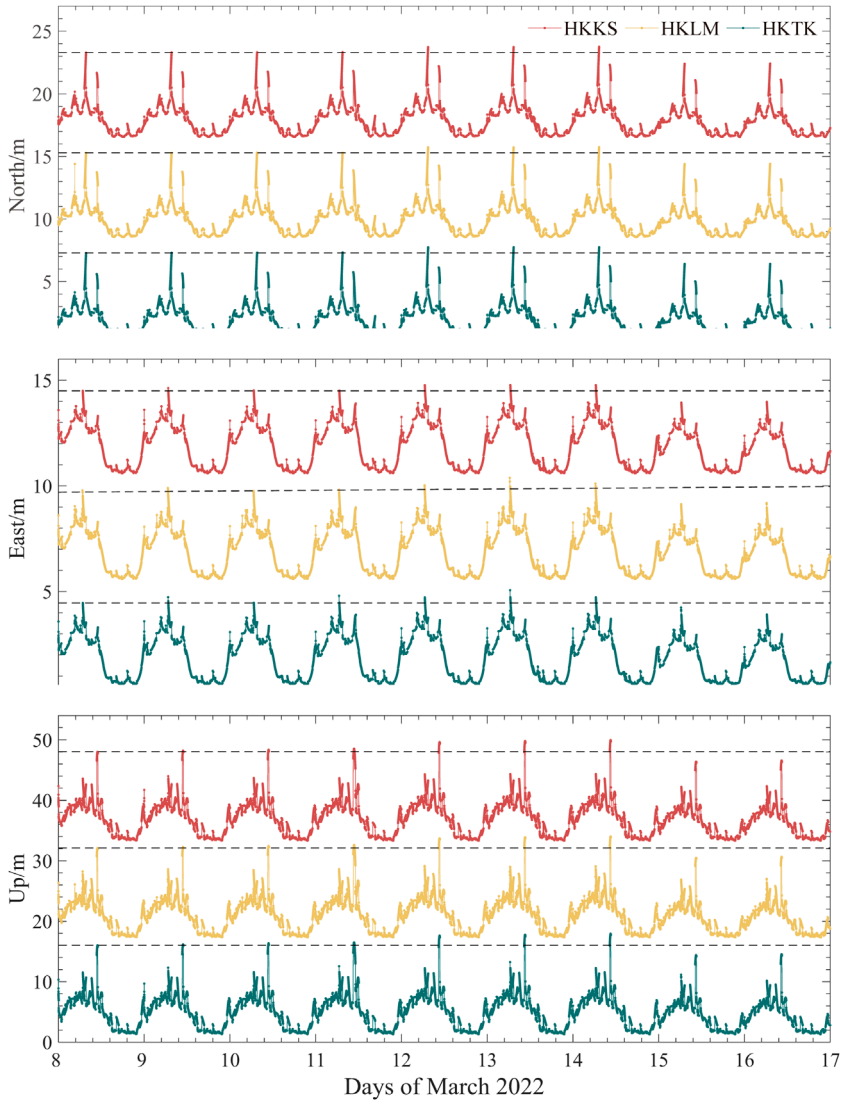

FIGURE 9
The positioning error of single-frequency kinematic PPP. The errors in the North component for each station have been shifted by 8 m, those in the East component has been shifted by 5 m, and the Up component has been shifted by 16 m.

TABLE 3 The convergence time during magnetic quiet days and magnetic storm days for kinematic and static PPP (kinematic PPP with a convergence threshold of 0.3 m and static PPP with a convergence threshold of 0.03 m).

	Station	Convergence time (min)			
		15 February	16 February	13 March	14 March
Kinematic (0.3 m)	HKKS	19.08	19.33	18.92	14.92
	HKLM	19.08	19.33	18.92	14.83
	HKTK	19.08	19.33	18.92	14.92
Static (0.03 m)	HKKS	94.75	94.33	122.58	124.58
	HKLM	94.67	92.25	124.75	124.83
	HKTK	95.00	94.58	124.50	124.50

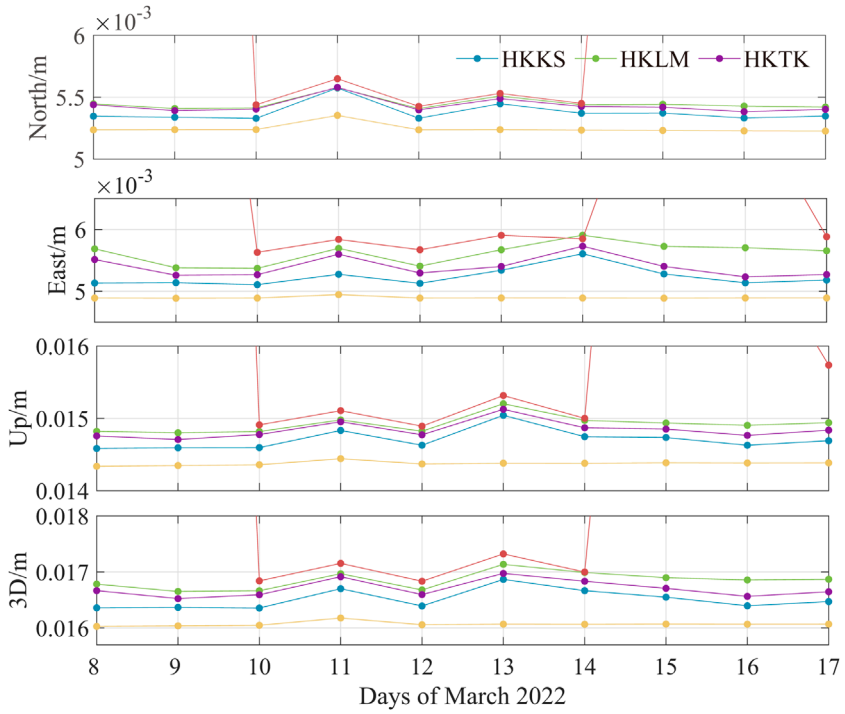

FIGURE 10
The RMS errors of RTKs for the HKKS, HKLM, and HKTK stations from March 8th to 17th, 2022. (The convergence time is set to 20 min).

TABLE 4 The convergence time of the magnetic quiet days and magnetic storm days for RTK (Unit: s).

Station	Convergence time (s)											
	15 February			16 February			13 March			14 March		
	North	East	Up	North	East	Up	North	East	Up	North	East	Up
HKKS	<5	<5	<5	<5	<5	<5	130	130	130	300	825	505
HKLM	<5	<5	<5	<5	<5	<5	<5	<5	<5	300	825	505
HKTK	20	20	20	<5	<5	<5	<5	<5	<5	305	825	505
HKCL	<5	<5	<5	220	220	220	300	900	495	305	826	505

the magnetospheric compression and the initial stage of the storm main phase caused ionospheric scintillations. In comparison, the intensity of the ionospheric scintillation in the initial storm phase just before the storm main phase is even more pronounced. The magnetospheric compression led to super strong-level scintillation. This phenomenon was not observed in previous events, such as St. Patrick's day storm events, because the magnetospheric compression resulting from the dynamic pressure enhancement structure overlaps with the main phase of the storm, making it difficult to distinguish (Nie et al., 2022b). It is interesting to separately analyze and compare the ionospheric scintillations caused by intense magnetospheric compression and storm main phases with ring current enhancement during the passage of ICMEs. This will be our next consideration in the near future.

Furthermore, we compared the positioning performances of the SPP, PPP, and RTK techniques in response to this intense storm. The single-frequency positioning accuracy of SPP and PPP is consistently lower, whereas dual-frequency positioning is better, as indicated in previous studies (Luo et al., 2018). For the single-frequency SPP and PPP, there was at least a 10% increase in the error during the π-day storm compared with the positioning accuracy after the storm, while the performance of the SPP and PPP dual-frequency positioning was almost unaffected. It means that magnetic storms have a greater impact on single-frequency systems, while

dual-frequency systems mitigate ionospheric errors, making them less affected by magnetic storms. Although dual-frequency PPP and RTK were still slightly affected, their accuracy remained two orders of magnitude greater than that of SPP.

For convergence time, the kinematic PPP seemed to be unaffected. However, compared to magnetic quiet days, static PPP convergence time increased by more than 30 min, while for RTK, due to its inherently faster convergence speed, it increased by only 13 min. Overall, RTK positioning performed the best during the magnetic storm, but only for the stations with short baselines (<30 km).

Data availability statement

The original contributions presented in the study are included in the article/Supplementary Material, further inquiries can be directed to the corresponding author.

Author contributions

WL: Data curation, Formal Analysis, Investigation, Visualization, Writing–original draft, Writing–review and editing. TL: Formal Analysis, Methodology, Visualization, Writing–original draft. PZ: Conceptualization, Funding acquisition, Supervision, Validation, Writing–review and editing. ZZ: Investigation, Resources, Writing–review and editing. MR: Investigation, Methodology, Visualization, Writing–review and editing. JW: Investigation, Methodology, Visualization, Writing–review and editing.

Funding

The author(s) declare that financial support was received for the research, authorship, and/or publication of this article. This work was partially supported by the Key-Area Research and Development Program of Guangdong Province (2020B0303020001), the National Natural Science Foundation of China (grant No. 42074205), the Guangdong Basic and Applied Basic Research Foundation (grant No. 2023B1515040021), and the Shenzhen Key Laboratory Launching Project (grant No. ZDSYS20210702140800001).

Acknowledgments

We would like to thank NASA OMNIWEB for providing the public modified high-resolution data based on the definitive Wind plasma data. We also sincerely acknowledge Dr. Ian Richardson, Dr. Hilary Cane, and Dr. Denny M. Oliveira for providing the lists of ICMEs and shocks.

Conflict of interest

The authors declare that the research was conducted in the absence of any commercial or financial relationships that could be construed as a potential conflict of interest.

Publisher's note

All claims expressed in this article are solely those of the authors and do not necessarily represent those of their affiliated organizations, or those of the publisher, the editors and the reviewers. Any product that may be evaluated in this article, or claim that may be made by its manufacturer, is not guaranteed or endorsed by the publisher.

References

Aa, E., Zhang, S. R., Erickson, P. J., Wang, W., Qian, L., Cai, X., et al. (2023). Significant mid-and low-latitude ionospheric disturbances characterized by dynamic EIA, EPBs, and SED variations during the 13–14 March 2022 geomagnetic storm. *J. Geophys. Res. Space Phys.* 128 (8), e2023JA031375. doi:10.1029/2023ja031375

Balan, N., Shiokawa, K., Otsuka, Y., Kikuchi, T., Vijaya Lekshmi, D., Kawamura, S., et al. (2010). A physical mechanism of positive ionospheric storms at low latitudes and midlatitudes. *J. Geophys. Res. Space Phys.* 115 (A2). doi:10.1029/2009ja014515

Bergeot, N., Bruyninx, C., Defraigne, P., Pireaux, S., Legrand, J., Pottiaux, E., et al. (2011). Impact of the Halloween 2003 ionospheric storm on kinematic GPS positioning in Europe. *GPS Solutions* 15, 171–180. doi:10.1007/s10291-010-0181-9

Buonsanto, M. J. (1999). Ionospheric storms—a review. *Space Sci. Rev.* 88 (3), 563–601. doi:10.1023/a:1005107532631

Ciraolo, L., Azpilicueta, F., Brunini, C., Meza, A., and Radicella, S. M. (2007). Calibration errors on experimental slant total electron content (TEC) determined with GPS. *J. geodesy* 81 (2), 111–120. doi:10.1007/s00190-006-0093-1

Collins, P., Bisnath, S., Lahaye, F., and Héroux, P. (2010). Undifferenced GPS ambiguity resolution using the decoupled clock model and ambiguity datum fixing. *Navigation* 57 (2), 123–135. doi:10.1002/j.2161-4296.2010.tb01772.x

Foster, J., and Rideout, W. (2005). Midlatitude TEC enhancements during the October 2003 superstorm. *Geophys. Res. Lett.* 32 (12). doi:10.1029/2004gl021719

Ge, M., Gendt, G., Rothacher, M. a., Shi, C., and Liu, J. (2008). Resolution of GPS carrier-phase ambiguities in precise point positioning (PPP) with daily observations. *J. Geodesy* 82, 389–399. doi:10.1007/s00190-007-0187-4

Geng, J., Meng, X., Dodson, A. H., Ge, M., and Teferle, F. N. (2010). Rapid re-convergences to ambiguity-fixed solutions in precise point positioning. *J. Geodesy* 84, 705–714. doi:10.1007/s00190-010-0404-4

Jacobsen, K. S., and Andalsvik, Y. L. (2016). Overview of the 2015 St. Patrick's day storm and its consequences for RTK and PPP positioning in Norway. *J. Space Weather Space Clim.* 6, A9. doi:10.1051/swsc/2016004

Jacobsen, K. S., and Schäfer, S. (2012). Observed effects of a geomagnetic storm on an RTK positioning network at high latitudes. *J. Space Weather Space Clim.* 2, A13. doi:10.1051/swsc/2012013

Kintner, M., Ledvina, M., and De Paula, E. (2007). GPS and ionospheric scintillations. *Space weather.* 5 (9), s09003. doi:10.1029/2006sw000260

Klobuchar, J. A. (1987). Ionospheric time-delay algorithm for single-frequency GPS users. *IEEE Trans. Aerosp. Electron. Syst.* (3), 325–331. doi:10.1109/taes.1987.310829

Li, Q., Su, X., Tao, C., Zhang, J., Liu, Z., Cui, J., et al. (2023) "Comprehensive analysis of the cycle slip detection threshold in kinematic PPP during geomagnetic storms," in Paper presented at the China satellite navigation conference. 83–92.

Li, X., Zhang, X., and Ge, M. (2011). Regional reference network augmented precise point positioning for instantaneous ambiguity resolution. *J. Geodesy* 85, 151–158. doi:10.1007/s00190-010-0424-0

Lovati, G., De Michelis, P., Consolini, G., Pezzopane, M., Pignalberi, A., and Berrilli, F. (2023). Decomposing solar and geomagnetic activity and seasonal dependencies to examine the relationship between GPS loss of lock and ionospheric turbulence. *Sci. Rep.* 13 (1), 9287. doi:10.1038/s41598-023-34727-2

Lu, Y., Wang, Z., Ji, S., and Chen, W. (2020). Assessing the positioning performance under the effects of strong ionospheric anomalies with multi-GNSS in Hong Kong. *Radio Sci.* 55 (8), 1–18. doi:10.1029/2019rs007004

Luo, X., Chen, Z., Gu, S., Yue, N., and Yue, T. (2023). Studying the fixing rate of GPS PPP ambiguity resolution under different geomagnetic storm intensities. *Space weather.* 21 (10), e2023SW003542. doi:10.1029/2023sw003542

Luo, X., Gu, S., Lou, Y., Xiong, C., Chen, B., and Jin, X. (2018). Assessing the performance of GPS precise point positioning under different geomagnetic storm conditions during solar cycle 24. *Sensors* 18 (6), 1784. doi:10.3390/s18061784

Moraes, A. d. O., Vani, B. C., Costa, E., Abdu, M. A., de Paula, E. R., Sousasantos, J., et al. (2018). GPS availability and positioning issues when the signal paths are aligned with ionospheric plasma bubbles. *Gps Solutions* 22, 95–12. doi:10.1007/s10291-018-0760-8

Nava, B., Coisson, P., and Radicella, S. (2008). A new version of the NeQuick ionosphere electron density model. *J. Atmos. Solar-Terrestrial Phys.* 70 (15), 1856–1862. doi:10.1016/j.jastp.2008.01.015

Nie, W., Rovira Garcia, A., Li, M., Fang, Z., Wang, Y., Zheng, D., et al. (2022a). The mechanism for GNSS-based kinematic positioning degradation at high latitudes under the March 2015 great storm. *Space weather.* 20 (6), e2022SW003132. doi:10.1029/2022sw003132

Nie, W., Rovira Garcia, A., Wang, Y., Zheng, D., Yan, L., and Xu, T. (2022b). On the global kinematic positioning variations during the September 2017 solar flare events. *J. Geophys. Res. Space Phys.* 127 (8), e2021JA030245. doi:10.1029/2021ja030245

Nie, W., Xu, T., Rovira-Garcia, A., Juan Zornoza, J. M., Sanz Subirana, J., González-Casado, G., et al. (2018). Revisit the calibration errors on experimental slant total electron content (TEC) determined with GPS. *Gps Solutions* 22 (3), 85–11. doi:10.1007/s10291-018-0753-7

Paziewski, J., Høeg, P., Sieradzki, R., Jin, Y., Jarmolowski, W., Hoque, M. M., et al. (2022). The implications of ionospheric disturbances for precise GNSS positioning in Greenland. *J. Space Weather Space Clim.* 12, 33. doi:10.1051/swsc/2022029

Poniatowski, M., and Nykiel, G. (2020). Degradation of kinematic PPP of GNSS stations in central Europe caused by medium-scale traveling ionospheric disturbances during the st. patrick's day 2015 geomagnetic storm. *Remote Sens.* 12 (21), 3582. doi:10.3390/rs12213582

Wielgosz, P., Kashani, I., and Grejner-Brzezinska, D. (2005). Analysis of long-range network RTK during a severe ionospheric storm. *J. Geodesy* 79, 524–531. doi:10.1007/s00190-005-0003-y

Xiang, Y., Lyu, S., and Yu, W. (2022). Identifying spurious cycle slips based on iterative filtering under disturbed ionospheric conditions for undifferenced GNSS observations. *Adv. Space Res.* 70 (11), 3582–3593. doi:10.1016/j.asr.2022.08.008

Yang, Z., and Morton, Y. J. (2020). Low-latitude GNSS ionospheric scintillation dependence on magnetic field orientation and impacts on positioning. *J. geodesy* 94 (6), 59. doi:10.1007/s00190-020-01391-7

Yang, Z., Morton, Y. J., Zakharenkova, I., Cherniak, I., Song, S., and Li, W. (2020). Global view of ionospheric disturbance impacts on kinematic GPS positioning solutions during the 2015 St. Patrick's Day storm. *J. Geophys. Res. Space Phys.* 125 (7), e2019JA027681. doi:10.1029/2019ja027681

Yao, Y., Zhang, R., Song, W., Shi, C., and Lou, Y. (2013). An improved approach to model regional ionosphere and accelerate convergence for precise point positioning. *Adv. Space Res.* 52 (8), 1406–1415. doi:10.1016/j.asr.2013.07.020

Yasyukevich, Y., Astafyeva, E., Padokhin, A., Ivanova, V., Syrovatskii, S., and Podlesnyi, A. (2018). The 6 September 2017 X-class solar flares and their impacts on the ionosphere, GNSS, and HF radio wave propagation. *Space weather.* 16 (8), 1013–1027. doi:10.1029/2018sw001932

Yuan, Y., Wang, N., Li, Z., and Huo, X. (2019). The BeiDou global broadcast ionospheric delay correction model (BDGIM) and its preliminary performance evaluation results. *NAVIGATION, J. Inst. Navigation* 66 (1), 55–69. doi:10.1002/navi.292

Zakharenkova, I., and Cherniak, I. (2021). Effects of storm-induced equatorial plasma bubbles on GPS-based kinematic positioning at equatorial and middle latitudes during the September 7–8, 2017, geomagnetic storm. *Gps Solutions* 25 (4), 132. doi:10.1007/s10291-021-01166-3

Zhang, B., Teunissen, P. J., Yuan, Y., Zhang, X., and Li, M. (2019). A modified carrier-to-code leveling method for retrieving ionospheric observables and detecting short-term temporal variability of receiver differential code biases. *J. geodesy* 93, 19–28. doi:10.1007/s00190-018-1135-1

Zhang, J., Richardson, I. G., Webb, D. F., Gopalswamy, N., Huttunen, E., Kasper, J. C., et al. (2007). Solar and interplanetary sources of major geomagnetic storms (Dst ≤ −100 nT) during 1996–2005. *J. Geophys. Res. Space Phys.* 112 (A10). doi:10.1029/2007JA012321

frontiers | Frontiers in Physics

TYPE Original Research
PUBLISHED 11 September 2024
DOI 10.3389/fphy.2024.1439949

Check for updates

OPEN ACCESS

EDITED BY
Olga V. Khabarova,
Tel Aviv University, Israel

REVIEWED BY
Siyao Xu,
University of Florida, United States
Valentina Zharkova,
Northumbria University, United Kingdom

*CORRESPONDENCE
Y. Wang,
wy@hit.edu.cn,
wingwy@mail.ustc.edu.cn

RECEIVED 28 May 2024
ACCEPTED 27 August 2024
PUBLISHED 11 September 2024

CITATION
Chen YL, Wang Y, Wei FS, Feng XS, Zhou ZL, Wang BY, Zuo PB, Jiang CW, Gu YX, Wang LD, Song XJ and Xu XJ (2024) Analytical solution of steady reconnection outflows in a time-varying three-dimensional reconnection model with generalized spatiotemporal distributions. *Front. Phys.* 12:1439949. doi: 10.3389/fphy.2024.1439949

COPYRIGHT
© 2024 Chen, Wang, Wei, Feng, Zhou, Wang, Zuo, Jiang, Gu, Wang, Song and Xu. This is an open-access article distributed under the terms of the Creative Commons Attribution License (CC BY). The use, distribution or reproduction in other forums is permitted, provided the original author(s) and the copyright owner(s) are credited and that the original publication in this journal is cited, in accordance with accepted academic practice. No use, distribution or reproduction is permitted which does not comply with these terms.

Analytical solution of steady reconnection outflows in a time-varying three-dimensional reconnection model with generalized spatiotemporal distributions

Y. L. Chen [1], Y. Wang [1]*, F. S. Wei[1], X. S. Feng [1], Z. L. Zhou[2], B. Y. Wang [1], P. B. Zuo[1], C. W. Jiang[1], Y. X. Gu [1], L. D. Wang [1], X. J. Song[3] and X. J. Xu[2]

[1]Shenzhen Key Laboratory of Numerical Prediction for Space Storm, College of Aerospace Science and Technology, Harbin Institute of Technology, Shenzhen, China, [2]State Key Laboratory of Lunar and Planetary Sciences, Macau University of Science and Technology, Macau, China, [3]Shandong Institute of Advanced Technology, Jinan, China

Magnetic reconnection is a fundamental mechanism for energy conversion in the realms of space physics, astrophysics, and plasma physics. Over the past few decades, obtaining analytical solutions for three-dimensional (3D) magnetic reconnection has remained a challenging endeavor. Due to the complexity and nonlinearity of the equations, analytical solutions can only be obtained when specific spatiotemporal distributions of magnetic fields or plasma flows are provided. Particularly, the evolution of reconnection flows in time-dependent 3D reconnection has not been analytically discussed. Additionally, quasi-steady magnetic reconnection persisting for several hours can be observed in the turbulent solar wind, which raises an important question: can steady reconnection flows theoretically exist in a time-dependent 3D magnetic reconnection model? In this study, a generalized analytical model for time-dependent kinematic 3D magnetic reconnection has been constructed. In the framework of pure analytical approach, it is firstly demonstrated that steady reconnection outflows can theoretically exist within a time-varying magnetic field. We have also analytically discussed the possibility of the existence of quasi-steady reconnection flows in 3D magnetic reconnection for turbulent magnetic fields in the solar wind. These findings broaden our understanding of the stability and necessary conditions for time-dependent 3D magnetic reconnection, offering new insights into quasi-steady reconnection phenomena in real cosmic environments.

KEYWORDS

magnetic reconnection, analytical solutions, stationary plasma flow, turbulent reconnection, solar wind reconnection

1 Introduction

Magnetic reconnection, recognized as a topological or geometrical rearrangement process of magnetic field [1], plays a significant role in the dynamics of diverse plasma environments [2–5]. Historically, the concept of magnetic reconnection advanced significantly through the exploration of two-dimensional (2D) steady-state models rooted in magnetohydrodynamic (MHD) theory [6–9]. In recent decades, significant achievements have been made in the study of magnetic reconnection, primarily through observation [10–13], numerical simulation [14–17], and experimental research [18–21]. These advancements have enriched our understanding of this fundamental phenomenon, uncovering and validating its intricate evolutionary characteristics across a wide range of astrophysical and laboratory environments. However, the theoretical analysis on magnetic reconnection, especially in seeking the analytical solutions for 3D magnetic reconnection, has faced numerous challenges due to the complexity and nonlinearity of the equations involved [22–25].

Magnetic reconnection and plasma dynamics are intricate processes governed by nonlinear coupling between magnetic fields and plasma flows. Obtaining analytical solutions within the MHD framework faces considerable challenges due to this nonlinearity. Even when equations such as the momentum and energy equations are simplified, deriving direct analytical solutions remains daunting. Consequently, previous analytical approaches have predominantly relied on simplifying theoretical equations and imposing specific constraints. A practical method involves combining Ohm's law and simplified Maxwell equations with a particular magnetic field configuration to deduce analytical solutions [26–28].

In order to simplify the analytical process, many authors have disregarded the time variable and concentrated exclusively on static magnetic reconnection analysis. By constructing different spatial distribution of magnetic fields, they have derived diverse analytical solutions that could address different types of magnetic reconnection scenarios to some extent [29–31]. Under the assumption of stagnation point flow driving [32–34] and based on the linear X-point theory [35], Craig et al. [36–38] developed a set of hybrid analytic solutions describing reconnection processes with X-type topology magnetic field lines and intricate current structures. In addition, a notable instance is the derivation of self-similar solutions [39], which simplify the intricate problem by linearly expanding a magnetized plasma under self-similar evolution conditions. Moreover, along with the localized resistivity assumption, pioneering works on the slippage reconnection process within a finite diffusion region [40, 41] resulted in the identification of kinematic solutions of the null or non-null magnetic reconnection [42–45] featuring a reverse rotational flow in a hyperbolic magnetic field.

Sporadic studies have addressed the scenarios involving temporal changes in analytical solutions for 3D magnetic reconnection [46–50]. While the inclusion of time variable makes the solution of the equation set more complex, often requiring the imposition of additional restrictions. By utilizing various initial conditions, Anderson and Priest [51] investigated the time-dependent solution of the MHD equations for magnetic annihilation in a time-varying stagnation point flow. Wilmot-smith et al. [52] examined a series of magnetic diffusion with assumed magnetic diffusivity under the effect of a defined magnetic flux velocity. Additionally, Hornig and Priest [26] attempted to incorporate a time-dependent factor in the expression of electric potential within the framework of the time-independent equation set. Most notably, all of these efforts cannot address how reconnection flows evolve over time. Recently, based on the method employed by Hornig et al. [26], we have constructed a time-dependent 3D model by directly introducing time variables into the equation set [53]. It has been found that spiral plasma flows can be generated if the magnetic field changes exponentially with time.

As mentioned above, the inherent complexity and nonlinearity of the governing equations in magnetic reconnection and plasma dynamics present formidable obstacles to deriving analytical solutions without imposing specific spatiotemporal distributions of magnetic fields and plasma flows. However, such distributions, tailored for analytical tractability, are seldom representative of real cosmic environments, thus constraining the practical utility of these solutions. Significantly, both magnetic fields and plasma flows exhibit intrinsic temporal variability, making stationary analytical solutions unsuitable for accurate predictions and empirical validation. The absence of temporal dynamics in these static solutions leads to significant discrepancies between theoretical predictions and empirical observations. Furthermore, in time-dependent 3D models, if the magnetic field varies with time, the deduced plasma flows will also exhibit temporal variations [53]. So, even if the time-dependent analytical solutions offer advancements by integrating temporal variations, they will still encounter challenges in elucidating quasi-steady reconnection phenomena.

The prolonged magnetic reconnection phenomena in the solar wind, characterized by the presence of a pair of Alfvenic reconnection jets, have been reported for years [54–56]. These reconnection jets, which are signatures of ongoing magnetic reconnection, have been observed to persist over extended periods, indicating the long-lasting nature of the reconnection process in the solar wind environment [57]. Observations reveal that such phenomena are very common, occurring approximately 1.5 times per day, with a typical reconnection rate of ~0.05, and can persist for at least 5 h [58]. Remarkably, the reconnection exhausts measured between 1 and 5.4 AU do not appear significantly broader than those measured between 0.3 AU and 1.0 AU, maintaining good planarity in their structure [59–61]. Intriguingly, given the turbulent nature of the solar wind, where magnetic fields and plasma flows vary continuously over time, it seems counterintuitive for such quasi-steady reconnection exhausts to exist from the perspective of time-dependent 3D analytical solutions [62]. Nevertheless, the inherent characteristic of turbulence is its unpredictability, which cannot be fully expressed analytically in four-dimensional spacetime. Consequently, researchers have mainly focused on providing theoretical analysis [63] and numerical simulations [64, 65] to incorporate the effect of turbulence on magnetic reconnection in earlier studies. Notably, the turbulence generated during magnetic reconnection is self-consistently simulated, appearing after 32–64 Alfven time and being caused by two beam instabilities with 3D Particle in cell simulations [66, 67]. Moreover, MHD simulations [68] demonstrate a fast growth of turbulent energy by 3 orders of magnitude over one Alfven time, indicating a

considerably shorter timescale for turbulence self-generation during reconnection. To date, however, quasi-steady reconnection flows in 3D magnetic reconnection for turbulent magnetic fields have never been proven through a purely theoretical analytical approach.

Therefore, the question arises: can steady reconnection theoretically persist within a time-varying magnetic field scenario? If generalized spatiotemporal distribution forms of the magnetic field and magnetic diffusivity are given, can we analytically obtain steady reconnection outflows from the time-dependent 3D magnetic reconnection model? Furthermore, if such steady reconnection outflows can occur in a time-varying magnetic field, what conditions must the spatiotemporal distributions of the magnetic field and magnetic diffusivity fulfill? In this letter, we analytically solve the time-dependent kinematic 3D magnetic reconnection with generalized spatiotemporal distribution forms of the magnetic field and magnetic diffusivity. The existence and the conditions of steady reconnection outflows are discussed.

2 Time-dependent magnetic reconnection model with generalized forms

Based on the method introduced by Hornig and Priest [26] and following a similar approach used in our previous studies [53], we construct a time-dependent model by integrating temporal variables directly into the Maxwell-Faraday equations. Consequently, the governing equations of the system can be succinctly expressed as follows:

$$\boldsymbol{E}+\boldsymbol{u}\times\boldsymbol{B}=\eta\boldsymbol{J}, \tag{1}$$

$$\nabla\times\boldsymbol{E}=-\partial\boldsymbol{B}/\partial t, \tag{2}$$

$$\nabla\cdot\boldsymbol{B}=0, \tag{3}$$

$$\nabla\times\boldsymbol{B}=\mu_0\boldsymbol{J}. \tag{4}$$

Here the first equation is Ohm's law, while the others are Maxwell's equations. Here, $\boldsymbol{u}$ denotes the velocity of the plasma, while $\boldsymbol{E}$, $\boldsymbol{B}$ and $\boldsymbol{J}$ refer to the electric field, magnetic field and current density respectively. η and μ_0 represent the magnetic diffusion coefficient and the permeability of the vacuum, respectively.

Previous studies have always facilitated analytical derivation and resolved the flow field by providing specific spatiotemporal distributions of $\boldsymbol{B}$ and η. However, as discussed in the introduction, quasi-steady reconnection exhausts could persist in turbulent solar wind, where the magnetic fields and magnetic diffusion coefficients cannot be given in any specific form. Therefore, in this work, we deviate from past practices by refraining from specifying particular spatiotemporal distributions of $\boldsymbol{B}$ and η. Instead, we adopt a more general approach and assume that the temporal and spatial variables can be expressed in a separable form. By following the similar derivation method [26, 53], the $\boldsymbol{B}$ can be expressed as follows:

$$\boldsymbol{B}(x,y,z,t)=\boldsymbol{B}(\boldsymbol{r})B(t) \tag{5}$$

here $\boldsymbol{r}$ represents the three components of the Cartesian coordinate system. The analytical expressions of field lines can be found by solving:

$$\partial\boldsymbol{X}(s,t)/\partial s=\boldsymbol{B}(\boldsymbol{X}(s,t)) \tag{6}$$

where s is the parameter satisfying $ds=d\lambda/|\boldsymbol{B}|$, and λ represents the distance along the magnetic field lines. Here we mainly discuss the variable separated case $\boldsymbol{X}(s,t)=\boldsymbol{X}(s)\boldsymbol{X}(t)$.

Then we can obtain the equations of the magnetic field lines $\boldsymbol{X}(\boldsymbol{r}_0,s)$ and the corresponding inverse mapping $\boldsymbol{X}_0(\boldsymbol{r},s)$ in term of an initial point $\boldsymbol{r}_0$:

$$\boldsymbol{X}=f(\boldsymbol{r}_0,s) \tag{7}$$

$$\boldsymbol{X}_0=F(\boldsymbol{r},s) \tag{8}$$

Furthermore, incorporating a time-dependent magnetic field allows us to express the electric field as follows:

$$\boldsymbol{E}=-\nabla\phi-\partial\boldsymbol{A}/\partial t \tag{9}$$

where $\boldsymbol{A}$ is the magnetic vector potential, and $\boldsymbol{B}=\nabla\times\boldsymbol{A}$. Substituting Equation 9 in Equation 1 yields

$$-\nabla\phi-\partial\boldsymbol{A}/\partial t+\boldsymbol{u}\times\boldsymbol{B}=\eta\boldsymbol{J} \tag{10}$$

Based on the analysis method of Hornig and Priest [26] and the boundary conditions of Chen et al. [53], the electric potential can be derived as:

$$\phi=-\int(\eta\boldsymbol{J}\cdot\boldsymbol{B}+\partial\boldsymbol{A}/\partial t\cdot\boldsymbol{B})ds+\phi_0 \tag{11}$$

Here, we still set $\phi_0=0$. Similarly, a general form of the local resistivity is given as $\eta=\eta(\boldsymbol{r})\eta(t)$, and substituting Equation 7 into Equation 11, we can obtain $\phi(\boldsymbol{X}_0,s)$. After which we get $\phi(\boldsymbol{X})$ by using Equation 8.

By taking the scalar product of both sides of Equation 10 with $\boldsymbol{B}$ and combining Equations 5, 6, the analytical expression for the velocity perpendicular to the magnetic field can be derived as:

$$\begin{aligned}\boldsymbol{u}_\perp&=(\boldsymbol{E}-\eta\boldsymbol{J})\times\boldsymbol{B}/|\boldsymbol{B}|^2\\&=\Big\{\nabla F\Big[\eta(t)B^2(t)\int\eta(\boldsymbol{r})\boldsymbol{J}(\boldsymbol{r})\cdot\boldsymbol{B}(\boldsymbol{r})ds+B'(t)B(t)\int\boldsymbol{A}(\boldsymbol{r})\cdot\\&\quad\boldsymbol{B}(\boldsymbol{r})ds\Big]-B'(t)\boldsymbol{A}(\boldsymbol{r})-\eta(t)B(t)F\big[\eta(\boldsymbol{r})\boldsymbol{J}(\boldsymbol{r})\big]\Big\}\times\boldsymbol{B}(\boldsymbol{r})/\\&\quad\times(|\boldsymbol{B}(\boldsymbol{r})|^2B(t))\end{aligned} \tag{12}$$

where F denotes the transformation mapping a function from vector $\boldsymbol{s}$ to one of $\boldsymbol{x}$. Note that the implicit form of the reconnection flow is intricate. To investigate the existence of steady reconnection plasma flows, the condition $\partial\boldsymbol{u}_\perp/\partial t=0$ in the generalized time-dependent system will be analyzed. To ensure meaningful results, we will discuss the case where both the magnetic field and the magnetic diffusivity vary with time ($\partial\eta/\partial t\neq0$ and $\partial B/\partial t\neq0$). Additionally, the dimensionless approach is employed for the sake of simplicity.

3 The existence of stationary plasma flow with generalized forms

The presence of a stationary plasma flow requires that the partial derivative of velocity with respect to time equals zero, $\partial\boldsymbol{u}_\perp/\partial t=0$. By performing a temporal partial differentiation on Equation 12, we have derived the conditions that guarantee the existence of a stationary plasma flow within the system:

$$k_1\left[\eta'(t)B(t)+\eta(t)B'(t)\right]+k_2B''(t)-k_3\left(B''(t)B(t)-B'(t)^2\Big/B^2(t)\right)-k_4\eta'(t)=0 \tag{13}$$

Where k_i are introduced as specific expressions for the sake of simplicity:

$$\begin{cases} k_1=\nabla F\left[\int \eta(\boldsymbol{r})\boldsymbol{J}(\boldsymbol{r})\cdot\boldsymbol{B}(\boldsymbol{r})ds\right]\times\boldsymbol{B}(\boldsymbol{r})\Big/\boldsymbol{B}^2(\boldsymbol{r}) \\ k_2=\nabla F\left[\int \boldsymbol{A}(\boldsymbol{r})\cdot\boldsymbol{B}(\boldsymbol{r})ds\right]\times\boldsymbol{B}(\boldsymbol{r})\Big/\boldsymbol{B}^2(\boldsymbol{r}) \\ k_3=\boldsymbol{A}(\boldsymbol{r})\times\boldsymbol{B}(\boldsymbol{r})/\boldsymbol{B}^2(\boldsymbol{r}) \\ k_4=F\left[\eta(\boldsymbol{r})\boldsymbol{J}(\boldsymbol{r})\right]\times\boldsymbol{B}(\boldsymbol{r})/\boldsymbol{B}^2(\boldsymbol{r}) \end{cases} \tag{14}$$

Neglecting the trivial solutions and assuming $B'(t)\neq 0, \eta'(t)\neq 0$, we infer three distinct categories of constraints on the stationary plasma flow from Equation 13: scenarios where each term is zero, situations where some terms are nonzero, and cases where every term is nonzero. Specifically, we systematically discussed the following six situations:

Case I, k_i in Equation 13 are all zero:

$$\begin{cases} k_1=0, \\ k_2=0, \\ k_3=0, \\ k_4=0. \end{cases} \tag{15}$$

From Equation 14 We deduce that:

$$\begin{cases} \nabla F\left[\int \eta(\boldsymbol{r})\boldsymbol{J}(\boldsymbol{r})\cdot\boldsymbol{B}(\boldsymbol{r})ds\right]=a_1\boldsymbol{B}(\boldsymbol{r}), \\ \nabla F\left[\boldsymbol{A}(\boldsymbol{r})\cdot\boldsymbol{B}(\boldsymbol{r})ds\right]=a_2\boldsymbol{B}(\boldsymbol{r}), \\ \boldsymbol{A}(\boldsymbol{r})=a_3\boldsymbol{B}(\boldsymbol{r}), \\ \boldsymbol{J}(\boldsymbol{r})=a_4\boldsymbol{B}(\boldsymbol{r}). \end{cases} \tag{16}$$

Here a_1, a_2, a_3 and a_4 are all nonzero constants. It is worth noting that in such a scenario, the system does not impose any requirements on the temporal variations of the magnetic field and magnetic diffusion coefficient. As long as the spatial distribution of the magnetic field and magnetic diffusion coefficient satisfies the equations mentioned above, it is sufficient to generate stationary plasma flow. However, the third equation in equation set (16) imply that the magnetic field should be at least irrotational, and the forth equation requires the magnetic field to be force-free.

Case II, $k_1\neq 0$ and the first term in Equation 13 is zero:

$$\begin{cases} \eta'(t)B(t)+\eta(t)B'(t)=0, \\ k_2=0, \\ k_3=0, \\ k_4=0. \end{cases} \tag{17}$$

We derive that:

$$\begin{cases} \left[\eta(t)B(t)\right]'=0, \\ \nabla F\left[\int \boldsymbol{A}(\boldsymbol{r})\cdot\boldsymbol{B}(\boldsymbol{r})ds\right]=a_1\boldsymbol{B}(\boldsymbol{r}), \\ \boldsymbol{A}(\boldsymbol{r})=a_2\boldsymbol{B}(\boldsymbol{r}), \\ \boldsymbol{J}(\boldsymbol{r})=a_3\boldsymbol{B}(\boldsymbol{r}). \end{cases} \tag{18}$$

Where a_1, a_2, a_3 are all nonzero constants. This case additionally requires that the partial derivative of the product of the magnetic diffusion coefficient and the magnetic field with respect to time is zero. Other requirements are similar to those in Case I.

Case III, $k_2\neq 0$ and the second term in Equation 13 is zero:

$$\begin{cases} k_1=0, \\ B''(t)=0, \\ k_3=0, \\ k_4=0. \end{cases} \tag{19}$$

We can get:

$$\begin{cases} \nabla F\left[\int \eta(\boldsymbol{r})\boldsymbol{J}(\boldsymbol{r})\cdot\boldsymbol{B}(\boldsymbol{r})ds\right]=a_1\boldsymbol{B}(\boldsymbol{r}), \\ B(t)=a_2t+a_3, \\ \boldsymbol{A}(\boldsymbol{r})=a_4\boldsymbol{B}(\boldsymbol{r}), \\ \boldsymbol{J}(\boldsymbol{r})=a_5\boldsymbol{B}(\boldsymbol{r}). \end{cases} \tag{20}$$

Where a_1, a_2, a_4, a_5 are all nonzero constants, and a_3 is constant. This case additionally requires that the magnetic field must change linearly with time. Other requirements are similar to those in Case I.

Case IV, $k_3\neq 0$ and the third term in Equation 13 is zero:

$$\begin{cases} k_1=0, \\ k_2=0, \\ B''(t)B(t)-B'(t)^2=0, \\ k_4=0. \end{cases} \tag{21}$$

It can be obtained that:

$$\begin{cases} \nabla F\left[\int \eta(\boldsymbol{r})\boldsymbol{J}(\boldsymbol{r})\cdot\boldsymbol{B}(\boldsymbol{r})ds\right]=a_1\boldsymbol{B}(\boldsymbol{r}), \\ \nabla F\left[\int \boldsymbol{A}(\boldsymbol{r})\cdot\boldsymbol{B}(\boldsymbol{r})ds\right]=a_2\boldsymbol{B}(\boldsymbol{r}), \\ B(t)=a_3e^{a_4t}, \\ \boldsymbol{J}(\boldsymbol{r})=a_5\boldsymbol{B}(\boldsymbol{r}). \end{cases} \tag{22}$$

Where a_1, a_2, a_3, a_5 are all nonzero constants, and a_4 is constant. This case additionally requires that the magnetic field must change exponentially with time. Other requirements are similar to those in Case I.

Besides, there are situations that bind the system even further:

Case V, both the first and third term in Equation 13 are zero:

$$\begin{cases} \eta'(t)B(t)+\eta(t)B'(t)=0, \\ k_2=0, \\ B''(t)B(t)-B'(t)^2=0, \\ k_4=0. \end{cases} \tag{23}$$

It suggests that:

$$\begin{cases} \eta(t)=a_2e^{-a_1t}, \\ \nabla F\left[\int \boldsymbol{A}(\boldsymbol{r})\cdot\boldsymbol{B}(\boldsymbol{r})ds\right]=a_3\boldsymbol{B}(\boldsymbol{r}), \\ B(t)=a_4e^{a_1t}, \\ \boldsymbol{J}(\boldsymbol{r})=a_5\boldsymbol{B}(\boldsymbol{r}). \end{cases} \tag{24}$$

Where a_1, a_2, a_3, a_4, a_5 are all nonzero constants. Based on the above conditions, the steady flow can exist when the temporal variation of the magnetic field and the magnetic diffusion coefficient can be expressed as an exponential relationship. Other requirements are similar to those in Case I.

Case VI, both the first and second term in Equation 13 are zero:

$$\begin{cases} \eta'(t)B(t)+\eta(t)B'(t)=0, \\ B''(t)=0, \\ k_3=0, \\ k_4=0. \end{cases} \tag{25}$$

It can be parsed that:

$$\begin{cases} \eta(t) = a_1/(a_2 t + a_3), \\ B(t) = a_2 t + a_3, \\ \boldsymbol{A}(\boldsymbol{r}) = a_4 \boldsymbol{B}(\boldsymbol{r}), \\ \boldsymbol{J}(\boldsymbol{r}) = a_5 \boldsymbol{B}(\boldsymbol{r}). \end{cases} \tag{26}$$

Here a_1, a_2, a_4, a_5 are all nonzero constants, and a_3 is constant. This situation requires that the magnetic diffusivity is inversely proportional to time, while the magnetic field varies linearly with time. Other requirements are similar to those in Case I.

It should be noted that the condition where both the second and third non-parametric terms are zero in Equation 13 does not hold since $\eta'(t) \neq 0$. Additionally, in other cases where Equation 13 contains non-zero terms, the presence of complex expressions makes it impractical to explicitly express their physical meaning. To maintain completeness, these cases are provided in the Supplementary Appendix SA1. Furthermore, unlike 2D magnetic reconnection, where reconnection occurs only at X-type null points, 3D magnetic reconnection can occur at locations where the magnetic field does not vanish. Consequently, the conditions required for steady reconnection flows in 3D magnetic reconnection discussed here from Equations 15–26 are distinct from those in classical reconnection models [6–8] and cannot be directly compared.

4 Discussion and conclusion

From the analysis of the above results, it can be observed that the existence conditions for steady reconnection flows impose very strict requirements on the spatial distribution of the magnetic field. However, in terms of the time variable, common variations such as linear or exponential changes can meet the requirements. Although very few regions simultaneously satisfy these conditions in actual cosmic space, it is proven that steady reconnection flows can be analytically obtained from the time-dependent 3D magnetic reconnection model. Specifically, if the spatiotemporal distributions of the magnetic field and magnetic diffusivity follow the constraints referred to above, steady reconnection can theoretically persist within a time-varying magnetic field scenario.

As introduced above, the solar wind is full of turbulence where the distribution of the magnetic field and the magnetic diffusion coefficient cannot meet any form of the above theoretical analysis, but we can still observe quasi-steady magnetic reconnection exhausts persisting for hours. Our work may shed some light on this phenomenon. According to Fourier's theorem, any periodic or non-periodic signal can be decomposed into a combination of harmonically related sinusoidal signals. Therefore, the turbulent magnetic field in the solar wind can be decomposed into a series of sinusoidal signals. If we can prove that there exists a quasi-steady flow field corresponding to a time-varying magnetic field such as a sinusoidal signal in 3D magnetic reconnection, then the turbulent solar wind might have the possibility to produce quasi-steady magnetic reconnection. Following the method adopted before, we assume a classical X-type magnetic field along with a sinusoidal time-dependent perturbation:

$$\boldsymbol{B}(\boldsymbol{r}, t) = \left(y/L, k^2 x/L, B_z\right)\left(B_1 + B_2 \sin(\omega\, t)\right) \tag{27}$$

Here the reconnecting field component, $B_{xy} = (y/L, k^2 x/L)$ and the guide field component B_z are specifically addressed to analyze the effect of the guide field on the stability of the reconnection outflows. To make Equations 1–4 analytically solvable, and by following the similar derivation method [26, 53], we construct the following magnetic vector potential:

$$\boldsymbol{A}(\boldsymbol{r}, t) = \left(k^2 xz/L, B_z x, y^2/(2L)\right)\left(B_1 + B_2 \sin(\omega\, t)\right) \tag{28}$$

Assuming $\boldsymbol{X}(s, t) = \boldsymbol{X}(s)X(t)$, the corresponding inverse mapping of $\boldsymbol{X}(x_0, s)$ can be written as:

$$X_0 = x\cosh(ks/L) - y\sinh(ks/L)/k \tag{29}$$

$$Y_0 = y\cosh(ks/L) - kx\sinh(ks/L), \tag{30}$$

$$Z_0 = -s + z. \tag{31}$$

Adopting the same boundary conditions [53], the magnetic diffusion coefficient is also set as:

$$\eta(x_0, y_0, s) = \eta_0 \exp\left(-\left(s^2 + x_0^2 + y_0^2\right)/l^2\right) \tag{32}$$

where l is a constant that governs the scale of a non-ideal region. Here, the electric field can be deduced from Equations 9, 11 and Equations 27–32. Then, the flow can be determined as follows:

$$\boldsymbol{u}_\perp = \frac{(\boldsymbol{E} - \eta \boldsymbol{J}) \times \boldsymbol{B}}{\boldsymbol{B}^2} \tag{33}$$

The solid lines in Figure 1 represent the magnetic field variations, while the dashed lines represent the outflows deduced from Equation 33. It is evident that the outflows exhibit corresponding periodic oscillations in response to the periodic variations of the magnetic field. In scenarios with lower guide field conditions, the system tends to amplify the fluctuations in the magnetic field, leading to increases in the amplitude of velocity disturbances. As the guide field increases, these disturbances are suppressed, and the oscillation amplitude of the outflows gradually decreases. Notably, when $B_z/B_{xy} > 0.2$, the outflow exhibits obvious stability. Hence, the presence of the guide field significantly enhances the stability of the reconnection outflow. Figure 1 also reveals that for a sinusoidally varying magnetic field, 3D magnetic reconnection can generate a quasi-steady flow that corresponds to these magnetic field variations if a suitable range of angular frequencies, disturbance amplitudes and guide field are satisfied.

It should be noted that the single X-type topology for solar wind reconnection exhausts has never been completely observed. There are only fragmentary observational evidences from multi-spacecraft measurements suggesting that the most likely geometric structure of the reconnection exhaust is a large-scale X-line shape [54–56, 61]. Since a single spacecraft can only observe the solar wind passing by it, providing essentially one-dimensional observations without three-dimensional information, the actual reconnection topology for solar wind could be more complex. However, our intention here was not to argue whether the reconnection exhaust should conform to such

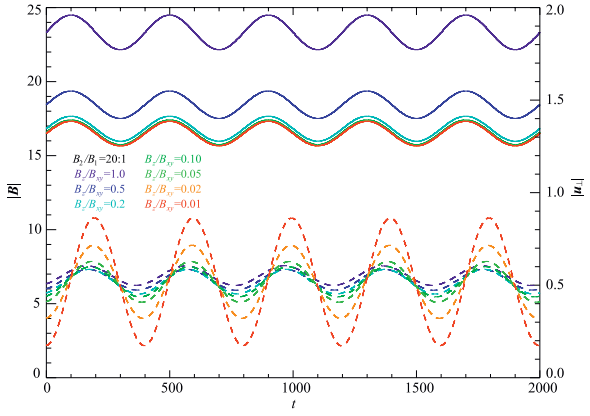

FIGURE 1
Schematic representation of the temporal variations in magnetic field (solid lines) and outflow (dashed lines) in a 3D magnetic reconnection for parameters: k = 2, L = 10, l = 1, B_1 = 20, B_2 = 1, ω = π/200, x = 2, y = 2, z = 2. Different colors denote different B_z/B_{xy}.

a classical X-type structure, but rather to discuss the possibility of quasi-steady reconnection flow. In addition, the above analysis does not essentially incorporate any turbulent components in the classical sense, whereas turbulence has been demonstrated in the literature to significantly affect magnetic field diffusivity, i.e., reconnection diffusion and reconnection rate [63, 65]. From this point of view, the analysis primarily represents a laminar flow perspective. Nevertheless, this approach could also serve as a purely theoretical framework for analytically validating the potential existence of quasi-steady flows in 3D magnetic reconnection within disturbed magnetic field configurations. By adopting Fourier's signal decomposition approach, the above efforts might still enhance our ability to interpret reconnection phenomena in turbulent solar wind.

In summary, due to the complexity and difficulty of analytical work, many previous studies have disregarded the time variable and focused exclusively on static magnetic reconnection analysis to deduce solutions. Consequently, most of these works cannot address how reconnection flows evolve over time. In this paper, we analytically solve the time-dependent kinematic 3D magnetic reconnection with generalized spatiotemporal distribution forms of the magnetic field and magnetic diffusivity. Although the required spatiotemporal distributions are too strict to be found in actual cosmic space, through a purely theoretical analytical approach, we have demonstrated for the first time that steady reconnection flow can exist. These results could contribute to a deeper understanding of the stability and conditions required for the existence of 3D magnetic reconnection, offering new insights into quasi-steady reconnection in various cosmic environment.

Data availability statement

The original contributions presented in the study are included in the article/Supplementary Material, further inquiries can be directed to the corresponding author.

Author contributions

YLC: Conceptualization, Data curation, Formal Analysis, Funding acquisition, Investigation, Methodology, Project administration, Resources, Software, Supervision, Validation, Visualization, Writing–original draft, Writing–review and editing. YW: Conceptualization, Data curation, Formal Analysis, Funding acquisition, Investigation, Methodology, Project administration, Resources, Software, Supervision, Validation, Visualization, Writing–review and editing. FSW: Conceptualization, Data curation, Formal Analysis, Funding acquisition, Investigation, Methodology, Project administration, Resources, Software, Supervision, Validation, Visualization, Writing–review and editing. XSF: Conceptualization, Data curation, Formal Analysis, Funding acquisition, Investigation, Methodology, Project administration, Resources, Software, Supervision, Validation, Visualization, Writing–review and editing. ZLZ: Conceptualization, Data curation, Formal Analysis, Funding acquisition, Investigation, Methodology, Project administration, Resources, Software, Supervision, Validation, Visualization, Writing–review and editing. BYW: Conceptualization, Data curation, Formal Analysis, Funding acquisition, Investigation, Methodology, Project administration, Resources, Software, Supervision, Validation, Visualization, Writing–review and editing. PBZ: Conceptualization, Data curation, Formal Analysis, Funding acquisition, Investigation, Methodology, Project administration, Resources, Software, Supervision, Validation, Visualization, Writing–review and editing. CWJ: Conceptualization, Data curation, Formal Analysis, Funding acquisition, Investigation, Methodology, Project administration, Resources, Software, Supervision, Validation, Visualization, Writing–review and editing. YXG: Conceptualization, Data curation, Formal Analysis, Funding acquisition, Investigation, Methodology, Project administration, Resources, Software, Supervision, Validation, Visualization, Writing–review and editing. LDW: Conceptualization, Data curation, Formal Analysis, Funding acquisition, Investigation, Methodology, Project administration, Resources, Software,

Supervision, Validation, Visualization, Writing–review and editing. XJS: Conceptualization, Data curation, Formal Analysis, Funding acquisition, Investigation, Methodology, Project administration, Resources, Software, Supervision, Validation, Visualization, Writing–review and editing. XJX: Conceptualization, Data curation, Formal Analysis, Funding acquisition, Investigation, Methodology, Project administration, Resources, Software, Supervision, Validation, Visualization, Writing–review and editing.

Funding

The author(s) declare that financial support was received for the research, authorship, and/or publication of this article. This work is jointly supported by the National Natural Science Foundation of China 42174199, Guangdong Basic and Applied Basic Research Foundation 2023B1515040021, Shenzhen Technology Project JCYJ20210324121210027 and RCJC20210609104422048, and Shenzhen Key Laboratory Launching Project No. ZDSYS20210702140800001.

Conflict of interest

The authors declare that the research was conducted in the absence of any commercial or financial relationships that could be construed as a potential conflict of interest.

Publisher's note

All claims expressed in this article are solely those of the authors and do not necessarily represent those of their affiliated organizations, or those of the publisher, the editors and the reviewers. Any product that may be evaluated in this article, or claim that may be made by its manufacturer, is not guaranteed or endorsed by the publisher.

Supplementary material

The Supplementary Material for this article can be found online at: https://www.frontiersin.org/articles/10.3389/fphy.2024.1439949/full#supplementary-material

References

1. Titov VS. Generalized squashing factors for covariant description of magnetic connectivity in the solar corona. *Astrophys J* (2007) 660:863–73. doi:10.1086/512671

2. Vytenis V. Theoretical models of magnetic field line merging. *Rev Geophys And Space Phys* (1975) 13:303–36. doi:10.1029/RG013i001p00303

3. Giovanelli RG. A theory of chromospheric flares. *Nature* (1946) 158:81–2. doi:10.1038/158081a0

4. Russell CT, Elphic RC. ISEE observations of flux-transfer events at the dayside magnetopause. *Geophys Res Lett* (1979) 6(1):33–6. doi:10.1029/GL006i001p00033

5. Lee LC, Fu ZF. A theory of magnetic-flux transfer at the earths magnetopause. *Geophys Res Lett* (1985) 12(2):105–8. doi:10.1029/GL012i002p00105

6. Parker EN. Sweet's mechanism for merging magnetic fields in conducting fluids. *J Geophys Res* (1957) 62:509–20. doi:10.1029/JZ062i004p00509

7. Sweet PA. The neutral point theory of solar flares. In: *Symposium - international astronomical Union* (1958). England: University of London Observatory, 123–34.

8. Petschek HE. Magnetic field Annihilation. In: The Physics of Solar Flares, Proceedings of the AAS-NASA Symposium; 28-30 October, 1963; Greenbelt, MD: Goddard Space Flight Center. Editor Wilmot NH Washington, DC, 425 (1964).

9. Birn J, Priest ER. *Reconnection of magnetic fields: magnetohydrodynamics and collisionless theory and observations*. Cambridge: Cambridge University Press (2007).

10. Burch JL, Torbert RB, Phan TD, Chen L-J, Moore TE, Ergun RE, et al. Electron-scale measurements of magnetic reconnection in space. *Science*. 2016;352(6290): aaf2939. doi:10.1126/science.aaf2939

11. Vilmer N, Mackinnon AL, Hurford GJ. Properties of energetic ions in the solar atmosphere from γ-ray and neutron observations. *Space Sci Rev* (2011) 159(1-4): 167–224. doi:10.1007/s11214-010-9728-x

12. Benz AO. Flare observations. *Living Rev Solar Phys* (2017) 14(1):2. doi:10.1007/s41116-016-0004-3

13. Phan TD, Bale SD, Eastwood JP, Lavraud B, Drake JF, Oieroset M, et al. Parker solar probe *in situ* observations of magnetic reconnection exhausts during encounter 1. *The Astrophysical J Suppl Ser* (2020) 246(2):34. doi:10.3847/1538-4365/ab55ee

14. Fujimoto K. Multi-scale kinetic simulation of magnetic reconnection with dynamically adaptive meshes. *Front Phys* (2018) 6. doi:10.3389/fphy.2018.00119

15. Sisti M, Faganello M, Califano F, Lavraud B. Satellite data based 3D simulation of kelvin helmholtz instability and induced magnetic reconnection at the earth's magnetopause. *Geophys Res Lett* (2019) 46(21):11597–605. doi:10.1029/2019gl083282

16. Lapenta G, Markidis S, Goldman MV, Newman DL. Secondary reconnection sites in reconnection-generated flux ropes and reconnection fronts. *Nat Phys* (2015) 11(8): 690–5. doi:10.1038/nphys3406

17. Pezzi O, Liang H, Juno JL, Cassak PA, Vásconez CL, Sorriso-Valvo L, et al. Dissipation measures in weakly collisional plasmas. *Monthly Notices R Astronomical Soc* (2021) 505(4):4857–73. doi:10.1093/mnras/stab1516

18. Rosenberg MJ, Li CK, Fox W, Igumenshchev I, Seguin FH, Town RP, et al. A laboratory study of asymmetric magnetic reconnection in strongly driven plasmas. *Nat Commun* (2015) 6:6190. doi:10.1038/ncomms7190

19. Bolaños S, Sladkov A, Smets R, Chen SN, Grisollet A, Filippov E, et al. Laboratory evidence of magnetic reconnection hampered in obliquely interacting flux tubes. *Nat Commun* (2022) 13(1):6426. doi:10.1038/s41467-022-33813-9

20. Yamada M, Chen LJ, Yoo J, Wang S, Fox W, Jara-Almonte J, et al. The two-fluid dynamics and energetics of the asymmetric magnetic reconnection in laboratory and space plasmas. *Nat Commun* (2018) 9(1):5223. doi:10.1038/s41467-018-07680-2

21. Angus JR, Link AJ, Schmidt AE. 1D kinetic study of pinch formation in a dense plasma focus: transition from collisional to collisionless regimes. *Phys Plasmas* (2021) 28(1):1–5. doi:10.1063/5.0028988

22. Hesse M, Schindler K. A theoretical foundation of general magnetic reconnection. *J Geophys Res* (1988) 93(A6):5559–67. doi:10.1029/JA093iA06p05559

23. Schindler K, Hesse M, Birn J. General magnetic reconnection, parallel electric fields, and helicity. *J Geophys Res* (1988) 93(A6):5547–57. doi:10.1029/JA093iA06p05547

24. Hantao J. Major scientific challenges and opportunities in understanding magnetic reconnection and related explosive phenomena in magnetized plasmas. *White Paper Plasma 2020 Decadal Surv* (2019) 1–4. doi:10.48550/arXiv.2004.00079

25. Pontin DI, Priest ER. Magnetic reconnection: MHD theory and modelling. *Living Rev Solar Phys* (2022) 19(1):1. doi:10.1007/s41116-022-00032-9

26. Hornig G, Priest E. Evolution of magnetic flux in an isolated reconnection process. *Phys Plasmas* (2003) 10:2712–21. doi:10.1063/1.1580120

27. Pontin DI, Hornig G, Priest ER. Kinematic reconnection at a magnetic null point: spine-aligned current. *Geophys and Astrophysical Fluid Dyn* (2004) 98(5):407–28. doi:10.1080/0309192042000272324

28. Pontin DI. Three-dimensional magnetic reconnection regimes: a review. *Adv Space Res* (2011) 47(9):1508–22. doi:10.1016/j.asr.2010.12.022

29. Titov VS, Tassi E, Hornig G. Exact solutions for steady reconnective annihilation revisited. *Phys Plasmas* (2004) 11(10):4662–71. doi:10.1063/1.1789159

30. Tassi E. Analytical solutions for reconnective magnetic annihilation. In: *AIP Conference Proceedings2004*. 76–9.

31. Mellor C, Priest ER, Titov VS. Exact solutions for spine reconnective magnetic annihilation. *Geophys Astrophysical Fluid Dyn* (2002) 96(2):153–71. doi:10.1080/03091920290004470

32. Priest ER, Sonnerup BUO. Theories of magnetic field annihilation. *Geophys J R Astronomical Soc* (1975) 41:405–13. doi:10.1111/j.1365-246X.1975.tb01623.x

33. Parker EN. Comments on the reconnexion rate of magnetic fields. *J Plasma Phys* (1973) 9(1):49–63. doi:10.1017/s0022377800007327

34. Sonnerup BUO, Priest ER. Resistive MHD stagnation-point flows at a current sheet. *J Plasma Phys* (1975) 14:283–94. doi:10.1017/S0022377800009570

35. Craig IJD, McClymont AN. Dynamic magnetic reconnection at an x-type neutral point. *Astrophys J* (1991) 371(1):L41–L4. doi:10.1086/185997

36. Craig IJD, Fabling RB, Henton SM, Rickard GJ. An exact solution for steady state magnetic reconnection in three dimensions. *Astrophysical J Lett* (1995) 455(2):L197–9. doi:10.1086/309822

37. Craig IJD, Henton SM. Exact solutions for steady-state incompressible magnetic reconnection. *Astrophys J* (1995) 450:280–8. doi:10.1086/176139

38. Craig IJD, Fabling RB. Exact solutions for steady-state, spine, and fan magnetic reconnection. *Astrophys J* (1996) 462:969–76. doi:10.1086/177210

39. Yang WH. Self-similar evolution of magnetized plasmas .2. nonequilibrium solutions and hubbles expansion. *Astrophys J* (1994) 425(2):439–41. doi:10.1086/173998

40. Priest ER, Hornig G, Pontin DI. On the nature of three-dimensional magnetic reconnection. *J Geophys Res* (2003) 108(A7). doi:10.1029/2002ja009812

41. Hornig G, Schindler K. Magnetic topology and the problem of its invariant definition. *Phys Plasmas* (1996) 3(3):781–91. doi:10.1063/1.871778

42. Pontin DI, Hornig G, Priest ER. Kinematic reconnection at a magnetic null point: fan-aligned current. *Geophys and Astrophysical Fluid Dyn* (2005) 99(1):77–93. doi:10.1080/03091920512331328071

43. Wilmot-Smith A, Hornig G, Priest E. Dynamic non-null magnetic reconnection in three dimensions. I. Particular solutions. *Proc R Soc A: Math Phys Eng Sci* (2006) 462(2074):2877–95. doi:10.1098/rspa.2006.1697

44. Wilmot-Smith AL, Priest ER. Flux tube disconnection: an example of three-dimensional reconnection. *Phys Plasmas* (2007) 14(102903):1–9. doi:10.1063/1.2783257

45. Wilmot-Smith AL, Hornig G, Priest ER. Dynamic non-null magnetic reconnection in three dimensions–II: composite solutions. *Geophys and Astrophysical Fluid Dyn* (2009) 103(6):515–34. doi:10.1080/03091920903164294

46. Wilmot-Smith AL, Hornig G. A time-dependent model for magnetic reconnection in the presence of a separator. *The Astrophysical J* (2011) 740(2):89. doi:10.1088/0004-637x/740/2/89

47. McMahon LC. Visco-resistive length scale in flux pile-up and series solutions for magnetic reconnection. *Phys Plasmas* (2017) 24(5). doi:10.1063/1.4982663

48. Priest ER, Titov VS, Grundy RE, Hood AW. Exact solutions for reconnective magnetic annihilation. *Proc Math Phys Eng Sci* (2000) 456:1821–49. doi:10.1098/rspa.2000.0588

49. Pritchett PL. The onset of magnetic reconnection in three dimensions. *Phys Plasmas* (2013) 20(8). doi:10.1063/1.4817961

50. Luo L, Xu X, Song L, Zhou M, Zhou Z, Man H, et al. The current tension electric field in the generalized Ohm's law. *Geophys Res Lett* (2024) 51(4). doi:10.1029/2023gl107191

51. Anderson C, Priest ER. Time-dependent magnetic annihilation at a stagnation point. *J Geophys Res Space Phys* (1993) 98(A11):19395–407. doi:10.1029/92ja02723

52. Wilmot-Smith AL, Priest ER, Hornig G. Magnetic diffusion and the motion of field lines. *Geophys and Astrophysical Fluid Dyn* (2005) 99(2):177–97. doi:10.1080/03091920500044808

53. Chen Y, Wang Y, Wei F, Feng X, Zhou Z, Wang B, et al. Analytical solutions for time-dependent kinematic three-dimensional magnetic reconnection. *PLOS ONE* (2023) 18(5):e0286138. doi:10.1371/journal.pone.0286138

54. Davis MS, Phan TD, Gosling JT, Skoug RM. Detection of oppositely directed reconnection jets in a solar wind current sheet. *Geophys Res Lett* (2006) 33(19):L19102. doi:10.1029/2006gl026735

55. Phan TD, Gosling JT, Davis MS, Skoug RM, Oieroset M, Lin RP, et al. A magnetic reconnection X-line extending more than 390 Earth radii in the solar wind. *Nature* (2006) 439(7073):175–8. doi:10.1038/nature04393

56. Wang Y, Wei FS, Feng XS, Zhang SH, Zuo PB, Sun TR. Energetic electrons associated with magnetic reconnection in the magnetic cloud boundary layer. *Phys Rev Lett* (2010) 105(19):195007. doi:10.1103/PhysRevLett.105.195007

57. Gosling JT. Magnetic reconnection in the solar wind. *Space Sci Rev* (2012) 172(1-4):187–200. doi:10.1007/s11214-011-9747-2

58. Gosling JT, Eriksson S, Blush LM, Phan TD, Luhmann JG, McComas DJ, et al. Five spacecraft observations of oppositely directed exhaust jets from a magnetic reconnection X-line extending $>4.26 \times 10^6$ km in the solar wind at 1 AU. *Geophys Res Lett* (2007) 34(20):L20108. doi:10.1029/2007gl031492

59. Gosling JT, Eriksson S, Schwenn R. Petschek-type magnetic reconnection exhausts in the solar wind well inside 1 AU: helios. *J Geophys Res Space Phys* (2006) 111(A10). doi:10.1029/2006JA011863

60. Gosling JT, Eriksson S, Skoug RM, McComas DJ, Forsyth RJ. Petschek-type reconnection exhausts in the solar wind well beyond 1 AU: ulysses. *The Astrophysical J* (2006) 644(1):613–21. doi:10.1086/503544

61. Gosling JT, Phan TD, Lin RP, Szabo A. Prevalence of magnetic reconnection at small field shear angles in the solar wind. *Geophys Res Lett* (2007) 34(15). doi:10.1029/2007gl030706

62. Li T, Priest E, Guo R. Three-dimensional magnetic reconnection in astrophysical plasmas. *Proc R Soc A: Math Phys Eng Sci* (2021) 477(2249). doi:10.1098/rspa.2020.0949

63. Lazarian A, Vishniac ET. Reconnection in a weakly stochastic field. *The Astrophysical J* (1999) 517:700–18. doi:10.1086/307233

64. Eyink G, Vishniac E, Lalescu C, Aluie H, Kanov K, Bürger K, et al. Flux-freezing breakdown in high-conductivity magnetohydrodynamic turbulence. *Nature* (2013) 497(7450):466–9. doi:10.1038/nature12128

65. Kowal G, Lazarian A, Vishniac ET, Otmianowska-Mazur K. Numerical tests of fast reconnection in weakly stochastic magnetic fields. *The Astrophysical J* (2009) 700(1):63–85. doi:10.1088/0004-637x/700/1/63

66. Muñoz PA, Büchner J. Kinetic turbulence in fast three-dimensional collisionless guide-field magnetic reconnection. *Phys Rev E* (2018) 98(4):043205. doi:10.1103/physreve.98.043205

67. Zharkova V, Xia Q. Kinetic plasma turbulence generated in a 3D current sheet with magnetic islands. *Front Astron Space Sci* (2021) 8. doi:10.3389/fspas.2021.665998

68. Kowal G, Falceta-Gonçalves DA, Lazarian A, Vishniac ET. Statistics of reconnection-driven turbulence. *The Astrophysical J* (2017) 838(2):91. doi:10.3847/1538-4357/aa6001

frontiers | Frontiers in Physics

TYPE Original Research
PUBLISHED 26 September 2024
DOI 10.3389/fphy.2024.1446646

Check for updates

OPEN ACCESS

EDITED BY
Andrey Samsonov,
University College London, United Kingdom

REVIEWED BY
Anton Artemyev,
University of California, Los Angeles, United States
Nikolai Erkaev,
Institute of Computational Modelling SB RAS, Russia

*CORRESPONDENCE
Guoqiang Wang,
wanggq@hit.edu.cn
Pingbing Zuo,
zuopb@hit.edu.cn

RECEIVED 10 June 2024
ACCEPTED 13 September 2024
PUBLISHED 26 September 2024

CITATION
Wei J, Wang G and Zuo P (2024) Study of the characteristics of electron firehose unstable conditions in the terrestrial magnetotail plasma sheet.
Front. Phys. 12:1446646.
doi: 10.3389/fphy.2024.1446646

COPYRIGHT
© 2024 Wei, Wang and Zuo. This is an open-access article distributed under the terms of the Creative Commons Attribution License (CC BY). The use, distribution or reproduction in other forums is permitted, provided the original author(s) and the copyright owner(s) are credited and that the original publication in this journal is cited, in accordance with accepted academic practice. No use, distribution or reproduction is permitted which does not comply with these terms.

Study of the characteristics of electron firehose unstable conditions in the terrestrial magnetotail plasma sheet

Jiayun Wei[1,2,3], Guoqiang Wang[1,2,4]* and Pingbing Zuo[1,2,3]*

[1]Institute of Space Science and Applied Technology, Harbin Institute of Technology, Shenzhen, China, [2]Shenzhen Key Laboratory of Numerical Prediction for Space Storm, Institute of Space Science and Applied Technology, Harbin Institute of Technology, Shenzhen, China, [3]Key Laboratory of Solar Activity and Space Weather, National Space Science Center, Chinese Academy of Sciences, Beijing, China, [4]Mengcheng National Geophysical Observatory, University of Science and Technology of China (or Anhui Earthquake Agency), Mengcheng, China

Electron firehose instabilities can be excited at dipolarization fronts and in the magnetic reconnection outflow in the terrestrial magnetotail, but their occurrence rate in the plasma sheet is unclear. Here, we investigate the characteristics of electron firehose unstable conditions in the magnetotail plasma sheet based on observations of the Magnetospheric Multiscale mission. We find an Alfvénic magnetic field fluctuation accompanied by a strong field-aligned current during a flapping motion. This fluctuation occurs where the local plasma is electron firehose unstable, indicating that the electron firehose instability in the plasma sheet can occur in the region besides dipolarization fronts and magnetic reconnection outflow. We statistically find that the local plasma near the neutral sheet has a small probability with the maximum value <1.4% to be electron firehose unstable, which mainly occurs in the central plasma sheet with $B_{XY}/B_L < 0.3$. The maximum probability of $T_{ef} > 0$ (electron firehose unstable condition) is ~1.36% (1.32%) at $B_{XY}/B_L \approx 0.05$ (0.15) during fast (non-fast) flows. During fast flows, the plasma near the neutral sheet tends to have a higher probability of $T_{ef} > 0$ when the local V_T is larger. During non-fast flows, the plasma near the neutral sheet tends to have a higher probability of $T_{ef} > 0$ when T_e is larger. The probability of $T_{ef} > 0$ shows a dawn-dusk asymmetry during fast flows and non-fast flows. In addition, the probability of $T_{ef} > 0$ during fast flows tends to be larger when the ambient B_Z is weak, which shows opposite characteristics during non-fast flows. These findings help to assess the importance of the role of electron firehose instabilities in the magnetotail plasma sheet.

KEYWORDS

electron firehose unstable, magnetic field fluctuation, plasma sheet, fast flow, non-fast flow

1 Introduction

Fast flows are essential to the transport of mass, magnetic flux, and energy in the terrestrial magnetotail [1, 2]. They might originate from magnetic reconnections [3, 4] or interchange instabilities [5]. Temperature anisotropies can be caused during fast flows [6, 7], which are able to provide free energy to excite various instabilities [8–11]. For example, ion firehose instabilities can be driven when $T_{i,||} > T_{i,\perp}$, where $T_{i,||}$ and $T_{i,\perp}$ are the parallel

and perpendicular ion temperatures with respect to the ambient magnetic field [10, 11]. Such instabilities also exist in the solar wind [12–15] and the terrestrial magnetosheath [16, 17].

Ion firehose instabilities include parallel and oblique modes [10, 11, 18–20]. In the terrestrial magnetotail, parallel firehose instabilities are more likely to occur near the neutral sheet [21], and can generate Pi2-band (40–150 s) Alfvénic fluctuations during fast flows [22, 23]. [24] further found that the parallel firehose unstable condition can affect the wave power of the Pi1-band (10–40 s) and Pi2-band fluctuations during fast flows. The probability of the plasma being parallel firehose unstable condition tends to be larger for the faster flow, and is positively correlated with the wave power of the Pi1/2-band fluctuations [24]. Oblique firehose instabilities can generate compressional fluctuations, which are linear-polarized and have a zero frequency [10]. A flapping motion of the current sheet was reported to might originate from the oblique firehose instability during a fast flow [19]. Later, [25] statistically found that both probabilities of the fast flows accompanied by large-amplitude neutral sheet oscillations and the plasma being oblique firehose unstable condition near the neutral sheet tend to be larger for faster flows. In addition, the oblique firehose unstable condition can affect the period of these oscillations. These results support that oblique firehose instabilities are a generation mechanism of some flapping motions [25].

Similar to ions, electron firehose instabilities driven by electron temperature anisotropy also have two modes based on linear theory and 2D Particle-In-Cell (PIC) simulation [26–29]. The parallel electron firehose mode is a parallel propagation with respect to the ambient magnetic field and is non-resonant with respect to electrons, while the oblique electron firehose mode is characterized by a lower instability threshold and higher growth rate, which is a non-propagated and is resonant with both electrons and ions [27, 29]; [26, 30, 31]. In the magnetotail, electron firehose instabilities can be excited at dipolarization fronts [32] and in the magnetic reconnection outflow [31]. These instabilities are believed to lead the electron to isotropization by cooling (heating) the electron in the parallel (perpendicular) direction with respect to the ambient field [31–33]. The magnetotail current sheet can become thin to the sub-ion scale [34, 35]. Energy conversion processes take place in the thin current sheet, where the anisotropic electrons can excite electron-dominated instabilities [34–36]. The occurrence rate of electron firehose instabilities helps to evaluate their impact on electrons in the plasma sheet, however, it is still unclear.

In this study, we statistically investigate the electron firehose unstable conditions in the plasma sheet using the data obtained from the Magnetospheric Multiscale (MMS) mission. We first show a magnetic field fluctuation event associated with the electron firehose instability in the plasma sheet, then statistically analyze the probability of the plasma being electron firehose unstable during fast flows and non-fast flows.

2 Observation

The MMS spacecraft, launched on March 2015, consists of four identical probes with an interspacecraft distance of 10–400 km [37]. In the present study, only the magnetic field and plasma data of the MMS1 probe from 2015 to 2022 are used without other statement since the interspacecraft distances among the probes are very small compared with the thickness of the plasma sheet. The used magnetic field data with a resolution of 16 Hz are from the fluxgate magnetometer (FGM) instrument [38], and the used plasma moment data with a resolution of 4.5 s are from the Fast Plasma Investigation (FPI) instrument [39].

2.1 An event associated with electron firehose instabilities

Figure 1 shows the magnetic field and ion moments observed by MMS1 between 15:00 and 16:00 UT on 20 July 2017. The MMS1 probe is located at [-23.3, 7.0, 3.0] R_E in the geocentric solar magnetospheric (GSM) coordinate system at 15:30 UT. The ion beta β_i, ratio of the ion thermal pressure to the magnetic pressure, is >0.5 during the whole interval, indicating that this probe is in the plasma sheet [40]. Figure 1A shows that B_X had a maximum variation from ~9.4 nT to −21 nT in the interval of 15:21–15:33 UT, and the sign of B_X has one reversal. Such a large variation of B_X meets the expectation of a flapping motion of the current sheet [41–43]. At ~15:24:20 UT, B_X suddenly changes from ~4 nT to −4 nT with almost unchanged of B_T. Figure 1D, E show that $V_{i,X}$ and $V_{i,Y}$ are dominant and the maximum value of the total ion velocity is ~216.9 km/s, suggesting that the sudden change of B_X occurs during a weak fast flow.

Timing analysis can be used to determine the propagation velocity along the normal direction of a one-dimensional current sheet [44, 45]. Assuming that the magnetic field fluctuation between 15:24:10 and 15:24:30 UT is one-dimensional, its propagation velocity is ~39.7 km/s determined by timing analysis. Thus, its length is ~794 km along the normal direction. At this time, the local ion gyroradius ρ_i is ~1001.9 km estimated by using the ambient ion temperature (~2.37 keV) and B_T (~4.96 nT). Thus, the size of the magnetic field fluctuation is ~0.79 ρ_i along the normal direction, indicating that this fluctuation is sub-ion scale.

Figure 2 shows the electron moments in the interval of 15:23–15:26 UT. B_X changes up to ~9.3 nT between 15:24:10 and 15:24:30 UT, while B_T is almost a constant, indicating that this fluctuation has an Alfvénic characteristic. The electron number density, velocities, and perpendicular temperature ($T_{e,\perp}$) have no significant change during the whole interval in Figure 2, while the parallel electron temperature ($T_{e,||}$) has a significant change. $T_{e,||}$ is > $T_{e,\perp}$ between 15:23 and 15:25 UT. The electron temperature anisotropy can excite electron firehose instabilities [27, 31, 33]. Based on the linear dispersion theory, the threshold of electron firehose instabilities is derived to be $T_{ef} = \frac{T_{e,||}}{T_{e,\perp}} - \frac{1}{1-1.29/\beta_{e,||}^{0.97}}$ when the instability growth rate is larger than 0.001, which applies when the parallel electron beta $\beta_{e,||}$ is in the range of 2–25 [27, 31]. $T_{ef} > 0$ denotes that the local plasma is electron firehose unstable, which means that this condition is able to excite electron firehose instabilities [27, 31]. Figure 2G shows that T_{ef} is >0 during the magnetic field fluctuation between 15:24:06 and 15:24:38 UT, and is <0 outside this fluctuation, indicating that this fluctuation might be generated by the electron firehose instability.

Figure 3 shows the current density between 15:23 and 15:26 UT, which is calculated by the curlometer technique [46]. It is regarded as reliable when the ratio of $|\nabla\cdot B|$ to $|\nabla\times B|$ is <0.2 [43, 47]. Thus, the

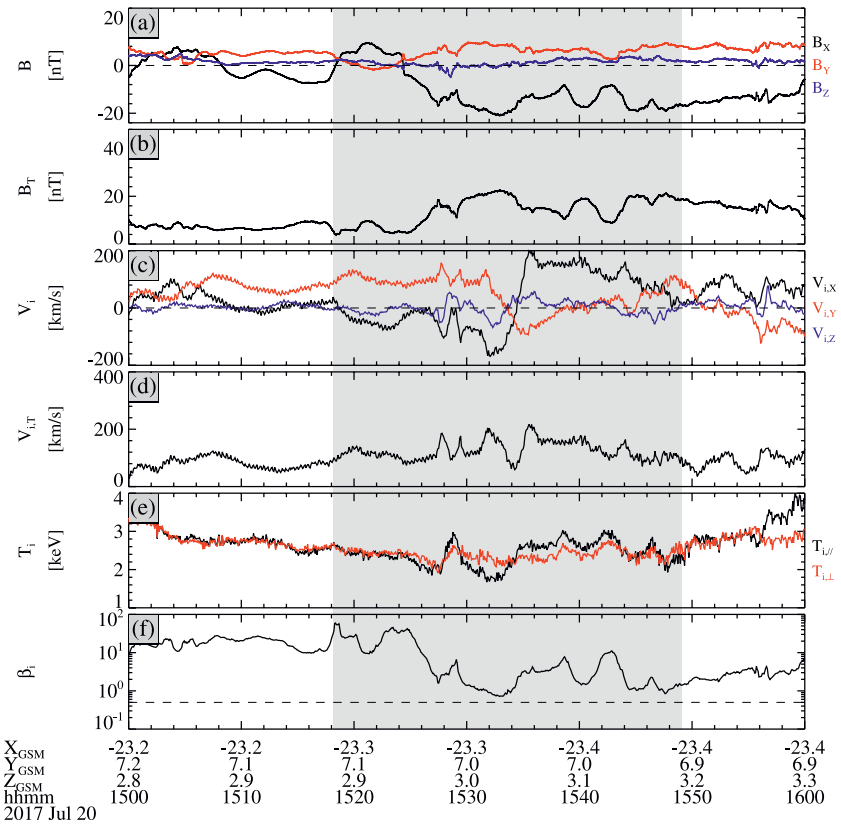

FIGURE 1
A fast flow event observed by MMS1 between 15:00 and 16:00 UT on 20 July 2017. From top to bottom: **(A)** the magnetic field in GSM, **(B)** the magnetic field strength, **(C)** ion velocities in GSM, **(D)** the total ion velocity, **(E)** the parallel (black) and perpendicular (red) ion temperatures, **(F)** ion beta. The gray region indicates the interval of a fast flow event.

current density is reliable in the interval 15:24:11.2–15:24:25.1 UT. The total current density tends to be larger with the maximum value of ~26.2 nA/m^2 when the MMS1 probe is closer to the neutral sheet. As shown in the shaded area, the parallel current density is dominant in this interval, indicating that the magnetic field fluctuation is accompanied by a strong field-aligned current. Field-aligned currents play a significant role in the process of the ionosphere-magnetosphere coupling [48–51]. In addition, electron firehose instabilities can cause the electron to be isotropic [31, 32]. To evaluate the importance of electron firehose instabilities in the plasma sheet, a question is raised, namely, what is the probability of the plasma being electron firehose unstable in the plasma sheet.

2.2 Electron firehose unstable conditions during fast flows and non-fast flows

To figure out the details of the electron firehose unstable conditions during fast flows and non-fast flows in the plasma sheet, we first select the fast flow events at $X_{GSM} < -10$ R_E and $|Y_{GSM}| < 12$ R_E using the following criteria, which are modified based on the selection criteria of bursty bulk flows proposed by Angelopoulos et al. [40]. A fast flow event is defined to be a segment of the continuous ion flow with a magnitude of $|\mathbf{V}_i| \geq 100$ km/s, during which $|\mathbf{V}_i|$ exceeds 150 km/s at least one sample. If two adjacent events are observed within 2 min, they are regarded to belong to the same fast flow event. In total, 5,675 fast flow events are selected.

Figure 4 shows the distribution of the data points in the space of ($\beta_{e,||}$, $T_{e,||}/T_{e,\perp}$) during the fast flows (a) and non-fast flows (b), where both the bin sizes of the logarithm of $\beta_{e,||}$ and $T_{e,||}/T_{e,\perp}$ are 0.02. About ~79.3% (84.8%) of the data points are observed at $T_{e,||}/T_{e,\perp} > 1$ during the fast flows (non-fast flows). The gray dashed line denotes the threshold of the electron firehose instability, i.e., $\frac{T_{e,||}}{T_{e,\perp}} = \frac{1}{1-1.29/\beta_{e,||}^{0.97}}$. The plasma is electron firehose unstable when the data points are above the dashed line. As shown in Figure 4, electrons have a very low probability of being firehose unstable, although the electrons with parallel temperature anisotropy dominate in the plasma sheet.

In the magnetotail, firehose instabilities are believed to be more likely to occur near the neutral sheet [21, 24, 52]. We consider the parameter B_{XY}/B_L as the relative distance away from the neutral sheet [53], where $B_{XY} = \sqrt{B_X^2 + B_Y^2}$, and B_L is the magnetic field strength in the magnetotail lobe determined by assuming that the lobe magnetic pressure is equal to the sum of the magnetic and ion thermal pressures in the plasma sheet.

Figure 5 shows the percentages of $2 \leq \beta_{e,||} \leq 25$ (a) and $T_{ef} > 0$ (b) at different values of $(B_X/|B_X|)\cdot B_{XY}/B_L$ with a step length of 0.05 during all the fast flows (black) and non-fast flows (orange). In Figure 5A, the percentage in each bin is determined by the data counts with $2 \leq \beta_{e,||} \leq 25$ divided by the total counts in that bin.

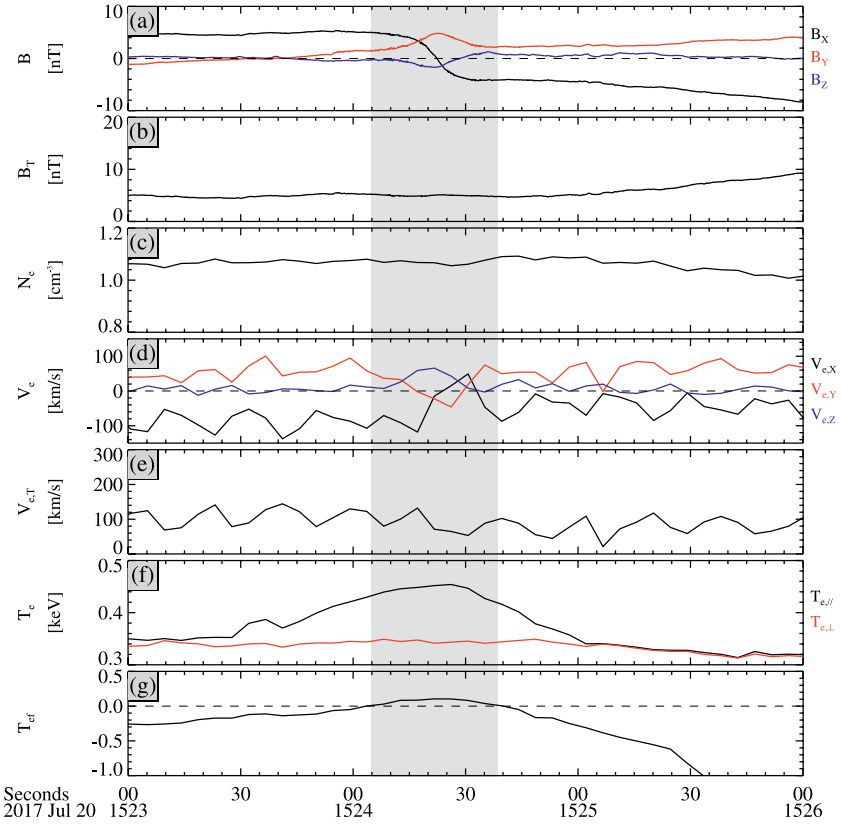

FIGURE 2
From top to bottom: **(A)** the magnetic field in GSM, **(B)** the magnetic field strength, **(C)** electron number density, **(D)** electron velocities in GSM, **(E)** the total electron velocity, **(F)** the parallel (blue) and perpendicular (red) electron temperatures, **(G)** the threshold of the electron firehose instability. The gray region indicates the interval of the magnetic field structure.

$(B_X/|B_X|)\cdot B_{XY}/B_L$ < (>) 0 denotes that the satellite is located on the south (north) side of the neutral sheet. One can find that the electrons with $2 \le \beta_{e,||} \le 25$ mainly occur in the region within $B_{XY}/B_L < 0.3$. The percentages of $2 \le \beta_{e,||} \le 25$ during the fast flows are approximately symmetrically distributed relative to $(B_X/|B_X|)\cdot B_{XY}/B_L = 0$, and have the maximum value at $B_{XY}/B_L \approx 0.15$ instead of $B_{XY}/B_L = 0$. The characteristics of the percentages of $2 \le \beta_{e,||} \le 25$ during the non-fast flows are similar to those during the fast flows. Since the threshold of the electron firehose instability T_{ef} $(= \frac{T_{e,||}}{T_{e,\perp}} - \frac{1}{1-1.29/\beta_{e,||}^{0.97}})$ is applicable under the condition of $2 \le \beta_{e,||} \le 25$ [27], we determine the probability of the plasma with $T_{ef} > 0$ by only considering the plasma under the condition of $2 \le \beta_{e,||} \le 25$ in our rest of paper.

Figure 5B shows that the percentages of $T_{ef} > 0$ during the fast flows (non-fast flows) have the maximum value at $B_{XY}/B_L \approx 0.05$ (0.15). In each bin, the percentage is determined by the data counts with $T_{ef} > 0$ and $2 \le \beta_{e,||} \le 25$ divided by the total counts with $2 \le \beta_{e,||} \le 25$ in that bin. The maximum percentage of $T_{ef} > 0$ during the fast flows is ~1.36%. And the plasma during the fast flows tends to have a higher probability of $T_{ef} > 0$ when closer to the neutral sheet. By contrast, the percentage of $T_{ef} > 0$ during the non-fast flows has the maximum value of ~1.32% at $B_{XY}/B_L \approx 0.15$.

Figure 6 shows the percentages of $T_{ef} > 0$ during the fast flows at different values of $(B_X/|B_X|)\cdot B_{XY}/B_L$ under different conditions of the local ion speed V_T. At $B_{XY}/B_L < 0.05$, the maximum percentages of $T_{ef} > 0$ are ~1.23%, 1.45%, and 1.86% when V_T is in the range of <100 km/s, 100–400 km/s, and >400 km/s, respectively, indicating that the plasma near the neutral sheet tends to have a slightly higher probability of being electron firehose unstable with the increase of the local V_T. The percentage of $T_{ef} > 0$ has the maximum value at $B_{XY}/B_L \approx 0.05$ when $V_T < 100$ km/s. Under the condition of the local $V_T > 400$ km/s, the percentage of $T_{ef} > 0$ has the maximum value at $B_{XY}/B_L \approx 0.1$. Obviously, the local V_T can affect the electron firehose unstable conditions during fast flows.

Figure 7 shows the percentages of $T_{ef} > 0$ during the fast flows (a) and non-fast flows (b) at different values of $(B_X/|B_X|)\cdot B_{XY}/B_L$ under different conditions of the electron number density N_e. Figure 7A shows that the percentage of $T_{ef} > 0$ has no significant change when N_e is in different range during the fast flows. As shown in Figure 7B, the maximum percentages of $T_{ef} > 0$ are ~2.58%, 1.07%, and 1.31% at $B_{XY}/B_L < 0.2$ when N_e is in the range of <0.2 cm^{-3}, 0.2–0.4 cm^{-3}, and >0.4 cm^{-3} during the non-fast flows, respectively. Under the condition of $N_e < 0.2$ cm^{-3}, the percentage of $T_{ef} > 0$ has the maximum value at $B_{XY}/B_L \approx 0.15$.

Figure 8 shows the percentages of $T_{ef} > 0$ during the fast flows (a) and non-fast flows (b) under different conditions of the electron temperature T_e. During the fast flows, the percentage of $T_{ef} > 0$ has no significant change when T_e is in the range of <0.8 keV, 0.8–1.4 keV, and >1.4 keV, respectively. During the non-fast flows, the maximum percentages of $T_{ef} > 0$ are ~0.97%, 1.51%, and 1.89% at $B_{XY}/B_L < 0.15$ when T_e is in the range of <0.8 keV,

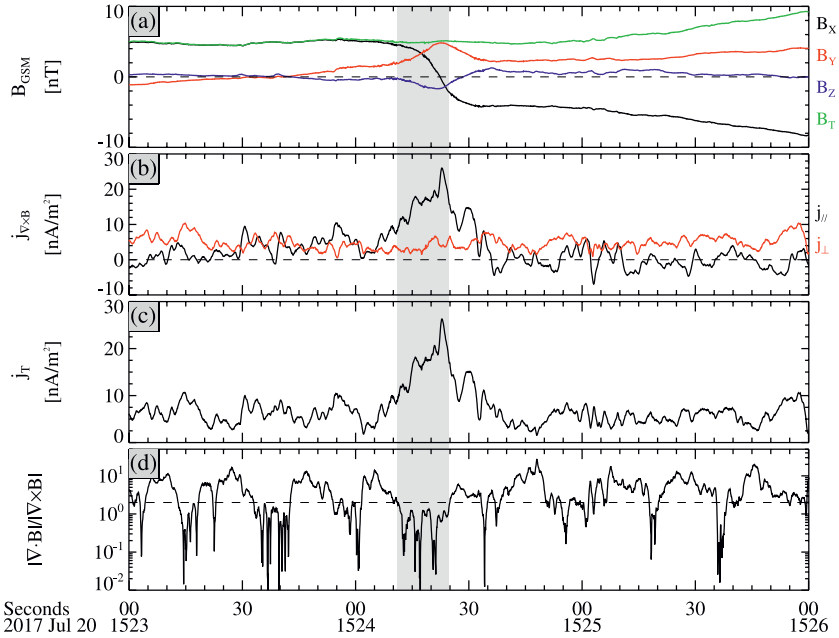

FIGURE 3
(A) The magnetic field in GSM, **(B)** the parallel and perpendicular components of the current density, **(C)** the total current density and **(D)** the ratio of |∇·B| to |∇×B| between 15:23 and 15:26 UT.

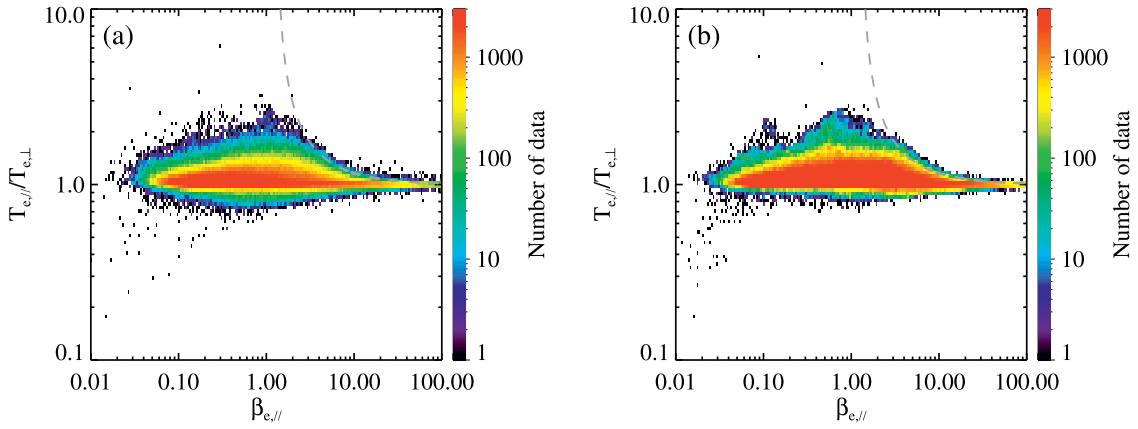

FIGURE 4
Number of data points in the space of ($\beta_{e,||}$, $T_{e,||}/T_{e,\perp}$) during the fast flows **(A)** and non-fast flows **(B)**. The color bar denotes the number of data points. The gray dashed line in each panel denotes $\frac{T_{e,||}}{T_{e,\perp}} = \frac{1}{1-1.29/\beta_{e,||}^{0.97}}$.

0.8–1.4 keV, and >1.4 keV, respectively, indicating that the plasma in this region tends to have a slightly higher probability of being electron firehose unstable with the increase of T_e. Under the condition of T_e > 0.8 keV, the percentage of T_{ef} > 0 has the maximum value at $B_{XY}/B_L \approx 0.15$.

According to the distribution of the percentages of T_{ef} > 0 in Figure 5, one can find that electron firehose instabilities are more likely to be excited at B_{XY}/B_L < 0.3 during the fast flows and non-fast flows. Next, we only analyze the characteristics of T_{ef} > 0 within B_{XY}/B_L < 0.3 in Figure 9 as well as in Figure 10. Figure 9A shows that the percentages of T_{ef} > 0 are ~0.65%, 0.90% and 0.66% (0.67%, 0.86% and 0.79%) during the fast flows (non-fast flows) at $-15 < X_{GSM} < -10$ R_E, $-20 < X_{GSM} < -15$ R_E and $-30 < X_{GSM} < -20$ R_E, respectively. The percentages of T_{ef} > 0 at $-20 < X_{GSM} < -15$ R_E is somewhat larger than that at $-15 < X_{GSM} < -10$ R_E and $-30 < X_{GSM} < -20$ R_E. Figure 9B shows the percentages of T_{ef} > 0 are ~0.80%, 0.74%, and 0.55% (0.87%, 1.38% and 0.38%) during the fast flows (non-fast flows) at $4 < Y_{GSM} < 12$ R_E, $-4 < Y_{GSM} < 4$ R_E and $-12 < Y_{GSM} < -4$ R_E, respectively. This suggests that both electron firehose unstable conditions during the fast flows and non-fast flows have a dawn-dusk asymmetry.

We regard the smoothed B_Z with a temporal window of 20 min as the ambient B_Z. Figure 10 shows that the percentages of T_{ef} > 0 during the fast flows (blue) are ~0.79% and 0.65% when the ambient B_Z is <3 nT and >3 nT, respectively. This indicates that the probability of

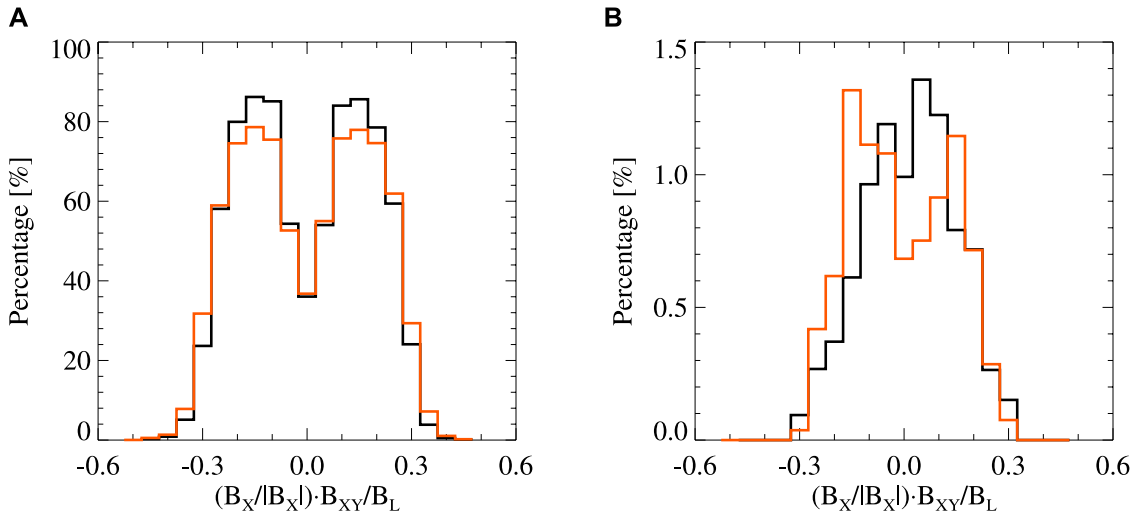

FIGURE 5
Percentages of $2 \le \beta_{e,||} \le 25$ **(A)** and $T_{ef} > 0$ **(B)** at different values of $(B_X/|B_X|)\cdot B_{XY}/B_L$ during all the fast flows (black) and non-fast flows (orange). The step length of $(B_X/|B_X|)\cdot B_{XY}/B_L$ is 0.05.

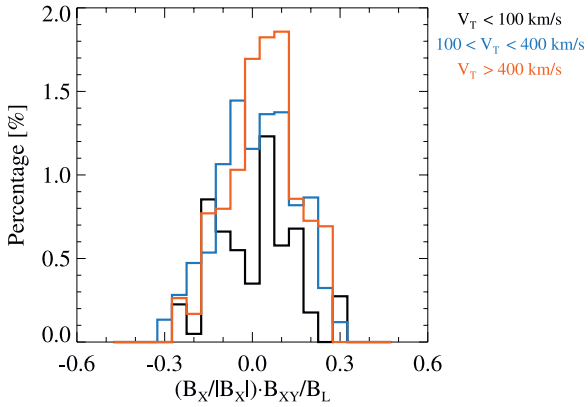

FIGURE 6
Percentages of $T_{ef} > 0$ at different values of $(B_X/|B_X|)\cdot B_{XY}/B_L$ during the fast flows when the local V_T is in the range of <100 km/s (black), 100–400 km/s (cyan), and >400 km/s (orange), respectively.

the electron firehose unstable condition is somewhat larger when the ambient B_Z is <3 nT than that when the ambient B_Z is >3 nT. One may expect that the waves generated by electron firehose instabilities during fast flows are more likely to occur during the stretch process of the plasma sheet than that during the dipolarization process. By contrast, the percentages of $T_{ef} > 0$ during the non-fast flows (orange) are ~0.68% and 0.88% when B_Z is <3 nT and >3 nT. This indicates that the ambient B_Z has an opposite effect on the electron firehose unstable condition during the non-fast flows.

3 Summary and discussion

Using the MMS1 data from 2015 to 2022, we investigate the electron firehose unstable condition in the magnetotail plasma sheet. Our findings are as follows:

a. A magnetic field fluctuation accompanied by a field-aligned current is found during a flapping motion. The fluctuation occurs near the neutral sheet, where the local plasma is electron firehose unstable, suggesting that this fluctuation might be generated by the electron firehose instability.
b. According to the theory of [27], the plasma being electron firehose unstable ($T_{ef} > 0$) mainly occurs within $B_{XY}/B_L < 0.3$. The probability of the plasma with $T_{ef} > 0$ tends to be larger with a maximum value of ~1.36% when closer to the neutral sheet during the fast flows. By contrast, the maximum probability is ~1.32% at $B_{XY}/B_L \approx 0.15$ during the non-fast flows.
c. During the fast flows, the plasma near the neutral sheet tends to have a higher probability of $T_{ef} > 0$ when the local V_T is larger. During non-fast flows, the plasma near the neutral sheet tends to have a higher probability of $T_{ef} > 0$ when T_e is larger.

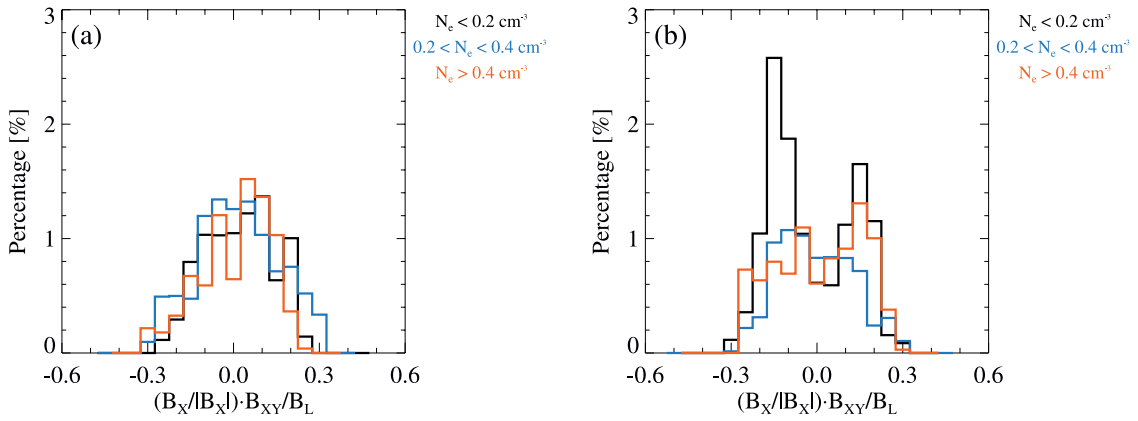

FIGURE 7
Percentages of $T_{ef} > 0$ at different values of $(B_X/|B_X|)\cdot B_{XY}/B_L$ during the fast flows **(A)** and non-fast flows **(B)** when N_e is in the range of <0.2 cm^{-3} (black), 0.2–0.4 cm^{-3} (cyan), and >0.4 cm^{-3} (orange), respectively.

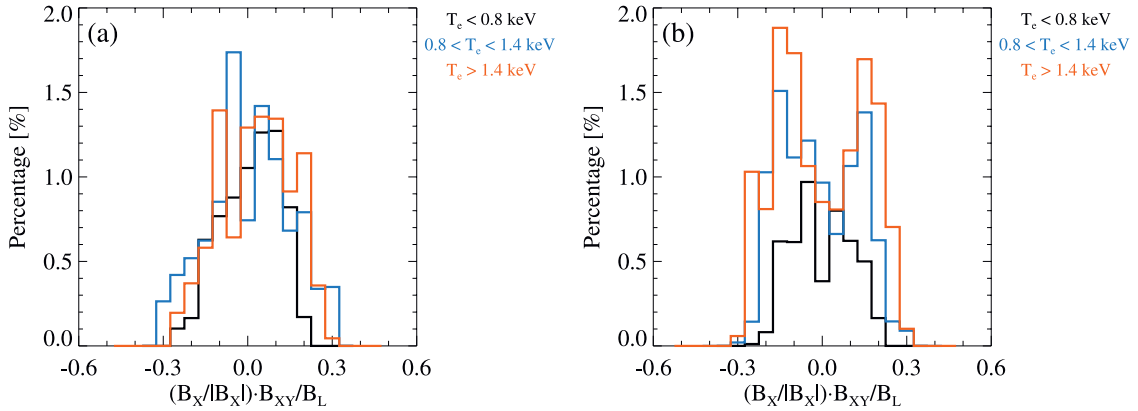

FIGURE 8
Percentages of $T_{ef} > 0$ at different values of $(B_X/|B_X|)\cdot B_{XY}/B_L$ during the fast flows **(A)** and non-fast flows **(B)** when T_e is in the range of < 0.8 keV (black), 0.8–1.4 keV (cyan), and >1.4 keV (orange), respectively.

d. Within $B_{XY}/B_L < 0.3$, the probability of $T_{ef} > 0$ shows a dawn-dusk asymmetry during the fast flows as well as during the non-fast flows. During the fast flows, the probability of $T_{ef} > 0$ is larger when the ambient B_Z is <3 nT than that when the ambient B_Z is >3 nT, which shows opposite characteristics during the non-fast flows.

Flapping motions are a large movement of the current sheet in the north-south direction [41, 43]. Field-aligned currents are reported to occur near the neutral sheet during flapping motions [54, 55]. Some flapping motions can create Pi2 (period: 40–150 s) pulsations on the ground via field-aligned currents flowing into the ionosphere along the magnetic field line [42, 56]. During flapping motions, the current carriers of the current density are dominant by electrons [55], and some field-aligned currents can be explained by the chaotic motion of electrons near the neutral sheet [51]. So far, the origin of the field-aligned current during flapping motions is still not fully understood. Figure 1 shows a magnetic field fluctuation observed at the neutral sheet during a flapping motion. We find that this fluctuation is sub-ion scale, and accompanied by a strong field-aligned current. This sub-ion scale fluctuation is Alfvénic, and occurs in the region where the local plasma is electron firehose unstable. These results suggest that this Alfvénic fluctuation is possibly generated by the electron firehose instability, which might be the origin of the field-aligned current during the flapping motion in Figure 1.

In the central thin current sheet, electrons have a weak temperature anisotropy with $T_{e,||}/T_{e,\perp} \approx 1.06$, and $T_{e,||}/T_{e,\perp}$ is mainly in the range of 1–1.2 [57]. Here, we mainly focus on the electrons with $2 \le \beta_{e,||} \le 25$, which mainly occur at $B_{XY}/B_L < 0.3$. The average $T_{e,||}/T_{e,\perp}$ of these electrons during the fast (non-fast) flows is ~1.07 (1.09), and ~61.6% (62.6%) of these electrons have the value of $T_{e,||}/T_{e,\perp}$ in the range of 1–1.2. Our findings suggest that the electrons at the central current sheet have a weak parallel temperature anisotropy regardless of whether the current sheet is thin or not. Although the probability of $T_{e,||}/T_{e,\perp} > 1$ for the electrons with $2 \le \beta_{e,||} \le 25$ is up to ~73.4% (78.9%) during the fast (non-fast) flows, these electrons have a very low probability of being firehose unstable (see Figure 4).

Fast flows can cause plasma temperature anisotropies to excite various instabilities, such as mirror instabilities and ion firehose instabilities [10, 11, 20]. Similar to ions, the plasma near the neutral

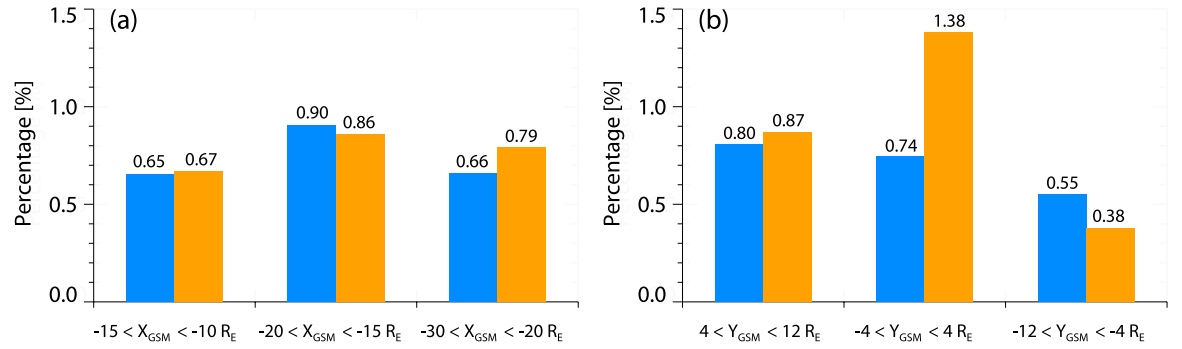

FIGURE 9
(A) Percentages of $T_{ef} > 0$ within $B_{XY}/B_L < 0.3$ during the fast flows (blue) and non-fast flows (orange) at $-15 < X_{GSM} < -10\ R_E$, $-20 < X_{GSM} < -15\ R_E$ and $-30 < X_{GSM} < -20\ R_E$, respectively. **(B)** Percentages of $T_{ef} > 0$ within $B_{XY}/B_L < 0.3$ during the fast flows (blue) and non-fast flows (orange) at $4 < Y_{GSM} < 12\ R_E$, $-4 < Y_{GSM} < 4\ R_E$ and $-12 < Y_{GSM} < -4\ R_E$, respectively.

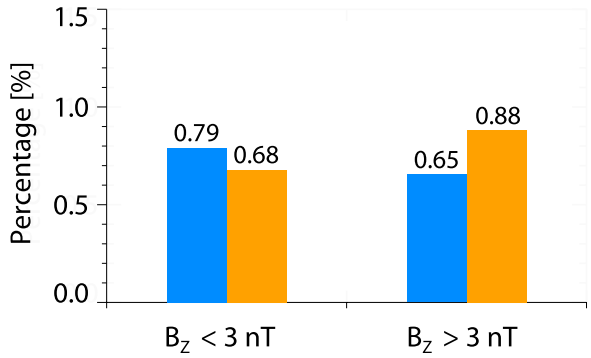

FIGURE 10
Percentages of $T_{ef} > 0$ under the condition of $B_{XY}/B_L < 0.3$ during the fast flows (blue) and non-fast flows (orange) when the ambient $B_Z < 3$ nT and $B_Z > 3$ nT, respectively.

sheet has the maximum probability of being electron firehose unstable overall during fast flows (see Figure 5). Thus, one may expect that instabilities in the plasma sheet are more likely to occur during fast flows. However, Figure 5B shows that the probability of the plasma being electron firehose unstable during the fast flows is very close to that during the non-fast flows. This suggests that fast flows have no significant contribution to the excitation of electron firehose instabilities in the plasma sheet. The plasma tends to have a slightly higher probability of being electron firehose unstable with the increase of T_e during the non-fast flows (see Figure 8). According to the definition of T_{ef}, T_{ef} tends to be larger with the increase of T_e if we assume that the other plasma parameters are constant. This might explain why the electrons during the non-fast flows tend to have a higher probability of being firehose unstable when T_e is larger.

Data availability statement

The original contributions presented in the study are included in the article/supplementary material, further inquiries can be directed to the corresponding author.

Author contributions

JW: Writing–original draft. GW: Writing–review and editing. PZ: Writing–review and editing.

Funding

The author(s) declare that financial support was received for the research, authorship, and/or publication of this article. This work was supported by Key-Area Research and Development Program of Guangdong Province (2020B0303020001), NSFC (42130204, 42241155), the Guangdong Basic and Applied Basic Research Foundation (Grant Nos 2019A1515011067, 2023B1515040021, 2022A1515011698, and 2023A1515030132), Shenzhen Natural Science Fund (the Stable Support Plan Program GXWD20201230155427003-20200822192703001), Shenzhen Science and Technology Research Program (JCYJ20210324121412034, JCYJ20210324121403009), National Key Research and Development Program of China (grant No. 2022YFF0503904), Shenzhen Key Laboratory Launching Project (ZDSYS20210702140800001), the Fundamental Research Funds for the Central Universities (HIT.OCEF.2022041), and Joint Open Fund of Mengcheng National Geophysical Observatory (No. MENGO-202315).

Acknowledgments

We acknowledge the data from the NASA MMS mission. We also acknowledge MMS project FGM and FPI teams.

Conflict of interest

The authors declare that the research was conducted in the absence of any commercial or financial relationships that could be construed as a potential conflict of interest.

Publisher's note

All claims expressed in this article are solely those of the authors and do not necessarily represent those of their affiliated organizations, or those of the publisher, the editors and the reviewers. Any product that may be evaluated in this article, or claim that may be made by its manufacturer, is not guaranteed or endorsed by the publisher.

References

1. Angelopoulos V, Coroniti FV, Kennel CF, Kivelson MG, Walker RJ, Russell CT, et al. (1997) Correction to Multipoint analysis of a bursty bulk flow event on April 11, 1985. *J Geophys Res Space Phys* 102(A1):211–2. doi:10.1029/96JA03217

2. Cao JB, Ma YD, Parks G, Reme H, Dandouras I, Nakamura R, et al. (2006) Joint observations by Cluster satellites of bursty bulk flows in the magnetotail. *J Geophys Res* 111(A4):A04206. doi:10.1029/2005JA011322

3. Machida S, Miyashita Y, Ieda A, Nishida A, Mukai T, Saito Y, et al. (1999). GEOTAIL observations of flow velocity and north-south magnetic field variations in the near and mid-distant tail associated with substorm onsets. *Geophys Res Lett* 26(6): 635–8. doi:10.1029/1999GL900030

4. Nagai T, Machida S. Magnetic reconnection in the near-Earth magnetotail (1998) *Geophys Monograph-American Geophys Union* 105:211–24. doi:10.1029/GM105p0211

5. Chen CX, Wolf RA (1993) Interpretation of high-speed flows in the plasma sheet. *J Geophys Res* 98(A12):21409–19. doi:10.1029/93JA02080

6. Kim H-S, Lee D-Y, Ohtani S-I, Lee E-S, Ahn B-H (2010) Some statistical properties of flow bursts in the magnetotail. *J Geophys Res Space Phys* 115(A12):A12229. doi:10.1029/2009JA015173

7. Runov A, Angelopoulos V, Sitnov M, Sergeev VA, Nakamura R, Nishimura Y, et al. (2011) Dipolarization fronts in the magnetotail plasma sheet. *Planet Space Sci* 59(7): 517–25. doi:10.1016/j.pss.2010.06.006

8. Gary SP, Fuselier SA, Anderson BJ (1993) Ion anisotropy instabilities in the magnetosheath. *J Geophys Res Space Phys* 98(A2):1481–8. doi:10.1029/92JA01844

9. Hasegawa A. Drift mirror instability in the magnetosphere. (1969) *Phys Fluids* 12(12):2642–50. doi:10.1063/1.1692407

10. Hellinger P, Matsumoto H. New kinetic instability: oblique Alfvén fire hose (2000) *J Geophys Res Space Phys* 105(A5):10519–26. doi:10.1029/1999JA000297

11. Quest KB, Shapiro VD. (1996) Evolution of the fire-hose instability: linear theory and wave-wave coupling. *J Geophys Res Space Phys* 101(A11):24457–69. doi:10.1029/96JA01534

12. Hellinger P, Trávníček P, Kasper JC, Lazarus AJ. (2006) Solar wind proton temperature anisotropy: linear theory and WIND/SWE observations. *Geophys Res Lett* 33(9):2006GL025925. doi:10.1029/2006GL025925

13. Hellinger P, Trávníček P. Parallel and oblique proton fire hose instabilities in the presence of alpha/proton drift: hybrid simulations (2006) *J Geophys Res Space Phys* 111(A1):2005JA011318. doi:10.1029/2005JA011318

14. Markovskii SA, Vasquez BJ. The effect of solar wind turbulence on parallel and oblique firehose instabilities (2022) *Astrophysical J* 924(2):111. doi:10.3847/1538-4357/ac3754

15. Opie S, Verscharen D, Chen CHK, Owen CJ, Isenberg PA (2022) Conditions for proton temperature anisotropy to drive instabilities in the solar wind. *Astrophysical J* 941(2):176. doi:10.3847/1538-4357/ac982f

16. DeWeese H, Maruca BA, Qudsi RA, Chasapis A, Pultrone M, Johnson E, et al. (2022) Alpha particle temperature anisotropy in earth's magnetosheath. *Astrophysical J* 941(1):12. doi:10.3847/1538-4357/ac9791

17. Maruca BA, Chasapis A, Gary SP, Bandyopadhyay R, Chhiber R, Parashar TN, et al. (2018) MMS observations of beta-dependent constraints on ion temperature anisotropy in earth's magnetosheath. *Astrophysical J* 866(1):25. doi:10.3847/1538-4357/aaddfb

18. Astfalk P, Jenko F. Parallel and oblique firehose instability thresholds for bi-kappa distributed protons (2016) *J Geophys Research-Space Phys* 121(4):2842–52. doi:10.1002/2015ja022267

19. Wang C, Liu Y, Xing X, Runov A, Artemyev A, Zhang X. An event study of simultaneous earthward and tailward reconnection exhaust flows in the earth's midtail (2020) *J Geophys Res Space Phys* 125(6):e2019JA027406. doi:10.1029/2019JA027406

20. Wu M, Volwerk M, Lu Q, Voeroes Z, Nakamura R, Zhang T. The proton temperature anisotropy associated with bursty bulk flows in the magnetotail (2013) *J Geophys Research-Space Phys* 118(8):4875–83. doi:10.1002/jgra.50451

21. Treumann RA, Baumjohann W. *Advanced space plasma physics*. London, United Kingdom: Imperial College Press (2001). p. 51–2.

22. Horton W, Xu BY, Wong HV (2004) Firehose driven magnetic fluctuations in the magnetosphere. *Geophys Res Lett* 31(6):L06807. doi:10.1029/2003GL018309

23. Horton W, Xu BY, Wong HV, Van Dam JW. Nonlinear dynamics of the firehose instability in a magnetic dipole geotail (2004) *J Geophys Research-Space Phys* 109(A9): A09216. doi:10.1029/2003JA010288

24. Wei J, Wang G, Zuo P. Statistical study of the relationship between pi1/2-band wave powers and firehose instability criterion during fast flows in the magnetotail plasma sheet (2022) *J Geophys Res Space Phys* 127(11):e2022JA030567. doi:10.1029/2022JA030567

25. Wei J, Wang G, Zuo P. Study of the relationship between large-amplitude neutral sheet oscillations and oblique firehose instabilities during fast flows in the terrestrial magnetotail (2024). *Phys Fluids* 36(5):056616. doi:10.1063/5.0206101

26. Camporeale E, Burgess D. Electron firehose instability: kinetic linear theory and two-dimensional particle-in-cell simulations (2008) *J Geophys Res* 113(A7):A07107. doi:10.1029/2008JA013043

27. Gary SP, Nishimura K (2003) Resonant electron firehose instability: particle-in-cell simulations. *Phys Plasmas* 10(9):3571–6. doi:10.1063/1.1590982

28. Hellinger P, Trávníček PM, Decyk VK, Schriver D (2014) Oblique electron fire hose instability: particle-in-cell simulations. *J Geophys Res Space Phys* 119(1):59–68. doi:10.1002/2013JA019227

29. Li X, Habbal SR. Electron kinetic firehose instability. *J Geophys Res* (2000) 105(A12):27377–85. doi:10.1029/2000JA000063

30. López RA, Micera A, Lazar M, Poedts S, Lapenta G, Zhukov AN, et al. (2022) Mixing the solar wind proton and electron scales. Theory and 2d-PIC simulations of firehose instability. *Astrophysical J* 930(2):158. doi:10.3847/1538-4357/ac66e4

31. Cozzani G, Khotyaintsev YV, Graham DB, André M (2023) Direct observations of electron firehose fluctuations in the magnetic reconnection outflow. *J Geophys Res Space Phys* 128(5):e2022JA031128. doi:10.1029/2022JA031128

32. Zhang X, Angelopoulos V, Artemyev AV, Liu J (2018) Whistler and electron firehose instability control of electron distributions in and around dipolarizing flux bundles. *Geophys Res Lett* 45(18):9380–9. doi:10.1029/2018GL079613

33. Artemyev AV, Angelopoulos V, Vasko IY, Petrukovich AA, Runov A, Saito Y, et al. (2020) Contribution of anisotropic electron current to the magnetotail current sheet as a function of location and plasma conditions. *J Geophys Res Space Phys* 125(1): e2019JA027251. doi:10.1029/2019JA027251

34. Nakamura R, Baumjohann W, Fujimoto M, Asano Y, Runov A, Owen CJ, et al. (2008) Cluster observations of an ion-scale current sheet in the magnetotail under the presence of a guide field. *J Geophys Res Space Phys* 113(A7):2007JA012760. doi:10.1029/2007JA012760

35. Zelenyi LM, Malova HV, Leonenko MV, Grigorenko EE, Popov VY (2022) Equilibrium configurations of super-thin current sheets in space plasma: characteristic scaling of multilayer structures. *J Geophys Res Space Phys* 127(11):e2022JA030881. doi:10.1029/2022JA030881

36. Kamaletdinov SR, Yushkov EV, Artemyev AV, Lukin AS, Vasko IY (2020) Superthin current sheets supported by anisotropic electrons. *Phys Plasmas* 27(8): 082904. doi:10.1063/5.0018063

37. Burch JL, Moore TE, Torbert RB, Giles BL (2016) Magnetospheric Multiscale overview and science objectives. *Space Sci Rev* 199(1–4):5–21. doi:10.1007/s11214-015-0164-9

38. Russell CT, Anderson BJ, Baumjohann W, Bromund KR, Dearborn D, Fischer D, et al. (2016) The magnetospheric Multiscale magnetometers. *Space Sci Rev* 199(1–4): 189–256. doi:10.1007/s11214-014-0057-3

39. Pollock C, Moore T, Jacques A, Burch J, Gliese U, Saito Y, et al. (2016) Fast plasma investigation for magnetospheric Multiscale. *Space Sci Rev* 199(1–4):331–406. doi:10.1007/s11214-016-0245-4

40. Angelopoulos V, Kennel CF, Coroniti FV, Pellat R, Kivelson MG, Walker RJ, et al. (1994) Statistical characteristics of bursty bulk flow events. *J Geophys Res* 99(A11): 21257–80. doi:10.1029/94JA01263

41. Zhang TL, Baumjohann W, Nakamura R, Balogh A, Glassmeier K -H (2002) A wavy twisted neutral sheet observed by CLUSTER. *Geophys Res Lett* 29(19) doi:10.1029/2002GL015544

42. Wang GQ, Volwerk M, Nakamura R, Boakes P, Zhang TL, Yoshikawa A, et al. (2014) Flapping current sheet with superposed waves seen in space and on the ground. *J Geophys Res Space Phys* 119(12). doi:10.1002/2014JA020526

43. Wang GQ, Zhang TL, Wu MY, Schmid D, Cao JB, Volwerk M (2019) Solar wind directional change triggering flapping motions of the current sheet: MMS observations. *Geophys Res Lett* 46(1):64–70. doi:10.1029/2018GL080023

44. Harvey CC. Spatial gradients and the volumetric tensor (1998) *ISSI Scientific Rep Ser* 1:307–22.

45. Sergeev V, Runov A, Baumjohann W, Nakamura R, Zhang TL, Balogh A, et al. (2004) Orientation and propagation of current sheet oscillations. *Geophys Res Lett* 31(5):L05807. doi:10.1029/2003GL019346

46. Dunlop MW, Balogh A, Glassmeier K-H, Robert P (2002) Four-point cluster application of magnetic field analysis tools: the curlometer. *J Geophys Res* 107(A11): 1384. doi:10.1029/2001JA005088

47. Wang GQ, Volwerk M, Zhang TL, Schmid D, Yoshikawa A (2017) High-latitude Pi2 pulsations associated with kink-like neutral sheet oscillations. *J Geophys Res Space Phys* 122(3):2889–99. doi:10.1002/2016JA023370

48. Kaufmann RL, Paterson WR, Frank LA. Magnetization of the plasma sheet (2004) *J Geophys Res* 109(A9). doi:10.1029/2003ja010148

49. Keiling A, Takahashi K. Review of Pi2 models. *Space Sci Rev* (2011) 161(1–4): 63–148. doi:10.1007/s11214-011-9818-4

50. Milan SE, Clausen LBN, Coxon JC, Carter JA, Walach M-T, Laundal K, et al. (2017) Overview of solar wind-magnetosphere-ionosphere-atmosphere coupling and the generation of magnetospheric currents. *Space Sci Rev* 206(1–4):547–73. doi:10.1007/s11214-017-0333-0

51. Wang GQ, Zhang TL, Wu MY, Xiao SD, Wang G, Chen YQ, et al. (2021) Field-aligned currents originating from the chaotic motion of electrons in the tilted current sheet: MMS observations. *Geophys Res Lett* 48(9). doi:10.1029/2020GL088841

52. Hietala H, Drake JF, Phan TD, Eastwood JP, McFadden JP (2015) Ion temperature anisotropy across a magnetotail reconnection jet. *Geophys Res Lett* 42(18):7239–47. doi:10.1002/2015GL065168

53. Xiao S, Zhang T, Wang G, Volwerk M, Ge Y, Schmid D, et al. (2017) Occurrence rate of dipolarization fronts in the plasma sheet: cluster observations. *Ann Geophysicae* 35(4):1015–22. doi:10.5194/angeo-35-1015-2017

54. Shen C, Rong ZJ, Li X, Dunlop M, Liu ZX, Malova HV, et al. (2008) Magnetic configurations of the tilted current sheets in magnetotail. *Ann Geophysicae* 26(11): 3525–43. doi:10.5194/angeo-26-3525-2008

55. Vasko IY, Artemyev AV, Petrukovich AA, Nakamura R, Zelenyi LM (2014) The structure of strongly tilted current sheets in the Earth magnetotail. *Ann Geophysicae* 32(2):133–46. doi:10.5194/angeo-32-133-2014

56. Sergeev V, Angelopoulos V, Carlson C, Sutcliffe P (1998) Current sheet measurements within a flapping plasma sheet. *J Geophys Research-Space Phys* 103(A5):9177–87. doi:10.1029/97ja02093

57. Zhang Z, Lu S, Lu Q, Wang R, Zhan C, Li X, et al. (2024) Statistical survey of thin current sheets in earth's magnetotail: MMS observations. *J Geophys Res Space Phys* 129(5):e2024JA032575. doi:10.1029/2024JA032575

frontiers | Frontiers in Astronomy and Space Sciences

TYPE Original Research
PUBLISHED 19 December 2024
DOI 10.3389/fspas.2024.1520141

Check for updates

OPEN ACCESS

EDITED BY
Boyi Wang,
Harbin Institute of Technology, China

REVIEWED BY
Alexei V. Dmitriev,
Lomonosov Moscow State University, Russia
Kun Zhang,
University of California, Los Angeles, United States

*CORRESPONDENCE
Xingran Chen,
chenxingran@must.edu.mo

RECEIVED 30 October 2024
ACCEPTED 20 November 2024
PUBLISHED 19 December 2024

CITATION
Chen X, Lu X, Zong Q, Zhang H, Liu Y and Zhou X (2024) Shock-induced radiation belt dynamics: simultaneous observations of "one-kick" acceleration and ultralow frequency modulation.
Front. Astron. Space Sci. 11:1520141.
doi: 10.3389/fspas.2024.1520141

COPYRIGHT
© 2024 Chen, Lu, Zong, Zhang, Liu and Zhou. This is an open-access article distributed under the terms of the Creative Commons Attribution License (CC BY). The use, distribution or reproduction in other forums is permitted, provided the original author(s) and the copyright owner(s) are credited and that the original publication in this journal is cited, in accordance with accepted academic practice. No use, distribution or reproduction is permitted which does not comply with these terms.

Shock-induced radiation belt dynamics: simultaneous observations of "one-kick" acceleration and ultralow frequency modulation

Xingran Chen[1,2]*, Xi Lu[3,2], Qiugang Zong[1,4], Hui Zhang[5,2], Ying Liu[1] and Xuzhi Zhou[4]

[1]State Key Laboratory of Lunar and Planetary Science, Macau University of Science and Technology, Macau SAR, China, [2]Geophysical Institute, University of Alaska Fairbanks, Fairbanks, AK, United States, [3]William B. Hanson Center for Space Sciences, University of Taxes at Dallas, Richardson, TX, United States, [4]Institute of Space Physics and Applied Technology, Peking University, Beijing, China, [5]School of Space Science and Technology, Shandong University, Weihai, China

We present conjunctive observations to study the prompt responses of radiation belt electrons during the interplanetary shock (IPS) event on 7 September 2017. As the IPS impinged the Earth, the Time History of Events and Macroscale Interactions (THEMIS) E spacecraft located near the dayside bow shock observed alternating features of solar wind and magnetosheath, indicating that the magnetosphere was repeatedly compressed. Following each compression, rapid increases of relativistic electron fluxes and the corresponding drift echoes were well identified over the energy and pitch-angle spectra obtained by the Van Allen Probes (RBSP) in the inner magnetosphere. Meanwhile, oscillations in the Pc4 range are embedded in the flux variations, appearing as straight stripes in the pitch-angle distributions observed by RBSP-B inside the wave active region and "boomerang" stripes in the observations obtained by RBSP-A ~6 MLT away. Such diverse signatures suggested an azimuthally confined ultralow frequency (ULF) wave. The patterns in the observed particle spectra agreed well with the theoretical predictions, by which we conclude that the surfing acceleration by the shock-induced pulse and the continuous modulation by the localized ULF wave conspired to cause significant disturbances to the Earth's radiation belt.

KEYWORDS

radiation belt, energetic electron, interplanetary shock, surfing acceleration, ultralow frequency wave, space weather

1 Introduction

The dynamics of radiation belt electrons is an outstanding yet unresolved question of geophysics (Friedel et al., 2002; Ripoll et al., 2020). Sudden increases of energetic electron flux in the inner magnetosphere can put space activities at risk, since astronauts and electronic devices are vulnerable under the exposure to these "killer" electrons (Zong et al., 2009). A number of fast relativistic electron buildup events were found to be correlated with the impact of an interplanetary shock (IPS) (Wilken et al., 1982; Blake et al., 1992; Foster et al., 2015; Kanekal et al., 2016; Hao et al., 2019; Zhang et al., 2024). The most well-known example of such shock-induced

radiation belt enhancement was recorded by the Combined Release and Radiation Effects Satellite (CRRES) during the intense storm sudden commencement (SSC) on 24 March 1991. Injection of ultra-relativistic (~15 MeV) electrons deep into the former slot region ($L \sim 2.5$) and large-amplitude (~40 mV/m) bipolar electric field impulse were observed almost instantaneously by the IPS arrival (Blake et al., 1992; Wygant et al., 1994). These unprecedented observations were first simulated by Li et al. (1993) using a guiding center test particle code. The impulsive electric field (IEF) swept through the radiation belt at a speed comparable to the drift velocity (in the order of 10^3 km/s) of the ultra-relativistic electrons. Those electrons in resonance with the pulse would be substantially accelerated and inward transported within a fraction of their drift period, which in turn can explain the prompt electron flux enhancement observed by CRRES. This model of radiation belt dynamics in response to IPS impingement is commonly referred to as the "one-kick" scenario, noting that the particles are efficiently energized mainly during the single passage of the shock-induced pulse. The physical framework has been complemented by magnetohydrodynamics (MHD) simulations (Hudson et al., 1997; Elkington et al., 2002) and successfully applied to several other events (Kanekal et al., 2016; Schiller et al., 2016; Hudson et al., 2017). In all these events, the initial flux enhancements of the relativistic electrons at different energies were followed by recurrent echoes at their respective drift periods. This periodic feature, known as the "drift echoes", is consistent with the theoretical prediction of the one-kick mechanism and widely used as a characteristic signature to understand the particle dynamics in the radiation belt (Hudson et al., 2020). However, Zong et al. (2009) reported coherent oscillations, distinct from the drift echoes, in the cases of both strong and weak IPS. The quasi-monochromatic ultralow frequency (ULF) oscillations were identified in the electromagnetic fields and across the energetic electron spectra. These ULF wave signatures were further attributed to the drift-resonance interaction (Southwood and Kivelson, 1981) between the magnetospheric electrons and the transverse Alfven waves excited by the IPS impingement. Subsequent studies also confirmed the important role of ULF waves in the shock-induced radiation belt dynamics (Zong et al., 2012; Mann et al., 2013; Hao et al., 2014; Foster et al., 2015; Zhang et al., 2020).

Although the significance of IEF and ULF wave has been generally acknowledged, the debate goes on about the dominant factor controlling the shock-induced radiation belt dynamics. A recent ultra-relativistic electron enhancement event, triggered by the IPS impingement on 16 July 2017, was studied by Hao et al. (2019) and Patel et al. (2019), in which the same observational data were analyzed but different physical pictures were suggested. Hao et al. (2019) verified the resonance condition and ascribed the electron flux variation observed by the Van Allen Probes to the drift-resonance interaction with the $m = 1$ poloidal mode ULF wave. They also pinpointed the "group-N" stripes in the electron flux spectrogram which could only be recognized away from the resonant energy (< 2 MeV) as circumstantial evidence for the ULF wave-particle interaction scenario. In addition, their conclusion was reinforced by the consistency between the observed particle signatures and the electron energy change calculated numerically on the basis of the revised drift-resonance theory (Zhou et al., 2016). In contrast, Patel et al. (2019) modeled the event via a MHD-test particle simulation where the energization and drift phase bunching of the electrons were driven by the shock-induced pulse. The time series and the energy spectra of the ultra-relativistic (~2 to 6 MeV) electron flux were, to a considerable extent, reproduced. Thus, Patel et al. (2019) argued that the one-kick mechanism alone could explain the electron dynamics in response to the IPS impact. Since both drift echoes and ULF modulations basically appear as periodic patterns, it could be controversial to evaluate the similarity between the actual measurements and the virtual observations, thereby leaving room for ambiguity in interpreting the data.

Nevertheless, the controversy depicts the necessity to outline the characteristic features to discriminate between the one-kick acceleration and the continuous ULF wave-particle interaction. In this paper, we investigate another typical IPS event on 7 September 2017 (Zhang et al., 2024). The signatures of drift echoes and ULF modulations were unambiguously extracted from the *in situ* measurements of radiation belt electrons. Our observations show that the two mechanisms conspired to cause the electron flux variations with comparable contributions.

2 Observations

Multi-point observations by the Advanced Composition Explorer (ACE), the Time History of Events and Macroscale Interactions during Substorms (THEMIS) spacecraft, and the Van Allen Probes (also known as the Radiation Belt Storm Probes, RBSP) are employed to study the IPS event on 7 September 2017. As shown in Figures 1a–c, an interplanetary fast forward shock transited ACE, which was located around the first Lagrangian point, at ~22:35 UT. The shock passage is characterized by an abrupt change of the plasma parameters. The southward interplanetary magnetic field (negative IMF B_z) enhanced from −10 nT to ~-25 nT. The solar wind velocity jumped from ~470 km/s to ~700 km/s and the proton number density doubled, which means that the dynamic pressure multiplied by a factor of ~3. The IPS then struck the Earth at ~23:00 UT, as registered by THEMIS-E in the dayside magnetosheath. The abrupt increase of dynamic pressure resulted in a prompt compression of the magnetosheath, manifested by an instantaneous enhancement of ion energy flux (shown in Figure 1e). It is notable that the energy flux spectrogram suddenly presented as a narrow beam-like structure ~80 s after the shock arrival. In contrast to the thermalized magnetosheath plasma, the ion beam concentrated at ~3 keV (corresponding to ~ 700 km/s), which indicates that the spacecraft crossed the bow shock into the solar wind. In other words, the magnetosphere was highly compressed by the shock-associated pressure pulse, so that THEMIS-E suddenly found itself out of the magnetosheath. Meanwhile, the SYM-H index (shown in Figure 1d) increased by 40 nT within 2 min. The sharp increase of SYM-H index, which is a typical feature of SSC (Chapman and Ferraro, 1940; Dessler et al., 1960), corresponded to the rapidly enhanced magnetopause current caused by the shock impingement. Additionally, we infer from the alternating features of magnetosheath and solar wind observed by THEMIS-E that the bow shock was moving to-and-fro during the event.

Herein, we focus on the initial shock-induced compression at ~23:00 UT and investigate the corresponding magnetospheric

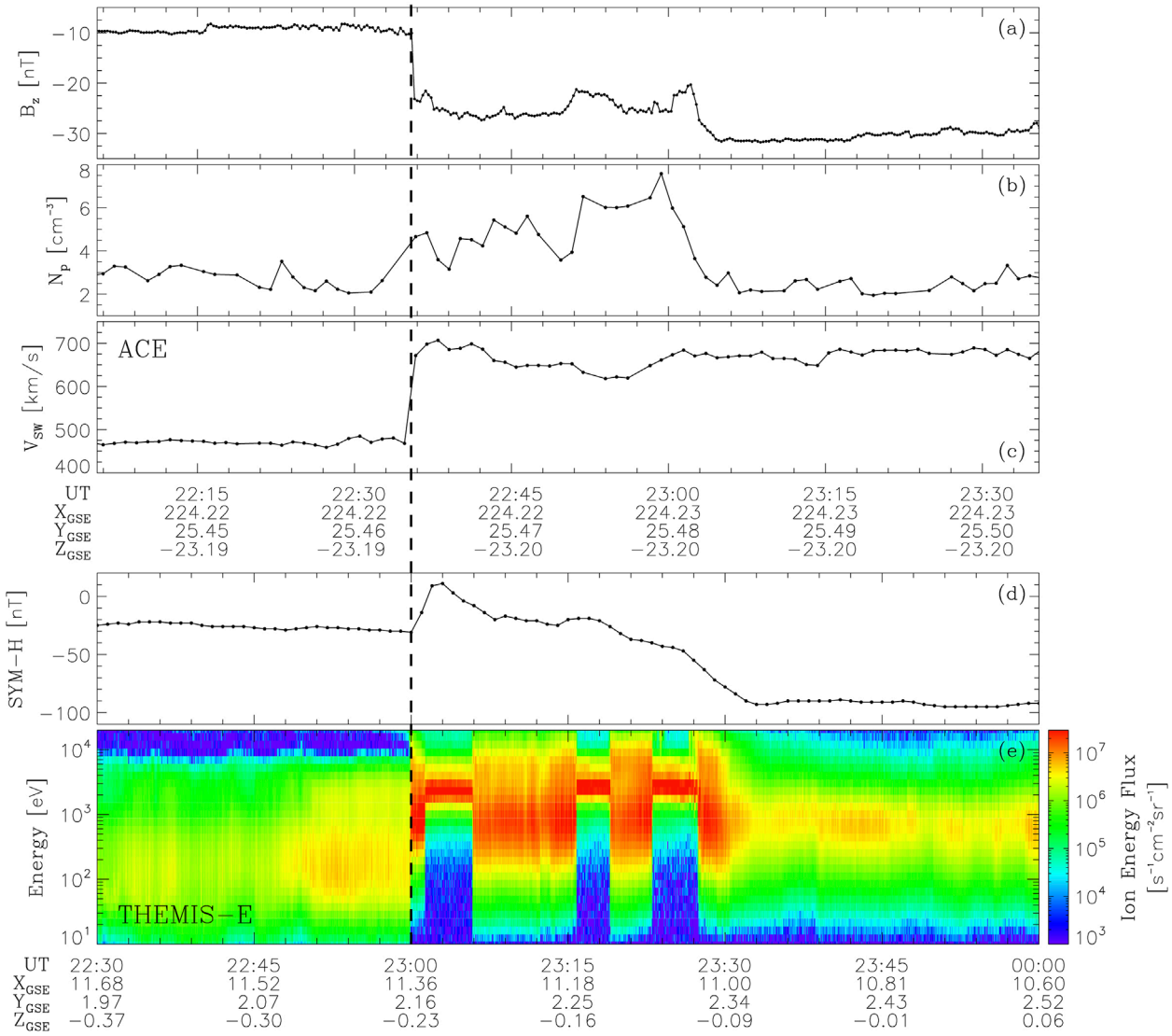

FIGURE 1
Overview of the 7 September 2017 interplanetary shock. **(a)** Z-component of the interplanetary magnetic field B_z, **(b)** proton number density N_p, and **(c)** bulk velocity V_{SW} observed by ACE in the solar wind. **(d)** SYM-H index. **(e)** Energy-time spectrogram of ion energy flux observed by THEMIS-E near the Bow shock. The vertical dashed line (here and in every other figures) marks the shock arrival at the dayside magnetosheath (23:00 UT).

responses. Figure 2 presents the electron differential flux measured by the Magnetic Electron Ion Spectrometer (MagEIS) (Blake et al., 2013) and the Relativistic Electron and Proton Telescope (REPT) (Baker et al., 2013) onboard the twin Van Allen Probes between 22:50 and 23:30 UT. During this interval, RBSP-A traveled inbound through the dusk-side (MLT ~15) outer radiation belt (L from ~5 to ~4) while RBSP-B was on its outbound pass (L from ~3 to ~4) in the dawn (MLT ~9) sector (See Figure 5 for the trajectories of the Van Allen Probes). Both RBSP-A and RBSP-B observed significant flux enhancements within 1 min after the IPS impinged on the dayside magnetosheath. The subsequent recurrences of the enhanced electron fluxes were also recorded by both spacecrafts. In other words, the radiation belt electron fluxes presented periodic variations, similar to previous studies (Zong et al., 2009; Foster et al., 2015; Hao et al., 2019). However, as shown in the pitch angle-time spectrograms, two types of periodic patterns can be recognized by their distinct periods. Specifically, recurrent echoes corresponding to the drift periods of the relativistic electrons, in the order of 10^3 *s*, were readily apparent. These periodic variations, identified as drift echoes, was attributed to the surfing acceleration by the shock-induced IEF (Zhang et al., 2024). Besides, the electron fluxes were observed to oscillate at the period of ~90 *s*. These Pc4 (Jacobs et al., 1964) oscillations appeared as dispersionless straight stripes in the observations of RBSP-B (Figures 2c–n, right panels). The stripes occurred almost immediately after the shock arrival and persisted for several cycles. The ~90 *s* oscillations were also presented in the observations of RBSP-A in the form of boomerang stripes (Hao et al., 2017). The oscillating boomerang-shaped patterns were most obvious at the 470, 597, and 749 *keV* energy channels (Figures 2C–E). As for higher energies, the patterns

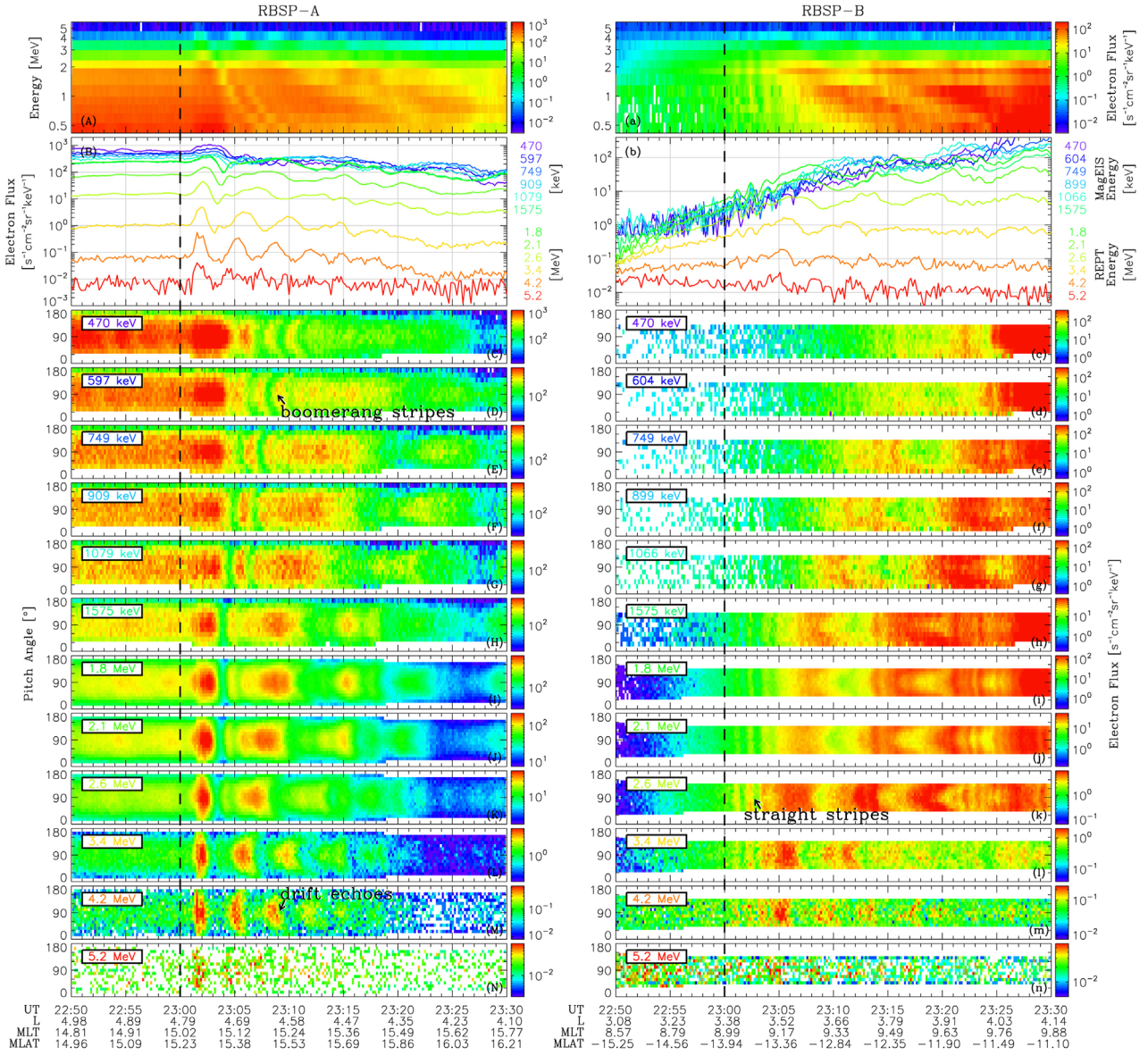

FIGURE 2
Observations of radiation belt electrons. **(A)** Energy-time spectrogram and **(B)** time series plot of electron fluxes measured by Van Allen Probe A. **(C–N)** Electron pitch angle distribution obtained by Van Allen Probe A. **(a–n)** Van Allen Probe B observations in the same format as Panels A–N. Typical patterns of the electron flux spectrum are annotated in Panels D, M, and k.

could still be recognized though they were embedded in the drift echoes. The correlation between the different-shaped stripes will be analyzed in Section 3. We will further demonstrate that the straight and boomerang stripes are the manifestations of localized ULF wave-particle interaction inside and outside the wave active region respectively. We will also apply wavelet analysis to achieve a more quantitative description of the electron flux variations.

Before elaborating on the particle signatures, we present the accompanied observations of electromagnetic fields. The magnetic fields measured by the Electric and Magnetic Field Instrument Suite and Integrated Science (EMFISIS) (Kletzing et al., 2013) onboard the Van Allen Probes are shown in Figures 3A–D and 3a–3d. Note that the International Geomagnetic Reference Field (IGRF) is subtracted. Thus, the background magnetic field associated with the change of spacecraft position is removed. In other words, the remaining variations represent the perturbations of the geomagnetic field caused by the IPS impingement. Here, we focus on the observations between 23:00 and 23:10 UT (highlighted with gray shades in Figure 3), since the instant response to the initial shock-induced compression is of our primary interest. As shown in Figures 3b, c, quasi-monochromatic ULF waves were observed by RBSP-B in the morning-side magnetosphere. The dominant period of the wave was ~90 *s*, the same as the stripes in the particle observations. In contrast, RBSP-A, located in the afternoon side (shown in Figures 3A–D), mainly recorded a rapid change of magnetic field (tens of *nT* within 2 min) whereas the coherent

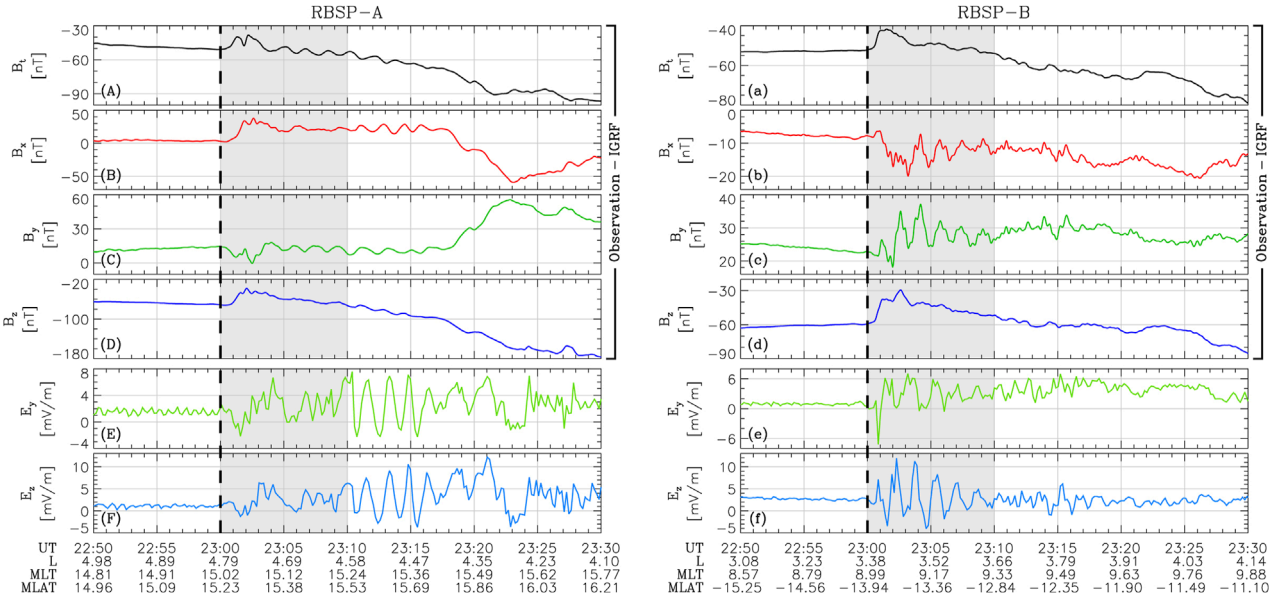

FIGURE 3
In-situ measurements of electric and magnetic fields. Van Allen Probe A observations of **(A)** magnetic field magnitude, **(B–D)** x,y, and z components of the magnetic field vector in the geocentric solar elliptic (GSE) coordinates, **(E, F)** y and z components of the electric field in the modified-GSE coordinates. **(a–f)** Van Allen Probe B observations in the same format as Panels A–F. The magnetic field measurements are presented with the International Geomagnetic Reference Field (IGRF) subtracted. The gray shades highlight the first 10 minutes following the shock arrival.

ULF signals were less apparent (see Supplementary Figure S1 in the supplementary materials for a more quantitative description of the wave amplitude). The local time dependent feature also occurred in the electric field measurements obtained by the Electric Field and Waves (EFW) instrument (Wygant et al., 2013). As shown in Figures 3E, F and 3e, 3f, for the first 10 minutes after the shock arrival, continuous ULF oscillations were only observed by RBSP-B at MLT ~9, while the electric field measured by RBSP-A at MLT ~15 appeared as irregular pulsations. Additionally, it is notable that large amplitude coherent ULF oscillations were also detected by RBSP-A later on (from ~23:10 to ~23:15 UT, Figures 3E, F). Besides, the magnetic field magnitude measured by RBSP-A exhibited periodic fluctuations (from ~23:05 to ~23:15 UT, Figure 3A), which might be associated with a compressional wave. We present a short discussion of these features in the Supplementary Material and leave them for future studies. In brief, the coordinated observations of electric and magnetic fields indicated that the transverse ULF wave immediately following the IPS arrival was localized in the dawn-side magnetosphere.

3 Interpretations and discussions

In contrast to previous studies where the one-kick acceleration by the shock-induced pulse and the continuous interaction with the ULF waves were regarded as competing scenarios, the co-existence of the two different types of periodic electron flux variations described in Section 2 implies that the two mechanisms applied a combined effect to the Earth's radiation belt. The characteristic particle signatures in the present event are highlighted in Figure 4, in the form of electron residual flux. The residual flux is defined as $\frac{j-j_0}{j_0}$, where j is the flux observed in a given energy channel and j_0 is the running average of j. Since the long-term trend is subtracted, the short-term perturbations upon the shock arrival are more explicitly visualized by the residual fluxes. The dispersion characteristics of the two types of periodic signatures can be clearly distinguished in Figures 4A, a. The patterns of drift echoes are increasingly tilted while the patterns of ULF waves are basically parallel. Additionally, as shown in Figures 4B, D, the boomerang stripes of ~ 90 *s* cadence can now be unambiguously identified in the MeV energy channels around 23:04 UT (whereas the shape of the corresponding stripes is less obvious in Figures 2I, K). Thus, Figure 4 strengthens our arguments on the electron flux observations that the multiple periodic features result from the combined effect of the one-kick acceleration and the ULF wave-particle interaction.

To substantiate our interpretations of the observational data, we quantitatively analyze the timing of the periodic patterns in the particle signatures. In general terms, provided a single increase of electron flux occurring over a limited azimuthal range around the magnetic local time ϕ^* at the time t^*, a particle detector located at ϕ might record a sequence of flux enhancements, as the electrons would move periodically along their drift shell. The timing of the n-th observation of the increased flux t_n is given by:

$$\frac{t_n - t^*}{T_d} = \frac{\phi - \phi^*}{24} + n - n_0 \tag{1}$$

where n_0 equals to 0 if $\phi < \phi^*$, otherwise n_0 equals to 1. The electron drift period T_d can be approximated by (Hamlin et al., 1961):

$$T_d = \frac{\pi |e| B_E R_E^2}{3\gamma m_e v^2 L}\left(0.35 + 0.15 \sin \alpha_{eq}\right)^{-1} \tag{2}$$

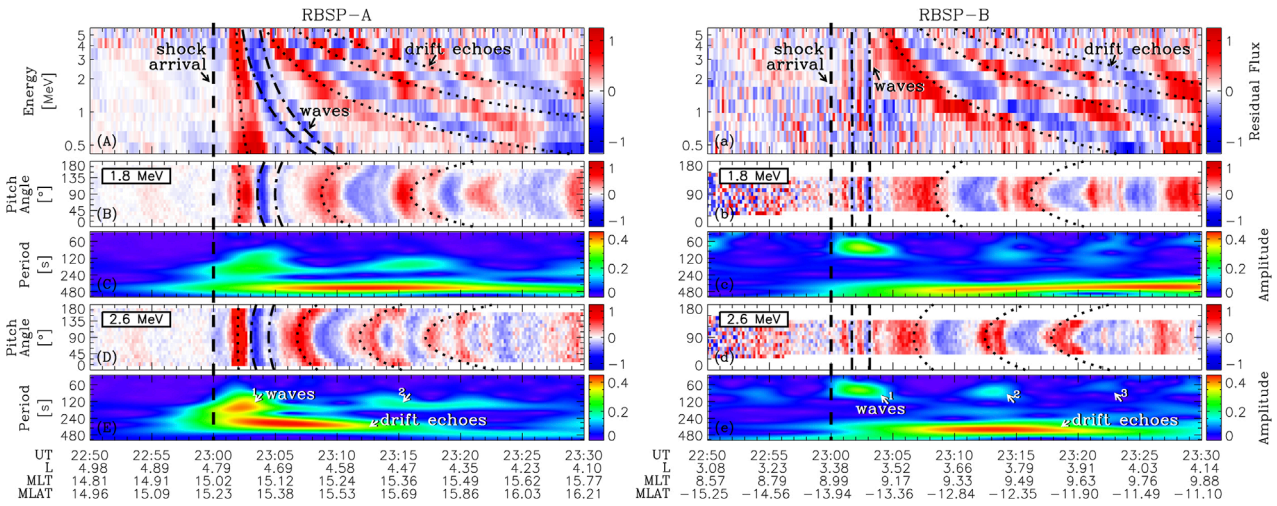

FIGURE 4
Characteristic signatures of radiation belt electrons in the form of wavelet amplitude spectrograms (Panels C, E, c, and e) and residual fluxes (Panels A, B, D, a, b, and d, corresponding to the original electron fluxes in Figures 2A, 2I, 2K, 2a, 2i, 2k).

where B_E is the magnitude of the geomagnetic field in the equatorial plane on the Earth's surface, $R_E \simeq 6.37 \times 10^3\ km$ is the Earth's radius, e and m_e are the charge and the rest mass of an electron, γ is relativistic Lorentz factor, v and α_{eq} are the velocity and the equatorial pitch angle of the electron, and L is the drift shell parameter.

In terms of the one-kick scenario, electrons can be energized as they traverse the IEF. The energization is most efficient when the electron motion matches the pulse propagation. Particularly, in the dusk flank, the azimuthal propagation of the IEF is in the same direction of the electron drift motion, which allows for a longer interaction time between the pulse and the electrons. On the contrary, the interaction time is shorter in the dawn flank, since the azimuthal velocities of the propagating pulse and the drifting electrons are in opposite directions. In other words, electrons in the dusk side may accumulate a larger net energy change. Thus, it is commonly found that the (equivalent) source region of the prompt electron flux variations produced by the shock-induced IEF is located in the dusk-side magnetosphere (Kanekal et al., 2016; Liu et al., 2017; Patel et al., 2019; Liu et al., 2019). Although the electron energy change occurs during the single passage of the IEF, particle detectors may observe a series of subsequent echoes, owing to the periodicity of the drift motion. In this case, the timing of the drift echoes can be theoretically derived by Equations 1, 2, with t^* and ϕ^* assigned as the equivalent time and location at which the electrons are most effectively accelerated by IEF. As shown in Figures 2, 4, the drift echoes observed in the present IPS event are consistent with one-kick scenario. Specifically, an almost dispersionless enhancement of energetic electron flux was first recorded by RBSP-A in the dusk-side outer radiation belt, indicating that the spacecraft was located in the equivalent acceleration region. The subsequent echoes detected by both RBSP-A and RBSP-B exhibited dependence on energy and pitch angle. Moreover, we derive the times t_n at which the drift echoes were expected to be observed in accordance to Equations 1, 2 (with the parameters assigned as $t^* = 23{:}01{:}45\ UT$ and $\phi^* = 14$). The theoretically predicted echoes (denoted by the dotted lines in Figure 4) agree with the actual measurements by the Van Allan Probes. Therefore, we ascribe one of the observed periodic electron flux variations to the drift echoes caused by the shock-induced IEF.

As for the continuous ULF wave-particle interaction, the oscillations of the particle fluxes within the wave active region are independent of pitch angle, thereby appearing as straight vertical stripes in the pitch angle-time spectrogram (Zong et al., 2009; Claudepierre et al., 2013; Chen et al., 2017). In addition, as the particles proceed with their drift motion, the oscillating signatures could also be observed outside the wave active region when the detector encounters those particles that were once modulated by the azimuthally localized ULF wave (Li et al., 2017). Since the drift velocity varies with pitch angle, the modulation patterns (i.e., the straight vertical stripes in the wave active region) would be distorted and transformed into curved boomerang stripes (Hao et al., 2017). Accordingly, the different-shaped stripes are regarded as the diagnostic particle signatures of the localized ULF wave-particle interaction (Zhao et al., 2020). For the present event, the vertical stripes of ~90 s cadence were observed by VAP-B, along with the oscillations of electric and magnetic fields at the same period. Meanwhile, VAP-A, separated by ~6 MLT, detected boomerang stripes with the absence of the corresponding wave electric and magnetic fields. Note that the distortion of the stripes depends on the energy and pitch angle of the electrons and the distance between the wave active region and the detector along the electron drift trajectory. Hence, we can employ Equations 1, 2 to quantitatively examine the correlation between the different-shaped stripes observed severally by the twin Van Allen Probes. Specifically, for each of the stripes, we define t^* and ϕ^* as the time when the straight vertical stripe was observed by RBSP-B and the location of the wave active region (represented by the MLT of RBSP-B), respectively. Then, we can derive the time t at which the

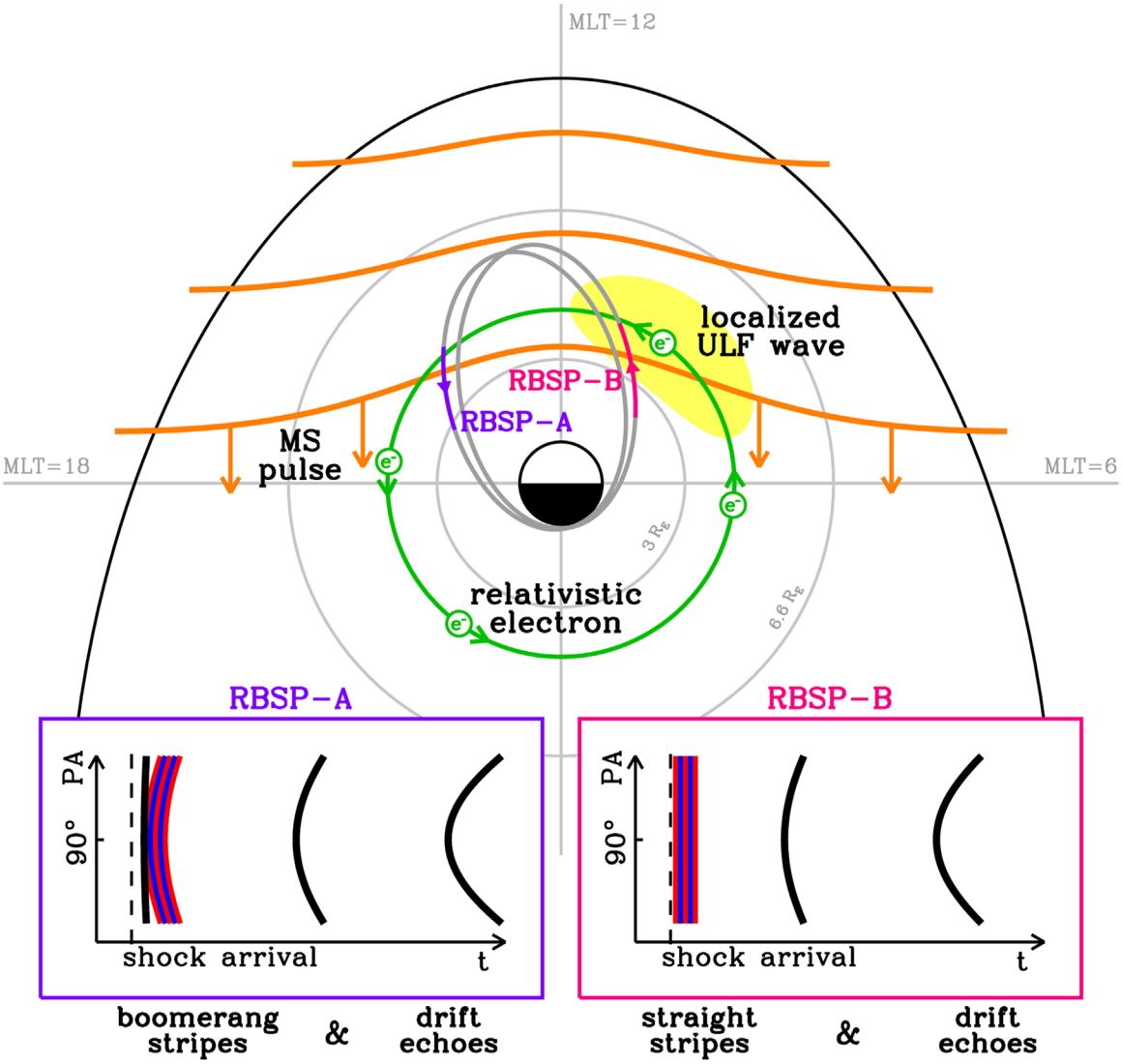

FIGURE 5
Schematic of the shock-induced radiation belt dynamics and the characteristic particle signatures.

other spacecraft would observe the distorted stripe by assigning ϕ as the MLT of RBSP-A and $n = 1$. As presented by the dashed-dotted lines in Figure 4, the shape and timing of the boomerang stripes are well reproduced. Thus, we verify that the other periodic particle signature, namely, the straight and boomerang-shaped stripes at the period of ~90 *s*, is the manifestation of the localized ULF wave-particle interaction.

In addition, we present the wavelet analysis of the 90° fluxes in Figures 4C, E, c, e. On the one hand, the long horizontal patterns in the wavelet amplitude spectrograms refer to the drift echoes. Consistency can be found among the wavelet period corresponding to the horizontal patterns here, the recurrence time of the drift echoes as shown in Figures 2, 4, and the drift period of the electrons as described in 2. On the other hand, 3 isolated amplitude enhancement appeared at ~90 *s*, which agrees with the 3 repeated compression of the magnetosphere observed by THEMIS-E (Figure 1e).

Finally, We sketch the combined effect of the shock-induced IEF and localized ULF waves in Figure 5. On the one hand, the IEF efficiently accelerated the energetic electrons in the dusk-side magnetosphere and caused the prompt electron flux enhancements. The periodic drift motion of the accelerated electrons gave rise to the recurrences of subsequent echoes. On the other hand, the azimuthally localized ULF waves produced the straight and boomerang-shaped stripes in the particle signatures observed inside and outside the wave active region, respectively.

4 Conclusion

The coordinated observations by the Van Allen Probes during the 7 September 2017 event presented the joint effect of the one-kick acceleration and the continuous interaction with the localized ULF waves. For relativistic electrons, the one-kick acceleration

was most effective in the dusk side, while the ULF wave-particle interaction was localized in the dawn-side magnetosphere in the present event. In a broader context, the two types of periodic electron flux variations, namely, the drift echoes and the different-shaped stripes, can be used as the characteristic particle signatures to discriminate between the one-kick acceleration and the localized ULF wave-particle interaction.

Data availability statement

Publicly available datasets were analyzed in this study. This data can be found here: https://cdaweb.gsfc.nasa.gov/pub/data/.

Author contributions

XC: Conceptualization, Visualization, Writing–original draft. XL: Writing–review and editing, Conceptualization. QZ: Conceptualization, Writing–review and editing. HZ: Conceptualization, Writing–review and editing. YL: Conceptualization, Writing–review and editing. XZ: Conceptualization, Writing–review and editing.

Funding

The author(s) declare that financial support was received for the research, authorship, and/or publication of this article. This work was supported by the Science and Technology Development Fund (FDCT) of Macau (grant number: 002/2024/SKL) and NASA contract NAS5-02099.

Acknowledgments

The authors acknowledge NASA's Space Physics Data Facility for providing the data in this study. XC, XL, and HZ would like to thank the space physics and aeronomy research group at UAF for helpful discussions.

Conflict of interest

The authors declare that the research was conducted in the absence of any commercial or financial relationships that could be construed as a potential conflict of interest.

The author(s) declared that they were an editorial board member of Frontiers, at the time of submission. This had no impact on the peer review process and the final decision.

Generative AI statement

The author(s) declare that no Generative AI was used in the creation of this manuscript.

Publisher's note

All claims expressed in this article are solely those of the authors and do not necessarily represent those of their affiliated organizations, or those of the publisher, the editors and the reviewers. Any product that may be evaluated in this article, or claim that may be made by its manufacturer, is not guaranteed or endorsed by the publisher.

Supplementary material

The Supplementary Material for this article can be found online at: https://www.frontiersin.org/articles/10.3389/fspas.2024.1520141/full#supplementary-material

References

Baker, D. N., Kanekal, S. G., Hoxie, V. C., Batiste, S., Bolton, M., Li, X., et al. (2013). The relativistic electron-proton telescope (rept) instrument on board the radiation belt storm probes (rbsp) spacecraft: characterization of earth's radiation belt high-energy particle populations. *Space Sci. Rev.* 179, 337–381. doi:10.1007/s11214-012-9950-9

Blake, J. B., Carranza, P. A., Claudepierre, S. G., Clemmons, J. H., Crain, W. R., Dotan, Y., et al. (2013). The magnetic electron ion spectrometer (mageis) instruments aboard the radiation belt storm probes (rbsp) spacecraft. *Space Sci. Rev.* 179, 383–421. doi:10.1007/s11214-013-9991-8

Blake, J. B., Kolasinski, W. A., Fillius, R. W., and Mullen, E. G. (1992). Injection of electrons and protons with energies of tens of mev into l < 3 on 24 march 1991. *Geophys. Res. Lett.* 19, 821–824. doi:10.1029/92GL00624

Chapman, S., and Ferraro, V. C. A. (1940). The theory of the first phase of a geomagnetic storm. *J. Geophys. Res.* 45, 245–268. doi:10.1029/TE045i003p00245

Chen, X. R., Zong, Q. G., Zhou, X. Z., Blake, J. B., Wygant, J. R., and Kletzing, C. A. (2017). Van Allen Probes observation of a 360° phase shift in the flux modulation of injected electrons by ULF waves. *Geophys. Res. Lett.* 44, 1614–1624. doi:10.1002/2016GL071252

Claudepierre, S. G., Mann, I. R., Takahashi, K., Fennell, J. F., Hudson, M. K., Blake, J. B., et al. (2013). Van allen probes observation of localized drift resonance between poloidal mode ultra-low frequency waves and 60 kev electrons. *Geophys. Res. Lett.* 40, 4491–4497. doi:10.1002/grl.50901

Dessler, A. J., Francis, W. E., and Parker, E. N. (1960). Geomagnetic storm sudden-commencement rise times. *J. Geophys. Res.* 65, 2715–2719. doi:10.1029/jz065i009p02715

Elkington, S. R., Hudson, M. K., Wiltberger, M. J., and Lyon, J. G. (2002). Mhd/particle simulations of radiation belt dynamics. *J. Atmos. Solar-Terrestrial Phys.* 64, 607–615. doi:10.1016/S1364-6826(02)00018-4

Foster, J. C., Wygant, J. R., Hudson, M. K., Boyd, A. J., Baker, D. N., Erickson, P. J., et al. (2015). Shock-induced prompt relativistic electron acceleration in the inner magnetosphere. *J. Geophys. Res. Space Phys.* 120, 1661–1674. doi:10.1002/2014JA020642

Friedel, R. H. W., Reeves, G. D., and Obara, T. (2002). Relativistic electron dynamics in the inner magnetosphere - a review. *J. Atmos. Solar-Terrestrial Phys.* 64, 265–282. doi:10.1016/S1364-6826(01)00088-8

Hamlin, D. A., Karplus, R., Vik, R. C., and Watson, K. M. (1961). Mirror and azimuthal drift frequencies for geomagnetically trapped particles. *J. Geophys. Res.* 66, 1–4. doi:10.1029/JZ066i001p00001

Hao, Y. X., Zong, Q.-G., Wang, Y. F., Zhou, X.-Z., Zhang, H., Fu, S. Y., et al. (2014). Interactions of energetic electrons with ulf waves triggered by interplanetary shock: van allen probes observations in the magnetotail. *J. Geophys. Res. Space Phys.* 119, 8262–8273. doi:10.1002/2014JA020023

Hao, Y. X., Zong, Q.-G., Zhou, X.-Z., Rankin, R., Chen, X. R., Liu, Y., et al. (2017). Relativistic electron dynamics produced by azimuthally localized poloidal mode ulf waves: boomerang-shaped pitch angle evolutions. *Geophys. Res. Lett.* 44, 7618–7627. doi:10.1002/2017GL074006

Hao, Y. X., Zong, Q. G., Zhou, X. Z., Rankin, R., Chen, X. R., Liu, Y., et al. (2019). Global-scale ulf waves associated with ssc accelerate magnetospheric ultrarelativistic electrons. *J. Geophys. Res. Space Phys.* 124, 1525–1538. doi:10.1029/2018JA026134

Hudson, M., Jaynes, A., Kress, B., Li, Z., Patel, M., Shen, X., et al. (2017). Simulated prompt acceleration of multi-mev electrons by the 17 march 2015 interplanetary shock. *Front. Neurosci.* 122, 10036–10046. doi:10.1002/2017JA024445

Hudson, M. K., Elkington, S. R., Li, Z., and Patel, M. (2020). Drift echoes and flux oscillations: a signature of prompt and diffusive changes in the radiation belts. *J. Atmos. Solar-Terrestrial Phys.* 207, 105332. doi:10.1016/j.jastp.2020.105332

Hudson, M. K., Elkington, S. R., Lyon, J. G., Marchenko, V. A., Roth, I., Temerin, M., et al. (1997). Simulations of radiation belt formation during storm sudden commencements. *J. Geophys. Res. Space Phys.* 102, 14087–14102. doi:10.1029/97JA03995

Jacobs, J. A., Kato, Y., Matsushita, S., and Troitskaya, V. A. (1964). Classification of geomagnetic micropulsations. *J. Geophys. Res.* 69, 180–181. doi:10.1029/JZ069i001p00180

Kanekal, S. G., Baker, D. N., Fennell, J. F., Jones, A., Schiller, Q., Richardson, I. G., et al. (2016). Prompt acceleration of magnetospheric electrons to ultrarelativistic energies by the 17 march 2015 interplanetary shock. *J. Geophys. Res. Space Phys.* 121, 7622–7635. doi:10.1002/2016JA022596

Kletzing, C. A., Kurth, W. S., Acuna, M., MacDowall, R. J., Torbert, R. B., Averkamp, T., et al. (2013). The electric and magnetic field instrument suite and integrated science (emfisis) on rbsp. *Space Sci. Rev.* 179, 127–181. doi:10.1007/s11214-013-9993-6

Li, L., Zhou, X.-Z., Zong, Q.-G., Rankin, R., Zou, H., Liu, Y., et al. (2017). Charged particle behavior in localized ultralow frequency waves: theory and observations. *Geophys. Res. Lett.* 44, 5900–5908. doi:10.1002/2017GL073392

Li, X., Roth, I., Temerin, M., Wygant, J. R., Hudson, M. K., and Blake, J. B. (1993). Simulation of the prompt energization and transport of radiation belt particles during the march 24, 1991 ssc. *Geophys. Res. Lett.* 20, 2423–2426. doi:10.1029/93GL02701

Liu, Y., Zong, Q. G., Zhou, X. Z., Hao, Y. X., and Liu, Z. Y. (2019). Understanding electron dropout echoes induced by interplanetary shocks: test particle simulations. *J. Geophys. Res. Space Phys.* 124, 6759–6775. doi:10.1029/2019JA027018

Liu, Z. Y., Zong, Q.-G., Hao, Y. X., Zhou, X.-Z., Ma, X. H., and Liu, Y. (2017). Electron dropout echoes induced by interplanetary shock: a statistical study. *J. Geophys. Res. Space Phys.* 122, 8037–8050. doi:10.1002/2017JA024045

Mann, I. R., Lee, E. A., Claudepierre, S. G., Fennell, J. F., Degeling, A., Rae, I. J., et al. (2013). Discovery of the action of a geophysical synchrotron in the earth's van allen radiation belts. *Nat. Commun.* 4, 2795. doi:10.1038/ncomms3795

Patel, M., Li, Z., Hudson, M., Claudepierre, S., and Wygant, J. (2019). Simulation of prompt acceleration of radiation belt electrons during the 16 july 2017 storm. *Geophys. Res. Lett.* 46, 7222–7229. doi:10.1029/2019GL083257

Ripoll, J. F., Claudepierre, S. G., Ukhorskiy, A. Y., Colpitts, C., Li, X., Fennell, J. F., et al. (2020). Particle dynamics in the earth's radiation belts: review of current research and open questions. *J. Geophys. Res. Space Phys.* 125, 1–48. doi:10.1029/2019JA026735

Schiller, Q., Kanekal, S. G., Jian, L. K., Li, X., Jones, A., Baker, D. N., et al. (2016). Prompt injections of highly relativistic electrons induced by interplanetary shocks: a statistical study of van allen probes observations. *Geophys. Res. Lett.* 43, 12317–12324. doi:10.1002/2016GL071628

Southwood, D. J., and Kivelson, M. G. (1981). Charged particle behavior in low-frequency geomagnetic pulsations 1. transverse waves. *J. Geophys. Res.* 86, 5643–5655. doi:10.1029/JA086iA07p05643

Wilken, B., Goertz, C. K., Baker, D. N., Higbie, P. R., and Fritz, T. A. (1982). The ssc on july 29, 1977 and its propagation within the magnetosphere. *J. Geophys. Res.* 87, 5901–5910. doi:10.1029/ja087ia08p05901

Wygant, J., Mozer, F., Temerin, M., Blake, J., Maynard, N., Singer, H., et al. (1994). Large amplitude electric and magnetic field signatures in the inner magnetosphere during injection of 15 mev electron drift echoes. *Geophys. Res. Lett.* 21, 1739–1742. doi:10.1029/94GL00375

Wygant, J. R., Bonnell, J. W., Goetz, K., Ergun, R. E., Mozer, F. S., Bale, S. D., et al. (2013). The electric field and waves instruments on the radiation belt storm probes mission. *Space Sci. Rev.* 179, 183–220. doi:10.1007/s11214-013-0013-7

Zhang, D., Liu, W., Li, X., Sarris, T. E., Hao, Y., and Zhang, Z. (2024). Surfing acceleration of radiation belt relativistic electrons induced by the propagation of interplanetary shock. *Geophys. Res. Lett.* 51. doi:10.1029/2024GL109285

Zhang, D., Liu, W., Li, X., Sarris, T. E., Wang, Y., Xiao, C., et al. (2020). Relation between shock-related impulse and subsequent ulf wave in the earth's magnetosphere. *Geophys. Res. Lett.* 47. doi:10.1029/2020GL090027

Zhao, X. X., Hao, Y. X., Zong, Q. G., Zhou, X. Z., Yue, C., Chen, X. R., et al. (2020). Origin of electron boomerang stripes: localized ulf wave-particle interactions. *Geophys. Res. Lett.* 47. doi:10.1029/2020GL087960

Zhou, X., Wang, Z., Zong, Q., Rankin, R., Kivelson, M. G., Chen, X., et al. (2016). Charged particle behavior in the growth and damping stages of ultralow frequency waves: theory and van allen probes observations. *J. Geophys. Res. Space Phys.* 121, 3254–3263. doi:10.1002/2016JA022447

Zong, Q.-G., Wang, Y. F., Zhang, H., Fu, S. Y., Zhang, H., Wang, C. R., et al. (2012). Fast acceleration of inner magnetospheric hydrogen and oxygen ions by shock induced ulf waves. *J. Geophys. Res. Space Phys.* 117. doi:10.1029/2012JA018024

Zong, Q. G., Zhou, X. Z., Wang, Y. F., Li, X., Song, P., Baker, D. N., et al. (2009). Energetic electron response to ulf waves induced by interplanetary shocks in the outer radiation belt. *J. Geophys. Res. Space Phys.* 114, 1–11. doi:10.1029/2009JA014393

frontiers | Frontiers in Astronomy and Space Sciences

TYPE Perspective
PUBLISHED 06 January 2025
DOI 10.3389/fspas.2024.1522139

Check for updates

OPEN ACCESS

EDITED BY
Andrey Samsonov,
University College London, United Kingdom

REVIEWED BY
Ravindra Desai,
University of Warwick, United Kingdom
Mike Hapgood,
Rutherford Appleton Laboratory,
United Kingdom

*CORRESPONDENCE
Denny M. Oliveira,
denny@umbc.edu

RECEIVED 04 November 2024
ACCEPTED 13 December 2024
PUBLISHED 06 January 2025

CITATION
Oliveira DM, Zesta E and Nandy D (2025) The 10 October 2024 geomagnetic storm may have caused the premature reentry of a Starlink satellite.
Front. Astron. Space Sci. 11:1522139.
doi: 10.3389/fspas.2024.1522139

COPYRIGHT
© 2025 Oliveira, Zesta and Nandy. This is an open-access article distributed under the terms of the Creative Commons Attribution License (CC BY). The use, distribution or reproduction in other forums is permitted, provided the original author(s) and the copyright owner(s) are credited and that the original publication in this journal is cited, in accordance with accepted academic practice. No use, distribution or reproduction is permitted which does not comply with these terms.

The 10 October 2024 geomagnetic storm may have caused the premature reentry of a Starlink satellite

Denny M. Oliveira[1,2]*, Eftyhia Zesta[2] and Dibyendu Nandy[3,4]

[1]Goddard Planetary Heliophysics Institute, University of Maryland, Baltimore, MD, United States, [2]Geospace Physics Laboratory, NASA Goddard Space Flight Center, Greenbelt, MD, United States, [3]Department of Physical Sciences, Indian Institute of Science Education and Research Kolkata, Kolkata, India, [4]Center of Excellence in Space Sciences India, Indian Institute of Science Education and Research Kolkata, Kolkata, India

In this short communication, we qualitatively analyze possible effects of the 10 October 2024 geomagnetic storm on accelerating the reentry of a Starlink satellite from very low-Earth orbit (VLEO). The storm took place near the maximum of solar cycle (SC) 25, which has shown to be more intense than SC24. Based on preliminary geomagnetic indices, the 10 October 2024, along with the 10 May 2024, were the most intense events since the well-known Halloween storms of October/November 2003. By looking at a preliminary version of the Dst index and altitudes along with velocities extracted from two-line element (TLE) data of the Starlink-1089 (SL-1089) satellite, we observe a possible connection between storm main phase onset and a sharp decay of SL-1089. The satellite was predicted to reenter on 22 October, but it reentered on 12 October, 10 days before schedule. The sharp altitude decay of SL-1089 revealed by TLE data coincides with the storm main phase onset. We compare the deorbiting altitudes of another three satellites during different geomagnetic conditions and observe that the day difference between actual and predicted reentries increases for periods with higher geomagnetic activity. Therefore, we call for future research to establish the eventual causal relationship between storm occurrence and satellite orbital decay. As predicted by previous works, SC25 is already producing extreme geomagnetic storms with unprecedented satellite orbital drag effects and consequences for current megaconstellations in VLEO.

KEYWORDS

geomagnetic storms, satellite megaconstellations, thermospheric mass density, satellite orbital drag, satellite reentry

1 Introduction

Intense solar wind perturbations, such as coronal mass ejections (CMEs), can greatly disturb the Earth's magnetic field due to the occurrence of geomagnetic storms (Akasofu, 1966; Gonzalez et al., 1994). Geomagnetic storms are global phenomena characterized by intense magnetospheric energy input into the ionosphere-thermosphere (IT) system. During active times, the primary energy sources that heat the atmosphere are Joule heating and particle precipitation (Knipp et al., 2004; Prölss, 2011). Such magnetospheric energy primarily leads the

thermosphere to heat and upwell globally driving the propagation of large-scale gravity waves and atmospheric wind surges (Bruinsma and Forbes, 2007; Prölss, 2011; Emmert, 2015). The atmosphere first responds to energy input at high latitudes within minutes of the storm main phase onset (Shi et al., 2017), whereas it responds globally ~ 3 h after storm main phase onset (Oliveira et al., 2017). While flying in low-Earth orbit (LEO, below 1,000 km altitude), due to increased levels of atmospheric density, satellites then experience enhanced levels of drag forces which in turn enhance orbital drag effects. Such effects are quantified by many parameters, including satellite geometry, drag coefficient, area-to-mass ratio, and thermospheric neutral mass density and ions, which is derived from drag acceleration measurements (Sutton et al., 2005; Chen et al., 2012; Mehta et al., 2023). Thermosphere heating and subsequent orbital drag effects usually occur during geomagnetic storms of different levels, but they are much more intense during extreme events (Krauss et al., 2015; Oliveira and Zesta, 2019; Zesta and Oliveira, 2019).

SpaceX is a private company that has recently launched thousands of satellites into LEO. That satellite megaconstellation is named Starlink, with the primary goal to provide internet service worldwide (Ren et al., 2022). One of the most recent examples of storm-time satellite orbital drag effects experienced in LEO is provided by Starlink satellites. According to Hapgood et al. (2022), 49 Starlink satellites were deployed on 3 February 2022 while a weak geomagnetic storm, classified as a G1 event, was raging on. As a result, 38 satellites did not make it to their intended altitude due to storm effects. Prior to early February 2022, SpaceX launched their satellites to very-low Earth orbit (VLEO) altitudes near 210 km where electric thrusters were turned on to uplift the satellite to operational altitudes around 500 km (Hapgood et al., 2022). However, the satellites typically perform a few orbits before being lifted up, but the environment was quite perturbed due to the minor geomagnetic storm occurrence (Dang et al., 2022; Fang et al., 2022; Berger et al., 2023).

If a weak geomagnetic storm can bring down satellites from VLEO, what can an extreme event do? In this short communication, we briefly discuss possible effects of the extreme geomagnetic storm of 10 October 2024 on forcing the premature reentry of a Starlink satellite, and compare it with the reentries of three other Starlink satellites during periods of less intense geomagnetic activity. Although our observations were performed with preliminary versions of and limited data sets, it is very likely that the storm cut short the reentry process of the satellite. However, solid causal relationships can only be achieved with further investigations using multi-data sets and conduction of numerical/empirical simulations. As predicted before, solar activity is increasing in the current solar cycle and they are already impacting satellite orbits in VLEO, as recently shown by Starlink satellites.

2 Data

We use OMNI IMF (interplanetary magnetic field) and selected solar wind parameter data, along with SYM-H geomagnetic index data, for the period 10–11 October 2024. Both OMNI and SYM-H data have resolution of 1 min (King and Papitashvili, 2005; Iyemori, 1990).

Geomagnetic activity is also represented by long-term 1-h Dst indices (Sugiura, 1964). Although with different resolutions, both Dst and SYM-H are frequently used to expresses ring current activity and geomagnetic storm intensities (Wanliss and Showalter, 2006). According to the World Data Center for Geomagnetism, Kyoto et al. (2015), final versions of the Dst index are only available from 1957 to 2020, whereas a provisional version of the index is available from 2021 to 2023. The 2024 version of the index is termed real-time/quick-look index. The key difference between the provisional Dst index and the real-time Dst index is that the provisional index is a more accurate representation of geomagnetic activity because it undergoes additional quality checks and manual corrections for data errors, while the real-time Dst is a quicker, less refined measurement used for immediate monitoring and forecasting, potentially containing inaccuracies due to unverified raw data. For these reasons, World Data Center for Geomagnetism, Kyoto et al. (2015), recommends use of real-time (quick-look) Dst data only for forecasting, diagnostic, and monitoring purposes (https://wdc.kugi.kyoto-u.ac.jp/dst_realtime/index.html).

For specification of satellites' orbital parameters represented by altitudes and velocities, we use Two-Line Element (TLE) data provided by the U.S. Space Force. TLE is a standardized format used to describe a satellite's orbital parameters, containing all the necessary information to calculate its position in space at a given time, presented in two lines of text. Each character in the file represents a specific orbital element like inclination, eccentricity, and mean anomaly, allowing for easy data exchange and prediction of a satellite's future path (e.g., Kizner and Belotserkovskiy, 2005). Altitudes and velocities are extracted from TLE data with the pyephem Python package (https://pypi.org/project/pyephem/). pyephem extracts satellite orbital parameters from TLE files based on physical principles of orbital mechanics, particularly Kepler's laws of planetary motion. The package then uses numerical methods to propagate the satellite's position over time, accounting for perturbative effects like gravitational anomalies, drag, and radiation pressure. This enables the accurate prediction of the satellite's trajectory and position at any given time based on the initial conditions provided in the TLE data (Rhodes, 2010). Satellite velocities are calculated from coverting the satellite's position from geodetic to cartesian coordinates, where $\vec{v} = d\vec{r}/dt$, with $\vec{dr} = (dx, dy, dz)$ being the geodetic displacement with respect to the Earth's center progated in a time step with $dt \sim 10$ s. The final altitude for each satellite is calculated using the corresponding decay epoch and TLE data. If a file for that particular decay epoch is not available, the latest TLE data file is used for the computations.

3 Observations

A CME associated with an X1.8 solar flare was observed by Solar and Heliospheric Observatory (SOHO) to be ejected from active region AR3848 on 9 October 2024 at 0212 UT (https://kauai.ccmc.gsfc.nasa.gov/CMEscoreboard/prediction/detail/3670). This particular CME impacted Earth on 10 October 2024 at around 1500 UT. Thus, the average speed of the CME on its way to 1 AU was ~1,200 km/s. Some of the space weather consequences of that CME are described below.

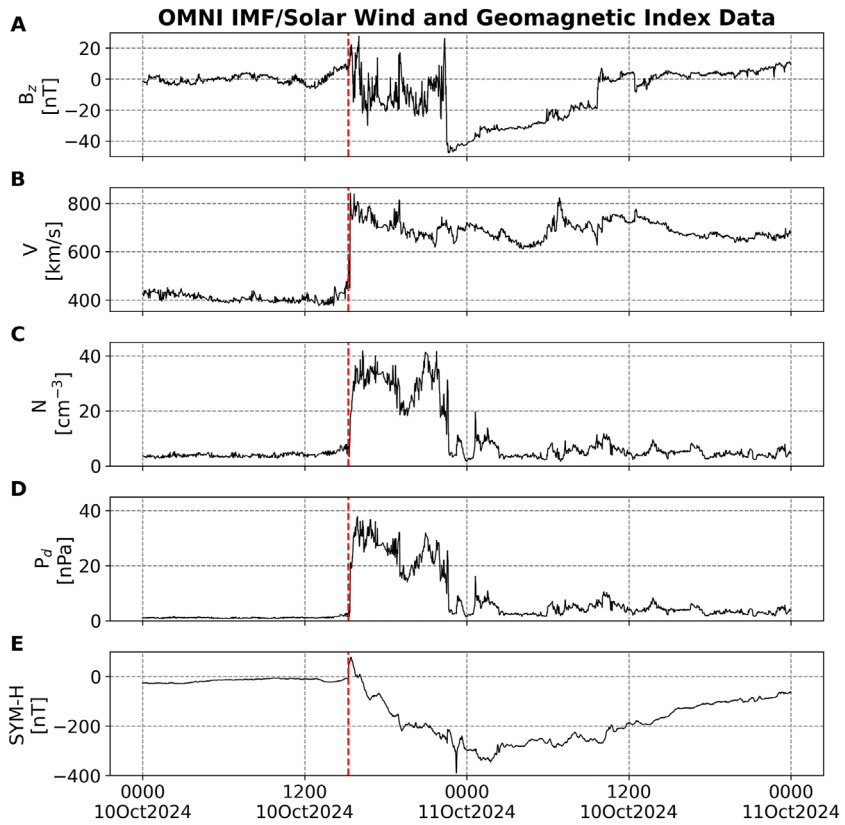

FIGURE 1
OMNI interplanetary magnetic field (IMF) and solar wind parameter profiles along with geomagnetic index data for the period 10–11 October 2024. **(A)**: IMF B_z component; **(B)**: solar wind flow speed; **(C)**: solar wind particle number density; **(D)**: solar wind ram pressure; and **(E)**: SYM-H geomagnetic index data. All data shown in the figure have resolution of 1 min. The dashed red line indicates the storm sudden commencement onset on 10 October 2024 at 1514 UT.

The IMF B_z component is shown in Figure1A. B_z stays relatively steady at nearly null values during 0000-1200 UT of 10 October, and ramps slowly up to values around 10 nT following a short period of negative values in the beginning of that day. As indicated by the red dashed vertical lines, the CME shock strikes the magnetosphere at 1514 UT of 10 October with a clear storm sudden commencement shown in Figure 1E. A few minutes following the shock, B_z jumps to values above 20 nT and later mostly shows negative values down to −20 nT. Nearly at the end of the storm main phase around 2225 UT of 10 October, B_z plunges from ~25 to ~ −50 nT, which may have contributed to a long storm recovery of a few days. Figure 1B indicates that the solar wind flow speed was mostly above 700 km/s. However, the solar wind number density (Figure1C) and dynamic pressure (Figure1D) stayed highly elevated (respectively above 30 cm^{-3} and 20 nPa) only during most of the main phase, and showed relatively low values throughout the recovery phase. Figure 1E indicates that the main phase ended at 11 October 0122 UT with minimum value of −335 nT, but it showed a −390 nT spike at 2314 UT of 10 October. Therefore, following the May 2024 extreme geomagnetic storm (Hayakawa et al., 2024), the October 2024 storm was the second most intense extreme event since the October/November storms of 2023 (Gopalswamy et al., 2005).

Unusually low-latitude auroras were seen during 10-11 October 2024. According to aurorasaurus.org, preliminary results show that the most equatorward observation of the aurora took place in the northern hemisphere near Jerome, Florida (N25°59′, W81°19′, 35.36° MLAT), and in the southern hemisphere, near Fishers Hill, Australia (S32°29′, E151°32′, −41.74° MLAT)[1]. Aurora observations at such low latitudes are quite common during extreme events (Boteler, 2019; Hayakawa et al., 2019; Bhaskar et al., 2020; Hayakawa et al., 2024). More detailed and conclusive analyses of the most equatorward observations of the aurora during October 2024 using worldwide observations as performed for the May 2024 event by Hayakawa et al. (2024) are under way.

Altitudes and velocities for the satellites and Dst data are shown in Figure 2. The reference satellite is Starlink-1089 (SL-1089), whose deorbiting process was the most severe. We take a

1 This information was visually obtained by clicking on the date/time tabs on the top right of the screen. We then selected early hours of 11 October 2024 (e.g., 1:00am). The geographic coordinates and location names were then obtained from Google Maps and by zooming in and clicking on the nearest pinned location.

reference altitude as 280 km because SL-1089 started its sharp decay at that altitude during the storm. Another three satellites, SL-2652, SL-1472, and SL-2360, are chosen for comparisons due to three reasons: 1) the satellites reentered during different geomagnetic conditions; 2) they were around the reference altitude (horizontal dashed black line) near the onset of some geomagnetic activity Figures 2C–F 3) the satellites had similar altitudes and orbital decay rates before reaching the reference altitude (Figure 2A; also see Supplementary Figures S1–S4 for lifetime altitudes of all satellites). Thus, this suggests all four satellites were already reentering before reaching the reference altitude. The highlighted grey area corresponds to 1 day to 4 days around the reference altitude epoch time to represent quiet- and storm-times during the October 2024 event. In addition, as shown in Figure 2B, the velocity rate of each satellite generally increases as the satellite decays due to change of gravitational potential energy into kinetic energy.

The satellites that passed through the reference altitude under different geomagnetic conditions are: SL-2360, quiet conditions; SL-1472, moderate conditions; SL-2652, severe conditions; and SL-1089, extreme conditions. Such storm classifications are based on minimum values of Dst during the storm period (Zesta and Oliveira, 2019). Figure 2A shows that the more intense the geomagnetic activity level, the sharper the orbital decay rate. We consider a satellite renters the atmosphere when it crosses the Kármán line at ~100 km (horizontal dashed magenta line), which is a commonly recognized boundary that defines the transition between Earth's atmosphere and outer space (von Kármán, 1956; McDowell, 2018). For each satellite, we define the predicted epoch, extracted from space-track.org, by searching each satellite under the tab "Decay/Reentry" and by taking the reentry epoch predicted on the day the satellite crossed the reference altitude. As shown in Table 1, there is a difference between time delay, in days, determined as the day difference between the predicted and actual reentries of each satellite. The absolute day difference is larger for satellites reentering under high geomagnetic activity levels. During geomagnetic active times, the satellites reentered before prediction, except the satellite under quiet time conditions (SL-2360), which reentered 2 days after prediction. Table 1 summarizes our findings and brings further information about all satellites.

4 Discussion, conclusion, and suggestions

Space Era is defined to have begun with the launching of Sputnik, the first satellite sent to space (Launius, 2004). Sputnik was launched in 1957, the solar maximum year of SC19 (Clette et al., 2023). Ephemeris data provided by one of the first Sputnik satellites was used by Jacchia (1959) to, as best we can see from published literature, observe storm-time drag effects in LEO for the first time in history. Curiously, the highest yearly sunspot number observation also occurred in SC19 during 1957 (Clette et al., 2023). Zesta and Oliveira (2019) define geomagnetic storms with minimum Dst/SYM-H indices below the threshold of −250 nT to cause extreme effects on thermospheric neutral mass density and subsequent satellite orbital drag (Oliveira and Zesta, 2019), and it is well known that higher density enhancements result from more intense storms (Krauss et al., 2018; Oliveira and Zesta, 2019; Krauss et al., 2020). Although Meng et al. (2019) reported on the occurrence of nearly 40 extreme geomagnetic storms recorded with minimum Dst < −250 nT since 1957, there are very few extreme events available to be studied with thermospheric neutral mass data derived from drag acceleration data collected by high-accuracy accelerometers. Oliveira and Zesta (2019) and Zesta and Oliveira (2019) identified only 7 extreme events recorded by CHAMP and GRACE since early 2,000 s. As pointed out by Oliveira et al. (2021), this makes our understanding of extreme storm-time thermospheric dynamic response and subsequent enhanced satellite orbital drag effects quite limited. Therefore, more extreme geomagnetic storms are needed to enhance our understanding of the effects described above.

Oliveira et al. (2021) suggested two possible approaches that can be undertaken in order to improve our understanding of extreme satellite orbital drag: look into extreme events and superstorms of the past or expect for new extreme events in the upcoming solar cycles. The first approach was already taken by Oliveira et al. (2020), who studied drag effects in LEO on hypothetical satellites flying in the atmosphere during three historical superstorms (October/November 1903; September 1909; and May 1921) along with the well-known, space-era geomagnetic storm of March 1989. The authors defined two storm characteristics: storm intensity, defined by the minimum Dst value at the beginning of the recovery phase, and storm duration, defined as the time between the (presumably) impact of the driving CME on the magnetosphere and the end of the main phase. The authors concluded that storm duration can be more effective in comparison to storm intensity when determining the severity of drag effects, as occurred in the case of the March 1989 event. As pointed out by Bhowmik and Nandy (2018), Nandy (2021), McIntosh et al. (2023), SC25 was expected to be stronger than SC24 based on sunspot number predictions. The magnetic activity causally connects solar phenomena to space weather effects around planetary objects such as the Earth and consequent impacts on human technologies (Nandy et al., 2023). The National Oceanic and Atmospheric Administration (NOAA) announced in mid October 2024 that the Sun has reached the solar maximum period of SC25 (https://tinyurl.com/3vcpt947). So far, two extreme geomagnetic storms have occurred in SC25: the event of May 2024 (Hayakawa et al., 2024) and the event of October 2024. We expect more intense solar-driven geomagnetic storms to occur over the next few years around the peak of the current sunspot cycle.

The Starlink event of February 2022 taught us that even a minor/moderate geomagnetic storm can significantly enhance satellite orbital drag in VLEO. For instance, Fang et al. (2022) demonstrated with Starlink density data and empirical model results that the thermosphere was quite perturbed between the altitudes of 200 km and 400 km, with density increases of 50%–125% with respect to pre-storm values. Since the satellites were flying low in the thermosphere (at altitudes mostly around 200 km), the satellites encountered downfall before the thrusters were activated for further uplift to higher altitudes (Hapgood et al., 2022). As clearly seen in Figure 1 of Oliveira et al. (2021), orbital drag effects dramatically increase at altitudes below 300 km (see CHAMP and GOCE altitudes during decommissioning) due to increasing density

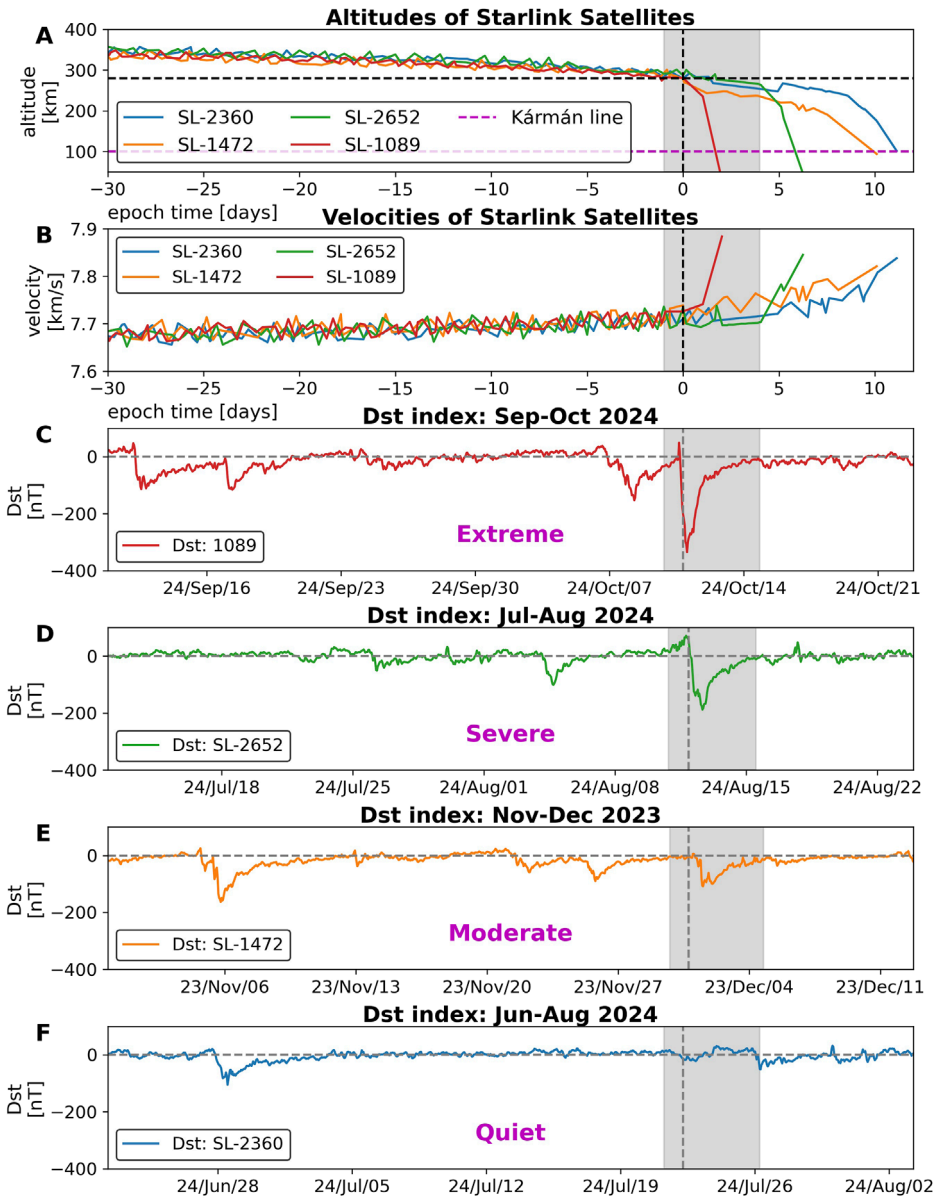

FIGURE 2
Altitudes/velocities and Dst data for four different Starlink satellites during their corresponding decay periods. **(A)**: Starlink altitudes; and **(B)**: Starlink velocities. The following panels indicate Dst index for the corresponding Starlink satellite. **(C)**: Sep-October 2024 (SL-1089); **(D)**: Jul-August 2024 (SL-2652); **(E)**: Nov-December 2023 (SL-1472); and **(F)**: Jun-August 2024 (SL-2360). The dashed vertical lines indicate a reference altitude at 280 km for each satellite. Data are plotted 30 and 10 days around the reference altitude. The grey highlighted area covers 1–4 days around the reference altitude onset.

levels, even during quiet times. Therefore, decommissioning satellite operations deserve special attention for tracking during orbital decay, particularly during geomagnetic storms for safe and accurate reentry operations.

SpaceX has made a commitment to safely de-orbit Starlink satellites in a time period of 2–5 years in order "to keep [ing] space safe, sustainable and accessible, protect [ing] astronauts and satellites in orbit and the public on the ground", as found in the document "Commitment to Space Sustainability (https://api.starlink.com/public-files/Commitment%20to%20Space%20Sustainability.pdf). Since SL-1089 was commissioned in January 2020, most likely it was already in reentry process at its fourth lifetime year when the October 2024 storm took place. As clearly seen in Figure 2A, SL-1089 decayed nearly 200 km within 48 h (10 October to 12 October). Although the satellite was scheduled to be decommissioned on 22 October 2024, as clearly seen in the smooth altitude decay since early September 2024 and reported by space-track.org, the satellite reentered on 12 October 2024. Ashruf et al. (2024) attributed the losses of 12 Starlink satellites to space weather conditions surrounding the 10 May 2024 extreme geomagnetic storm. However, though those satellites decayed nearly 200 km in 3 days, the authors did not make it clear whether the satellites

TABLE 1 IDs and orbital information of the four Starlink satellites used in this study. Satellite launch dates were obtained from https://aerospace.org/reentries/ followed by the satellite NORAD ID. Estimates of the reentry dates are obtained from the last TLE by propagating predictions in time until the satellite reaches the Karman line.

	SL-1089	SL-2652	SL-1472	SL-2360
NORAD ID	44967	48451	45736	47900
Launch epoch	20/01/07 02:19	21/05/09 06:42	20/06/13 09:21	21/03/14 10:01
Last TLE file date	24/10/11 20:41	24/08/17 03:56	23/12/08 20:30	24/08/01 09:18
Epoch of reference altitude	24/10/10 20:00	24/08/11 22:00	23/11/30 18:11	24/07/22 06:00
Predicted reentry epoch	24/10/22 00:00	24/08/25 00:00	23/12/08 00:00	24/07/31 00:00
Reentry epoch	24/10/12 20:41	24/08/18 03:56	23/12/10 20:30	24/08/02 09:18
Day difference in reentry epoch	−10	−7	−2	+2
Satellite age (years)	4.77	3.28	3.49	3.39
Quiet-time decay rate (km/day)	1.82	1.64	1.19	1.81
Storm-time decay rate (km/day)	128.52	38.05	18.34	15.78
Minimum Dst after t_0 (nT)	−335	−188	−108	−76
Geomagnetic activity level	Extreme	Severe	Moderate	Quiet

had already begun their reentries before the storm. As seen in Figure 2C, the extreme storm of October 2024 event had a minimum (quick-look) Dst value of −335 nT. Although the main phase of extreme geomagnetic storms tend to develop quite fast within a few hours (Aguado et al., 2010; Cid et al., 2013), the October 2024 event had a relatively long storm development duration (~11 h). Such a combination of storm intensity and duration can cause extreme enhancements of thermospheric neutral mass density and subsequent orbital drag in LEO/VLEO (Oliveira et al., 2020). As a result, the extreme geomagnetic storm of October 2024 presumably cut the reentry process of SL-1089 short by 10 days. This observation indicates that reentry operations of satellites should be monitored closely during storm times, particularly during extreme events. Such approach will help improve premature losses of satellites, accurate reentry locations, and effective collision-avoidance procedures. Such extreme orbital decay effects should be considered in the future since the number of extreme storms and the number of satellites in LEO/VLEO will be even larger in the years to come (Oliveira et al., 2021).

Finally, it should be pointed out that this is a preliminary analysis of the premature reentry of Starlink-1089 in October 2024. This is due to the use of preliminary data (2024 quick-look/real-time Dst data), and the current lack of density data provided by the satellite. Moreover, the use of less-refined Dst data is enough to determine the storm intensity (represented by minimum Dst values), and the occurrence time of storm main phase onset. Therefore, we recommend further analyses of this event as performed before for the Starlink event of February 2022 by approaching data analyses and numerical/empirical model investigations (Dang et al., 2022; Fang et al., 2022; Berger et al., 2023; Baruah et al., 2024).

Data availability statement

Publicly available datasets were analyzed in this study. This data can be found here: space-track.org.

Author contributions

DO: Conceptualization, Data curation, Formal Analysis, Funding acquisition, Investigation, Methodology, Writing–original draft, Writing–review and editing. EZ: Funding acquisition, Resources, Supervision, Validation, Writing–review and editing. DN: Conceptualization, Formal Analysis, Funding acquisition, Investigation, Validation, Writing–review and editing.

Funding

The author(s) declare that financial support was received for the research, authorship, and/or publication of this article. DMO acknowledges financial support provided by UMBC's START (Strategic Awards for Research Transitions) program (grant # SR25OLIV). DMO and EZ thank the financial support provided by the NASA HGIO program through grant 80NSSC22K0756. DMO and EZ also acknowledge financial support by NASA's Space Weather Science Applications Operations 2 Research. DN's

involvement in space weather research is sustained by the Ministry of Education, Government of India and a private philanthropic grant at the Center of Excellence in Space Sciences India, IISER Kolkata.

Conflict of interest

The authors declare that the research was conducted in the absence of any commercial or financial relationships that could be construed as a potential conflict of interest.

Generative AI statement

The author(s) declare that no Generative AI was used in the creation of this manuscript.

Publisher's note

All claims expressed in this article are solely those of the authors and do not necessarily represent those of their affiliated organizations, or those of the publisher, the editors and the reviewers. Any product that may be evaluated in this article, or claim that may be made by its manufacturer, is not guaranteed or endorsed by the publisher.

Supplementary material

The Supplementary Material for this article can be found online at: https://www.frontiersin.org/articles/10.3389/fspas.2024.1522139/full#supplementary-material

References

Aguado, J., Cid, C., Saiz, E., and Cerrato, Y. (2010). Hyperbolic decay of the Dst index during the recovery phase of intense geomagnetic storms. *J. Geophys. Res.* 115. doi:10.1029/2009JA014658

Akasofu, S.-I. (1966). Electrodynamics of the magnetosphere: geomagnetic storms. *Space Sci. Rev.* 6, 21–143. doi:10.1007/BF00213406

Ashruf, A. M., Bhaskar, A., Vineeth, C., Pant, T. K., and M, A. V. (2024). Loss of 12 Starlink satellites due to pre-conditioning of intense space weather activity surrounding the extreme geomagnetic storm of 10 may 2024. *arXiv:2410.16254*. doi:10.48550/arXiv.2410.16254

Baruah, Y., Roy, S., Sinha, S., Palmerio, E., Pal, S., Oliveira, D. M., et al. (2024). The loss of Starlink satellites in february 2022: how moderate geomagnetic storms can adversely affect assets in low-earth orbit. *Space. Weather* 22, e2023SW003716. doi:10.1029/2023SW003716

Berger, T. E., Dominique, M., Lucas, G., Pilinski, M., Ray, V., Sewell, R., et al. (2023). The thermosphere is a drag: the 2022 Starlink incident and the threat of geomagnetic storms to low Earth orbit space operations. *Space. Weather* 21, e2022SW003330. doi:10.1029/2022SW003330

Bhaskar, A., Hayakawa, H., Oliveira, D. M., Blake, S., Silverman, S., and Ebihara, Y. (2020). An analysis of trouvelot's auroral drawing on 1/2 March 1872: plausible evidence for recurrent geomagnetic storms. *J. Geophys. Res. Space Phys.* 125, e2020JA028227. doi:10.1029/2020JA028227

Bhowmik, P., and Nandy, D. (2018). Prediction of the strength and timing of sunspot cycle 25 reveal decadal-scale space environmental conditions. *Nat. Commun.* 9, 5209. doi:10.1038/s41467-018-07690-0

Boteler, D. H. (2019). A 21st century view of the March 1989 magnetic storm. *Space Weather.* 17, 1427–1441. doi:10.1029/2019SW002278

Bruinsma, S. L., and Forbes, J. M. (2007). Global observation of traveling atmospheric disturbances (TADs) in the thermosphere. *Geophys. Res. Lett.* 34. doi:10.1029/2007GL030243

Chen, G.-m., Xu, J., Wang, W., Lei, J., and Burns, A. G. (2012). A comparison of the effects of CIR– and CME–induced geomagnetic activity on thermospheric densities and spacecraft orbits: case studies. *J. Geophys. Res.* 117. doi:10.1029/2012JA017782

Cid, C., Palacios, J., Saiz, E., Cerrato, Y., Aguado, J., and Guerrero, A. (2013). Modeling the recovery phase of extreme geomagnetic storms. *J. Geophys. Res.* 118, 4352–4359. doi:10.1002/jgra.50409

Clette, F., Lefvre, L., Chatzistergos, T., Hayakawa, H., Carrasco, V. M. S., Arlt, R., et al. (2023). Recalibration of the sunspot-number: status report. *Sol. Phys.* 298, 44. doi:10.1007/s11207-023-02136-3

Dang, T., Li, X., Luo, B., Li, R., Zhang, B., Pham, K., et al. (2022). Unveiling the space weather during the Starlink satellites destruction event on 4 february 2022. *Space Weather.* 20, e2022SW003152. doi:10.1029/2022SW003152

Emmert, J. T. (2015). Thermospheric mass density: a review. *Adv. Space Res.* 56, 773–824. doi:10.1016/j.asr.2015.05.038

Fang, T.-W., Kubaryk, A., Goldstein, D., Li, Z., Fuller-Rowell, T., Millward, G., et al. (2022). Space weather environment during the SpaceX Starlink satellite loss in february 2022. *Space Weather.* 20, e2022SW003193. doi:10.1029/2022SW003193

Gonzalez, W. D., Joselyn, J. A., Kamide, Y., Kroehl, H. W., Rostoker, G., Tsurutani, B. T., et al. (1994). What is a geomagnetic storm? *J. Geophys. Res.* 99, 5771–5792. doi:10.1029/93JA02867

Gopalswamy, N., Barbieri, L., Lu, G., Plunkett, S. P., and Skoug, R. M. (2005). Introduction to the special section: violent Sun-Earth connection events of October-November 2003. *Geophys. Res. Lett.* 32. doi:10.1029/2005GL022348

Hapgood, M., Liu, H., and Lugaz, N. (2022). SpaceX – sailing close to the space weather? *Space Weather.* 20, e2022SW003074. doi:10.1029/2022SW003074

Hayakawa, H., Ebihara, Y., Mishev, A., Koldobskiy, S., Kusano, K., Bechet, S., et al. (2024). The solar and geomagnetic storms in may 2024: a flash data report. *Astrophysical J.* doi:10.3847/1538-4357/ad9335

Hayakawa, H., Ebihara, Y., Willis, D. M., Toriumi, S., Iju, T., Hattori, K., et al. (2019). Temporal and spatial evolutions of a large sunspot group and great auroral storms around the Carrington event in 1859. *Space Weather* 17, 1553–1569. doi:10.1029/2019SW002269

Iyemori, T. (1990). Storm-time magnetospheric currents inferred from mid–latitude geomagnetic field variations. *J. Geomagnetism Geoelectr.* 42, 1249–1265. doi:10.5636/jgg.42.1249

Jacchia, L. G. (1959). Corpuscular radiation and the acceleration of artificial satellites. *Nature* 183, 1662–1663. doi:10.1038/1831662a0

King, J. H., and Papitashvili, N. E. (2005). Solar wind spatial scales in and comparisons of hourly Wind and ACE plasma and magnetic field data. *J. Geophys. Res.* 110, 1–9. doi:10.1029/2004JA010649

Kizner, Z., and Belotserkovskiy, A. (2005). Orbital mechanics of satellites: two-line elements and their usage. *Acta Astronaut.* 56, 43–54. doi:10.1016/j.actaastro.2004.07.001

Knipp, D., Tobiska, W., and Emery, B. (2004). Direct and indirect thermospheric heating sources for solar cycles 21—23. *Sol. Phys.* 224, 495–505. doi:10.1007/s11207-005-6393-4

Krauss, S., Behzadpour, S., Temmer, M., and Lhotka, C. (2020). Exploring thermospheric variations triggered by severe geomagnetic storm on 26 august 2018 using GRACE follow-on data. *J. Geophys. Res. Space Phys.* 125. doi:10.1029/2019JA027731

Krauss, S., Temmer, M., and Vennerstrom, S. (2018). Multiple satellite analysis of the Earth's thermosphere and interplanetary magnetic field variations due to ICME/CIR events during 2003-2015. *J. Geophys. Res. Space Phys.* 123, 8884–8894. doi:10.1029/2018JA025778

Krauss, S., Temmer, M., Veronig, A., Baur, O., and Lammer, H. (2015). Thermospheric and geomagnetic responses to interplanetary coronal mass ejections observed by ACE and GRACE: statistical results. *J. Geophys. Res. Space Phys.* 120, 8848–8860. doi:10.1002/2015JA021702

Launius, R. D. (2004). *Frontiers of space exploration*. Westport, Connecticut: Greenwood Press.

McDowell, J. C. (2018). The edge of space: revisiting the karman line. *Acta Astronaut.* 151, 668–677. doi:10.1016/j.actaastro.2018.07.003

McIntosh, S. W., Leamon, R. J., and Egeland, R. (2023). Deciphering solar magnetic activity: the (solar) hale cycle terminator of 2021. *Front. Astronomy Space Sci.* 10. doi:10.3389/fspas.2023.1050523

Mehta, P. M., Paul, S. N., Crisp, N. H., Sheridan, P. L., Siemes, C., March, G., et al. (2023). Satellite drag coefficient modeling for thermosphere science and mission operations. *Adv. Space Res.* 72, 5443–5459. doi:10.1016/j.asr.2022.05.064

Meng, X., Tsurutani, B. T., and Mannucci, A. J. (2019). The solar and interplanetary causes of superstorms (minimum Dst −250 nT) during the space age. *J. Geophys. Res. Space Phys.* 124, 3926–3948. doi:10.1029/2018JA026425

Nandy, D. (2021). Progress in solar cycle predictions: sunspot cycles 24–25 in perspective. *Sol. Phys.* 296, 54. doi:10.1007/s11207-021-01797-2

Nandy, D., Baruah, Y., Bhowmik, P., Dash, S., Gupta, S., Hazra, S., et al. (2023). Causality in heliophysics: magnetic fields as a bridge between the Sun's interior and the Earth's space environment. *J. Atmos. Solar-Terrestrial Phys.* 248, 106081. doi:10.1016/j.jastp.2023.106081

Oliveira, D. M., and Zesta, E. (2019). Satellite orbital drag during magnetic storms. *Space Weather.* 17, 1510–1533. doi:10.1029/2019SW002287

Oliveira, D. M., Zesta, E., Hayakawa, H., and Bhaskar, A. (2020). Estimating satellite orbital drag during historical magnetic superstorms. *Space Weather.* 18, e2020SW002472. doi:10.1029/2020SW002472

Oliveira, D. M., Zesta, E., Mehta, P. M., Licata, R. J., Pilinski, M. D., Kent Tobiska, W., et al. (2021). The current state and future directions of modeling thermosphere density enhancements during extreme magnetic storms. *Front. Astronomy Space Sci.* 8. doi:10.3389/fspas.2021.764144

Oliveira, D. M., Zesta, E., Schuck, P. W., and Sutton, E. K. (2017). Thermosphere global time response to geomagnetic storms caused by coronal mass ejections. *J. Geophys. Res. Space Phys.* 122 (10), 762–10782. doi:10.1002/2017JA024006

Prölss, G. (2011). Density perturbations in the upper atmosphere caused by the dissipation of solar wind energy. *Surv. Geophys.* 32, 101–195. doi:10.1007/s10712-010-9104-0

Ren, Y., Jin, S., Lu, Y., Gao, H., and Sun, S. (2022). The development status of Starlink and its countermeasures. *Mod. Def. Technol.* 50, 11–17. doi:10.3969/j.issn.1009-086x.2022.02.002

Rhodes, B. (2010). PyEphem: a Python package for high-precision astronomy and satellite tracking

Shi, Y., Zesta, E., Connor, H. K., Su, Y.-J., Sutton, E. K., Huang, C. Y., et al. (2017). High-latitude thermosphere neutral density response to solar wind dynamic pressure enhancement. *J. Geophys. Res. Space Phys.* 122 (11), 11,559–11,578. doi:10.1002/2017JA023889

Sugiura, M. (1964). "Hourly values of equatorial Dst for the IGY," in *Annals of the international geophysical year* (Oxford, United Kingdom: Pergamon Press), 35, 9–48.

Sutton, E. K., Forbes, J. M., and Nerem, R. S. (2005). Global thermospheric neutral density and wind response to the severe 2003 geomagnetic storms from CHAMP accelerometer data. *J. Geophys. Res.* 110, 1–10. doi:10.1029/2004JA010985

von Kármán, T. (1956). The problem of reaching cosmic velocities. *Aeronaut. Eng. Rev.* 15, 18–23.

Wanliss, J. A., and Showalter, K. M. (2006). High-resolution global storm index: Dst versus SYM–H. *J. Geophys. Res.* 111. doi:10.1029/2005JA011034

World Data Center for Geomagnetism, Kyoto, Nose, M., Iyemori, T., Sugiura, M., and Kamei, T.(2015). Geomagnetic Dst index. [Data Set]. (Version v1). *World Data Center*. doi:10.17593/14515-74000

Zesta, E., and Oliveira, D. M. (2019). Thermospheric heating and cooling times during geomagnetic storms, including extreme events. *Geophys. Res. Lett.* 46 (12), 12739–12746. doi:10.1029/2019GL085120

frontiers | Frontiers in Physics

TYPE Original Research
PUBLISHED 10 January 2025
DOI 10.3389/fphy.2024.1503092

Check for updates

OPEN ACCESS

EDITED BY
Yi Wang,
Harbin Institute of Technology,
Shenzhen, China

REVIEWED BY
Yufei Hao,
Chinese Academy of Sciences (CAS), China
Shichen Bai,
Shandong University, China

*CORRESPONDENCE
Xi Lu,
xlu11@alaska.edu,
xi.lu@utdallas.edu
Terry Liu,
terryliuzixu@ucla.edu

RECEIVED 28 September 2024
ACCEPTED 10 December 2024
PUBLISHED 10 January 2025

CITATION
Lu X, Liu T, Chen X, Otto A and Zhang H (2025) Simultaneous observations of MHD hot flow anomaly and kinetic foreshock bubble and their impacts.
Front. Phys. 12:1503092.
doi: 10.3389/fphy.2024.1503092

COPYRIGHT
© 2025 Lu, Liu, Chen, Otto and Zhang. This is an open-access article distributed under the terms of the Creative Commons Attribution License (CC BY). The use, distribution or reproduction in other forums is permitted, provided the original author(s) and the copyright owner(s) are credited and that the original publication in this journal is cited, in accordance with accepted academic practice. No use, distribution or reproduction is permitted which does not comply with these terms.

Simultaneous observations of MHD hot flow anomaly and kinetic foreshock bubble and their impacts

Xi Lu[1,2]*, Terry Liu[3]*, Xingran Chen[1], Antonius Otto[1] and Hui Zhang[1]

[1]Geophysical Institute, University of Alaska Fairbanks, Fairbanks, AK, United States, [2]William B. Hanson Center for Space Sciences, University of Texas at Dallas, Richardson, TX, United States, [3]Department of Earth, Planetary, and Space Sciences, University of California, Los Angeles, Los Angeles, CA, United States

Hot flow anomalies (HFAs) and foreshock bubbles (FBs) are two types of transient phenomena characterized by flow deflected and hot cores bounded by one or two compressional boundaries in the foreshock. Using conjunction observations by the Time History of Events and Macroscale Interactions during Substorms (THEMIS) mission, we present an MHD HFA with a core filled with magnetosheath material around the bow shock and a typical kinetic FB associated with foreshock ions upstream of the bow shock, occurring simultaneously under the same solar wind/interplanetary magnetic field (IMF) conditions. The displacements of the bow shock moving back and forth along the sun-earth line are observed. Electron energy shows enhancements from ~50 keV in the FB to ~100 keV in the HFA core, suggesting additional acceleration process across the bow shock within the transient structure. The magnetosheath response of an HFA core-like structure with particle heating and electron acceleration is observed by the Magnetospheric Multiscale (MMS) mission. Ultralow frequency waves in the magnetosphere modulating cold ion energy are identified by THEMIS, driven by these transient structures. Our study improves our understanding of foreshock transients and suggests that single spacecraft observations are insufficient to reveal the whole picture of foreshock transients, leading to an underestimation of their impacts (e.g., particle acceleration energy and spatial scale of disturbances).

KEYWORDS

hot flow anomalies, foreshock bubbles, magnetohydrodynamics, bow shock, THEMIS

1 Introduction

Hot flow anomalies (HFAs) [1, 2] and foreshock bubbles (FBs) [3–8] are different types of transient structures in the Earth's foreshock region [9]. HFAs are characterized by one or two compressional boundaries and a low-density, heated core with significant

flow deflection [2]. The typical duration and spatial scale of HFAs are a few minutes and 1–2 R_E, respectively [10, 11], and they can extend away from the Earth's bow shock to 4.7 R_E [12]. FBs are observed as a density depletion accompanied by strong heating and flow deflection, followed by a shock boundary on the upstream side [5]. They typically measure 5–10 R_E along the solar wind flow direction [4, 13], and their transverse spatial scale can be as large as the foreshock width seen in global hybrid simulations [5].

A rotational discontinuity (RD) or a tangential discontinuity (TD) can transfer the kinetic energy of foreshock ions to thermal energy, leading to the development of HFAs or FBs through the Hall current driven by demagnetized foreshock ions upstream of the bow shock [14, 15]. In this study, we refer to these as kinetic HFAs and FBs, as they are generated from kinetic effects of foreshock ions. Although the FBs are first believed to be generated only by RDs in the solar wind [5], subsequent observations have shown that the TD can be an efficient driver for FBs as for HFAs [16] if the gyroradii of foreshock ions are larger than the thickness of TDs [3, 4, 17]. When the supersonic solar wind encounters the bow shock, some plasmas is reflected and transitions sunward (see review by [18]). An RD or TD can distort the magnetic field lines, which demagnetize the back-streaming foreshock ions. Depending on how the foreshock ions interact with the RD or TD, either an HFA with one or two compressional boundaries or an FB with a secondary shock can form due to different Hall current geometries through similar kinetic process (e.g., [19, 20]). The newly formed shock upstream of the FB can reflect incoming solar wind and generate a new foreshock region [21], while also accelerating particles through Fermi acceleration as it moves toward the bow shock [22, 23]. With the magnetic field piling up at the upstream shock, electrons can be energized to hundreds of keV through betatron acceleration [24]. Additionally, both observations and simulations show that HFAs and FBs can disturb the local bow shock and further affect the magnetosheath, magnetopause, and, consequently, the magnetosphere (e.g., [13, 25–27]).

MHD HFAs, on the other hand, can be described by MHD models and thus differ from kinetic HFAs (as well as FBs) in their processes of generation, locations, populations and core conditions [28–30]. MHD HFAs are produced by low-density flux tubes upstream of the bow shock, while kinetic HFAs are associated with discontinuities propagating along the bow shock surface [10, 14]. MHD HFAs are generated at the bow shock, whereas kinetic HFAs are generated upstream of the bow shock [2]. The ion distribution within MHD HFAs is more Maxwellian compared to that in kinetic HFAs, which are associated with suprathermal foreshock ions. The densities with the cores of kinetic HFA are consistently lower than the ambient solar wind density, while MHD HFAs exhibit density depletions in their cores relative to the ambient magnetosheath density. This is because MHD HFAs with high-density cores are generated through the interaction between low-density flux tubes and the oblique fast shock, which stretches denser magnetosheath plasmas outwards to fill the core region [28]. The earthward low-density flux tubes are not only solar wind structures but also include other foreshock transients with low density, such as foreshock cavities [31] and foreshock density holes (DHs) [32, 33], which convect with discontinuities that do not directly generate HFAs.

Previous studies show that either the kinetic process or the MHD method can independently form foreshock transients. In this study, conjugate observations reveal that these two formation mechanisms can coexist within a local area. Two spacecraft from the Time History of Events and Macroscale Interactions During Substorms (THEMIS) observed a kinetic FB and an MHD HFA simultaneously. This may enhance our understanding of HFAs and improve comprehension of foreshock transients. Understanding the formation mechanisms is a necessary step toward forecasting the disturbances driven by these transient structures.

2 Data

The Advanced Composition Explorer (ACE) and the Deep Space Climate Observatory (DSCOVR) are used to identify upstream solar wind discontinuities. At the Lagrange 1 (L1) point, solar wind plasma parameters (density, bulk velocity and temperature) are measured by the solar wind electron, proton and alpha monitor (SWEPAM) [34] aboard ACE [35, 36] and the Faraday cup boarded on DSCOVR [37, 38]. The available resolutions of the data from these two instruments are 64 s and ~4.5 s, respectively. Magnetic field data with a 1 s time resolution are provided by the magnetic field experiment (MAG) [39] on ACE and the magnetometer on DSCOVR.

Near the Earth's bow shock, THEMIS [40], consisting of three spacecraft (THA, THD and THE), provides plasma data measured by the electrostatic analyzer (ESA) [41] and magnetic field data from the fluxgate magnetometer (FGM) [42], both with a time resolution of ~2.76 s. The solid state telescope (SST) [43] provides pitch angle and energy spectra of suprathermal electrons.

The Magnetospheric Multiscale Mission (MMS) [44] is used to track the magnetosheath responses caused by foreshock transients. Fast survey mode data for plasma parameters (time resolution ~4.5 s) and magnetic fields (time resolution 1/16 s) are obtained from the fast plasma investigator (FPI) [45] and the flux magnetometers [46], respectively. The energetic particle detector (EDP) provides the electron spectrum (time resolution ~2.5 s) and the pitch angle distribution (time resolution ~19.7 s) through the fly's eye energetic particle sensor (FEEPS) [47].

3 Case study

Multi-point observations of THA and THE on 29 September 2017, show that an HFA with a high-density core (relative to the solar wind density) and a typical FB (Figure 1, marked by purple shadows) formed under the same IMF conditions at ~08:32 UT. Two spacecraft are situated close to the bow shock, with THE positioned nearer to the subsolar point (Figure 1O). They cross the bow shock from the magnetosheath into the foreshock at ~08:26 UT and return to the magnetosheath at ~08:37/08:38 UT (Figures 2E, 3E). The estimated geometries of the bow shock and magnetopause are from the bow shock model [48] and the magnetopause model [49], respectively (black curves in Figure 1O). The y-component of the magnetic fields (B_y) is ~0 on the downstream side of the transients and positive on the upstream side for both observations, indicating a discontinuity corresponding to the transient structures (Figures 1B, I). Before THA and THE return to the magnetosheath,

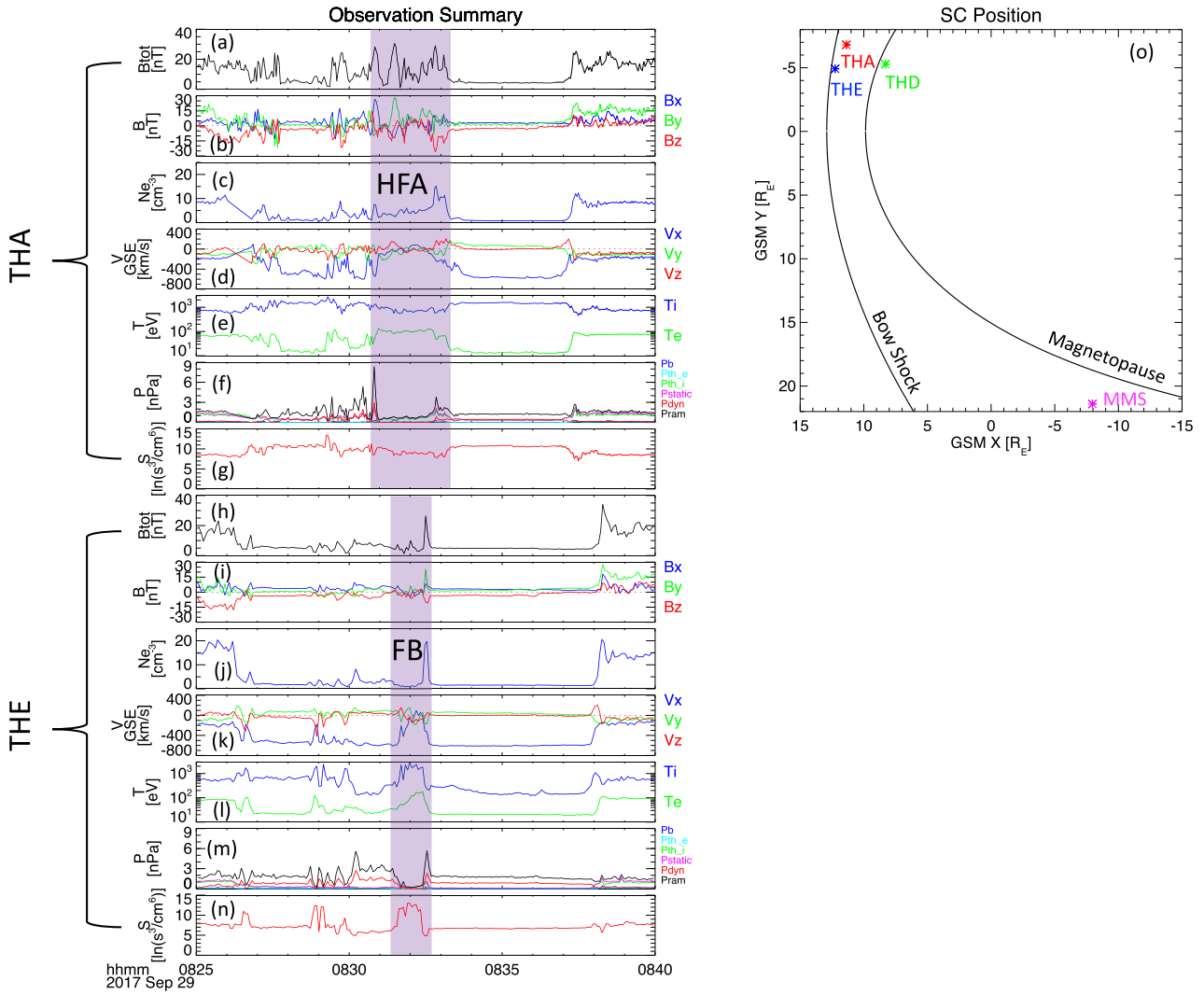

FIGURE 1
THA and THE observations of events on 29 September 2017, and the locations of the spacecraft in GSM coordinates. Panels **(A–G)** and **(I–N)** are magnetic field strength, magnetic field vectors in GSE coordinates, electron density, ion bulk velocity in GSE coordinates, electron and ion temperatures, pressures and the entropy for THA and THE, respectively. Panel **(O)** shows the positions of THA, THD, THE and MMS1 and the two black solid curves are the estimated bow shock and the magnetopause.

B_z changes from negative to 0 around 08:36 UT (Figures 1B, I), suggesting another discontinuity. The bow shock normal, derived from the shock crossings, is between [0.98, 0.02, −0.18] and [0.85, 0.14, −0.50] based on the coplanarity method ($\hat{\boldsymbol{n}}_s = \pm \frac{(\Delta \boldsymbol{B} \times \Delta \boldsymbol{V}) \times \Delta \boldsymbol{B}}{|(\Delta \boldsymbol{B} \times \Delta \boldsymbol{V}) \times \Delta \boldsymbol{B}|}$, where Δ represents the difference between the upstream value and downstream values of the quantities). Both spacecraft are in a quasi-parallel foreshock geometry ($\theta_{Bn} \approx 33° < 45°$) when they cross the bow shock into the solar wind (around 08:28 UT, Figures 1B, I).

The HFA observed by THA, located at [11.3, −6.2, −3.0] R_E in GSE coordinates, has two compressional boundaries in density (Figure 1C). Inside the core region, the electron density is greater than that of the ambient solar wind (~1 cm^{-3}) but lower than the magnetosheath value (~8 cm^{-3}). The flow is significantly deflected from earthward to sunward at the core (Figure 1D), and the temperatures of ions (~750 eV) and electrons (~100 eV) are comparable to those in the magnetosheath (Figure 1E). The total ram pressure ($P_{ram} = 2P_{dyn} + P_{th} + P_B$, where the dynamic pressure $P_{dyn} = n_e m_p v_n^2$, the thermal pressure $P_{th} = n_i k T_i + n_e k T_e$, and the magnetic pressure $P_B = \frac{B^2}{2\mu_0}$) reaches the maximum at the leading boundary (~08:30:50 UT) and drops to less than 1 nPa at the core (Figure 1F). The entropy of the single fluid ($S = -\frac{1}{n}\int d^3v\, f \ln f$ in unit of ln(s^3/cm^6), where n is the number density in cm^{-3} and f is the phase space density distribution in s^3/cm^6) [50] is expressed as the integral of the particle distribution, and the result is overestimated by the foreshock ions in the ambient of the HFA (Figures 1G, 2E). These characteristics indicate that this HFA is an MHD HFA [28–30]. The energy of electrons increases from several keV to above 50 keV (Figures 2C, D), likely due to the betatron acceleration from the compressed magnetic field strength (Figure 2A) at the trailing boundary, moving into the core along the field lines [24]. The ion distributions in the core region are shown in the GSE-XY plane

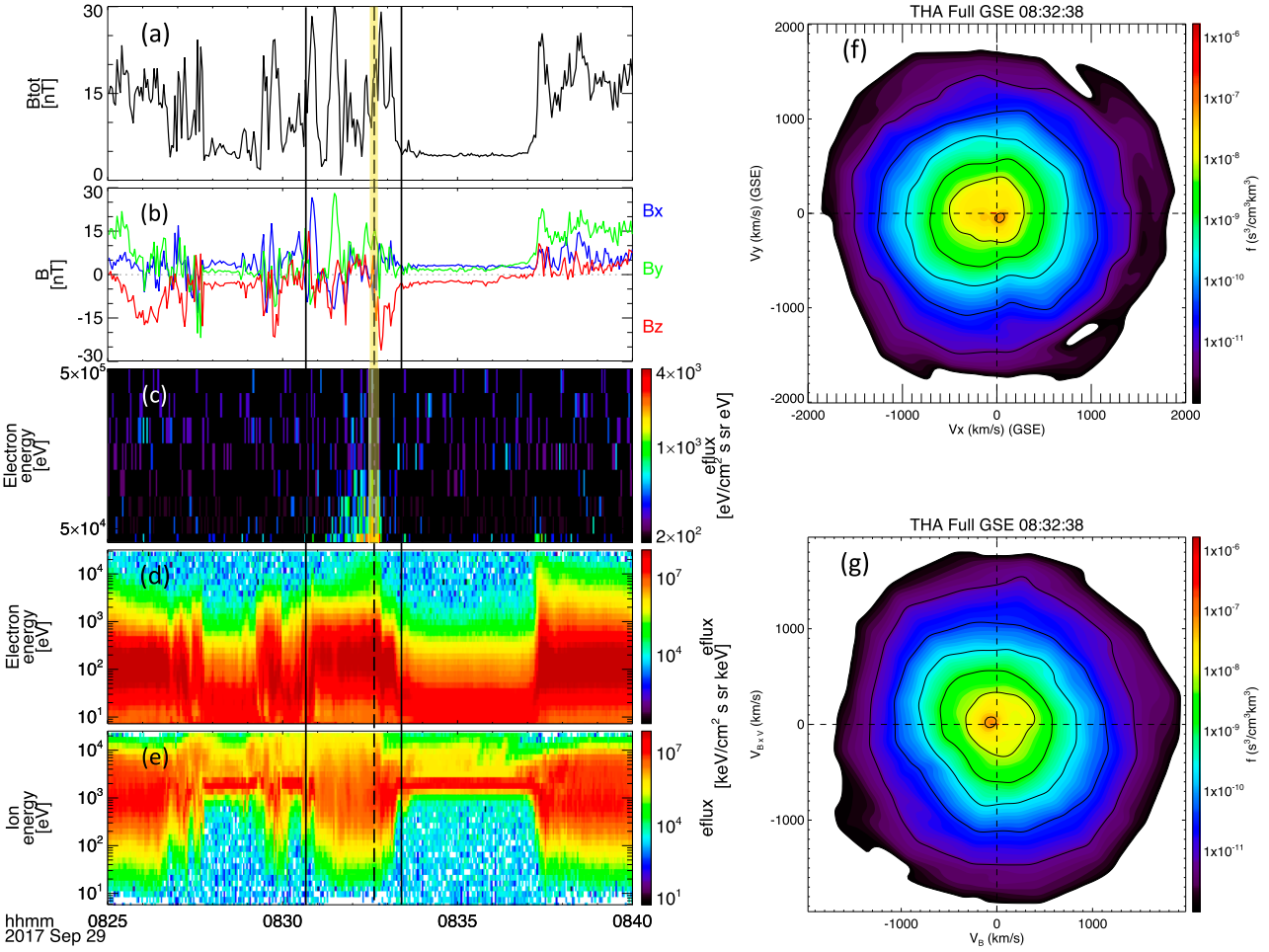

FIGURE 2
THA's observation of **(A)** magnetic field strength, **(B)** magnetic field vectors, **(C, D)** electron spectra, and **(E)** ion spectrum. The black solid lines mark the boundaries of the hot flow anomaly, and the dashed line marks the time of the velocity distributions in panel **(F)** and **(G)**. The energy enhancement is marked by yellow shadow in panels **(A–C)**.

(Figure 2F) and in the BE plane (where the *x*-axis is along the magnetic field direction and the *y*-axis contains the B × V vector) (Figure 2G). The core material consists of a single component (Figure 2E) and exhibits the asymmetry along the magnetic field lines (Figure 2G) [51].

The FB observed by THE, located at [12.2, −4.9 -1.6] R_E in GSE coordinates, shows a low-density core with compressions in magnetic field strength and electron density on the upstream side at ~08:32:30 UT (Figures 1H, J). Using the coplanarity method and mass flux conservation ($V_s = \frac{(n_u V_u - n_d V_d)\cdot \hat{\boldsymbol{n}}_s}{n_u - n_d}$, where the subscript *d* represents the downstream and *u* represents the upstream), we find that the upstream edge is propagating toward Earth with a speed of V_s = 238.12km/s and a normal $\hat{\boldsymbol{n}}_s$ = [−0.96, 0.26, 0.10], consistent with typical FBs (e.g., [7]). There is a strong deflection of the ion bulk flow, along with heating of both electrons and ions, and an enhancement of entropy in the core (Figures 1K, L, N). The total ram pressure drops to nearly 0 in the core and is significantly enhanced at the boundary (Figure 1M), which differs from the MHD HFA. Figures 3C, D show that electrons within the FB are energized to above 50 keV. The gradual increase in electron energy shown in Figure 3D is consistent with Fermi acceleration (see model comparison in Supplementary Figure S1 in the supplementary material) as the FB shock progressively propagates toward the bow shock [22]. Betatron acceleration [24] plays a minor role in the core region but likely dominates at the compressional boundary. For electrons above 30 keV, the acceleration appears weaker compared to that within the HFA. It is possible that the electrons accelerated by the FB could be further accelerated when reaching the HFA, potentially due to further field strength enhancement. The pitch angles of these electrons suggest a direction toward the upstream (Figure 3B), indicating that they are not from the solar wind but are associated with the bow shock and the transient structure. It is clear to see solar wind beam and foreshock ions in the ambient solar wind in the ion distributions (Figures 3F, K). Inside the FB, the solar wind beam weakens and becomes separated from foreshock ions (Figures 3G–J), which is distinct from the observations within the MHD HFA.

At the L1 point, ACE (located at [231.2, 40.8, −17.5] R_E in GSE coordinates) and DSCOVR (located at [227.7, −37.0, 10.4] R_E in GSE coordinates) identified two discontinuities in

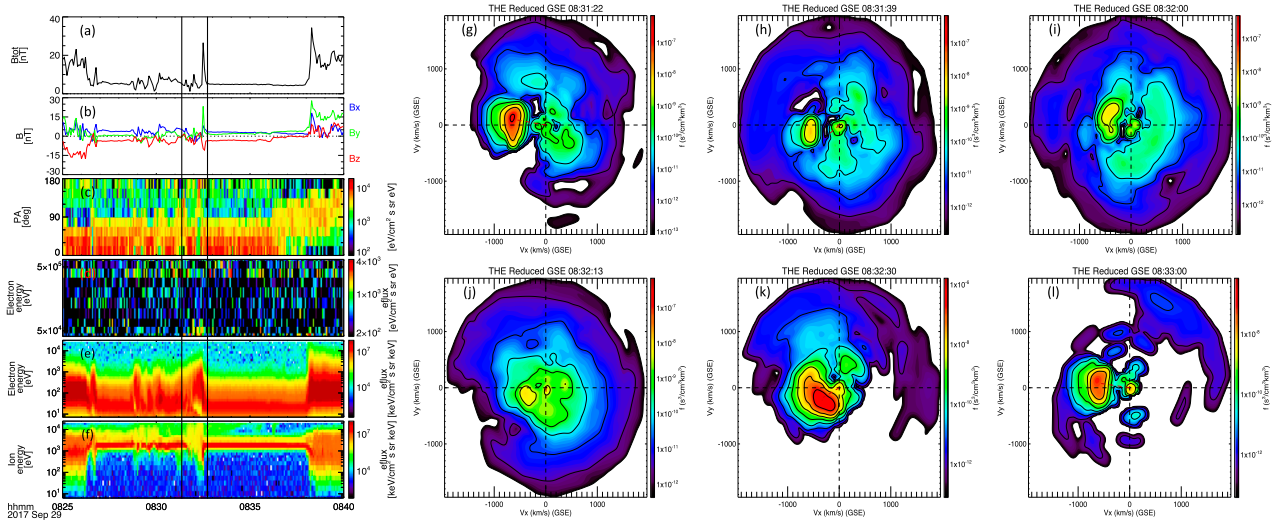

FIGURE 3
THE's observation of **(A)** magnetic field strength, **(B)** magnetic field vectors, **(C)** electron pitch angle for energy above 30 keV, **(D, E)** electron spectra and **(F)** ion spectrum. The black solid lines mark the boundaries of the foreshock bubble. Panels **(G–L)** are velocity distributions, where **(K)** is at the boundary, **(H–J)** are inside foreshock bubble's core and **(G)** and **(L)** are in the ambient solar wind.

the solar wind, indicated by changes in B_y from negative or ~0 to positive, and in B_z from negative to positive or ~0 (Figures 4B, C, H, I, marked by dashed lines; also see comparison in cone angle and clock angle in Supplementary Figure S2 in the supplementary material). The separation between the two discontinuities is 2–4 min, consistent with THEMIS observations. ACE does not show a clear density depletion (Figure 4D). Possibly due to its higher time resolution, DSCOVR observed multiple density depletion structures (Figure 4J), accompanied by proton temperature depletion as well (Figure 4K). Thus, these structures are not pressure balanced (Figure 4L), and their nature and origins remain unclear.

To further confirm that the first discontinuity, who contributes to the formation of the transients, is the same one observed by THEMIS, we compute the normal directions of it for comparison between THEMIS, ACE and DSCOVR. Using the minimum variance analysis (MVA) method on ACE's magnetic field, the normal directions are close to those derived from the cross product ($\hat{\mathbf{n}}_{\mathrm{TD}} = \pm \frac{\mathbf{B}_u \times \mathbf{B}_d}{|\mathbf{B}_u \times \mathbf{B}_d|}$). For the first discontinuity, we have $n_{1_{\mathrm{MVA}}} = \pm[0.90, -0.43, 0.02]$ and $n_{1_{\mathrm{TD}}} = \pm[0.80, -0.44, 0.40]$. The angle between the two normal directions is 22.6°, providing reasonable ground to assume that the first discontinuity is a TD. Measurement at DSCOVR shows that the normal direction of the first TD is $[0.64, -0.57, 0.51]$. Using the cross product method at THEMIS, the normal of the first TD (using background field on two sides of transient structures) is $n_{1_{\mathrm{THA}}} = \pm[0.65, -0.07, 0.76]$ or $n_{1_{\mathrm{THE}}} = \pm[0.68, 0.09, 0.73]$, which are roughly consistent with ACE and DSCOVR observations. The propagation time of the first TD from ACE to THEMIS is calculated to be 31.3 min, using $n_{1_{\mathrm{TD}}}$ and $V_{sw} = [-634.4, -15.4, -14.6]$ km/s, which roughly align with observed times (~40 min). The ~9 min discrepancy may arise from measurement uncertainty from ACE (which is currently not well calibrated), leading to a deviation from the correct direction in the calculation. From the DSCOVR data, the estimated duration is calculated to be 37.9 min, which agrees with the observation and is considered more reliable.

Approximately 5 min after the observations around the bow shock by THEMIS, MMS1 (located at [-7.9, 21.2, 6.3] R_E in GSE coordinates on the dusk side) in the magnetosheath detects the same magnetic field profile with an HFA core-like structure (Figure 5, marked in purple shadow). The density drops from ~7.0 cm^{-3} to 2.3 cm^{-3}, followed by an enhancement to 13.3 cm^{-3} (Figure 5C). The bulk velocity is slightly deflected, averaging to $V_{M'sh} = [-465.0, 183.7, 87.8]$ km/s (Figure 5D). Electron and ion temperatures are doubled in the low-density region compared to the ambient conditions (Figures 5E, F). The entire structure is pressure-balanced (Figure 5G). Some electrons are observed to be energized above 50 keV in the spectra around 08:36–08:38 UT (Figures 5I, J). The pitch angle of the energetic electrons is anti-parallel to the magnetic field within the structure and mainly parallel in the background (also see Supplementary Figure S3 in the supplementary material). Because the IMF is sunward, the localized anti-parallel asymmetry suggests that these energetic electrons locally originate from the bow shock side (Figure 5H), further confirming that the transient structure acts as an accelerator. Using the coplanarity method and the conservation of mass flux, the upstream boundary of the HFA moves in the direction of $\hat{\boldsymbol{n}}_s = [-0.93, 0.33, 0.15]$ at a speed $V_s = 153.0$km/s. The calculated time delay from the THEMIS location to MMS is ~6 min, based on the TD normal direction measured by DSCOVR, which is consistent with the observation.

THD on the downstream side of THA and THE (Figure 1O; around the same MLT sector) observes clear ULF waves (Figure 6C) in the magnetosphere [52], with a period comparable to the time

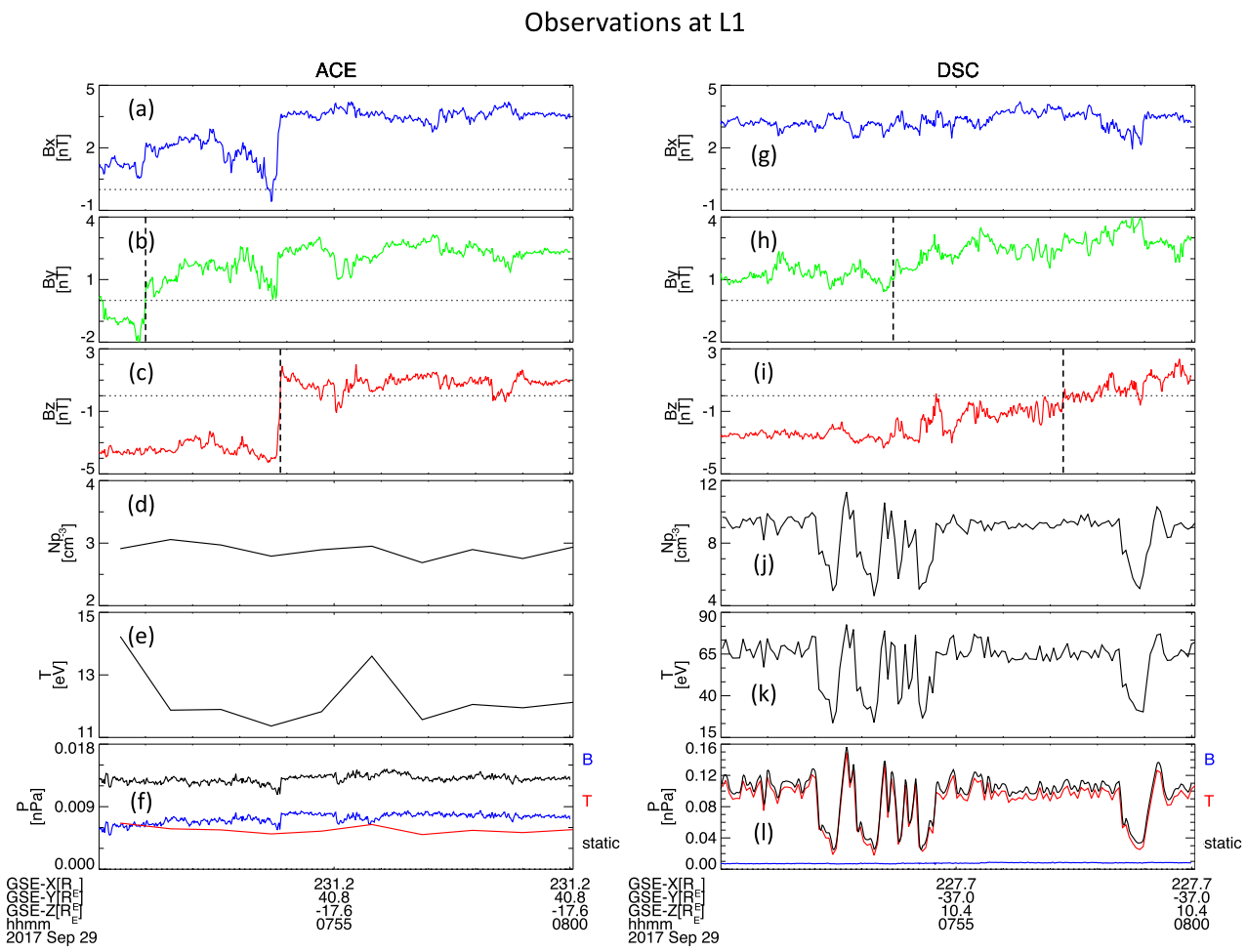

FIGURE 4
ACE and DSCOVR observations in the upstream solar wind. Panels **(A–C)** and **(G–I)** are magnetic field vectors in GSE coordinates. **(D, J)** are proton density, and **(E, K)** are proton temperatures. **(F, L)** show the magnetic pressures, thermal pressures and static pressures. Four dash lines mark two discontinuities across and after the transients.

scale of the MHD HFA. The velocity oscillations associated with the ULF waves (Figure 6E) modulate the energy of cold ions (Figure 6H), consistent with Wang et al. [17]. This modulation causes cold ion energy to periodically increase to levels detectable by ESA, thereby affecting the ion temperature (Figure 6F). These conjunction observations from THEMIS to MMS indicate that the transient structures are localized structures convecting with the discontinuities from the dawn side to the dusk side, continuously accelerating electrons and disturbing the local magnetosphere.

4 Discussion and summary

Using conjunction observations from three THEMIS spacecraft and one MMS spacecraft, we demonstrate that a kinetic FB and an MHD HFA can occur simultaneously, accelerating electrons up to 100 keV and locally disturbing the magnetosheath and magnetosphere while convecting from the dawn side to the dusk side with solar wind discontinuities. The coexistence of an FB and an HFA indicates the limitation of single spacecraft observations, which may not reveal the full scope of foreshock transients. For example, if only one spacecraft had been observing the small FB, the electron acceleration energy (~50 keV vs ~100 keV) and the scale (~1 min vs. ~3 min) of the disturbances in the bow shock, magnetosheath, and magnetosphere could have been significantly underestimated. The existence of MHD HFAs might also have been overlooked. In the future, more conjunction observations are essential to enhance our understanding of the formation and impacts of foreshock transients.

In the previous study, a 2.5-D global hybrid simulation reproduced both an FB and an HFA coexisting with a single discontinuity (see run 6 in [6]). We observe this situation for the first time. In the simulation, as a rotational discontinuity (RD) moves into the foreshock, a planar FB can form due to the interaction between the RD and the back-streaming ions. When the RD continues to convect and interacts with the bow shock, the FB dissipates while an HFA forms. The core of an FB can shift the displacements of the bow shock and magnetosheath outward due to its low dynamic pressure, potentially acting as a

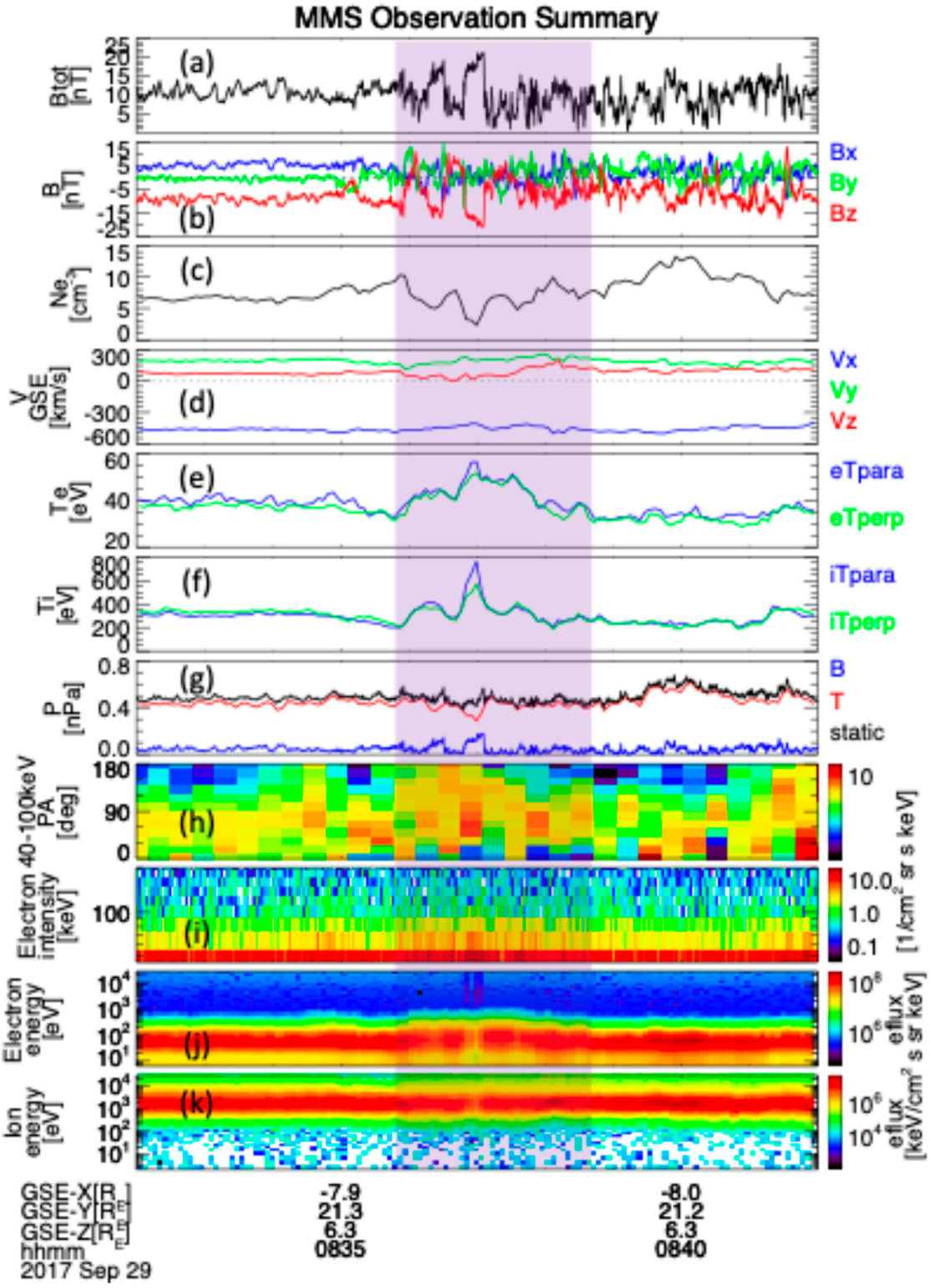

FIGURE 5
MMS observation in the magnetosheath. Panels are **(A)** magnetic field strength, **(B)** magnetic field vectors in GSE coordinates, **(C)** electron density, **(D)** ion bulk velocity, **(E)** electron temperatures, **(F)** ion temperatures, **(G)** magnetic pressure, thermal pressure and static pressure, **(H)** pitch angle of electrons between 40 and 100 keV, **(I)** electron intensity above 50 keV, **(J)** electron energy spectrum and **(K)** ion energy spectrum.

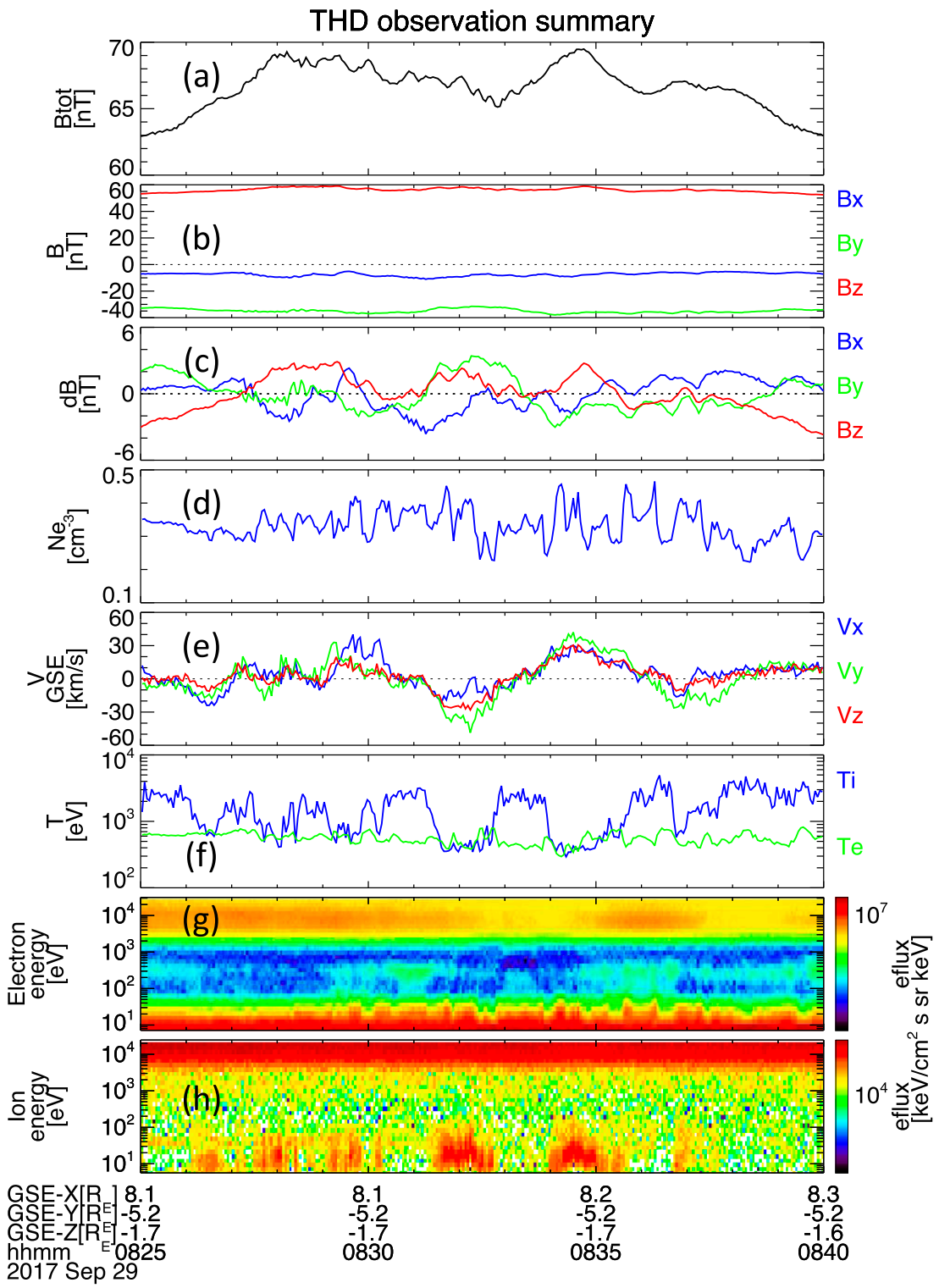

FIGURE 6
THD observation in the magnetosphere. Panels are **(A)** magnetic field strength, **(B)** magnetic field vectors in GSE coordinates, **(C)** magnetic field variations relative to the time average dB, **(D)** electron density, **(E)** ion bulk velocity, **(F)** ion and electron temperatures, **(G)** electron energy spectrum and **(H)** ion energy spectrum.

low-density flux tube that generates HFAs and explains the simultaneous observations. However, in our cases, the FB itself is unlikely large enough to be the direct driver, so there could be a combination of other processes. Previous observations and simulations by Otto and Zhang [28] indicate that a low-density flux tube can drive MHD HFAs, such as those observed by DSCOVR. This low-density flux tube does not have to be solar wind structures, but can also be some other foreshock transients, such as foreshock

density holes [29, 30, 33] and foreshock cavities [53]. Further analysis is still needed to uncover the mechanisms behind the coexistence of an FB and an HFA.

How electrons are accelerated to 100 keV around the bow shock remains an open question. Our results suggest a possibility of multi-step acceleration. Electrons may first be energized within a foreshock transient, e.g., through Fermi acceleration. As these electrons reach the bow shock along with the foreshock transient, the significant enhancement of field strength associated with the development of an MHD HFA may further energize them through betatron acceleration and other possible mechanisms. This scenario suggests that foreshock transients could energize electrons through an additional step when interacting with the bow shock, leading to higher acceleration capability than previously thought. Further observations and modeling efforts are needed to confirm this scenario.

Data availability statement

Publicly available datasets were analyzed in this study. This data can be found here: MMS data are available at MMS Science Data Center (https://lasp.colorado.edu/mms/sdc/public/). THEMIS data are available at http://themis.ssl.berkeley.edu/index.shtml. ACE and DSCOVR data are available at NASA's Coordinated Data Analysis Web (CDAWeb, https://cdaweb.gsfc.nasa.gov).

Author contributions

XL: Formal analysis, Investigation, Visualization, Writing-original draft, Writing–review and editing. TL: Conceptualization, Formal analysis, Funding acquisition, Investigation, Methodology, Validation, Writing–review and editing. XC: Writing–review and editing. AO: Conceptualization, Writing–review and editing. HZ: Conceptualization, Writing–review and editing.

Funding

The author(s) declare that financial support was received for the research, authorship, and/or publication of this article. This work was supported by NSF award AGS-2247760 to TL.

Acknowledgments

T.Z.L. acknowledges ISSI team led by Primoz Kajdic for helpful discussion. We thank the SPEDAS team and the NASA Coordinated Data Analysis Web (CDAWeb, http://cdaweb.gsfc.nasa.gov/). THEMIS dataset is available at https://themis.ssl.berkeley.edu/index.shtml. MMS dataset is available at https://lasp.colorado.edu/mms/sdc/public/.

Conflict of interest

The authors declare that the research was conducted in the absence of any commercial or financial relationships that could be construed as a potential conflict of interest.

Generative AI statement

The author(s) declare that no Generative AI was used in the creation of this manuscript.

Publisher's note

All claims expressed in this article are solely those of the authors and do not necessarily represent those of their affiliated organizations, or those of the publisher, the editors and the reviewers. Any product that may be evaluated in this article, or claim that may be made by its manufacturer, is not guaranteed or endorsed by the publisher.

Supplementary material

The Supplementary Material for this article can be found online at: https://www.frontiersin.org/articles/10.3389/fphy.2024.1503092/full#supplementary-material

References

1. Schwartz SJ, Chaloner CP, Christiansen PJ, Coates AJ, Hall DS, Johnstone AD, et al. An active current sheet in the solar wind. *Nature* (1985) 318(6043):269–71. doi:10.1038/318269a0

2. Zhang H, Sibeck DG, Zong QG, Gary SP, McFadden JP, Larson D, et al. Time history of events and macroscale interactions during substorms observations of a series of hot flow anomaly events. *J Geophys Res Space Phys* (2010) 115(A12). doi:10.1029/2009ja015180

3. Liu Z, Turner DL, Angelopoulos V, Omidi N. THEMIS observations of tangential discontinuity-driven foreshock bubbles. *Geophys Res Lett* (2015) 42(19):7860–6. doi:10.1002/2015gl065842

4. Liu TZ, Turner DL, Angelopoulos V, Omidi N. Multipoint observations of the structure and evolution of foreshock bubbles and their relation to hot flow anomalies. *J Geophys Res Space Phys* (2016) 121(6):5489–509. doi:10.1002/2016ja022461

5. Omidi N, Eastwood JP, Sibeck DG. Foreshock bubbles and their global magnetospheric impacts. *J Geophys Res Space Phys* (2010) 115(A6). doi:10.1029/2009ja014828

6. Omidi N, Lee SH, Sibeck DG, Turner DL, Liu TZ, Angelopoulos V. Formation and topology of foreshock bubbles. *J Geophys Res Space Phys* (2020) 125(9):e2020JA028058. doi:10.1029/2020ja028058

7. Turner DL, Omidi N, Sibeck DG, Angelopoulos V. First observations of foreshock bubbles upstream of Earth's bow shock: characteristics and comparisons to HFAs. *J Geophys Res Space Phys* (2013) 118(4):1552–70. doi:10.1002/jgra.50198

8. Turner DL, Liu TZ, Wilson III LB, Cohen IJ, Gershman DG, Fennell JF, et al. Microscopic, multipoint characterization of foreshock bubbles with Magnetospheric Multiscale (MMS). *J Geophys Res Space Phys* (2020) 125(7):e2019JA027707. doi:10.1029/2019ja027707

9. Eastwood JP, Lucek EA, Mazelle C, Meziane K, Narita Y, Pickett J, et al. The foreshock. *Space Sci Rev* (2005) 118:41–94. doi:10.1007/s11214-005-3824-3

10. Schwartz SJ, Paschmann G, Sckopke N, Bauer TM, Dunlop M, Fazakerley AN, et al. Conditions for the formation of hot flow anomalies at Earth's bow shock. *J Geophys Res Space Phys* (2000) 105(A6):12639–50. doi:10.1029/1999ja000320

11. Facskó G, Nemeth Z, Erdős G, Kis A, Dandouras I. A global study of hot flow anomalies using Cluster multi-spacecraft measurements. *Ann geophysicae* (2009) 27(5):2057–76. doi:10.5194/angeo-27-2057-2009

12. Liu TZ, Wang CP, Wang B, Wang X, Zhang H, Lin Y, et al. ARTEMIS observations of foreshock transients in the midtail foreshock. *Geophys Res Lett* (2020) 47(21):e2020GL090393. doi:10.1029/2020gl090393

13. Archer MO, Turner DL, Eastwood JP, Schwartz SJ, Horbury TS. Global impacts of a foreshock bubble: magnetosheath, magnetopause and ground-based observations. *Planet Space Sci* (2015) 106:56–66. doi:10.1016/j.pss.2014.11.026

14. Thomas VA, Winske D, Thomsen MF, Onsager TG. Hybrid simulation of the formation of a hot flow anomaly. *J Geophys Res Space Phys* (1991) 96(A7):11625–32. doi:10.1029/91ja01092

15. Liu TZ, An X, Zhang H, Turner D. Magnetospheric multiscale observations of foreshock transients at their very early stage. *The Astrophysical J* (2020) 902(1):5. doi:10.3847/1538-4357/abb249

16. Omidi N, Sibeck DG. Formation of hot flow anomalies and solitary shocks. *J Geophys Res Space Phys* (2007) 112(A1). doi:10.1029/2006ja011663

17. Wang C-P, Wang X, Liu TZ, Lin Y. A foreshock bubble driven by an IMF tangential discontinuity: 3D global hybrid simulation. *Geophys Res Lett* (2021) 48:e2021GL093068. doi:10.1029/2021GL093068

18. Zhang H, Zong Q, Connor H, Delamere P, Facskó G, Han D, et al. Dayside transient phenomena and their impact on the magnetosphere and ionosphere. *Space Sci Rev* (2022) 218(5):40. doi:10.1007/s11214-021-00865-0

19. Vu A, Liu TZ, Zhang H, Delamere P. Hybrid simulations of a tangential discontinuity-driven foreshock bubble formation in comparison with a hot flow anomaly formation. *J Geophys Res Space Phys* (2022) 127(6):e2021JA029973. doi:10.1029/2021ja029973

20. Vu A, Liu TZ, Angelopoulos V, Zhang H. 2.5-D local hybrid simulations of hot flow anomalies under various magnetic field geometries. *J Geophys Res Space Phys* (2024) 129(5):e2023JA032301. doi:10.1029/2023ja032301

21. Liu TZ, Hietala H, Angelopoulos V, Turner DL. Observations of a new foreshock region upstream of a foreshock bubble's shock. *Geophys Res Lett* (2016) 43(10):4708–15. doi:10.1002/2016gl068984

22. Liu TZ, Lu S, Angelopoulos V, Hietala H, Wilson LB, III. Fermi acceleration of electrons inside foreshock transient cores. *J Geophys Res Space Phys* (2017) 122:9248–63. doi:10.1002/2017JA024480

23. Liu TZ, Lu S, Angelopoulos V, Lin Y, Wang XY. Ion acceleration inside foreshock transients. *J Geophys Res Space Phys* (2018) 123(1):163–78. doi:10.1002/2017ja024838

24. Liu TZ, Angelopoulos V, Lu S. Relativistic electrons generated at Earth's quasi-parallel bow shock. *Sci Adv* (2019) 5(7):eaaw1368. doi:10.1126/sciadv.aaw1368

25. Wang B, Liu T, Nishimura Y, Zhang H, Hartinger M, Shi X, et al. Global propagation of magnetospheric Pc5 ULF waves driven by foreshock transients. *J Geophys Res Space Phys* (2020) 125(12):e2020JA028411. doi:10.1029/2020ja028411

26. Wang B, Zhang H, Liu Z, Liu T, Li X, Angelopoulos V. Energy modulations of magnetospheric ions induced by foreshock transient-driven ultralow-frequency waves. *Geophys Res Lett* (2021) 48(10):e2021GL093913. doi:10.1029/2021gl093913

27. Wang B, Liu J, Han D, Wang Y, Feng X. Statistical study of hot flow anomaly induced ground magnetic ultra-low frequency oscillations. *J Geophys Res Space Phys* (2024) 129(8):e2024JA032667. doi:10.1029/2024ja032667

28. Otto A, Zhang H. Bow shock transients caused by solar wind dynamic pressure depletions. *J Atmos Solar-Terrestrial Phys* (2021) 218:105615. doi:10.1016/j.jastp.2021.105615

29. Lu X, Otto A, Zhang H, Liu T, Chen X. The bow shock and magnetosheath responses to density depletion structures. *J Geophys Res Space Phys* (2024) 129(5):e2024JA032566. doi:10.1029/2024ja032566

30. Lu X, Otto A, Zhang H, Liu T, Chen X. Observations and simulations of a double-core hot flow anomaly. *Geophys Res Lett* (2024) 51:e2024GL110363. doi:10.1029/2024GL110363

31. Sibeck DG, Phan TD, Lin R, Lepping RP, Szabo A. Wind observations of foreshock cavities: a case study. *J Geophys Res Space Phys* (2002) 107(A10). doi:10.1029/2001ja007539

32. Parks GK, Lee E, Mozer F, Wilber M, Lucek E, Dandouras I, et al. Larmor radius size density holes discovered in the solar wind upstream of Earth's bow shock. *Phys Plasmas* (2006) 13(5). doi:10.1063/1.2201056

33. Lu X, Zhang H, Liu T, Vu A, Pollock C, Wang B. Statistical study of foreshock density holes. *J Geophys Res Space Phys* (2022) 127(4):e2021JA029981. doi:10.1029/2021ja029981

34. McComas DJ, Bame SJ, Barker P, Feldman WC, Phillips JL, Riley P, et al. Solar wind electron proton alpha monitor (SWEPAM) for the Advanced Composition Explorer. In: *The advanced composition explorer mission* (1998).

35. Chiu MC, Von-Mehlem UI, Willey CE, Betenbaugh TM, Maynard JJ, Krein JA, et al. ACE spacecraft. *Space Sci Rev* (1998) 86:257–84. doi:10.1007/978-94-011-4762-0_13

36. Stone EC, Frandsen AM, Mewaldt RA, Christian ER, Margolies D, Ormes JF, et al. The advanced composition explorer. *Space Sci Rev* (1998) 86:1–22. doi:10.1007/978-94-011-4762-0_1

37. Valero FP, Herman J. DSCOVR, the first Deep space earth and solar observatory. *Cell Biol Instrumentation: UV Radiat Nitric Oxide Cell Death Plants* (2006) 371.

38. Burt J, Smith B. Deep space climate observatory: the DSCOVR mission. In: *2012 IEEE aerospace conference* (2012).

39. Smith CW, L'Heureux J, Ness NF, Acuna MH, Burlaga LF, Scheifele J. The ACE magnetic fields experiment. In: *The advanced composition explorer mission* (1998).

40. Angelopoulos V. *The THEMIS mission*. New York: Springer (2009).

41. McFadden JP, Carlson CW, Larson D, Ludlam M, Abiad R, Elliott B, et al. The THEMIS ESA plasma instrument and in-flight calibration. *Space Sci Rev* (2008) 141:277–302. doi:10.1007/s11214-008-9440-2

42. Auster HU, Glassmeier KH, Magnes W, Aydogar O, Baumjohann W, Constantinescu D, et al. The THEMIS fluxgate magnetometer. *Space Sci Rev* (2008) 141:235–64. doi:10.1007/s11214-008-9365-9

43. Angelopoulos V, Sibeck D, Carlson CW, McFadden JP, Larson D, Lin RP, et al. First results from the THEMIS mission. *Space Sci Rev* (2008) 141:453–76. doi:10.1007/s11214-008-9378-4

44. Burch JL, Moore TE, Torbert RB, Giles BH. Magnetospheric multiscale overview and science objectives. *Space Sci Rev* (2016) 199:5–21. doi:10.1007/s11214-015-0164-9

45. Pollock C, Moore T, Jacques A, Burch J, Gliese U, Saito Y, et al. Fast plasma investigation for magnetospheric multiscale. *Space Sci Rev* (2016) 199:331–406. doi:10.1007/s11214-016-0245-4

46. Torbert RB, Russell CT, Magnes W, Ergun RE, Lindqvist PA, LeContel O, et al. The FIELDS instrument suite on MMS: scientific objectives, measurements, and data products. *Space Sci Rev* (2016) 199:105–35. doi:10.1007/s11214-014-0109-8

47. Mauk BH, Blake JB, Baker DN, Clemmons JH, Reeves GD, Spence HE, et al. The energetic particle detector (EPD) investigation and the energetic ion spectrometer (EIS) for the magnetospheric multiscale (MMS) mission. *Space Sci Rev* (2016) 199:471–514. doi:10.1007/s11214-014-0055-5

48. Wu DJ, Chao JK, Lepping RP. Interaction between an interplanetary magnetic cloud and the Earth's magnetosphere: motions of the bow shock. *J Geophys Res Space Phys* (2000) 105(A6):12627–38. doi:10.1029/1999ja000265

49. Shue JH, Song P, Russell CT, Steinberg JT, Chao JK, Zastenker G, et al. Magnetopause location under extreme solar wind conditions. *J Geophys Res Space Phys* (1998) 103(A8):17691–700. doi:10.1029/98ja01103

50. Bittencourt JA. *Fundamentals of plasma physics*. Springer Science and Business Media (2013).

51. Liu TZ, Angelopoulos V, Vu A, Zhang H, Otto A, Zhang K. THEMIS observations of magnetosheath-origin foreshock ions. *J Geophys Res Space Phys* (2024) 129(2):e2023JA031969. doi:10.1029/2023ja031969

52. Hartinger MD, Turner DL, Plaschke F, Angelopoulos V, Singer H. The role of transient ion foreshock phenomena in driving Pc5 ULF wave activity. *J Geophys Res Space Phys* (2013) 118:299–312. doi:10.1029/2012JA018349

53. Sibeck DG, Lee SH, Omidi N, Angelopoulos V. Foreshock cavities: direct transmission through the bow shock. *J Geophys Res Space Phys* (2021) 126(5):e2021JA029201. doi:10.1029/2021ja029201

frontiers | Frontiers in Astronomy and Space Sciences

TYPE Opinion
PUBLISHED 21 March 2025
DOI 10.3389/fspas.2025.1565669

Check for updates

OPEN ACCESS

EDITED BY
Nithin Sivadas,
National Aeronautics and Space Administration, United States

REVIEWED BY
Qusai Al Shidi,
West Virginia University, United States

*CORRESPONDENCE
U. Villante,
umberto.villante@aquila.infn.it

RECEIVED 23 January 2025
ACCEPTED 19 February 2025
PUBLISHED 21 March 2025

CITATION
Villante U (2025) Comment to the paper "Azimuthal size scales of solar wind periodic density structures" by Di Matteo et al. (2024). *Front. Astron. Space Sci.* 12:1565669. doi: 10.3389/fspas.2025.1565669

COPYRIGHT
© 2025 Villante. This is an open-access article distributed under the terms of the Creative Commons Attribution License (CC BY). The use, distribution or reproduction in other forums is permitted, provided the original author(s) and the copyright owner(s) are credited and that the original publication in this journal is cited, in accordance with accepted academic practice. No use, distribution or reproduction is permitted which does not comply with these terms.

Comment to the paper "Azimuthal size scales of solar wind periodic density structures" by Di Matteo et al. (2024)

U. Villante*

Dipartimento Scienze Fisiche e Chimiche, Università and Area di Ricerca in Astrogeofisica, L'Aquila, Italy

KEYWORDS

solar wind, magnetosphere, fluctuations, discrete frequencies, methods of analysis

Introduction

In a recent paper, Di Matteo et al. (2024) proposed a sophisticated analysis of the quasi-periodic variations of the solar wind (*SW*) number density (N_{SW}), referred to as Periodic Density Structures (*PDSs*; $f \approx 0.45$–4.65 mHz), which were observed by two spacecraft (Wind and ARTEMIS-P1) in the interplanetary medium. They obtained results which, in my opinion, are important also in the context of the scientific debate regarding the fluctuations at discrete frequencies observed in the magnetosphere (mostly in range $f \approx$ 1–5 mHz). Indeed, the occurrence, the origin and the characteristics of these fluctuations (which play an important role in the magnetospheric dynamics) have been examined, in the last decades, in a large number of papers, often with controversial results mainly related to their relationships with *SW* fluctuations at similar frequencies and to the possible existence (and stability) of sets of favorite magnetospheric frequencies [review by Di Matteo and Villante (2024) and papers therein referenced]. On the other hand, in recent years, some papers highlighted some critical aspects of the data analysis which might have influenced the conclusions of several investigations. In particular, Di Matteo and Villante (2017) and Di Matteo and Villante (2018) applied two different methods adopted in the scientific literature (the Welch method, *WM*, and the Multitaper method and F-test, *MTM*) to the same data sets and showed that the *WM*/*MTM* agreement in the identification of the wave occurrence and frequency estimate might occur only in ≈50% of cases, both in the *SW* and in the magnetosphere. In addition, an analysis conducted by Villante et al. (2022) revealed different characteristics in the fluctuations of the *SW* dynamic pressure (P_{SW}) when the same *SW* stream was observed by two spacecraft at different places in front of the magnetosphere. All these aspects make ambiguous the analysis of the relationships between the *SW* and the magnetospheric fluctuations; as we discuss in this note, the results proposed by Di Matteo et al. (2024) add other interesting elements in this context.

The comparison between PSDs and magnetospheric fluctuations at discrete frequencies

In their analysis, Di Matteo et al. (2024) examined the characteristics of *PDS* with periods ranging from a few minutes to a few hours (radial length scale of tens to several thousands of megameters). In particular, they conducted a robust estimate of the spectral properties of the N_{SW} fluctuations (they also examined the interplanetary magnetic field's intensity, not

considered in the present note) in the frequency range $f \approx$ 0.45–4.65 mHz, that were associated with 68 *PDS*s observed by Wind and ARTEMIS-P1 in front of the magnetosphere over 9 years (2012–2020) and occurring during intervals of high density (maximum values above 15 cm^{-3}), slow *SW* streams (below 450 km/s); they also determined the level of coherence between the events observed by the two spacecraft, obtaining interesting results. Namely,

- 79 out of 158 events of N_{SW} fluctuations identified by Wind occurred in the same frequency range (within ±0.3 mHz) of the corresponding events detected by P1 (P1 identified 166 events). In practice, for the same *SW* parcels, comparable frequencies were estimated at the spacecraft positions for about half of events; meanwhile, the frequency to be attributed to the other half of the events that will impact the magnetosphere is uncertain. In this context it is interesting to remind that Viall et al. (2009), who examined the frequencies of *PDSs* and dayside magnetospheric oscillations in the $f = 0.5$–5.0 mHz range using 11 years of Wind and GOES observations (1995–2005), reported that in ≈54% of the *SW* segments with a spectral peak, at least one of the same discrete frequencies was statistically significant in the corresponding magnetospheric data segment. Eventually, according to the results of Di Matteo et al. (2024), this percentage of correspondence between the frequencies of *SW* and magnetospheric fluctuations might be related to *SW* events in which the estimated frequencies of fluctuations would have been the same at different places in front of the magnetosphere.
- Considering only the events characterized by high level of coherence (43) between Wind and P1, the percentage of agreement is higher below $f \approx 1$ mHz (≈59%), progressively decreasing and practically vanishing at higher frequencies. Reinforcing previous arguments, these conclusions are important in this context in that the frequencies below ≈1 mHz have been rarely explored in the magnetosphere; consequently, the analysis of the relationship between *SW* and magnetospheric fluctuations could likely have been investigated mostly in a frequency range ($f \approx$ 1–5 mHz) in which the agreement between the frequencies of *SW* fluctuations observed at two different places might be poor.
- In extreme cases, moreover, Wind and P1 provided, for the same *PDS*, very different results: for example, for a parcel observed on 1 January 2014, Wind identified a single fluctuation event ($f \approx 1.8$ mHz; **Table 1** in Di Matteo et al., 2024) while four peaks emerged in the power spectra at P1 ($f \approx$ 0.7, ≈1.5, ≈2.2, ≈3.7 mHz). It confirms that the aspects of the *SW* fluctuations often differ significantly between the observations of the same *SW* parcel at different places (Villante et al., 2022; **Figure 2**). All these arguments suggest caution before assuming a definite identification of the characteristics of the compressive fluctuations impinging the magnetosphere when the event is observed by a single spacecraft (Di Matteo and Sivadas, 2022).
- Obviously, the global frequency distributions of events at Wind and P1 are not the same (**Figure 5** in Di Matteo et al., 2024). Nevertheless, in both cases, they manifest the highest occurrence at $f \approx$ 0.5–0.8 mHz (a frequency range rarely explored in magnetospheric investigations, as previously remarked), with some evidence for enhancements around $f \approx 1.9$ mHz, and, less explicit, around $f \approx$ 2.7–2.9 mHz and $f \approx$ 3.2–3.8 mHz. Interestingly, in the last 30 years, several papers, proposed the possible existence of frequencies more common than others for magnetospheric fluctuations, in particular $f_1 \approx 1.3$, $f_2 \approx 1.9$ (most common), $f_3 \approx$ 2.6–2.7, and $f_4 \approx$ 3.2–3.4 mHz (e. g., Samson et al., 1991; Ruohoniemi et al., 1991; Samson et al., 1992; Walker et al., 1992; Francia and Villante, 1997; Villante et al., 2001). In this sense, corroborating the conclusions of several analysis in favor of magnetospheric fluctuations directly driven by compressional *SW* modes approximately at the same frequencies (Kepko et al., 2002; Kepko and Spence, 2003; Villante et al., 2007; Viall et al., 2009; Villante et al., 2013, 2016), the results of Di Matteo et al. (2024) might confirm, at least in a statistical sense, that several magnetospheric fluctuations at discrete frequencies might be associated with the interaction of *PDS*s with the magnetosphere.

Conclusion

As discussed in the previous paragraph, several results obtained for PDS by Di Matteo et al. (2024) might find correspondence in those obtained, over many years, in the analysis of the magnetospheric fluctuations at discrete frequencies (such as the enhancements of the event occurrence at given discrete frequencies, more evident around $f \approx 1.9$ mHz …; review by Di Matteo and Villante (2024) and papers therein referenced). On the other hand, other aspects such as the general ≈50% of (dis)agreement between the frequencies of fluctuations observed by the two spacecraft (Di Matteo and Villante, 2017, Di Matteo and Villante, 2018) as well as the strong disagreement in the fluctuations content occasionally obtained when the same SW parcel is observed at different places confirm that, as underlined by Di Matteo and Villante (2024), further investigations of the relationship between SW and magnetospheric fluctuations should pay careful attention to several critical aspects which may strongly influence the results of the data analysis (i.e., the method of data processing which may be critical for the identification of events; the unambiguous identification of the characteristics of the SW fluctuations impinging the magnetosphere); in addition, it is useful to remind that the magnetospheric response is expected to be different in different regions (and intermixed with concurring local generation processes) and strongly influenced, at least in terms of the frequency of fluctuations, by the daily, seasonal and solar cycle variation of the local resonant frequency.

Author contributions

UV: Writing–original draft.

Funding

The author declares that no financial support was received for the research, authorship, and/or publication of this article.

Acknowledgments

Thanks to M. Piersanti (University of L'Aquila), this research activity was carried out within the Ministry of University and Research, MUR, with the project PRIN2022 No. 2022ZBBBRY "Characterization of the Lithosphere-Ionosphere coupling during seismic phenomena", CUP E53D23004560006.

Conflict of interest

The author declares that the research was conducted in the absence of any commercial or financial relationships that could be construed as a potential conflict of interest.

Generative AI statement

The authors declare that no Generative AI was used in the creation of this manuscript.

Publisher's note

All claims expressed in this article are solely those of the authors and do not necessarily represent those of their affiliated organizations, or those of the publisher, the editors and the reviewers. Any product that may be evaluated in this article, or claim that may be made by its manufacturer, is not guaranteed or endorsed by the publisher.

References

Di Matteo, S., Katsavrias, C., Kepko, L., and Viall, N. M. (2024). Azimuthal size scales of solar wind periodic density Structures. *Astrophys. J.* 969 (67), 67. doi:10.3847/1538-4357/ad479e

Di Matteo, S., and Sivadas, N. (2022). Solar-wind/magnetosphere coupling: understand uncertainties in upstream conditions. *Front. Astron. Space Sci.* 9. doi:10.3389/fspas.2022.1060072

Di Matteo, S., and Villante, U. (2017). The identification of solar wind waves at discrete frequencies and the role of the spectral analysis techniques: the Identification of Solar Wind Waves. *J. Geophys. Res.* 122 (5), 4905–4920. doi:10.1002/2017JA023936

Di Matteo, S., and Villante, U. (2018). The identification of waves at discrete frequencies at the geostationary orbit: the role of the data analysis techniques and the comparison with solar wind observations. *J. Geophys. Res.* 123, 1953–1968. doi:10.1002/2017JA024922

Di Matteo, S., and Villante, U. (2024). Simultaneous occurrence of magnetospheric fluctuations at different discrete frequencies (f ≈ 1 – 5 mHz): a review, sub. *Space Sci. Rev. C.*

Francia, P., and Villante, U. (1997). Some evidence of ground power enhancements at frequencies of global magnetospheric modes at low latitude. *Ann. Geophys.* 15 (17), 17–23. doi:10.1007/s00585-997-0017-2

Kepko, L., and Spence, H. E. (2003). Observations of discrete, global magnetospheric oscillations directly driven by solar wind density variations. *J. Geophys. Res.* 108 (A6), 1257. doi:10.1029/2002JA009676

Kepko, L., Spence, H. E., and Singer, H. J. (2002). ULF waves in the solar wind as direct drivers of magnetospheric pulsations: ULF waves in solar wind. *Geophys. Res. Lett.* 29 (8), 39–1394. doi:10.1029/2001GL014405

Ruohoniemi, J. M., Greenwald, R. A., Baker, K. B., and Samson, J. C. (1991). HF radar observations of Pc 5 field line resonances in the midnight/early morning MLT sector. *J. Geophys. Res.* 96 (A9), 15697–15710. doi:10.1029/91JA00795

Samson, J. C., Greenwald, R. A., Ruohoniemi, J. M., Hughes, T. J., and Wallis, D. D. (1991). Magnetometer and radar observations of magnetohydrodynamic cavity modes in the Earth's magnetosphere. *Can. J. Phys.* 69 (8-9), 929–937. doi:10.1139/p91-147

Samson, J. C., Harrold, B. G., Ruohoniemi, J. M., and Greenwald, R. A. (1992). Field line resonances associated with MHD waveguides in the magnetosphere. *Geophys. Res. Lett.* 19 (5), 441–444. doi:10.1029/92GL00116

Viall, N. M., Kepko, L., and Spence, H. E. (2009). Relative occurrence rates and connection of discrete frequency oscillations in the solar wind density and dayside magnetosphere. *J. Geophys. Res.* 114 (A1). doi:10.1029/2008JA013334

Villante, U., Del Corpo, A., and Francia, P. (2013). Geomagnetic and solar wind fluctuations at discrete frequencies: a case study. *J. Geophys. Res.* 118 (1), 218–231. doi:10.1029/2012JA017971

Villante, U., Di Matteo, S., and Piersanti, M. (2016). On the transmission of waves at discrete frequencies from the solar wind to the magnetosphere and ground: a case study. *J. Geophys. Res.* 121 (1), 380–396. doi:10.1002/2015JA021628

Villante, U., Francia, P., and Lepidi, S. (2001). Pc5 geomagnetic field fluctuations at discrete frequencies at a low latitude station. *Ann. Geophys.* 19 (3), 321–325. doi:10.5194/angeo-19-321-2001

Villante, U., Francia, P., Vellante, M., di Giuseppe, P., Nubile, A., and Piersanti, M. (2007). Long-period oscillations at discrete frequencies: a comparative analysis of ground, magnetospheric, and interplanetary observations. *J. Geophys. Res.* 112 (A4), 04210. doi:10.1029/2006JA011896

Villante, U., Recchiuti, D., and Di Matteo, S. (2022). The transmission of ULF waves from the solar wind to the magnetosphere: an analysis of some critical aspects. *Front. Astron. Space Sci.* 9, 835539. doi:10.3389/fspas.2022.835539

Walker, A. D. M., Ruohoniemi, J. M., Baker, K. B., Greenwald, R. A., and Samson, J. C. (1992). Spatial and temporal behavior of ULF pulsations observed by the Goose Bay HF Radar. *J. Geophys. Res.* 97 (A8), 12187–12202. doi:10.1029/92JA00329

frontiers | Frontiers in Astronomy and Space Sciences

TYPE Original Research
PUBLISHED 04 April 2025
DOI 10.3389/fspas.2025.1383946

Check for updates

OPEN ACCESS

EDITED BY
Yulia Bogdanova,
Rutherford Appleton Laboratory,
United Kingdom

REVIEWED BY
Mike Hapgood,
Rutherford Appleton Laboratory,
United Kingdom
Bingbing Wang,
University of Alabama in Huntsville,
United States

*CORRESPONDENCE
Ran Huo,
huor@iat.cn

RECEIVED 08 February 2024
ACCEPTED 11 March 2025
PUBLISHED 04 April 2025

CITATION
Song X, Huo R, Xu S, Chen X and Luo X (2025) The SDEMMA model for galactic cosmic ray and its dosimetric application.
Front. Astron. Space Sci. 12:1383946.
doi: 10.3389/fspas.2025.1383946

COPYRIGHT
© 2025 Song, Huo, Xu, Chen and Luo. This is an open-access article distributed under the terms of the Creative Commons Attribution License (CC BY). The use, distribution or reproduction in other forums is permitted, provided the original author(s) and the copyright owner(s) are credited and that the original publication in this journal is cited, in accordance with accepted academic practice. No use, distribution or reproduction is permitted which does not comply with these terms.

The SDEMMA model for galactic cosmic ray and its dosimetric application

Xiaojian Song[1], Ran Huo[1]*, Songying Xu[1,2], Xuemei Chen[1,2] and Xi Luo[1]

[1]Particle Physics Research Center, Shandong Institute of Advanced Technology, Jinan, China, [2]School of Physics and Technology, University of Jinan, Jinan, China

Introduction: Future crewed missions to Mars will encounter substantially elevated radiation levels compared to low Earth orbit operations. To address this challenge, we present the Space-Dependent Energetic cosmic ray Modulation using MAgnetic spectrometer (SDEMMA) model, a novel framework for modeling galactic cosmic ray (GCR) dynamics in deep-space environments.

Methods: The model employs stochastic differential equations with outer boundary conditions derived from contemporary local interstellar spectrum models. Time-dependent diffusion and drift coefficients were optimized through Markov Chain Monte Carlo parameter fitting against 2006-2019 observational data from the space-borne magnetic spectrometers of AMS-02 and PAMELA.

Results: SDEMMA extends GCR spectral calculations to radial positions beyond 1.0 AU, explicitly resolving radial gradients under diverse heliospheric conditions. The framework provides spatiotemporally resolved GCR spectra for charge numbers Z=1–28 at rigidities >0.2 GV, covering the inner heliosphere between Earth and Mars and currently the 2006-2019 epoch.

Discussion: Implementation demonstrates the model's operational utility: dose equivalent rates behind 30 g/cm^2 polyethylene shielding during a flux minimum range from 14-17 cSv/yr, with variance attributable to quality factor selection.

KEYWORDS

galactic cosmic ray, solar modulation, stochastic differential equation, spatial dependence, fluence-to-dose conversion coefficient, dose equivalent rate

1 Introduction

While radiation exposure for astronauts in a low Earth orbit or even during a journey to the Moon can now be considered less challenging, this problem is still not well understood in the next natural step for a journey to the Mars. Due to the absence of the geomagnetic field shielding and a longer trip which last for years, the radiation level is much higher. Few *in situ* measurements have been performed. The Radiation Assessment Detector (RAD) on the Mars Science Laboratory (MSL), also known as the Curiosity rover, made the first-ever measurement during the transit from Earth to Mars in the 2011 Mars mission time window (Zeitlin et al., 2013). The total measured dose equivalent rate is 1.81 ± 0.33 mSv/d. Analysis also shows that behind an average shielding of 16 g/cm^2, the galactic cosmic rays (GCR) made the dominant dose contribution in the energy range of ~300 MeV/n to ~10 GeV/n, while the solar energetic particles only contributed approximately 5%. Then the dose

contribution of GCR is calculated by a rescaling of the MSL/RAD results under different solar modulation conditions in Guo et al. (2015). During the 2016 time window, a Liulin-MO dosimeter on the ExoMars Trace Gas Orbiter conducted a second measurement that was claimed to be consistent with the first MSL/RAD measurement (Semkova et al., 2018), given the modulation condition difference.

Such GCRs induced radiation dose in the transit orbit represents the most important radiation exposure during the human exploration of Mars (Guo et al., 2024), since GCRs are a continuous radiation source that is hard to shield against. On the other hand, the SEP events can be shielded in a better shelter part of a spacecraft for a few hours. And once on the planet, Mars' atmosphere provides some protection, and a sub-surface shelter gives even more protection. Therefore, this important problem deserves further study. Without expensive *in situ* measurements, our goal is to develop a model-based calculation for the cumulative radiation dose experienced by astronauts on the journey to Mars (HelMod, 2024; Opher et al., 2023). This calculation scheme is aimed to (a) cover various possible Mars mission time windows under different solar modulation conditions, (b) provide full radial dependence, and (c) be applied to realistic target astronaut phantoms with flexible shielding. The goal involves researches in several broad field, and we plan to achieve it in a step by step manner. In the present paper we will mainly address the more "academic" GCR related issue (a and b), and keep the discussion of the space dosimetry (c) only at an illustrative level. The more realistic "engineering" dosimetric values will be provided in a forthcoming publication.

GCR spectra are influenced by solar activity, with the solar wind and interplanetary magnetic field playing crucial roles in their modulation. This variability with time is continuously captured by numerous experiments conducted on or around the Earth. Here, we use data in time series from space-borne magnetic spectrometers, specifically the PAMELA and the AMS-02 (Adriani et al., 2013; Martucci et al., 2018; Marcelli et al., 2020; Aguilar et al., 2018; 2021; 2022). Furthermore, the encountered GCR spectra of the astronauts also vary at different radial locations. This variability cannot be covered by most previous measurements, including the PAMELA and the AMS-02. Our approach is to explicitly expand the calculation previously limited to the 1.0 AU slice (O'Neill et al., 2015; Slaba and Whitman, 2019; Boschini et al., 2016) to other radial locations in the inner solar system. With at least the solar modulation effect, the calculated GCR spectra dataset forms a GCR model, which we have named the Space-Dependent Energetic cosmic ray Modulation using MAgnetic spectrometer (SDEMMA) model. Except that its 1.0 AU spectra has been integrated with the ICRP123 fluence-to-dose conversion coefficient (ICRP123 et al., 2013) for the unshielded astronaut dose rate (Chen et al., 2023), this new GCR model is comparable to the Badhwar-O'Neill series of models (O'Neill et al., 2015; Slaba and Whitman, 2019), the HelMod model (Boschini et al., 2016), etc. It can be used for general purposes beyond space dosimetry, and will be long-term supported.

As an example for its dosimetric application, we use this model to calculate the astronaut radiation dose rate between the Earth's and the Mars' orbit. While the SDEMMA GCR model provides the number of the incident particles for each species at each kinetic energy, the dose calculation needs another factor, which is the expected dose equivalent caused by a single incident particle (the fluence-to-dose-equivalent conversion coefficient). We have used several sets of fluence-to-dose-equivalent conversion coefficient, including the ones calculated by ourselves using the particle physics toolkit GEANT4 (Agostinelli et al., 2003; Allison et al., 2006; Allison et al., 2016). The dose equivalent rates are obtained in time series upon integration with the two factors.

The paper is organized as follows. In Section 2 we review the GCR spectra calculation method, including the stochastic differential equation (SDE) approach and the local interstellar spectra as the outer boundary conditions. We pay special attention to the heliospheric environment modeling, as well as the data from the PAMELA and the AMS-02 experiments and the fitting procedure to determine the diffusion and drift coefficients. In Section 3 we present a detailed discussion of the GCR flux, which depends on rigidities, GCR species, time, and radial positions. These two sections actually define the SDEMMA model. Then we introduce the fluence-to-dose-equivalent conversion coefficient and calculate the dose equivalent rate in Section 4, using three shielding settings: the unshielded case for uncertainty demonstration, the MSL/RAD shielding case for validation, and the optimized shielding thickness for the reference values. Finally, we summarize in Section 5.

2 The GCR spectra calculation scheme

The spectra of GCRs are related to their phase space density through $p^2 f(\vec{r},\vec{p})$, where $\vec{r}$ is the position, $\vec{p}$ is the momentum with p as its magnitude, and $f(\vec{r},\vec{p})$ is the phase space density. The evolution of phase space density is governed by the Boltzmann equation, which states that the total derivative of the phase space density is determined by collision terms. In the environment of the heliosphere, it becomes the Parker's transport equation, which reads

$$\frac{\partial f}{\partial t} = -\left(\vec{v}_{\rm sw} + \vec{v}_{\rm d}\right)\cdot\nabla f + \frac{1}{3}\left(\nabla\cdot\vec{v}_{\rm sw}\right)\frac{\partial f}{\partial \ln p} + \nabla\cdot\left(\vec{\vec{K}}\cdot\nabla f\right). \quad (1)$$

Here, $\vec{v}_{\rm sw}$ and $\vec{v}_{\rm d}$ are the background solar wind and pitch angle-averaged drift velocities, and in the first term of the right hand side they give the convection and the drift effects, respectively. The middle term represents the adiabatic cooling effect caused by expansion of the solar wind. The diffusion coefficient tensor, $\vec{\vec{K}}$, is a result of the small-scale turbulence of the heliospheric magnetic field (HMF).

As an application of the Feynman-Kac formula treatment of the stochastic diffusion process, the Parker's transport Equation 1 can be reformulated into an equivalent set of 3D SDEs for the GCR phase space coordinates (Zhang, 1999)

$$d\vec{r} = \left(\nabla\cdot\vec{\vec{K}} - \vec{v}_{\rm sw} - \vec{v}_{\rm d}\right)ds + \vec{\vec{\sigma}}\cdot{\rm d}\vec{W} \quad (2)$$

with $\vec{\vec{\sigma}}\cdot\vec{\vec{\sigma}} = 2\vec{\vec{K}}$, and

$$dp = \frac{1}{3}p\left(\nabla\cdot\vec{v}_{\rm sw}\right){\rm d}s. \quad (3)$$

Here, three spatial dimensions (r, θ, ϕ) have been considered. $s = -t$ is the backward time. The differential random noises ${\rm d}\vec{W}$ superimposed on the deterministic motion describe the Wiener

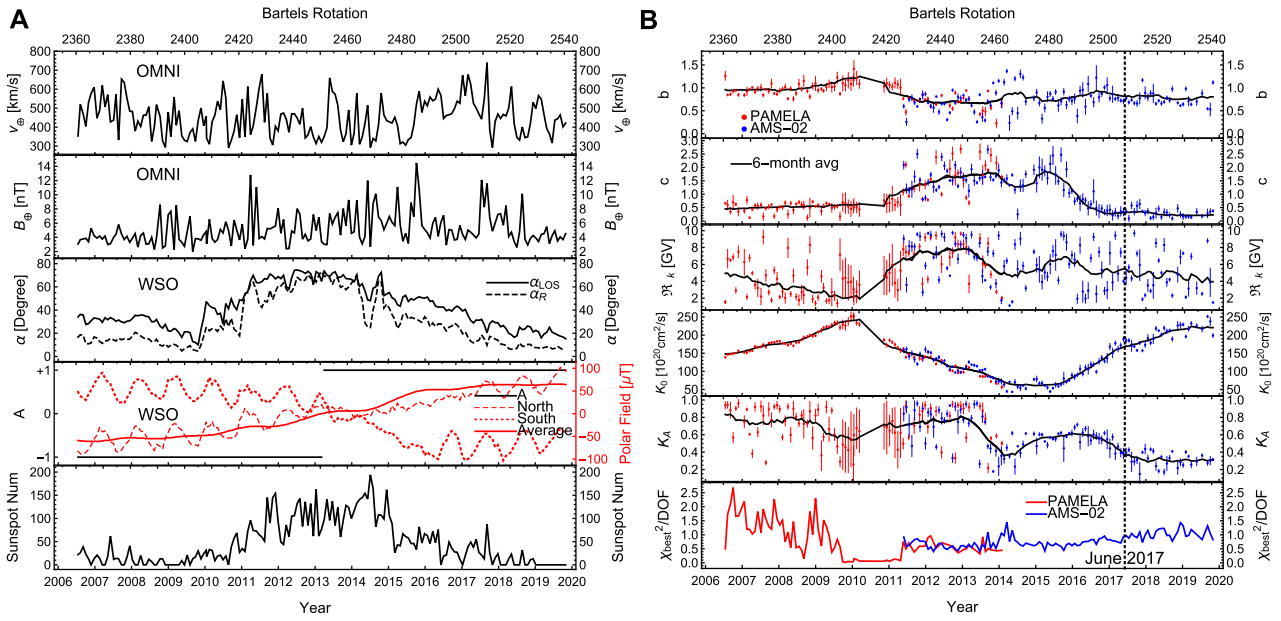

FIGURE 1
The time series of the four observational parameters **(A)**, and the five fitted parameters through the MCMC process and the corresponding χ^2 **(B)**. In the left panels, all the observables have been smoothed by their averages over each Bartels rotation (27 days) for better visual, but in real calculations higher time resolution data are used. The WSO provide two versions of the HCS tilt angle definitions, here we use the classical "line-of-sight" definition (solid curve), but also plot the "radial" definition (dashed curve) for reference. The polarity A is defined as the sign of the averaged solar polar magnetic field, and this average is defined through the north and south polar magnetic field, here they are plotted altogether. The sunspot number (SSN) is another frequently used observable for solar activity, so we have also plotted for reference. In the right panels, for each variable we also plot the smoothing of 6 months' average. Fitting prior to June 2017 has already been given by Song et al. (2021).

TABLE 1 The list of variables for our current SDEMMA spectra. The major part of the calculation consists of $91\times28\times166\times7=2960776$ data points. The flux for each point is based on a statistics of 3,000 pseudoparticles.

Sampling variables	Range	Number of samplings	Sampling description
Rigidity	0.2–100 GV	91	Equal spacing in logrithm
GCR species	Z = 1to 28	28	All elements
Date	Jun 2006 to Oct 2019	166	Average of every Bartels period if measured
Radial Location	1.0 to 1.6 AU	7	Every 0.1 AU

diffusion process. The phase space coordinates are not for a single GCR particle, but for a macroscopically small but microscopically large phase space region which still contains a large number of GCR particles. The initial-boundary value problem for the phase space density distribution $f(\vec{r},\vec{p})$ can now be solved through a Monte Carlo simulation of a Markov stochastic process for each small piece of phase space, which avoids the need for numerical solutions of the complicated partial differential equation.

The local interstellar spectra for protons from Corti et al. (2019), for iron from Boschini et al. (2021), and for all other elements from Boschini et al. (2020) are used as the outer boundary conditions (Song et al., 2021). They are implemented at 120 AU where the heliopause locates. The spectra of the all the $Z=1-28$ GCR elements can be calculated with these boundary conditions.

2.1 Modeling the heliospheric environment

Our modeling of the heliospheric environment is identical to that of Song et al. (2021). Here, we provide a brief review of the four specific models in the Radial-Tangential-Normal coordinates: the solar wind velocity $\vec{v}_{sw}$ (Equation 4), the HMF $\vec{B}$ (Equations 5-8), the diffusion tensor $\vec{\vec{K}}$ (Equations 11-13), and the drift velocity $\vec{v}_d$ (Equations 9, 10). Simply put, there are four time-dependent parameters in the first two models ($\vec{v}_{sw}$ and $\vec{B}$) that are determined observationally: $v_\oplus$, $B_\oplus$, α and A. And the last two models contain five time-dependent parameters that are fitted to data using the Markov Chain Monte Carlo (MCMC) processes: $b, c, \Re_K, K_0$ in the diffusion tensor $\vec{\vec{K}}$, and K_A in the drift velocity $\vec{v}_d$. One can refer to Figure 1 for a glance.

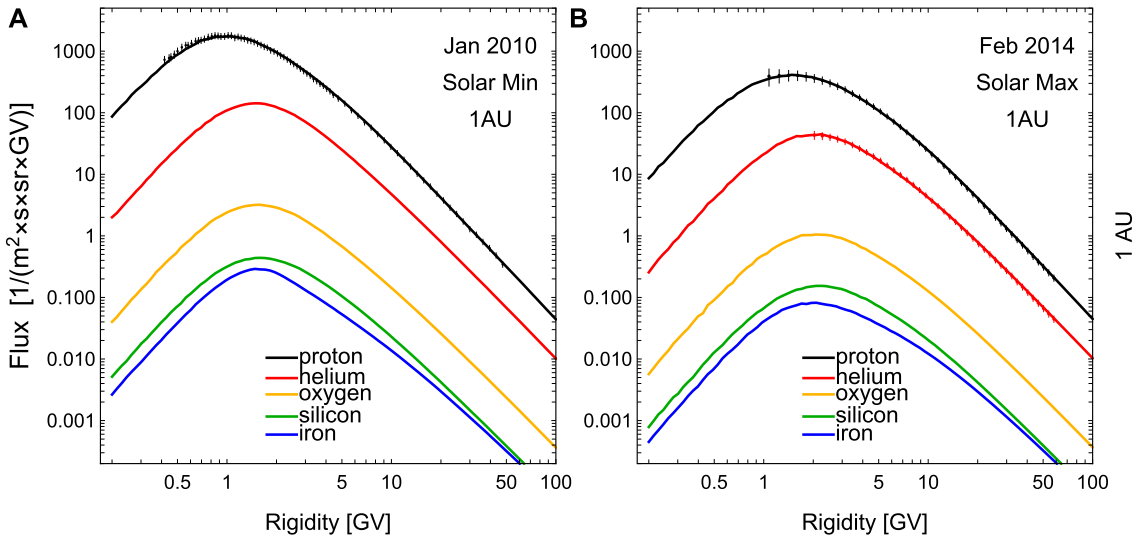

FIGURE 2
The SDE calculated spectra for proton (black), helium (red), oxygen (orange), silicon (green), and iron (blue) at 1.0 AU, at the solar minimum **(A)** and maximum **(B)** respectively. The PAMELA and AMS-02 measured proton and helium GCR spectra for the corresponding periods are also shown, except for the PAMELA helium data which is not for one Bartels rotation. Due to the finite sampling number in the SDE method (3,000 pseudoparticles per energy bin), the spectra show some fluctuation on the low rigidity side (see also discussion in Section 3.4).

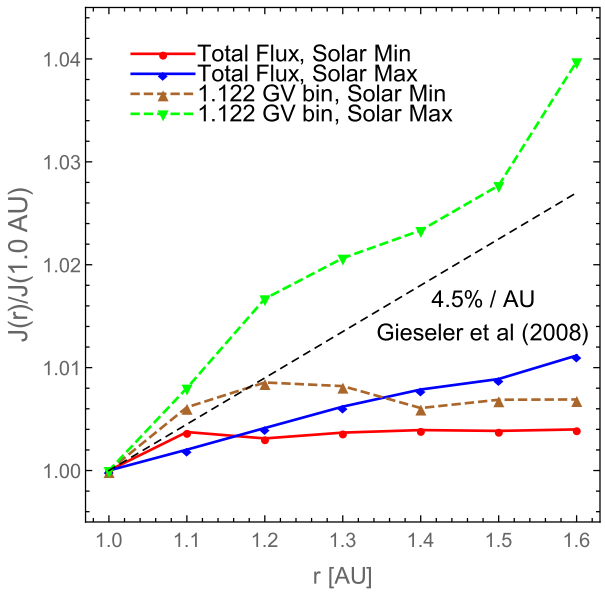

FIGURE 3
The flux $J(r)/J(1.0\mathrm{AU})$ ratios as a function of radial position r between 1.0 and 1.6 AU. For both the "total flux" integrated over the 0.2 – 100 GV rigidity range and the single bin flux, their values at various locations are normalized with the respective values at Earth ($r = 1.0$ AU), then further averaged over all the $Z = 1 – 28$ elements in order to reduce statistical fluctuations. The single bin $J(r)$ of 1.122 GV best matches the previous measurement of Gieseler et al. (2008) of the helium 125 – 200 MeV/n (0.997 – 1.285 GV) bin and the carbon 147 – 198 MeV/n (1.088 – 1.278 GV) bin. The gray dashed line shows the measured central value of 4.5%/AU of Gieseler et al. (2008).

2.1.1 Solar wind

The solar wind velocity up to the termination shock is given by Potgieter et al. (2014)

$$\vec{v}_{sw}(r,\theta) = v_{\oplus}\left(1-\exp\left[\frac{40}{3}\left(\frac{r_{\odot}-r}{r_{\oplus}}\right)\right]\right)\left(1.475-0.4\tanh\left[6.8\left(\alpha+\frac{\pi}{12}-\left|\theta-\frac{\pi}{2}\right|\right)\right]\right)\vec{e}_r, \quad (4)$$

where $v_{\oplus}$ is the observed solar wind speed near Earth, for which we use the daily OMNI data. $r_{\odot} = 0.005$ AU is the radius of the Sun, $r_{\oplus} = 1$ AU is the radial position of the Earth. α is the observational tilt angle of the wavy heliospheric current sheet (HCS) from the L model, and we use the Wilcox Solar Observatory data which is given every 10 days. The first bracketed factor describes the radial acceleration behavior of the solar wind. After the acceleration, the speed remains almost constant until reaching the termination shock. The second bracketed factor describes the behavior in the polar direction. At two polar directions ($\theta \to 0$ and $\theta \to \pi$) and/or for a small tilt of the HCS α (or during weak solar activity), the factor tends to be large and approaches 1.875. And for locations near the equator and/or for a large α (or during strong solar activity), the factor tends to be small and approach 1.075 (Potgieter et al., 2014). This depiction of the spatial and temporal distribution of the solar wind is valid up to the termination shock.

Outside the termination shock of 90 AU, the solar wind transitions from supersonic to subsonic speeds. Here, the velocity is assumed to decrease to 40% of the value just inside the termination shock (Li et al., 2008), then follow an inverse square law (r^{-2}) as further moves out. The heliosheath is acting as a "modulation barrier", in which our solar wind does not expand, exerting no adiabatic cooling effect on the incoming GCR particles. The enhanced modulation observed in the heliosheath is not accounted

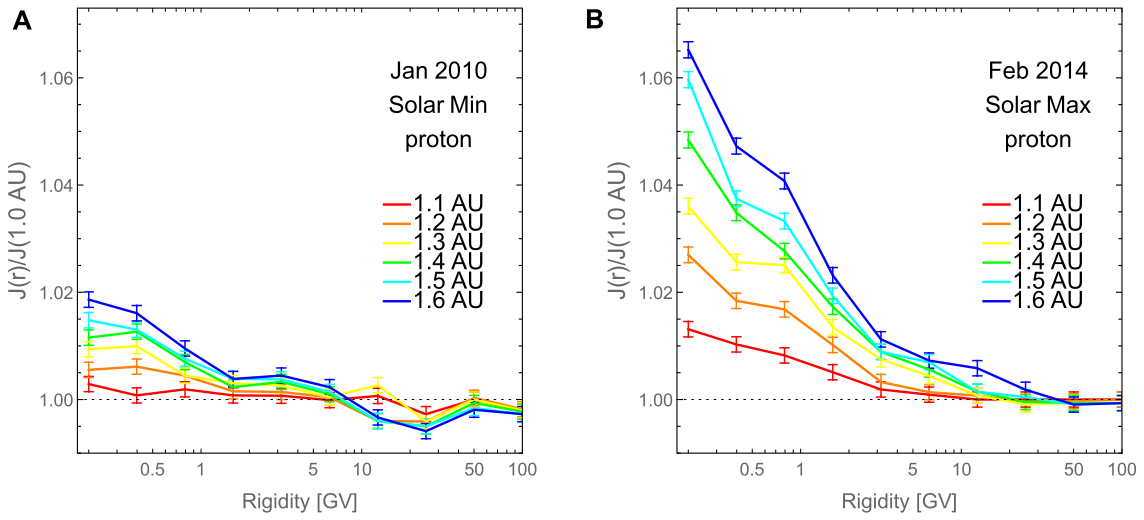

FIGURE 4
The proton flux $J(r)/J(1.0\text{AU})$ ratios as a function of rigidity, for six radial positions and two solar modulation conditions: solar minimum [January 2010, **(A)**], and solar maximum [February 2014, **(B)**]. The errorbar is from a simple $1/\sqrt{N}$ estimation with $N = 10^6$ (dedicated running with high statistics).

TABLE 2 Comparison of the Badhwar-O'Neil 2020 model, the HelMod model and our SDEMMA model.

	Badhwar-O'Neil (2020)	HelMod	SDEMMA
Open Access	No	Yes	Yes
Transport Equation	1D, analytical solution	2D, SDE	3D, SDE
Fitted Variable	ϕ_Z	K_0	$\vec{K}$ and $\vec{v}_d$
Fitted Data	ACE/CRIS, SSN	SSN, NMCR	AMS-02, PAMELA
Fitted Way	Time series as a whole	Time series as a whole	Point by point in time series
$\lvert Rd\rvert$ proton helium	3% 3%	2.9% 3.8%	0.64% 0.89%
Forecast	Yes	Yes	In development

for in our calculation, and our modeling is not entirely accurate or comprehensive. However, we expect that this inconsistency will not have a significant numerical impact on our final spectra calculation, as our focus of the inner solar system region of 1.0 – 1.6 AU is very far from the heliosheath. Moreover, there is some dependence of the inferred local interstellar spectra on the modulation process in the heliosheath, consequently the calculated GCR spectra (Langner and Potgieter, 2004; Langner et al., 2003).

2.1.2 Heliospheric magnetic field

The used 3D HMF is the Parker's spiral with a polar region enhancement (Jokipii and Kota, 1989).

$$\vec{B}(r,\theta,\phi) = -\frac{AB_{\oplus}}{r^2}\,\mathrm{sgn}\left[\theta-\theta'\right]\left(\vec{e}_r + \xi\vec{e}_\theta - \Psi\vec{e}_\varphi\right), \tag{5}$$

$$\theta' = \frac{\pi}{2} - \tan^{-1}\left[\tan\alpha\,\sin\left[\phi + \frac{(r-r_\odot)\,\Omega}{v_{sw}}\right]\right], \tag{6}$$

$$\xi = \frac{r\delta_m}{r_\odot \sin\theta}, \tag{7}$$

$$\Psi = \frac{(r-r_\odot)\,\Omega\sin\theta}{v_{sw}}. \tag{8}$$

Here, $A = \pm 1$ is the observed polarization of the HMF, being positive (negative) indicates that the HMF points outward (inward) in the northern hemisphere of the Sun. $B_\oplus$ is the observational HMF strength near the Earth. The sources of the A and $B_\oplus$ are also the above Wilcox Solar Observatory data and the daily OMNI satellite data, respectively. The $\mathrm{sgn}(x) = x/|x|$ is the signum function. $\Omega = 2.66\times10^{-6}$/s is the angular rotation speed of the Sun. The colatitude θ' is the separation between the north and south hemispheres caused by the undulating HCS at the phase angle ϕ. In addition to the standard Parker spiral, the term $\xi\vec{e}_\theta$ acts as a correction for the observed HMF increase at a large radial distance in the polar heliosphere. This term ensures divergence-free behavior, as introduced by Jokipii and Kota (1989). Here, the perturbation

10.3389/fspas.2025.1383946

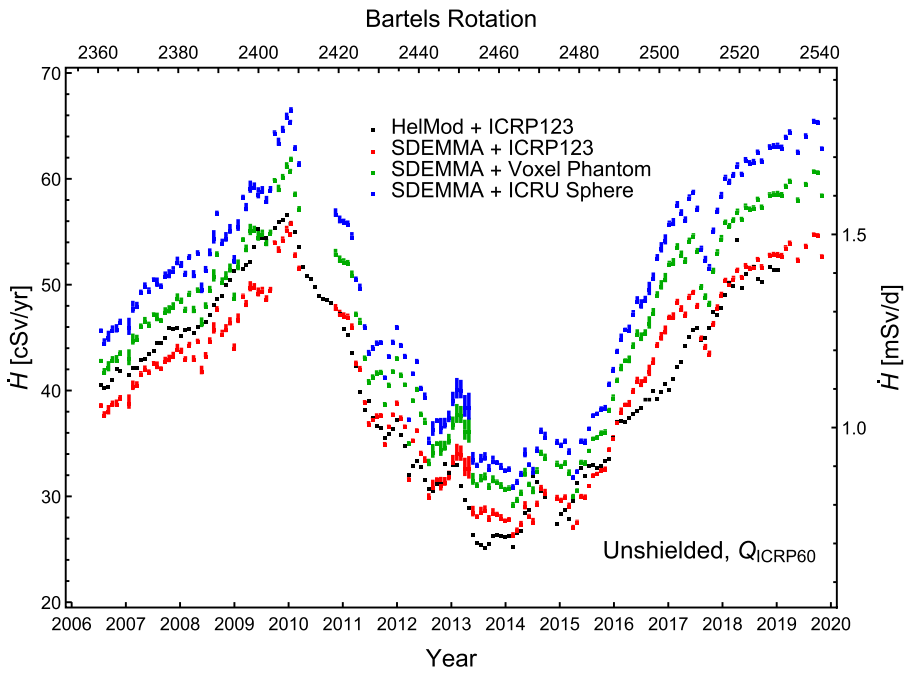

FIGURE 5
The unshielded dose equivalent rate $\dot{H}$ time series during June 2006 and October 2019, for four combinations of GCR models and fluence-to-dose conversion coefficients: the HelMod model combined with the ICRP123 dose coefficient (black points), the SDEMMA model combined with the ICRP123 dose coefficient (red vertical bars), the SDEMMA model combined with our independently calculated dose coefficient set using the ICRP110 human voxel phantom (green vertical bars), and the SDEMMA model combined with dose coefficient calculated use the ICRU sphere (blue vertical bars). For SDEMMA models, vertical bars indicate the range of $\dot{H}$ achieved in the radial range of 1.0 – 1.6 AU. And for the first three combinations which are all based on detailed human phantoms, $\dot{H}$ shown is the weighted (by the tissue weighting factor) sum of the dose equivalent rates of 15 sensitive organs/tissues.

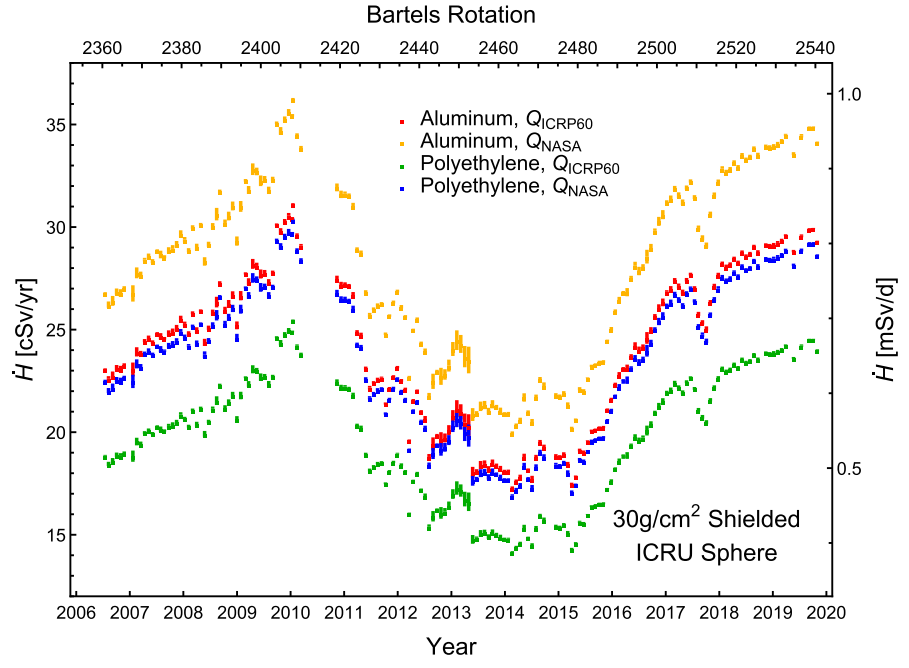

FIGURE 6
The dose equivalent rate $\dot{H}$ time series during June 2006 and October 2019 for the ICRU sphere, after an optimized shielding with depth of 30 g/cm^2. Here we have considered the two materials of aluminum and polyethylene for the shielding structure, and two quality factors of Q_{ICRP60} and Q_{NASA} in the dose equivalent calculation.

parameter in the equatorial plane δ_m is set to be 2×10^{-5} (Qin and Shen, 2017; Boschini et al., 2016). To avoid a singularity, $\delta_m/\sin\theta$ is set equal to the value $\delta_m/\sin(1°)$ when $\theta<1°$ or $\theta>179°$ (Raath et al., 2016).

2.1.3 Diffusion and drift coefficients

In contrast to the two aforementioned models which are determined through observation and have become quite distinctive, there are numerous options in the literature for diffusion and drift coefficients. Here, we use a set of parameterized coefficients as provided by Potgieter (2013). Compared with diffusion coefficients that are more theoretically motivated (e.g., Qin and Zhang, 2014), our parametrized coefficients usually have the advantage of reproducing observational spectra with greater precision, but at the cost of complexity in making forecast.

The drift velocity is given by Potgieter (2013)

$$\begin{aligned}\vec{v}_{\rm d}(\mathfrak{R},r,\theta,\phi)&=\nabla\times\left(K_A\frac{\mathrm{sgn}[q]\,\mathfrak{R}\beta}{3}\frac{(\mathfrak{R}/\mathfrak{R}_A)^2}{1+(\mathfrak{R}/\mathfrak{R}_A)^2}\frac{\vec{B}}{B^2}\right),\\&=-K_A\frac{\mathrm{sgn}[q]\,\mathfrak{R}\beta}{3}\frac{(\mathfrak{R}/\mathfrak{R}_A)^2}{1+(\mathfrak{R}/\mathfrak{R}_A)^2}\frac{A}{B_\oplus}\left(\mathrm{sgn}[\theta-\theta']\nabla\times\vec{g}\right.\\&\left.-\delta(\theta-\theta')\vec{g}\times\nabla(\theta-\theta')\right),\end{aligned}\tag{9}$$

with

$$\vec{g}=\frac{r^2\left(\vec{e}_r+\xi\vec{e}_\theta-\Psi\vec{e}_\varphi\right)}{1+\xi^2+\Psi^2}.\tag{10}$$

Here, $\mathfrak{R}=pc/q$ is the rigidity of the particle, and for nonrelativistic case the particle momentum $p=mv$. m and v are the mass and speed of the particle, respectively, and q is the particle's charge. K_A is the overall dimensionless drift coefficient to be fitted, which ranges from 0 to 1, with $K_A=1$ describing undisturbed drift without the competition of scattering. $\beta=v/c$ is the ratio of the particle's speed to the speed of light. Note that this ratio is an implicit function of rigidity, as $\beta=pc/E=Ze\mathfrak{R}/\sqrt{(Ze\mathfrak{R})^2+m^2c^4}$. $\mathfrak{R}_A=0.9$ GV empirically, and the corresponding factor smoothly connects the high rigidity drift region and the low rigidity scattering region, where small-scale turbulence plays a central role. B is the magnitude of the HMF.

The diffusion tensor is given by its components (Potgieter, 2013).

$$K_\parallel=K_0\beta\left(\frac{\sqrt{1+\Psi^2}B_\oplus}{B}\right)\left(\frac{\mathfrak{R}}{\mathfrak{R}_0}\right)^b\left(\frac{(\mathfrak{R}/\mathfrak{R}_0)^3+(\mathfrak{R}_K/\mathfrak{R}_0)^3}{1+(\mathfrak{R}_K/\mathfrak{R}_0)^3}\right)^{\frac{c-b}{3}},\tag{11}$$

$$K_{\perp,r}=0.02K_\parallel,\tag{12}$$

$$K_{\perp,\theta}=\left(2+\tanh\left[8\left(\left|\theta-\frac{\pi}{2}\right|-\frac{7\pi}{36}\right)\right]\right)K_{\perp,r}.\tag{13}$$

Here K_0 is the overall diffusion coefficient to be fitted in units of $10^{20}\,\mathrm{cm}^2/\mathrm{s}$, $\mathfrak{R}_0=1$ GV empirically. The coefficient is a smooth connection of two asymptotic power laws, with their indices of b and c to be fitted for the low and high rigidity region, respectively. The last parameter to be fitted is $\mathfrak{R}_K$, which determines the transition to the asymptotic power law on the high rigidity side.

Finally we would like to make comment on the validity of the spectra calculation at locations different from the 1.0 AU. Since all of the above models hold for the entire spatial heliosphere region, for given observational and fitted parameter in time series, the calculation of GCR spectra is equally accurate at other locations within the heliosphere, especially at the range of 1.0 – 1.6 AU between the orbits of Earth and Mars. In fact, the current work is extending the scope of our previous work by generalizing the 1.0 AU slice provided in Song et al. (2021); Chen et al. (2023) to other radial locations. The same generalization is conceptually claimed by other similar SDE works as well (e.g., Boschini et al., 2022).

2.2 The data source and fitting

As mentioned, the Alpha Magnetic Spectrometer (AMS) 02 detector is one of the most effective tools for measuring GCR spectra. It was launched in May 2011 and installed on the International Space Station at an altitude of about 400 km. The detector can measure all the GCR elements with atomic numbers ranging from 1 to 28, with a strong capability for discriminating between elements and controlling errors. The PAMELA detector is another space-borne magnetic spectrometer before the AMS-02, which was launched in June 2006 into an orbit at an altitude of 350 – 600 km. As magnetic spectrometers, both of them utilize the Lorentz force to bend the trajectory of incident charged particles. By measuring the deflection as well as the energy loss in the detector, the charge of GCRs can be precisely determined (Aguilar et al., 2021), which is crucial for dosimetry. On the other hand, the two spectrometers are still in the geomagnetic field, which will partially shield the incident GCR from being measured, particularly for low rigidities. But such shielding effect depends on geographic location and direction. By selecting the events above the geographic-location-and-direction dependent geomagnetic cutoff rigidity determined in the backtracing process (e.g., see Aguilar et al., 2015), the AMS and PAMELA group were able to discriminate and measure the primary GCR down to low rigidities in high latitude region. Both spectrometers have published time-dependent spectral measurements for the GCR proton and helium (the solar energetic particle flux has been manually removed already in the published data), which consist of approximately 88% and 11% of GCR flux respectively. Measurements for heavier elements as well as extended time span are underway at the AMS-02.

We determine the time-series of the aforementioned five parameters by fitting them to the time-dependent spectra measured by AMS-02 and PAMELA in the proton and helium channels (Adriani et al., 2013; Martucci et al., 2018; Marcelli et al., 2020; Aguilar et al., 2018; 2021; 2022). In Figure 1 we have plotted the four observables ($v_\oplus$, $B_\oplus$, α, and A) in the left panel and the five fitted parameters (b, c, $\mathfrak{R}_K$, K_0, and K_A) in the right panel as time series. For each Bartels rotation, or every 27 days, fitting is performed using a Markov Chain Monte Carlo method (Song et al., 2021; Chen et al., 2023). In the relevant SDE simulation, it takes some time for each pseudoparticle to move backward and reach the heliopause. During this time, we use the time-dependent solar wind and HMF. Specifically, we implement a stepwise approach using the observed time series of $v_\oplus, B_\oplus, \alpha, A$, while assuming that the fitting parameters b, c, R_k, K_0, K_A remain constant. The 6-month average of the fitted time series in Figure 1 is only used to provide a clear depiction of the trend for each quantity, and we utilize the best fit at each time point. There is an overlap period for the PAMELA and AMS-02 experiments, but in the plot, they are treated as independent fits.

The GCR spectra data are provided in the form of time series only for the proton and helium channels. Therefore, the fitting of diffusion and drift coefficients is performed only for these two species. However, Song et al. (2021) was able to fit both the proton channel and the helium channel with the same parameter set. This indicates the universality of the diffusion and drift coefficients for different GCR species (Tomassetti et al., 2018; Corti et al., 2019; Wang et al., 2019; Ngobeni et al., 2020; Fiandrini et al., 2021). In fact, the diffusion and drift coefficients are statistical measures of the small and large scale magnetic field irregularities. For GCRs with the same rigidity, the local curvature radius of the trajectory of an incident charged particle is determined by the ratio of the rigidity to the magnetic field strength, regardless of the particle's type or mass. It implies the same trajectory for particles with the same rigidity, explaining the universality of the drift coefficient for all GCR species. On the other hand, the diffusion coefficient is determined by the interaction between particles and waves/turbulence. According to quasi linear theory, the particle with the same gyro-radius resonates with the same waves, thus the resonant condition determines that particles with the same rigidity have the same diffusion coefficient. So here we use the best fits of the combined proton and helium data as the universal coefficients, and apply them to calculate the other 26 elements.

3 The calculated GCR spectra

The GCR flux is calculated on a four-dimensional grid, which is summarized in Table 1. Figure 2 shows sample calculations for three dimensions at 1.0 AU, namely during solar minimum and maximum as two representative dates, in each panel for five representative GCR species and the whole rigidity range.

3.1 The rigidity

The calculated range of rigidity is always from 0.2 to 100 GV for all elements. As a result of the MCMC fitting process, the calculated spectra accurately reproduce the measured proton and helium spectra in the rigidity region where PAMELA and AMS-02 have conducted direct measurements (Song et al., 2021; Chen et al., 2023), as a validation of the model. However, due to the finite thickness of the apparatus, low-energy/rigidity GCRs are blocked in the detector and cannot be detected, causing the measured rigidity to terminate at 1 GV for a proton and 1.65 GV for helium for the AMS-02. Beneath these minimal rigidities, one must work with the calculated spectra. As seen in Figure 2, the flux asymptotically vanishes as the rigidity decreases on the low-rigidity side (Moraal and Potgieter, 1982). The GCR spectra also decrease on the high rigidity side, following a power law with a well-known spectral index of approximately −2.7.

3.2 The GCR species

Although heavy ions are less abundant, their dose contribution can be enhanced by powers of their nuclear charge (Z), due to the nature of the Bethe-Bloch stopping power as well as the biological effectiveness. As a result, their dose contribution can be comparable to that of protons or helium. In the 1.0 AU calculation of Chen et al. (2023), it is noted that the five elements shown in Figure 2 together with magnesium are the most significant contributors to radiation dose, accounting for over 70% of the unshielded astronaut effective dose equivalent. These elements also represent all fractional contributions greater than 5% from a single element. Due to the smallness of the radial gradient, as demonstrated below, we expect that this behavior will persist across the entire spatial range.

The AMS-02 measurements for heavy elements extend to silicon and iron channels, but they are now in the form of averages over many years, and results with even shorter period have not been published yet. On the other hand, the ACE/CRIS experiment provides time-dependent measurement for heavy elements, but the detector type is calorimeter rather than magnetic spectrometer. Since we define our model using only the time-dependent data from space-borne magnetic spectrometers, the ACE/CRIS data for heavy elements are used only for cross check, but not for fitting. We respect the aforementioned universality of the diffusion and drift coefficients in calculations of other heavy elements for theoretical consistency. In Chen et al. (2023) we have compared our calculated spectra to the measurements averaged over many years for the elements with available data, and found good agreement.

3.3 The time dependence

Solar activity is known for its stochastic fluctuations in addition to its well-known 11-year cycle, which consists of a solar maximum and a solar minimum in each cycle. Many issues related to the time dependence have already been addressed in the previous discussion of Section 2.2. One can also refer to Song et al. (2021) for more information about the GCR spectra prior to June 2017, and a comparison in the form of dose rate time series in Chen et al. (2023) for the 1.0 AU slice result.

Starting from June 2006 of the beginning of the PAMELA experiment (Adriani et al., 2013; Martucci et al., 2018; Marcelli et al., 2020), the original fitting up to June 2017 in Song et al. (2021) is further extended to October 2019, in order to match the latest available AMS-02 time-dependent proton and helium data (Aguilar et al., 2018; Aguilar et al., 2021; Aguilar et al., 2022). New data after October 2019 will be implemented as soon as they become available.

Currently the model does not include forecast for future GCR spectra, which is crucial for future spacecraft design and space mission planing. For future solar modulation, all the GCR spectra forecast should be based on the forecast of future heliospheric environment parameters. A new GCR spectra forecast approach has been developed with the machine learning technique in Du et al. (2025), which uses the same previous GCR spectra data but not the Parker's transport equation. A more traditional approach of forecast based on solving the Parker's transport equation, more similar to the current forecast of Badhwar-O'Neil model and HelMod model, is also under development.

3.4 The radial dependence

In Gieseler et al. (2008) the radial gradient was measured to be $(4.5 \pm 0.6)\%$/AU in the 125 – 200 MeV/n helium channel and the 147 – 198 MeV/n carbon channel during 1997–2006. The two above channels both correspond to a bin of central rigidity of 1.122 GV in our calculated spectra. The fact that higher GCR flux is observed at an outer position can be simply explained by the scattering of the GCR particles in the heliosphere, that part of the GCRs can be scattered back into the interstellar medium as they enter the heliosphere. As they enter deeper, more GCRs will be scattered back, and the flux will be lower.

In Figure 3 we present several flux ratios $J(r)/J(1.0\text{AU})$ as functions of the radial position. We can observe a distinct positive radial gradient, at least for the two solar maximum configurations. The radial gradient for the astronaut's radiation dose should be closer to the radial gradient of the total integrated flux, rather than that of the representative low rigidity bin of 1.122 GV. In our calculation, we can clearly distinguish the radial dependence between a solar minimum and a solar maximum, with that at a solar maximum noticeably larger. The measurement made by Gieseler et al. (2008) over a period of 9 years can be considered as a weighted average, yeilding a radial gradient between our solar minimum case and the maximum case of the corresponding 1.122 GV bin.

In Figure 4 we plot the flux ratios $J(r)/J(1.0\text{AU})$ as a function of rigidity for two extreme epochs. The previous Figure 3 has already shown that the radial gradient is greater at low rigidities and smaller at high rigidities. Such phenomena are being continuously demonstrated now. Here we do not directly use the calculation results described in Table 1 with the default statistics of 3,000 pseudoparticles each, but increase the statistics to 10^6 each to reduce the statistical noise. In summary, as we have demonstrated, the radial gradient consistently remains small for any GCR element at any given time. Ignoring this gradient may result in a maximum error of only a few percents.

Note that there are various techniques for solving Parker's transport equation. Beyond the SDE method, there is another class of method, which is the alternating directional implicit (ADI) method (Potgieter and Moraal, 1985). Different from the SDE method which introduces the stochastic motion for a traced pseudoparticle and solves the problem in a Monte Carlo way, the ADI method focus on directly solving the partial differential equation in a deterministic way. In the latter approach a static equilibrium phase space density flow configuration is solved, then information across the whole spatial region is immediately extracted. On the other hand, in the SDE method the calculation of spectrum can only be done spatial point by spatial point, so if a radial gradient is the primary goal the SDE calculation is relatively less effective. But since the sampled pseudoparticle is simulated in real time, as mentioned before we can adopt a dynamical heliospheric environment with the observed $v_\oplus, B_\oplus, \alpha, A$ time series. This is an advantage over the ADI method, the assumed static heliospheric environment of which is indeed inconsistent with its nature of time variability.

3.5 Comparison with other models

In Table 2 we present a simple comparison of our SDEMMA model with other recent GCR models, including the latest version of the Badhwar-O'Neill models (O'Neill et al., 2015; Slaba and Whitman, 2019) and the HelMod model (Boschini et al., 2016). All versions of NASA's Badhwar-O'Neill models are based on a one-dimensional (radial) solution to Parker's transport equation. Only one time-dependent variable, the modulation potential ϕ_Z, is developed to control the modulation effect, but for different element it is fitted to different values. In the latest 2020 version, the data set used for fitting is the ACE/CRIS data, when available, and the SSN is used otherwise. On the other hand, similar to ours, the HelMod model is also based on the SDE solution of Parker's full (two-dimensional) transport equation. The SSN and CR neutron monitor data are used to fit the modulation. For both the Badhwar-O'Neil 2020 model and the HelMod model, the AMS-02 and PAMELA time-dependent spectra are used for calibration at a level of average over many years, but not for exact direct fitting of the solar modulation time series. It is natural that our GCR model provides better agreement with the AMS-02 and PAMELA data as the baseline, with an average absolute relative difference $|Rd|$ (O'Neill et al., 2015) of less than one percent in the proton and helium channels. In comparison, the Badhwar-O'Neill 2020 model and the HelMod model show an average absolute relative difference of about 3%.

A dedicated and more comprehensive comparison of GCR models is given in Liu et al. (2024), which includes our model, the BON2020 model, the HelMod model, as well as the CREME model (Tylka et al., 1997; Adams et al., 2012) and DLR model (Matthiä et al., 2013).

4 Induced dose equivalent rate between Earth's and Mars' orbit

Based on the SDEMMA model, we calculate the astronaut dose equivalent rate $\dot{H}$ induced by the isotropic GCR flux between the Earth's and the Mars' orbit. It is given by

$$\dot{H} = \sum_{\mathrm{R}} \int d\mathfrak{R}\, 4\pi \frac{d^4 N_{\mathrm{R}}}{dA dt d\Omega d\mathfrak{R}} \frac{(\Delta E_{\mathrm{R}}/m)\, Q}{dN_{\mathrm{R}}/dA} = \sum_{\mathrm{R}} \int d\mathfrak{R}\, 4\pi J_{\mathrm{R}} \left(\frac{D_{\mathrm{R}} Q}{\Phi_{\mathrm{R}}} \right). \tag{14}$$

By cancelling the factors such as $d\mathfrak{R}$, dN_{R} and dA, the first equation reduces eventually to $\dot{H} \sim (\Delta E_{\mathrm{R}}/m)Q/t$ as the definition of dose equivalent rate with all particles' contribution. And in the second equation, the two factors reduce respectively to the GCR spectra $J_{\mathrm{R}}(\mathfrak{R}) = \frac{d^4 N_{\mathrm{R}}}{dA dt d\Omega d\mathfrak{R}}$ and the fluence-to-dose-equivalent conversion coefficients $\frac{D_{\mathrm{R}} Q}{\Phi_{\mathrm{R}}} = \frac{(\Delta E_{\mathrm{R}}/m)Q}{dN_{\mathrm{R}}/dA}$. Here N_{R} is number of incident particle of radiation "R", A is a cross section of the incident particle beam, Ω is the solid angle for the incident flux. ΔE_{R} is the energy loss of radiation "R", m is the corresponding target mass, so $D_{\mathrm{R}} = \Delta E_{\mathrm{R}}/m$ is the energy deposited in unit mass, namely the absorbed dose. Q is the quality factor which converts the physical absorbed dose to the medical dose equivalent, which has two definitions: the ICRP60 definition (ICRP60, 1991) and the NASA definition (Cucinotta et al., 2011). $\Phi_{\mathrm{R}} = dN_{\mathrm{R}}/dA$ is the fluence for radiation "R".

The fluence-to-dose-equivalent conversion coefficient has the meaning of the expected dose equivalent caused by a single incident particle, if the incident particle is integrated over all contributing area on the normal plane of its "beam" direction. It is calculated by particle physics Monte Carlo code. We have calculated the isotropic fluence-to-dose-equivalent conversion coefficients using the Monte Carlo toolkit GEANT4 (Agostinelli et al., 2003; Allison et al., 2006; Allison et al., 2016) using the ICRU sphere[1] as the dose counter, for all the $Z = 1 - 28$ GCR elements and 27 – 36 energy points ranging from 1 MeV/n to 100 GeV/n for each element. Except for using the simplified target of the ICRU sphere rather than the detailed human voxel phantom (ICRP110, 2009), the calculation procedures are the same as the series of independently developed dose coefficient sets by ourselves (Chen et al., 2025), such as the linear energy transfer and quality factor calculation methods. Compared with the only published dose coefficient set of ICRP123 (2013) for the same $Z = 1 - 28$ elements and energy range and the detailed human voxel phantom, we have the freedom to considered characteristic shielding configurations as an essential improvement of the naked human phantom assumption. This is achieved by setting an extra shielding shell around the target dose counter in the world construction of the simulation, where the shell has a certain dimension, shape, and chemical composition. Then the simulated incident particle will interact with the shielding structure before it hits the dose counter. The shielded dose coefficients are defined as the expected (average) dose equivalent caused by a single incident particle before entering any shielding.

4.1 Unshielded case

The first $\dot{H}$ calculation set is for the unshielded case, and the results using the ICRP60 quality factor are collected in Figure 5. We have tested several combinations of different GCR spectra models (our SDEMMA model and the alternative HelMod model (Boschini et al., 2016)) with different fluence-to-dose-equivalent conversion coefficients (the ICRP123 dose coefficient (ICRP123, 2013), our independently calculated dose coefficient set using the ICRP110 human voxel phantom (Chen et al., 2025), and our independently calculated dose coefficient set using the ICRU sphere). Since the SDEMMA model provides GCR spectra at seven different radial locations at per 0.1 AU, the range of the seven $\dot{H}$ values form a small vertical bar for each time point. Moreover, based on the ICRP110 human voxel phantom, the first three calculations yield dose equivalent rates $\dot{H}_T$ for each of the 15 sensitive organs/tisse "T", and the $\dot{H}$ shown is the weighted sum of the $\dot{H}_T$s by the tissue weight factor (ICRP103, 2007) (the effective dose equivalent). We can see that the dose equivalent rate differences between the HelMod and the SDEMMA GCR models are smaller than those between different dose coefficient sets of ~11%. $\dot{H}$ for detailed human voxel phantom are 3% – 5% lower than those for the ICRU sphere.

1 The ICRU sphere is a phantom used in radiation protection. It has a diameter of 30 cm, and a hypothetical tissue equivalent material of density 1 g/cm3 and composition of oxygen 76.2%, carbon 11.1%, hydrogen 10.1% and nitrogen 2.6%.

4.2 MSL/RAD shielding

The MSL/RAD shielding during the cruise stage in the transit orbit is too complicated to simulate exactly. In simulation we simplify the shielding to three aluminum layers: 30% of the detector acceptance is shielded by a mass thickness of 1 g/cm^2, 50% is shielded by a mass thickness of 9 g/cm^2, and the remainder 20% is shielded by a mass thickness of 56 g/cm^2. The average is 16 g/cm^2, the same as the averaged MSL/RAD shielding thickness. On the other hand, beneath the shielding the mass thickness of the detector is small, giving negligible self-shielding. Therefore, the target dose counter has been manually divided into the surface part (with 2 mm thickness) and the remainder part. The surface part emulates the detector with negligible self-shielding, and the remainder should give values closer to the effective dose equivalent of real human phantom.

We have performed two round of simple simulations. The first one also using the same isotropic GCR incidence and the ICRU sphere gives a dose equivalent rate of 2.07 mSv/d averaged over the MSL/RAD time window. While the isotropy is the case for the astronaut in deep space, the MSL/RAD detector has a small field of view of 30° (Zeitlin et al., 2013). While an energetic particle can penetrate the dose counter and induce dose on the other side opposite to its incidence, this cannot be measured by the MSL/RAD. The second simulation uses a plane beam and target, and gives a dose equivalent rate of 1.20 mSv/d if the flux is scaled to 4π solid angle. The MSL/RAD measured dose equivalent rate of 1.75 ± 0.30 mSv/d purely from the GCR contribution (Guo et al., 2015) is between the two. Note that the remainder part of the dose counter in the two simulations both give smaller dose-equivalent rates (~50%– ~ 70%), due to the self-shielding.

4.3 Optimized 30 g/cm^2 shielding

The last $\dot{H}$ calculation set is for shieldings with mass thickness of 30 g/cm^2. In addition to the Bethe-Bloch stopping effect which slows down the incident particle and decreases the dose, shielding materials also produce secondary particles when hit by energetic incident particle, and those secondary particles can contribute dose when hitting the astronaut as well. For light proton and helium the secondary particles will eventually increase the dose. So there is an optimized depth which balances the production of secondary particles (increase with shielding depth) and the Bethe-Bloch stopping, and the depth is determined to be 30 g/cm^2 (Guo et al., 2017).

Figure 6 shows our final $\dot{H}$ calculation with the ICRU sphere and optimized shielding mass thickness. As for shielding material, aluminum is currently widely used in space as structural material, but polyethylene is an optimized baseline choice for its high electron-number-to-mass ratio which facilitates the Bethe-Bloch stopping effect (Naito et al., 2020). We have also varied the quality factor Q definition. As seen, at the flux minimum in the covered period, the dose equivalent rates induced by GCR behind optimized polyethylene shielding are ~14 cSv/yr using the ICRP60 quality factor and ~17 cSv/yr using the NASA quality factor, while at the flux maximum the rates are ~25 cSv/yr and ~30 cSv/yr, respectively.

The fluence-to-dose-equivalent conversion coefficient and dose equivalent rate calculation using the detailed human voxel phantom will be provided in a forthcoming publication.

5 Summary

We have presented a model for the modulated galactic cosmic ray spectra called SDEMMA. This model is based on data from the space-borne magnetic spectrometers PAMELA and AMS-02. In this model, we use the 3D stochastic differential equation method (Equations 2, 3) to calculate spectra, incorporating the recently developed local interstellar spectra of galactic cosmic rays for all the $Z = 1 - 28$ elements. Heliospheric environment modelings based on observational inputs and MCMC fittings are used. This model enables us to precisely reproduce the time-dependent measurements of PAMELA and AMS-02 (Adriani et al., 2013; Martucci et al., 2018; Marcelli et al., 2020; Aguilar et al., 2018; 2021; 2022) with a margin of error of just a few percent, regardless of energy and GCR species. We extend the spectra calculation to other radial locations in the inner solar system beyond the previous focus at 1.0 AU, which is relevant to the Mars mission.

We have also developed a set of fluence-to-dose-equivalent conversion coefficients based on simplified dose counter but several shielding considerations. Combining the SDEMMA GCR model and the dose coefficients, the astronaut radiation dose equivalent rates on the transfer orbit are calculated using Equation 14, for the considered period with an explicit radial dependence.

Data availability statement

The SDEMMA dataset for GCR spectra time series can be downloaded as a zip file from https://en.iat.cn/resource.

The OMNI solar wind and HMF data are available from the GSFC website https://omniweb.gsfc.nasa.gov. The Wilcox Solar Observatory HCS data is available from the WSO website http://wso.stanford.edu/. The sun spot number data is available from the Solar Influences Data analysis Center website https://www.sidc.be.

The PAMELA proton and helium spectra time series can be extracted from https://tools.ssdc.asi.it/CosmicRays/chargedCosmicRays.jsp. The AMS-02 proton and helium spectra tables in time series are available via the corresponding supplemental material and data links of Phys. Rev. Lett. 121, 051101 (2018), Phys. Rep. 894, 1 (2021), and Phys. Rev. Lett. 128, 231102 (2022) at the AMS group publication page https://ams02.space/publications.

The HelMod GCR spectra time series are available from https://www.helmod.org/index. php?view=article&id=76:transfer-orbit-fluence&catid=14. The fluence-to-dose-equivalent conversion coefficients for the ICRU sphere can be downloaded as a zip file from https://en.iat.cn/resource.

The ICRP123 fluence-to-dose-equivalent conversion coefficients are available via the "Supplemental Material" link at the ICRP123 publication URL https://www.icrp.org/publication.asp?id=ICRP%20Publication%20123.

Author contributions

XS: Data curation, Formal Analysis, Investigation, Methodology, Resources, Software, Validation, Writing–review and editing. RH: Conceptualization, Funding acquisition, Project administration, Supervision, Visualization, Writing–original draft, Writing–review and editing. SX: Data curation, Writing–review and editing. XC: Data curation, Writing–review and editing. XL: Funding acquisition, Methodology, Software, Writing–review and editing.

Funding

The author(s) declare that financial support was received for the research and/or publication of this article. The presented work was supported by the Shandong Institute of Advanced Technology start funding (2020106R01, 2020106R02) and the NSFC grants (U2106201).

Acknowledgments

We are grateful to the useful discussion with Jingnan Guo, Tong Su, Weiwei Xu and Vladimir Mikhailov. The generative AI of Wordvice AI and DeepSeek-R1 have been used for English improvement.

Conflict of interest

The authors declare that the research was conducted in the absence of any commercial or financial relationships that could be construed as a potential conflict of interest.

Publisher's note

All claims expressed in this article are solely those of the authors and do not necessarily represent those of their affiliated organizations, or those of the publisher, the editors and the reviewers. Any product that may be evaluated in this article, or claim that may be made by its manufacturer, is not guaranteed or endorsed by the publisher.

References

Adams, J. H., Barghouty, A. F., Mendenhall, M. H., Reed, R. A., Sierawski, B. D., Warren, K. M., et al. (2012). Creme: the 2011 revision of the cosmic ray effects on micro-electronics code. *IEEE Trans. Nucl. Sci.* 59, 3141–3147. doi:10.1109/TNS.2012.2218831

Adriani, O., Barbarino, G. C., Bazilevskaya, G. A., Bellotti, R., Boezio, M., Bogomolov, E. A., et al. (2013). Time dependence of the proton flux measured by pamela during the 2006 july-2009 december solar minimum. *Astrophys. J.* 765, 91. doi:10.1088/0004-637x/765/2/91

Agostinelli, S., Allison, J., Amako, K., Apostolakis, J., Araujo, H., Arce, P., et al. (2003). Geant4—a simulation toolkit. *Nucl. Instrum. Methods Phys. Res. Sect. A Accel. Spectrom. Detect. Assoc. Equip.* 506, 250–303. doi:10.1016/S0168-9002(03)01368-8

Aguilar, M., Aisa, D., Alpat, B., Alvino, A., Ambrosi, G., Andeen, K., et al. (2015). Precision measurement of the proton flux in primary cosmic rays from rigidity 1 GV to 1.8 TV with the alpha magnetic spectrometer on the international space station. *Phys. Rev. Lett.* 114, 171103. doi:10.1103/PhysRevLett.114.171103

Aguilar, M., Ali Cavasonza, L., Alpat, B., Ambrosi, G., Arruda, L., Attig, N., et al. (2018). Observation of fine time structures in the cosmic proton and helium fluxes with the alpha magnetic spectrometer on the international space station. *Phys. Rev. Lett.* 121, 051101. doi:10.1103/PhysRevLett.121.051101

Aguilar, M., Ali Cavasonza, L., Ambrosi, G., Arruda, L., Attig, N., Barao, F., et al. (2021). The alpha magnetic spectrometer (AMS) on the international space station: Part II - results from the first seven years. *Phys. Rep.* 894, 1–116. doi:10.1016/j.physrep.2020.09.003

Aguilar, M., Ali Cavasonza, L., Ambrosi, G., Arruda, L., Attig, N., Barao, F., et al. (2022). Properties of daily helium fluxes. *Phys. Rev. Lett.* 128, 231102. doi:10.1103/PhysRevLett.128.231102

Allison, J., Amako, K., Apostolakis, J., Araujo, H., Arce Dubois, P., Asai, M., et al. (2006). Geant4 developments and applications. *IEEE Trans. Nucl. Sci.* 53, 270–278. doi:10.1109/TNS.2006.869826

Allison, J., Amako, K., Apostolakis, J., Arce, P., Asai, M., Aso, T., et al. (2016). Recent developments in Geant4. *Nucl. Instrum. Methods Phys. Res. Sect. A Accel. Spectrom. Detect. Assoc. Equip.* 835, 186–225. doi:10.1016/j.nima.2016.06.125

Boschini, M., Della Torre, S., Gervasi, M., La Vacca, G., and Rancoita, P. (2022). The transport of galactic cosmic rays in heliosphere: the HelMod model compared with other commonly employed solar modulation models. *Adv. Space Res.* 854, 2636–2648. doi:10.1016/j.asr.2022.03.026

Boschini, M. J., Della Torre, S., Gervasi, M., Grandi, D., Jóhannesson, G., La Vacca, G., et al. (2021). The discovery of a low-energy excess in cosmic-ray iron: evidence of the past supernova activity in the local bubble. *Astrophys. J.* 913, 5. doi:10.3847/1538-4357/abf11c

Boschini, M. J., Della Torre, S., Gervasi, M., La Vacca, G., and Rancoita, P. G. (2016). Propagation of cosmic rays in heliosphere: the HELMOD model. *Adv. Space Res.* 207, 2859–2879. doi:10.1016/j.asr.2017.04.017

Boschini, M. J., Torre, S. D., Gervasi, M., Grandi, D., Jóhannesson, G., Vacca, G. L., et al. (2020). Inference of the local interstellar spectra of cosmic-ray nuclei $Z \leq 28$ with the GalProp–HelMod framework. *Astrophys. J. Suppl.* 250, 27. doi:10.3847/1538-4365/aba901

Badhwar-O'Neill(2014). Galactic cosmic ray flux model description. *NASA Technical Reports-2015-218569*

Chen, L., Chen, X., Huo, R., Xu, S., and Xu, W. (2025). Astronaut dose coefficients calculated using GEANT4 and comparison with icrp123. *Radiat. Environ. Biophysics* XX, XXX.

Chen, X., Xu, S., Song, X., Huo, R., and Luo, X. (2023). Astronaut radiation dose calculation with a new galactic cosmic ray model and the AMS-02 data. *Space weather.* 21, e2022SW003285. doi:10.1029/2022SW003285

Corti, C., Potgieter, M. S., Bindi, V., Consolandi, C., Light, C., Palermo, M., et al. (2019). Numerical modeling of galactic cosmic-ray proton and helium observed by ams-02 during the solar maximum of solar cycle 24. *Astrophysical J.* 871, 253. doi:10.3847/1538-4357/aafac4

Cucinotta, F. A., Kim, M.-H. Y., and Chappell, L. J. (2011). Space radiation cancer risk projections and uncertainties - 2010. *NASA Tech. Reports-2011-216155.*

Du, Y.-L., Song, X., and Luo, X. (2025). Deep learning the forecast of galactic cosmic-ray spectra. *Astrophysical J. Lett.* 978, L36. doi:10.3847/2041-8213/ada427

Fiandrini, E., Tomassetti, N., Bertucci, B., Donnini, F., Graziani, M., Khiali, B., et al. (2021). Numerical modeling of cosmic rays in the heliosphere: analysis of proton data from ams-02 and pamela. *Phys. Rev. D.* 104, 023012. doi:10.1103/PhysRevD.104.023012

Gieseler, J., Heber, B., Dunzlaff, P., Müller-Mellin, R., Klassen, A., and Gomez-Herrero, R. (2008). "The radial gradient of galactic cosmic rays: ulysses KET and ACE CRIS Measurements," in *International cosmic ray conference. Vol. 1 of international cosmic ray conference*, 571–574.1. Available online at https://ui.adsabs.harvard.edu/abs/2008ICRC

Guo, J., Slaba, T. C., Zeitlin, C., Wimmer-Schweingruber, R. F., Badavi, F. F., Böhm, E., et al. (2017). Dependence of the martian radiation environment on atmospheric depth: modeling and measurement. *J. Geophys. Res. Planets* 122, 329–341. doi:10.1002/2016JE005206

Guo, J., Wang, B., Whitman, K., Plainaki, C., Zhao, L., Bain, H. M., et al. (2024). Particle radiation environment in the heliosphere: status, limitations, and recommendations. *Adv. Space Res.* doi:10.1016/j.asr.2024.03.070

Guo, J., Zeitlin, C., Wimmer-Schweingruber, R. F., Hassler, D. M., Posner, A., Heber, B., et al. (2015). Variations of dose rate observed by MSL/RAD in transit to Mars. *Astronomy and Astrophysics* 577, A58. doi:10.1051/0004-6361/201525680

HelMod (2024). Available online at: https://www.helmod.org/index.php?view=article&id=76:transfer-orbit-fluence&catid=14.

ICRP103 (2007). 2007 recommendations of the international commission on radiological protection. ICRP publication 103. *Ann. ICRP* 37.

ICRP110 (2009). Adult reference computational phantoms. ICRP publication 110. *Ann. ICRP* 39.

ICRP123, Dietze, G., Bartlett, D. T., Cool, D. A., Cucinotta, F. A., Jia, X., et al. (2013). ICRP, 123. Assessment of radiation exposure of astronauts in space. ICRP Publication 123. *Ann. ICRP* 42, 1–339. doi:10.1016/j.icrp.2013.05.004

ICRP60 (1991). 1990 recommendations of the international commission on radiological protection. ICRP publication 60. *Ann. ICRP* 21.

Jokipii, J. R., and Kota, J. (1989). The polar heliospheric magnetic field. *Geophys. Res. Lett.* 16, 1–4. doi:10.1029/GL016i001p00001

Langner, U. W., and Potgieter, M. S. (2004). Solar wind termination shock and heliosheath effects on the modulation of protons and antiprotons. *J. Geophys. Res. Space Phys.* 109. doi:10.1029/2003JA010158

Langner, U. W., Potgieter, M. S., and Webber, W. R. (2003). Modulation of cosmic ray protons in the heliosheath. *J. Geophys. Res. Space Phys.* 108. doi:10.1029/2003JA009934

Li, H., Wang, C., and Richardson, J. D. (2008). Properties of the termination shock observed by voyager 2. *Geophys. Res. Lett.* 35. doi:10.1029/2008GL034869

Liu, W., Guo, J., Wang, Y., and Slaba, T. C. (2024). A comprehensive comparison of various galactic cosmic-ray models to the state-of-the-art particle and radiation measurements. *Astrophysical J. Suppl. Ser.* 271, 18. doi:10.3847/1538-4365/ad18ad

Marcelli, N., Boezio, M., Lenni, A., Menn, W., Munini, R., Aslam, O. P. M., et al. (2020). Time dependence of the flux of helium nuclei in cosmic rays measured by the pamela experiment between 2006 july and 2009 december. *Astrophys. J.* 893, 145. doi:10.3847/1538-4357/ab80c2

Martucci, M., Munini, R., Boezio, M., Felice, V. D., Adriani, O., Barbarino, G. C., et al. (2018). Proton fluxes measured by the PAMELA experiment from the minimum to the maximum solar activity for solar cycle 24. *Astrophys. J.* 854, L2. doi:10.3847/2041-8213/aaa9b2

Matthiä, D., Berger, T., Mrigakshi, A. I., and Reitz, G. (2013). A ready-to-use galactic cosmic ray model. *Adv. Space Res.* 51, 328. doi:10.1016/j.asr.2012.09.022

Moraal, H., and Potgieter, M. S. (1982). Solutions of the spherically-symmetric cosmic-ray transport equation in interplanetary space. *Astrophysics Space Sci.* 84, 519–533. doi:10.1007/BF00651330

Naito, M., Kodaira, S., Ogawara, R., Tobita, K., Someya, Y., Kusumoto, T., et al. (2020). Investigation of shielding material properties for effective space radiation protection. *Life Sci. Space Res.* 26, 69–76. doi:10.1016/j.lssr.2020.05.001

Ngobeni, M. D., Aslam, O. P. M., Bisschoff, D., Potgieter, M. S., Ndiitwani, D. C., Boezio, M., et al. (2020). The 3d numerical modeling of the solar modulation of galactic protons and helium nuclei related to observations by pamela between 2006 and 2009. *Astrophysics Space Sci.* 365, 182. doi:10.1007/s10509-020-03896-1

O'Neill, P., Golge, S., and Slaba, T. C. (2015). Galactic cosmic ray flux model description. *NASA Technical Reports-2015-218569*

Opher, M., Richardson, J., Zank, G., Florinski, V., Giacalone, J., Sokol, J. M., et al. (2023). Solar wind with hydrogen ion charge exchange and large-scale dynamics (shield) drive science center. *Front. Astronomy Space Sci.* 10. doi:10.3389/fspas.2023.1143909

Potgieter, M. S. (2013). Solar modulation of cosmic rays. *Living Rev. Sol. Phys.* 10, 3. doi:10.12942/lrsp-2013-3

Potgieter, M. S., and Moraal, H. (1985). A drift model for the modulation of galactic cosmic rays. *Astrophys. J.* 294, 425–440. doi:10.1086/163309

Potgieter, M. S., Vos, E. E., Boezio, M., De Simone, N., Di Felice, V., and Formato, V. (2014). Modulation of galactic protons in the heliosphere during the unusual solar minimum of 2006 to 2009. *Sol. Phys.* 289, 391–406. doi:10.1007/s11207-013-0324-6

Qin, G., and Shen, Z.-N. (2017). Modulation of galactic cosmic rays in the inner heliosphere, comparing with pamela measurements. *Astrophysical J.* 846, 56. doi:10.3847/1538-4357/aa83ad

Qin, G., and Zhang, L.-H. (2014). The modification of the nonlinear guiding center theory. *Astrophysical J.* 787, 12. doi:10.1088/0004-637X/787/1/12

Raath, J. L., Potgieter, M. S., Strauss, R. D., and Kopp, A. (2016). The effects of magnetic field modifications on the solar modulation of cosmic rays with a SDE-based model. *Adv. Space Res.* 57, 1965–1977. doi:10.1016/j.asr.2016.01.017

Semkova, J., Koleva, R., Benghin, V., Dachev, T., Matviichuk, Y., Tomov, B., et al. (2018). Charged particles radiation measurements with liulin-mo dosimeter of frend instrument aboard exomars trace gas orbiter during the transit and in high elliptic mars orbit. *Icarus* 303, 53–66. doi:10.1016/j.icarus.2017.12.034

Slaba, T. C., and Whitman, K. (2019). The badhwar - O'neill 2020 model. *NASA Technical Reports-2019-220419*

Song, X., Luo, X., Potgieter, M. S., Liu, X., and Geng, Z. (2021). A numerical study of the solar modulation of galactic protons and helium from 2006 to 2017. *Astrophys. J. Suppl.* 257, 48. doi:10.3847/1538-4365/ac281c

Tomassetti, N., Barão, F., Bertucci, B., Fiandrini, E., Figueiredo, J., Lousada, J., et al. (2018). Testing diffusion of cosmic rays in the heliosphere with proton and helium data from ams. *Phys. Rev. Lett.* 121, 251104. doi:10.1103/PhysRevLett.121.251104

Tylka, A., Adams, J., Boberg, P., Brownstein, B., Dietrich, W., Flueckiger, E., et al. (1997). Creme96: a revision of the cosmic ray effects on micro-electronics code. *IEEE Trans. Nucl. Sci.* 44, 2150–2160. doi:10.1109/23.659030

Wang, B.-B., Bi, X.-J., Fang, K., Lin, S.-J., and Yin, P.-F. (2019). Time-dependent solar modulation of cosmic rays from solar minimum to solar maximum. *Phys. Rev. D.* 100, 063006. doi:10.1103/PhysRevD.100.063006

Zeitlin, C., Hassler, D. M., Cucinotta, F. A., Ehresmann, B., Wimmer-Schweingruber, R. F., Brinza, D. E., et al. (2013). Measurements of energetic particle radiation in transit to mars on the mars science laboratory. *Science* 340, 1080–1084. doi:10.1126/science.1235989

Zhang, M. (1999). A markov stochastic process theory of cosmic-ray modulation. *Astrophys. J.* 513, 409–420. doi:10.1086/306857

frontiers | Frontiers in Astronomy and Space Sciences

TYPE Original Research
PUBLISHED 12 May 2025
DOI 10.3389/fspas.2025.1601296

Check for updates

OPEN ACCESS

EDITED BY
Nithin Sivadas,
National Aeronautics and Space Administration, United States

REVIEWED BY
Daniel Billett,
University of Saskatchewan, Canada
Weijia Zhan,
University of Colorado Boulder, United States

*CORRESPONDENCE
Katherine Davidson,
ktd0008@uah.edu

RECEIVED 27 March 2025
ACCEPTED 24 April 2025
PUBLISHED 12 May 2025

CITATION
Davidson K, Zou Y, Lamarche L, Bhatt A and Conde M (2025) Characterization of F-region neutral wind response times and its controlling factors during substorms. *Front. Astron. Space Sci.* 12:1601296. doi: 10.3389/fspas.2025.1601296

COPYRIGHT
© 2025 Davidson, Zou, Lamarche, Bhatt and Conde. This is an open-access article distributed under the terms of the Creative Commons Attribution License (CC BY). The use, distribution or reproduction in other forums is permitted, provided the original author(s) and the copyright owner(s) are credited and that the original publication in this journal is cited, in accordance with accepted academic practice. No use, distribution or reproduction is permitted which does not comply with these terms.

Characterization of F-region neutral wind response times and its controlling factors during substorms

Katherine Davidson[1]*, Ying Zou[2], Leslie Lamarche[3], Asti Bhatt[3] and Mark Conde[4]

[1]Department of Space Science, University of Alabama in Huntsville, Huntsville, AL, United States, [2]Johns Hopkins Applied Physics Laboratory, Laurel, MD, United States, [3]SRI International, Menlo Park, CA, United States, [4]Department of Physics, University of Alaska Fairbanks, Fairbanks, AK, United States

Ion-neutral coupling is responsible for dissipating energy deposited into the high-latitude ionosphere during geomagnetically active periods. The neutral wind response time, or the ion-neutral coupling efficiency, is not well characterized, with a wide range of reported response times. Additionally, how this coupling efficiency varies with geomagnetic activity level is not well understood, with few studies addressing the impact of geomagnetic activity level on neutral wind response time. In this study, a statistical analysis of the neutral wind response time during substorm periods is performed. We use data from Scanning Doppler Imagers (SDIs) and the Poker Flat Incoherent Scatter Radar (PFISR) to calculate the neutral wind response time using the new weighted windowed time-lagged correlation method. Substorm events were found using SuperMAG substorm lists and All Sky Imagers (ASIs). This statistical analysis resulted in 23 substorm events, with an average response time of ~16 min. To determine the controlling factors of this response time, geomagnetic and ionospheric parameters, such as IMF strength and orientation, SYM/H index, AE index, and electron density, are investigated for the statistical substorm set. A superposed epoch analysis of the parameters is performed to determine average geospace conditions required for fast neutral wind responses. It was found that quiet-time conditions in AE and SYM-H indices, a southward turning of IMF around 1.5 h before substorm onset time, and large electron densities lead to faster neutral wind response times. Based on the geomagnetic indices results, it was suggested that thermospheric pre-conditioning may play a role in neutral wind response times.

KEYWORDS

ionosphere, thermosphere, space weather, systems coupling, substorm

1 Introduction

High-latitude ionosphere-thermosphere coupling is a crucial dynamic for dissipating energy deposited into Earth's upper atmosphere during geomagnetic storms and substorms. Ionosphere-thermosphere coupling in the form of ion-neutral collisions create an ion-drag force, which sets the F-region neutral atmosphere in motion. The resulting thermospheric winds redistribute mass and energy deposited into Earth's upper atmosphere. However, because the thermosphere is more massive than the ionosphere, and is also subjected to

pressure-gradient, advection, and other forces, the neutral wind response will often be delayed from changes in ionospheric flow. This time delay, or neutral wind response time, is a key indicator of the ion-neutral coupling efficiency, and it is not well understood. Additionally, the controlling factors of this coupling efficiency, such as geomagnetic activity strength or ionospheric parameters, are not well characterized.

It is important to know whether the coupling efficiency strengthens as geomagnetic activity strength increases since ion-neutral coupling is responsible for dissipating the high-latitude energy deposited during substorms. This parameter would affect how long the ionosphere remains highly-energized, putting LEO satellites at risk of increased satellite drag and de-orbit. It is generally understood that an increase in geomagnetic activity level will increase ion-neutral coupling through an enhanced electron density, therefore decreasing the neutral wind response time. Faster neutral wind responses for higher levels of geomagnetic activity have also been observed. For example, Kosch et al. (2001) used the Kp index to indicate a geomagnetically active and quiet period of time, and found that the e-folding time was 1.8 and 3.3 h for an active and quiet period, respectively. Ponthieu et al. (1988) studied the response times during a solar maximum event and solar minimum event, and found that the e-folding time during solar minimum was an order of magnitude larger than at solar maximum. A statistical study of 902 nights spanning across solar maximum and solar minimum years found that geomagnetic polar cap wind speeds were around 200 m/s in solar minimum and 800 m/s in solar maximum, with a strong dependence on Kp index (Killeen et al., 1995). These studies focused more on large-scale differences of the neutral wind response time, studying the effects of solar maximum vs. solar minimum or geomagnetic storm vs. geomagnetic quiet time.

While geomagnetic storms cause a large-scale magnetospheric disturbance lasting a few days, substorms are explosive releases of energy lasting only about 1–3 h (Tanskanen, 2009). It has been shown that the energy deposited into the high-latitude ionosphere can range from 30% up to 100% of the magnetic energy stored in the magnetotail during substorms (Tanskanen et al., 2002; Akasofu, 2013; Spencer et al., 2019). This explosive release causes rapid changes in the high-latitude ionospheric convection. Reconfiguration of the ionospheric convection pattern occurs on the time scale of minutes (Wing et al., 2002; Yu and Ridley, 2009). In addition to rapid reconfiguration, plasma flow has also been shown to increase on the order of hundreds to thousands of meters per second over intervals of 10–20 min (Sánchez et al., 1996). Neutral winds are driven by these rapid flows due to increased ion-neutral collisions from substorm associated particle precipitation. However, the neutral wind response time during these intense substorm injections are not well characterized. Previous studies typically use observational methods to determine the neutral wind response time during substorms, which leads to a wide range of reported response times, from immediate responses to a time scale of tens of minutes (Cai et al., 2019; Billett et al., 2020; Zou et al., 2021).

Substorms also cause a significant enhancement in energetic particle precipitation, with the power of diffuse, monoenergetic, and wave electron aurora having been shown to increase by 310%, 71%, and 170%, respectively, during a substorm cycle (Wing et al., 2013). While electron density enhancements due to substorms typically peak in the E-region altitudes (Kaeppler et al., 2020; Grandin et al., 2024; Oyama et al., 2014), the thermosphere in this region is much denser and ion-neutral collisions here often impede ionospheric ExB drift (Sangalli et al., 2009). Therefore, neutral wind responses to plasma convection are typically much slower in the E-region, on the order of hours (Richmond et al., 2003; Billett et al., 2020). The F-region, however, still sees significant electron density enhancements during substorms. During substorm recovery, quasiperiodic brightenings of the aurora, known as pulsating aurora (Jones et al., 2011), have been shown to be associated with soft electron precipitation in the F-region (Oyama et al., 2014; Fukizawa et al., 2021). A case study done by Liu et al. (2008) used the NORSTAR multispectral imager (MSI) and found equatorward moving streamers in the 630.0 nm emission line (F-region) prior to substorm onset. Kepko et al. (2009) observed an equatorward moving diffuse auroral patch in the 630.0 nm emission line just before substorm onset. Gillies et al. (2017) used a REGO ASI and the Resolute Bay Incoherent Scatter Radar-Canadian (RISR-C) to study 630.0 nm auroral emissions and found that at the 220–240 km altitude range, electron density increased within red discrete arcs and in the region of diffuse aurora. This evidence shows that the F-region thermosphere would be subjected to a significant ion-drag force during substorms due to the enhanced precipitation, however it is still unclear how efficient this forcing is.

Similarly, few studies have been done regarding the relative strength of geomagnetic activity on neutral wind response, *e.g.*, the response during a 300 nT substorm vs. the response during a 600 nT substorm. One such study was performed by Omaya et al. (2023), where hourly mean winds from 9 years of FPI data were binned by a SuperMAG (SME) index and found that zonal dusk winds had larger westward flows for increased SME. Another study by Zou et al. (2021) constructed a statistical wind morphology as a function of magnetic latitude, local time and AE^* index and also found that wind speeds increased as AE^* increased, with AE^* being the maximum AE value in the past 2 hours of individual measurements. While these studies show that neutral winds have a dependence on the strength of geomagnetic activity level, there is still limited information on how the neutral wind response time, and the ion-neutral coupling efficiency, varies with geomagnetic activity level.

In this study, we perform a statistical analysis of the neutral wind response time and its controlling factors during substorm periods. Section 2 describes the instrumentation, event selection criteria, and methodology. Section 3.1 provides the results of the statistical survey, and Sections 3.2 and 3.3 details two case studies from the event list. Sections 3.4 and 3.5 presents a superposed epoch analysis of the geomagnetic conditions and electron density of the events, respectively, and Section 3.6 discusses other possible controlling factors of the neutral wind response time. The work is summarized in Section 4.

2 Materials and methods

2.1 Scanning Doppler Imagers

The 630.0 nm emissions from the Poker Flat (PKR, 65.1°N, −147.5°E) and Toolik Lake (TLK, 68.6°N, −149.6°E) Scanning Doppler Imager (SDI) are used to observe thermospheric parameters (Conde and Smith, 1995; 1997; 1998; Conde and

Nicolls, 2010). The 630.0 nm emission spectra originate from atomic oxygen around 230 km, placing our observations in the F-region thermosphere. SDIs are Fabry-Perot interferometers that observe emission spectra in 115 subregions of the field-of-view (FOV). Line-of-sight (LOS) velocities for each subregion are inferred from the Doppler shifts, with the rest wavelength derived from the average spectra of the entire FOV. Horizontal wind vectors are derived from the LOS velocities using a monostatic fitting method, which assumes that vertical winds are constant across the FOV and the zonal gradient of meridional winds is negligible. The calculation method is derived thoroughly in Conde and Smith (1998). The resulting horizontal wind vectors have a spatial resolution of 0.5° at the zenith and 1° near the FOV edge. The FOV of the SDIs are around 10° in diameter. The wind vectors have a temporal resolution of 1–5 min. Errors in the monostatically fit wind vectors are estimated to be <15–20 m/s (Anderson et al., 2012a; b; Dhadly et al., 2015). Thermospheric winds have been shown to deviate from quiet time averages by nearly 500 m/s during geomagnetically active periods (Omaya et al., 2023), and therefore our storm and substorm focused events will have wind variations much larger than the wind errors.

2.2 Poker Flat Incoherent Scatter Radar

The Poker Flat Incoherent Scatter Radar (PFISR) (65.1°N, −147.5°E geographic) is an Advanced Modular Incoherent Scatter Radar (AMISR) and is used to measure ionospheric parameters. PFISR is a phased array radar, which allows for multi-directional scanning and faster scanning than dish antenna radars, leading to higher spatial and temporal resolutions. Long pulse mode is employed, which targets the F-region ionosphere. Radio waves are incoherently scattered from the free electrons in the ionosphere, and the return power yields the electron density. The Doppler shift of the return spectra provides the LOS ion drift velocity. Similar to the SDIs, the LOS velocities are inverted into horizontal drift vectors by assuming that the velocity vectors are homogeneous in the east-west direction across the radar FOV. Errors arise from the nonlinear least squares fitting procedure, and are provided along with the horizontal velocity vectors. A more detailed methodology is provided in Heinselman and Nicolls (2008). Spatial and temporal resolution, as well as spatial FOV, varies based on the beam orientations of various experiment modes. The FOV ranges from 2–4° MLAT with a spatial resolution of 0.25° - 0.5°, and temporal resolution of 1–5 min.

This study uses an updated version of the Heinselman and Nicolls (2008) algorithm that makes strict use of Modified Apex coordinates (Richmond, 1995; Laundal and Richmond, 2017) to solve for the covariant components of the velocity more rigorously, then transforms back into standard geodetic vectors. Furthermore it applies filtering based on quality flags in the LoS data and makes use of robust error propagation to nominally improve the estimates of 3D velocity (Lamarche, 2024).

PFISR is also used to obtain electron density profiles for the upper atmosphere. The area of the return spectra provides the electron density for each beam of the radar. This area is corrected for the damping of the spectra due to the ratio of the electron to ion temperature. Each beam configuration has a beam that is parallel to the magnetic field line, at an elevation angle of 77.5°. We use the electron density profile along this beam so that we are observing electron density enhancements due to particle precipitation.

2.3 Time history of events and Macroscale Interactions during substorms ground-based observatories

The Time History of Events and Macroscale Interactions during Substorms all-sky imagers (THEMIS ASIs (Mende et al., 2008)) are white light CCD cameras that are used to capture auroral patterns. Images are recorded at a cadence of 3 s and projected onto an altitude of 110 km. The Fort Yukon (FYKN; geographic 66.6^{o}N, −145.2^{o}N) and Gakona stations (GAKO, 62.4^{o}N, −145.2^{o}E) are mainly used, which have large common FOVs with the SDIs. The ASIs have a circular FOV with around a 9° diameter, and a spatial resolution of around 1 km at the zenith and a temporal resolution of 3 s.

In addition to the ASIs, each THEMIS ground-based observatory (GBO) contains a fluxgate magnetometer (GMAG) (Russell et al., 2009). The magnetometers provide 3-component magnetic field measurements, North-South, East-West, and Vertical, with a 2 Hz cadence. The measurements correspond to a 100 km radius region about 100 km above the GBO.

2.4 OMNI data

High-resolution (1- and 5-min) solar wind magnetic field and plasma data sets are provided by NASA/GSFC's Space Physics Data Facility's OMNIWeb service. The OMNI data set is attained by time shifting magnetic field and plasma data from the Wind, ACE, IMP eight and Geotail satellites from the satellite location to Earth's bow shock, accounting for the propagation time of the solar wind. The data used from the OMNI data set includes the interplanetary magnetic field (IMF) measurements as well as the AE and SYM/H indices, which are computed at the WDC for Geomagnetism at the University of Kyoto. It is important to note that the IMF conditions are the conditions at the bow shock, and the solar wind will take an additional ~7–10 min to reach the magnetopause (Cousins and Shepherd, 2010). However, in this study we are more concerned with the trend of IMF conditions between events, so no additional shift is made for our analysis.

2.5 Event selection criteria and methodology

A search was performed from 2012–2015 for substorm events using both the Newell and Gjerloev (2011) and Forsyth et al. (2015) SuperMAG substorm lists. Both lists utilize the SuperMAG AL (SML) index in order to identify substorms. While there is some variation in methodology between the two lists, both are used in order to increase the possible number of substorm events. Because these lists use the SML index to identify substorms, they may include both magnetospheric and auroral substorms. Magnetospheric substorms are classified by an energy dissipation in the nightside auroral oval and auroral substorms are defined by the

auroral signature, which includes a brightening of the equatorward auroral arc followed by poleward expansion (Rostoker et al., 1980; Akasofu, 1964; Nishimura and Lyons, 2021). Auroral substorms will have signatures of a magnetospheric substorm, but magnetospheric substorms will not always have the associated auroral substorm signatures. Nevertheless, we are looking for events with enhanced geomagnetic activity and sudden plasma enhancements that may be imposed upon the neutral wind, which can occur for both magnetospheric and auroral substorms, making the SuperMAG substorm lists suitable for this study.

One requirement was that the substorm events are not coincident with large geomagnetic storms (SYM/H <−50 nT), since storms are associated with large, global-scale variations of the plasma and neutral populations and in this study, we are more interested in the local effects of substorm forcing. For the substorm events, simultaneous operations of PFISR and SDI were required, and it was preferred to have ASI operations for each event. Additional requirements were clear sky conditions (no cloud coverage) in ASI and SDI data, and relatively low error (<20%) in the derived PFISR velocity vectors provided by AMISR. Because the instruments provide data around 62° - 72° magnetic latitude and the SDIs and ASIs only operate in the nighttime, the substorm onsets are limited to nightside auroral oval, between 07:00 UT and 14:00 UT and 20–03 MLT, where 11:00 UT corresponds to magnetic midnight in the Alaskan region. It was also required that substorm onsets occurred near the observation sites in order to ensure a response can be observed in the ionosphere and thermosphere. This means substorms whose growth phase or poleward expansion phase crosses over the data FOV. It is also preferred to have substorm onset MLT within 2 h of the SDI MLT, however, events that fell out of this location range were still included if a neutral wind response was observed. Events where no response is observed in either the neutral wind vectors or plasma flow vectors were omitted, which can occur if substorm onset is near magnetic midnight, at which the neutral winds can be subject to the strong cross-polar jet (Conde et al., 2001; Smith et al., 1998; Meriwether Jr. et al., 1988). We defined responses of the plasma flow to be a change of around 500 m/s in 20 min and responses of the wind to be around 50 m/s in 30 min. This search resulted in 23 events over the 4 year period. Though there were many more substorms during this period, it is difficult to fulfill all requirements for each substorm event due to frequent cloud coverage in the Alaska region, resulting in a relatively low event number. However, trends in the neutral wind response time were still observed with our event list.

SDI data is obtained in the form of skymap, aligned geomagnetically, with zonal and meridional wind vectors at each viewing location of the SDI from the Monthly Data Archive maintained by UAF. To make keograms, or latitude vs. time plots, of the zonal and meridional winds, data is binned by 1° latitude and a center slice is taken 2.5° east and west of the central magnetic longitude. The data is averaged over each latitude bin for smoothing. PFISR eastward/northward velocity vectors are obtained from MadrigalWeb in the form of keograms, in geomagnetic coordinates. Both the PFISR and SDI data are interpolated to a 5 min interval time-series, which is the average sampling time for both data-sets. This is done because SDI and PFISR have different recorded data times, and need to be interpolated to a common time interval in order to run the analysis. The PFISR data is then smoothed in time by taking a sliding 10 min (two data point) average. This is because the plasma can be highly variable due to the rapidly changing magnetospheric coupling (Murr and Hughes, 2001), and only the meso-to large-scale responses to substorms are relevant for this study. Finally, auroral keograms are obtained from the aurora-asi-lib python package developed by Shumko et al. (2022).

For each event, a time-series of the zonal plasma and neutral wind velocity was selected at a single latitude, within 1° of each other. The main focus of this study is the zonal direction because in the pre-midnight sector, where most our substorm events occur, ion convection is primarily aligned in the east-west direction along the eastward electrojet and therefore do not see much response in the meridional direction compared to the zonal direction (Davidson et al., 2024; Zou et al., 2018). Neutral wind response times were then calculated by performing a weighted windowed time-lagged correlation (WWTLC) analysis, as described by Davidson et al. (2024). This method provides a time-dependent, observation based response time, with a lag time every 15 min. The e-folding time was additionally calculated, which is a theory based calculation of the neutral wind response time which assumes ion-drag is the only driving force. The Equation 1, first derived by Baron and Wand (1983), is given as

$$\tau = \frac{\boldsymbol{V} - \boldsymbol{U}}{\partial \boldsymbol{U}/\partial t} \tag{1}$$

where $\mathbf{V}$ is the horizontal plasma vector and $\mathbf{U}$ is the horizontal wind vector. The time-series data has a 5-min temporal resolution, and therefore the e-folding time calculation gives a neutral wind response time every 5 min.

3 Results and discussion

3.1 Statistical summary

A summary of the 23 events can be found in Table 1. From left to right, this table includes the date, SuperMAG substorm onset time, WWTLC time range, WWTLC time of the substorm window, e-folding time range, and e-folding time median of the substorm window. The substorm window is defined as the 2 h window with the substorm onset at its midpoint. This study focused on this substorm onset window in order to study the neutral wind's immediate response to substorm forcing. Substorm onset WWTLC response times ranged from 0–70 min, with an average response time of ~16 min. This response time is in line with the more recent observed neutral wind response times on the order of tens of minutes (Aruliah and Griffin, 2001; Anderson et al., 2011; Conde et al., 2018; Zou et al., 2018). The substorm window e-folding times ranged from 69–163 min, with an average of 109 min. This is significantly longer than the WWTLC response times. However, as discussed in Davidson et al. (2024), the e-folding time may not be fully representative of the neutral wind response time. Therefore, only the WWTLC response times are used to study the controlling factors of the neutral wind response time. To investigate the controlling factors of the neutral wind response time, short and long response time events are first defined. Based on the average response time of ~16 min, short response time events are classified as those with response times ≤15 min and long response time events

10.3389/fspas.2025.1601296

TABLE 1 Neutral wind response times of substorm events.

Date	Onset time (UT)	Weighted WTLC range (min)	Onset window lag time (min)	E-folding time range (min)	Substorm median E-folding time (min)
2012 January 21	11:29	25–35	25	19–292	89
2012 February 15	7:33	5–25	20	15–351	114
2013 January 10	10:36	10–15	10	9–262	80
2013 January 26	8:34	5–85	15	19–336	92
2013 February 2	9:18	5–155	25	10–275	98
2013 February 7	11:24	30–90	35	27–355	132
2013 February 28	8:02	0–15	15	24–356	125
2013 March 1	8:34	0–105	10	23–321	84
2013 March 13	8:03	0–40	20	2–286	163
2013 March 29	8:05	5–20	15	27–317	100
2014 January 26	9:06	55–100	70	21–353	118
2014 March 18	8:01	10–120	15	23–343	130
2014 March 26	7:08	5–20	5	3–309	112
2014 October 29	7:39	20–50	30	37–310	129
2014 November 3	7:21	0–15	5	20–348	89
2014 November 8	8:19	10–15	15	18–309	80
2014 November 10	7:44	5–15	10	6–284	86
2014 November 14	8:21	0–10	5	4–351	157
2014 November 22	9:44	25–40	30	15–359	162
2015 February 12	12:35	0–10	0	13–350	130
2015 March 3	9:38	0–110	5	1–292	72
2015 March 10	9:32	0–60	0	6–344	69
2015 December 31	8:30	15–25	15	33–315	98

are defined as those with response times ≥20 min. This grouping resulted in 15 short response time events and eight long response time events. Then, the IMF conditions and ionospheric parameters were studied for short and long response events, respectively, to determine any controlling factors of the neutral wind response time.

3.2 2014 March 18

An example of a substorm event with a relatively short neutral wind response time is shown in Figure 1. The left panel shows geomagnetic conditions, including the IMF |B| and Bz component, the SYM/H index, the AE index, intensity keogram from the FYKN ASI, and long-pulse electron density from PFISR. The right panel shows the plasma and wind responses, including the zonal plasma flow keogram, zonal wind keogram, zonal plasma (solid blue curve) and wind (dashed red curve) time-series plot, and the weighted WTLC time. This event occurred on 2014 March 18, with substorm onset at 08:01 UT, 20.88 MLT and 67.65° MLAT from the Newell and Gjerloev (2011) substorm list. The geomagnetic conditions of this event show a southward turning of IMF around 06:45 UT, 1 h and 15 min before substorm onset, with southward IMF maintained for a few hours after onset. IMF By is initially eastward, but begins turning westward around 1 h and 15 min before substorm onset,

and remains westward for the duration of the event. The SYM-H index shows very weak or little enhancement of the ring current during this event (>−15 nT), indicating a quiet time substorm. The AE index was small leading up to substorm onset time (<200 nT) and rapidly increased to around 600 nT immediately following onset time. Auroral intensity data from the FYKN ASI shows a steady growth phase that expanded equatorward from around 71° at 05:30 UT to around 66° just before 08:00 UT. Equatorward brightening of the arc began around 7:15 UT, but poleward expansion did not occur until just before 08:00 UT. The electron density data shows a large electron density enhancement before 07:00 UT. This is most likely associated with daytime solar EUV ionization, which has been shown to enhance electron densities from around 8–20 MLT for the equinox months (Lovati et al., 2023; Kim et al., 2020; Cai et al., 2007). Local electron precipitation due to the substorm began around 7:30 UT above 300 km, extended down to around 150 km at substorm onset time, then receded back to higher altitudes after about 1 h. There was an additional large electron density enhancement extending between 300–500 km starting around 10:30 UT. However, this enhancement is outside the studied period of the substorm window and not applicable to the current study. In order to better quantify the electron densities during these events, we obtain a range of electron density by averaging the minimum five values and maximum five values in the 2 hour substorm window across the entire altitude FOV. This is done because the precipitation altitude range varies between events, and instead of subjectively selecting the precipitation altitude range, we average the bottom five and top five values to eliminate outliers that may be caused by the background electron density. The electron density for this event ranges from 2.60 x 10^8 m^{-3} to 2.71 x 10^{11} m^{-3}.

The plasma and neutral wind response to the substorm can be seen in the right panel of Figure 1. Figure 1F shows a keogram of the eastward component of the plasma's horizontal velocity vector. The plasma flow was initially westward, and accelerated to a stronger westward flow around 7:00 UT. At around 7:30 UT, plasma accelerated eastward and reached a maximum eastward velocity at around 8:15 UT. Plasma turned westward again around 8:45 UT, and weakened to a near stagnant flow in the following 2 h. At substorm onset time, 8:01 UT, Poker Flat is roughly located around 21 MLT, placing our observations just eastward of the substorm onset location of 20.88 MLT. It has been shown that eastward of the substorm expansion phase auroral bulge, ionospheric currents are eastward (Gjerloev and Hoffman, 2001), which corresponds to the eastward plasma flow shown in this event. Figure 1G shows a keogram of the eastward neutral wind, extending from 65° - 72° MLAT. At around 71° MLAT, the neutral wind reached a maximum westward velocity around 7:15 UT. Without larger FOV plasma data, which only covers around 66° - 67° MLAT in this case, it cannot be observed whether or not plasma is driving these westward accelerations. Although, based on the auroral keogram showing precipitation at these latitudes and studies that show ion-drag is a dominant neutral wind driver (Killeen and Roble, 1984), it is likely that this westward wind was associated with westward ionospheric plasma flows. The westward wind extended equatorward in time, with the entire latitude FOV showing westward wind starting around 7:30 UT. At the PFISR latitude range (66° - 67° MLAT), the wind accelerated eastward around substorm onset time, weakening the westward wind until it reached a minimum speed around 8:30 UT. The wind accelerated westward again, reaching a maximum speed around 9:30 UT, before stagnating around 10:30 UT.

The time-series of the zonal plasma and neutral wind velocity is shown in Figure 1H. The plasma flow is shown as a solid blue curve and the wind velocity is shown as a dashed red curve. The time-series data was taken from the keograms at the 66.5° bin and 67° bin, respectively. This data shows four acceleration periods of the plasma flow, similar to the observations in the keograms. There was an initial westward acceleration around 7:00 UT, an eastward acceleration around 7:30 UT, a westward acceleration around 8:15 UT, and a final eastward acceleration around 9:15 UT. The wind time-series data shows a very close following of this pattern, but with some of the accelerations delayed by around 15 min. The wind did not fully turn eastward at 8:30 UT like the plasma flow did, but that is because the plasma accelerated westward again before the wind could catch up to the eastward flow. Such close following of this acceleration pattern indicates a strong coupling between the plasma and the neutrals.

The calculated weighted WTLC neutral wind response times are shown in Figure 1I. The response time ranges from 10–105 min, although the 105 min response time corresponds to the last window of the event, where the plasma flow and wind have stagnated and therefore have less distinct features to match for the correlation calculation. The response time of the substorm window is 15 min, and the response time shortened to 10 min as the substorm progressed. The blue shaded region of Figure 1H shows the substorm window used for analysis. The solid red curve shows the wind shifted by 15 min, corresponding to the weighted WTLC time of the substorm window. This shift aligns the eastward acceleration of the wind to the eastward acceleration of the plasma at 7:30 UT as well as the westward accelerations at 8:15 UT. This analysis confirms the 15 min response time of the substorm window.

3.3 2014 November 22

An example of a substorm event with a relatively long neutral wind response time is shown in Figure 2. This event took place on 2014 November 22, with substorm onset at 09:44 UT, 21.22 MLT and 65.35° MLAT from the Newell and Gjerloev (2011) substorm list. The geomagnetic conditions in the left panel of Figure 2 shows that IMF is mostly southward before the substorm, with some periodic reversals to northward IMF. IMF By experiences periodic reversals from eastward to westward prior to substorm onset, but is mostly weakly-directional from around 1 h before onset time to around 1 h after onset time. Around substorm onset time, IMF switched from southward to northward IMF and remains northward for around 2 h. The SYM/H index was slightly more enhanced for this event before onset time (<−20 nT), indicating more geomagnetic activity prior to the substorm. The SYM/H levels were still below that of a geomagnetic storm, however. The AE index was active before the substorm, fluctuating around 200–300 nT for around 4 h. At substorm onset time, the AE index increased to around 600 nT, but was not as sharp of an increase as the short response time substorm events. Auroral intensity data from the FYKN ASI keogram shows that auroral activity occurred a few hours before substorm onset, around 06:00 UT, but still show some poleward expansion of the auroral arc around 68° MLAT at substorm onset.

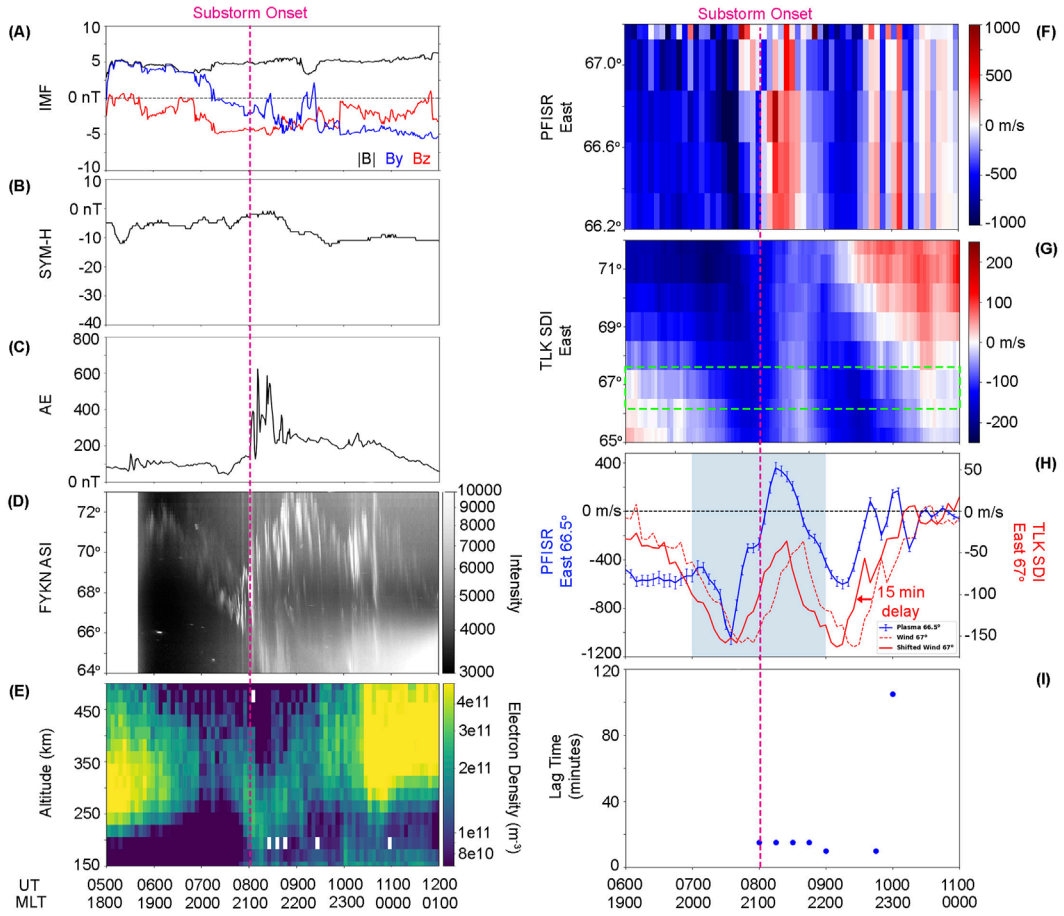

FIGURE 1
Summary of substorm event on 2014 March 18. Left panel **(A–E)** shows the IMF magnitude and southward component, the SYM/H index, the AE index, auroral keogram, and PFISR electron density. Right panel shows the **(F,G)** zonal plasma and wind velocity keograms, **(H)** zonal velocity time-series, with a dashed red line for the zonal wind and solid red line for the zonal wind shifted by the substorm window WWTLC time, and **(I)** the WWTLC response time vs. time. The magenta line in both the left and right panel indicates substorm onset. The green box in panel (G) highlights the PFISR FOV. The blue shading in panel (H) indicates the substorm window.

Electron density was slightly enhanced throughout the night, with larger enhancements starting around 08:30 UT at 250 km, where the plasma and neutral observations are. The electron density ranges from 1.17 x 10^8 m^{-3} to 4.08 x 10^{11} m^{-3}.

The plasma and neutral wind response can be seen in the right panel of Figure 2. Zonal plasma flow was initially strongly westward, then stagnated around 07:45 to 08:45 UT. At around 08:45 UT, the plasma became strongly westward again before quickly accelerating eastward, and became eastward flow by substorm onset time. This behavior was most likely due to multiple reconfigurations of ionospheric convection experienced during geomagnetically active periods, as we see AE activity enhancements before substorm onset. The zonal wind was initially westward above 65° MLAT and eastward below 65°, indicating a strong wind shear at that latitude. The westward wind expanded equatorward, and the zonal wind became westward across all the entire FOV about 1 h before onset time, and shifted eastward around 45 min after substorm onset.

The time-series of the zonal plasma and wind velocity, taken at 67° MLAT for both species (Figure 2H), exhibits the same behavior as described by the keograms. Both the plasma and the wind were initially westward. The plasma accelerated eastward around 07:30 UT into a stagnant flow between around 07:45–8:45 UT. The zonal wind also accelerated eastward at around 08:30 UT, and plateaued into a weaker westward wind between around 09:00 UT and 09:45 UT. This plateau likely occurred due to the lack of ionospheric forcing with a near 0 m/s flow. The plasma then began accelerating eastward around 9:15 UT, 30 min before onset time. The wind accelerated eastward around 09:45 UT, 30 min after the plasma eastward acceleration. This behavior indicates that the wind was following the plasma flow accelerations, but were clearly lagged behind by 30–45 min.

The calculated weighted WTLC response times in Figure 2I confirm the observational lag time estimate of the time-series, with neutral wind response times ranging from 25–40 min. The response time was longer before substorm onset, minimized around onset time, and then increased again. The response time of the substorm window was 30 min, as shown by the red solid curve in Figure 2I. This delay more closely matches the eastward accelerations of the plasma and the wind before substorm onset time. However, the shifted wind places the eastward acceleration just before (5 min)

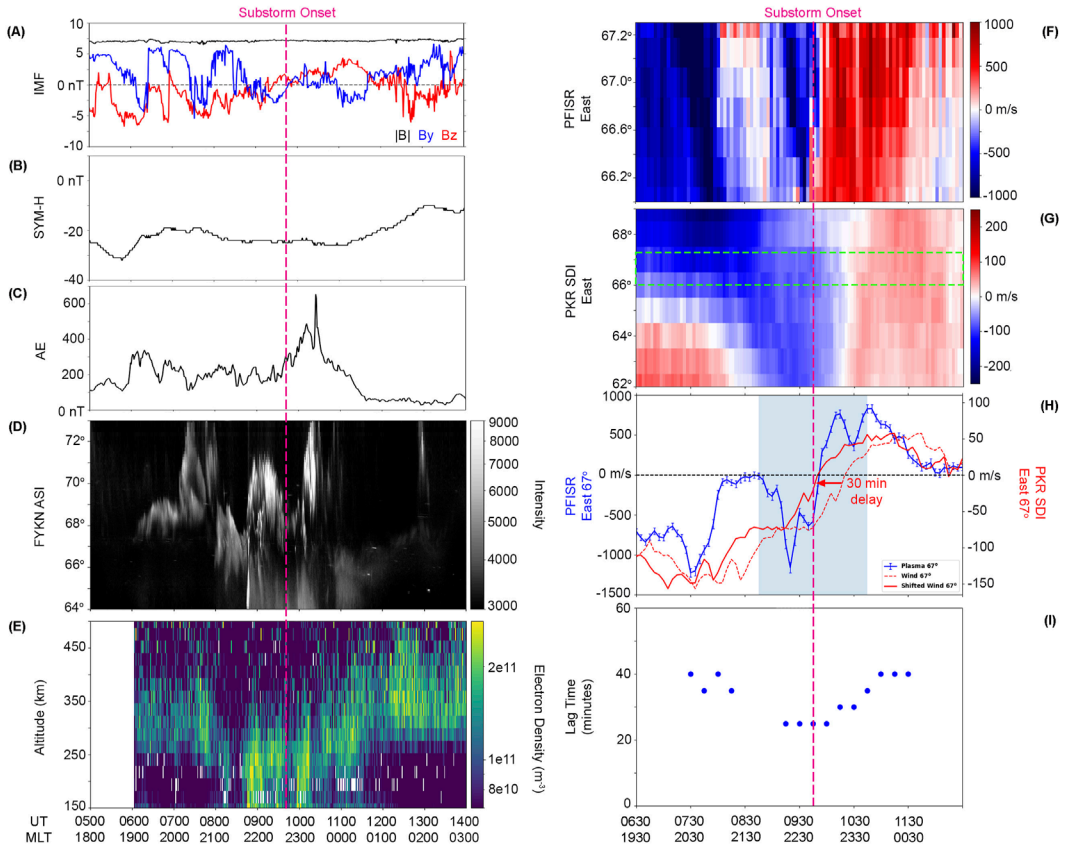

FIGURE 2
Summary of substorm event on 2014 November 22. Left panel **(A–E)** shows the IMF magnitude and southward component, the SYM/H index, the AE index, auroral keogram, and PFISR electron density. Right panel shows the **(F,G)** zonal plasma and wind velocity keograms, **(H)** zonal velocity time-series, with a dashed red line for the zonal wind and solid red line for the zonal wind shifted by the substorm window WWTLC time, and **(I)** the WWTLC response time vs. time. The magenta line in both the left and right panel indicates substorm onset. The green box in panel **(G)** highlights the PFISR FOV. The blue shading in panel **(H)** indicates the substorm window.

the eastward acceleration of the plasma, which is within the error limitations of the method laid out in Davidson et al. (2024). A 5 min error gives a substorm window response time of 25 min, which is still categorized as a long response event.

3.4 Superposed epoch analysis of geomagnetic conditions

The case studies showed clear differences in the geomagnetic conditions between the short and long response events. For the short response event, Bz turned southward around 1.5 h before substorm onset time. Meanwhile, the long response event showed Bz turning northward around 2 h before substorm onset time and was northward at substorm onset time. The short response event had a SYM/H index greater than −15 nT, consistent with a quiet-time substorm based on the storm time threshold of the SYM/H index (SYM/H ≤−80 nT (Hutchinson et al., 2011)). The long response event, however, occurred during a period of enhanced geomagnetic activity (SYM/H around −20 to −30 nT), although it is still beneath the threshold of a geomagnetic storm. This enhancement may exist because the event occurred during the recovery phase of a geomagnetic storm. Alternatively, frequent periods of southward IMF in the days prior to the event could have resulted in increased convection cycles and therefore more ring current injections. This is referred to as a geomagnetically active period for the remaining discussion. Additionally, the short response event exhibited no substorm activity prior to substorm onset, based on both the Newell and Gjerloev (2011) and Forsyth et al. (2015) substorm identification methods which both require a rapid decrease in the SML index for a sustained period of time. The long response event exhibited frequent enhancements, up to 400 nT, of the AE index prior to substorm onset time, indicating previous substorm activity. In order to better quantify these differences, and observe whether or not they are occurring on a statistical scale, a superposed epoch analysis (SEA) was performed of the geomagnetic conditions for the short and long response cases using the groupings discussed in Section 3.1. The SEA analysis ±8 h from the SuperMAG substorm onset time.

The superposed epoch analysis was performed on IMF magnitude, By, Bz, AE index, and SYM/H index and is shown in Figure 3. The red line represents the SEA median, while the blue shaded region is the 25^{th} and 75^{th} percentile range. The short and long response SEA are shown in the left and right panel, respectively. The median IMF magnitude is similar between

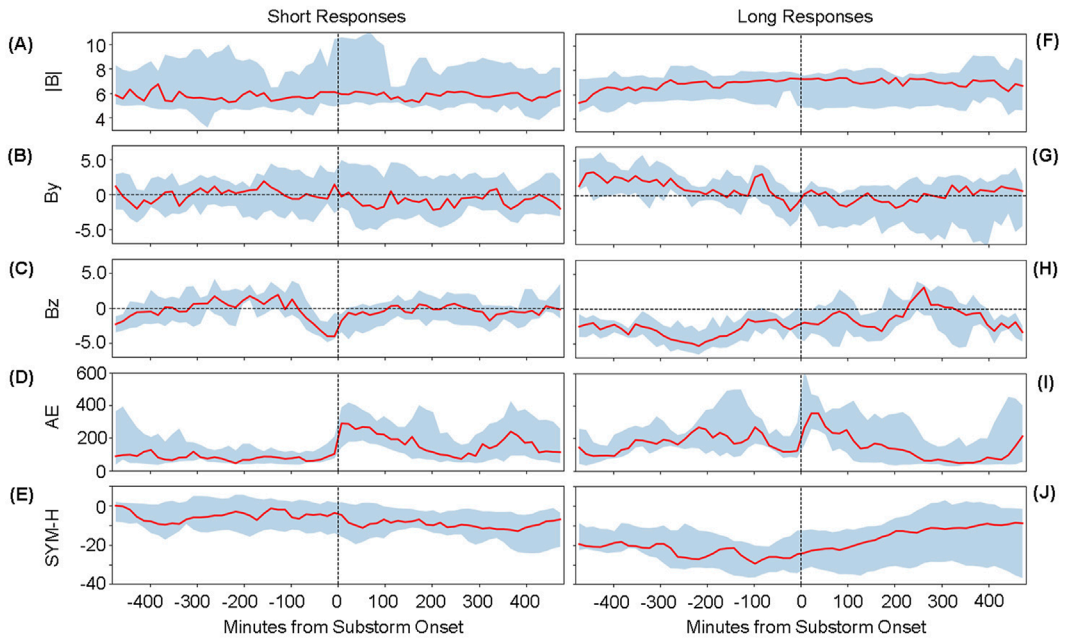

FIGURE 3
Superposed epoch analysis of IMF |B|, By, Bz, AE and SYM/H index for the short **(A–E)** and long **(F–J)** response time events, where the epoch is the SuperMAG substorm onset time.

the short and long response events, with average median values of 5.80 nT and 6.90 nT, respectively. However, the range of the IMF magnitude is larger for the short responses events, with the maximum 75^{th} percentile value at 11.05 nT as compared to 9.22 nT for the long response events. The IMF By component has no strong directional trends for the short response events, with median values ranging from −2.20 nT to 1.91 nT and an average median value of −0.43 nT. The IMF By component for the long response events are mostly positive before substorm onset, with the median values ranging from −2.19 nT and 3.37 nT and an average median value of 1.26 nT. After substorm onset, the IMF By is weakly directional, with the median values ranging from −1.77 nT and 1.50 nT and an average median value of −0.03 nT. The percentile range, however, reaches more duskward values, reaching −7.35 nT after substorm onset as compared to −4.45 nT before substorm onset. However, these trends are weak and are most likely not the dominant component of the neutral wind response time.

The trends in the IMF Bz component, the AE index, and the SYM/H index are more apparent. For the short response events, the median IMF Bz component turns southward 82.5 min before substorm onset, reaches a minimum value of −4.06 nT 7.5 min before onset time, and remains southward until 112.5 min after onset, where it becomes mostly non-directional for the remainder of the SEA time. The percentile range is small, with an average range of 4.44 nT, indicating that this trend is strong among all events. For the long response events, the median IMF Bz component is southward for the 8 h leading up to substorm onset time, with median values ranging from −5.32 nT and −1.50 nT. The median IMF Bz component does not turn northward again until 232.5 min after substorm onset time. Before substorm onset time, the percentile range is small, with an average range of 3.06 nT, indicating that the trend of sustained southward IMF prior to substorm onset for long response events is strong. After substorm onset, the IMF Bz component is more variable, with a larger average percentile range of 4.56 nT.

For the short response events, the median AE index is relatively weak leading up to onset time, ranging from 45.0 to 125.7 nT. The median AE index sharply increases to 288.3 nT 7.5 min after substorm onset time, then steadily decreases to its pre-substorm levels around 3.5–4.0 h after substorm onset. In the hours leading up to substorm onset time, the percentile range is very small, with the average range being 90.6 nT in the 247.5 min leading up to substorm onset. After substorm onset, the percentile range increases to an average range of 218.5 nT. This increase is most likely due to the varying strengths and recovery phases of the individual substorms. However, it is clear that quiet AE index conditions (<100 nT) prior to substorm onset is a strong trend for the short response events. For the long response events, the median AE index is more variable prior to substorm onset, ranging from 91.7 nT to 268.5 nT. At substorm onset time, the median AE index sharply increases, reaching a maximum of 353.7 nT 22.5 min after onset time. The median AE index then returns to quiet time values (<100 nT) around 4 h after onset time. The percentile range varies greatly before substorm onset time, with an average range of 185.2 nT and a maximum range of 415.2 nT. This indicates that while long response events generally have a more active AE index prior to substorm onset, the level of activity can vary between events. The average percentile range after substorm onset is 246.1 nT, more similar to the short response events and again indicating a variation in the individual substorm strengths and recovery.

For the short response events, the median SYM/H is relatively weak throughout the duration of the SEA time, ranging from

−13.0 nT to 0.0 nT, and have no discernible trends around substorm onset time. The percentile range is relatively small, with an average range of 15.6 nT. For the long response events, the median SYM/H index is larger, ranging from −29.5 nT to −8.5 nT. The median SYM/H index is larger before substorm onset as compared to after substorm onset, with an average median of −23.2 nT (−14.9) before (after) onset time. The percentile range is also smaller before onset time, with an average range of 16 nT as compared to 26.8 nT after substorm onset.

The presence of southward IMF prior to substorm onset time allows for magnetic energy to load into the magnetotail, which is then unloaded at onset time. The loading process has been shown to last around 40 min once southward IMF begins (Nagai et al., 2005). Since the IMF for the short response events turn southward around 82.5 min before onset time, this would allow enough time to load the magnetotail for an energetic substorm. The long responses events experience southward IMF for many hours before substorm onset, and several loading and unloading cycles may occur during this time, potentially decreasing the amount of energy being stored and released upon each cycle since the unloading process does not require a minimum lobe flux growth (Nishimura and Lyons, 2021). This lower energy injection could result in slower neutral wind response times from having weaker ion-drag forcing. The trends in both the AE and SYM/H index indicate that neutral winds are more likely to respond quickly during geomagnetically quiet conditions, *e.g.*, little to no variation in the AE index and AE index values of less than 100 nT and SYM/H index values greater than −20 nT. Conversely, the long response events are associated with heightened geomagnetic activity, *e.g.*, variations in the AE index greater than 200 nT and SYM/H index values between −40 nT and −20 nT. These events may be compound substorm events or substorms that occur in the recovery phase of a geomagnetic storm, which would cause pre-substorm variations in the AE index and an enhanced SYM/H index. Studies have shown that compound substorm events increase the number of high-energy electrons in the precipitating particle population (Partamies et al., 2021), which would theoretically decrease the ion-neutral coupling time due to increased collisions. However, this result mainly impacts the lower E− and D-region ionosphere, and there have been few studies regarding the effects of compound substorms on F-region precipitation. Alternatively, studies have shown that wind speeds increase with increasing geomagnetic activity level (Omaya et al., 2023). A more perturbed initial state of the thermosphere could cause longer response times than a quiet initial state of the thermosphere, since the thermosphere is more massive and tends to keep its momentum, it would be more difficult for the ionosphere to change the direction of the thermosphere. Additionally, increased geomagnetic activity could result in thermospheric upwelling from Joule heating. An increase in thermospheric density at the F-region altitude could inhibit the ion-drag force, increasing the response time. Similarly, a study by Billett et al. (2020) has shown that E-region winds respond slower to changes in ionospheric convection during substorms as compared to F-region winds, most likely due to the higher density of the E-region. A more thorough analysis of the large-scale background thermospheric winds and density for these events are needed to determine the thermospheric pre-conditions impact on the neutral wind response time.

3.5 Superposed epoch analysis of electron density

Based on two case studies, differences in the electron density data are less obvious. The short response event had an electron density range from 2.60 x 10^8 - 2.71 x 10^{11} m^{-3}, while the long response event had an electron density range from 1.17 x 10^8 - 4.08 x 10^{11} m−3. While the long response event had a higher maximum electron density, these singular statistical values does not take into the consideration at what altitude or what time the electron density enhancement was in relation to substorm onset. For example, the electron density for the short response event maximizes around substorm onset time, while the long response event has periodic enhancements of the electron density throughout the event, and is not as coherent as the electron density profiles of the short response event. Again, in order to better quantify the trends in electron density between the short and long response events, a superposed epoch analysis was performed on the electron density profiles from PFISR. In order to capture the altitude variations in the electron density, a 2-dimensional epoch analysis was performed where the altitude was sorted into 15 km bins and the SEA was performed on each bin. The SEA is performed for ±80 min from the SuperMAG substorm onset time. Two events were omitted from this analysis: 2014 March 26 and 2014 November 14. The 2014 March 26 event occurs close to the dayside electron density enhancement and biased the substorm electron density enhancements. The 2014 November 14 event did not have long-pulse data available for the F-region electron density.

The results of this SEA are shown in Figure 4, where the top and bottom panels shows the median electron density for the short and long response events, respectively. The electron density is larger for the short response events than for the long response events, ranging from 7.90 x 10^9 - 2.03 x 10^{11} m^{-3} with an average median of 9.14 x 10^{10} m^{-3}, as compared to 1.77 x 10^{10} - 1.90 x 10^{11} m^{-3} with an average median of 8.27 x 10^{10} m^{-3}. Additionally, the electron density is larger in the 30 min leading up to and at substorm onset time for the short response events than for the long response events. From 32.5 min before to 2.5 min after substorm onset, the average median electron density is 9.15 x 10^{10} m^{-3} for the short response events and 7.66 x 10^{10} m^{-3} for the long response events. The pre-onset precipitation for the short response events could be due to precipitation during the growth phase of the substorm, which lasts around 1 h (Huang et al., 2003; Bargatze et al., 1999; McPherron et al., 1986). The long response events have electron density enhancements throughout the SEA time with no significant changes around substorm onset time. There is, however, an electron density enhancement around 15 min after onset time at 150 km. This altitude range is closer to the E-region ionosphere, and is outside the studied region. The electron density enhancements for the short response events are centralized between around 225–400 km before substorm onset, decreases to around 175–325 km at substorm onset time, and then increases its range again to 150–450 km after onset time. This behavior is an indication that the energy of the precipitation electrons increases at substorm onset, allowing the particles to penetrate further into the ionosphere. The 630.0 nm emissions of our observations are around 230 km (Sobral et al., 1993), which lies within the electron density enhancement region at substorm

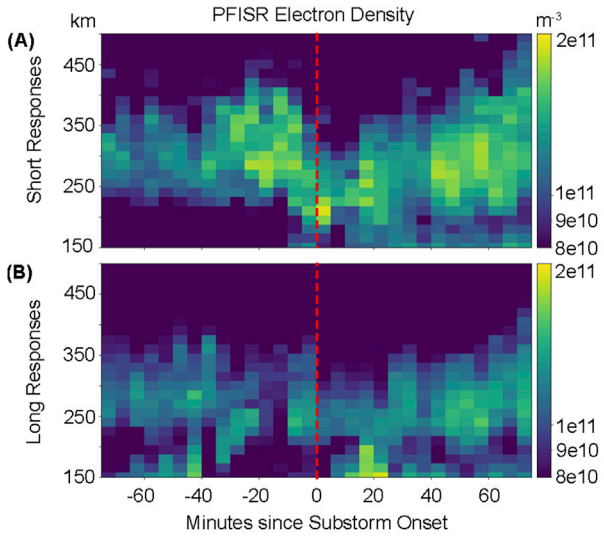

FIGURE 4
Superposed epoch analysis of PFISR's long-pulse electron density data for the **(A)** short response and **(B)** long response events, where the epoch is the SuperMAG substorm onset time.

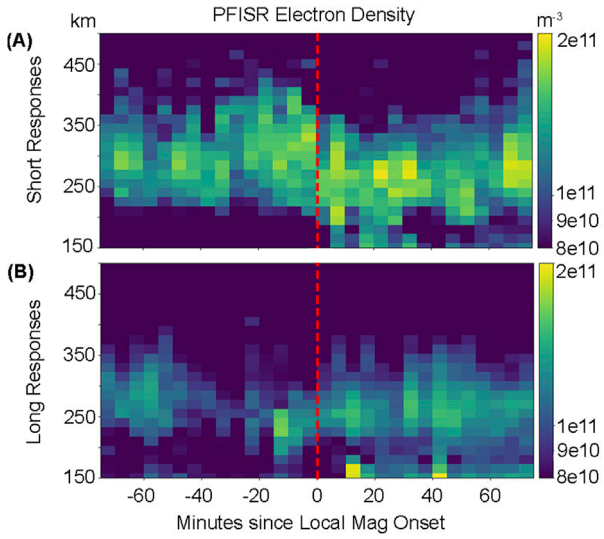

FIGURE 5
Superposed epoch analysis of PFISR's long-pulse electron density data for the **(A)** short response and **(B)** long response events, where the epoch is the local magnetometer perturbation onset time.

onset for the short response events. The long response events have electron density enhancements around 240–375 km for the duration of the SEA, with some enhancements below 175 km around 40–60 min before onset time and 15–80 min after onset time. These enhancements may be higher in altitude than our 630.0 nm emission observations, though the F-region can exist in a broad altitude range (150–400 km) and can vary in altitude during geomagnetically disturbed times (Yin et al., 2006). Therefore, some error can exist in the projected altitude of the F-region (Gillies et al., 2017), and more careful analysis is needed to determine whether or not these electron density enhancements exist within the observed altitude range.

Some events not shown in this publication exhibited a delay in electron density from substorm onset time. One possible explanation is that the SuperMAG substorm lists rely on global indices to identify onset times and location. If PFISR is not located near the global onset location, this could result in delays in the local electron density enhancements while our observations move into the substorm electrojet region. To investigate this possibility, the THEMIS ground magnetometer station located at Poker Flat was utilized to identify the local perturbation onset time. For each event, the onset of perturbations in the northward component of the magnetic field was visually identified and then used as the epoch time in the electron density superposed epoch analysis. The perturbations of the northward component of the magnetic field represent the strength of the substorm electrojet, which is aligned east-west.

The results of this SEA are shown in Figure 5. The new local epoch times altered the spread of electron density enhancements in both the short and long response events. The short response events now show more consistent electron density enhancements throughout the SEA time, instead of being centralized around substorm onset time. The electron density is more enhanced in the 30 min after onset time than for the SuperMAG epoch time, with an average median of 9.16 x 10^{10} m^{-3} for the local onset time as compared to 9.05 x 10^{10} m^{-3} for the SuperMAG onset time from 2.5–37.5 min after epoch time. The long response events still do not show much variation of electron precipitation around onset time, though the electron density around 15 min before onset time is slightly larger, with the maximum median at 1.65 x 10^{11} m^{-3} as compared to 1.46 x 10^{11} m^{-3}. The electron precipitation altitude range is similar for both epoch times for both the short and long response events. The electron density is still larger for the short response events than for the long response events, with an average median of nine. x25 x 10^{10} m^{-3} as compared to 7.75 x 10^{10} m^{-3} 22.5 min before and after local onset. The SEA using local magnetometer onset epoch times are subject to human error, since the perturbations were visually identified from the magnetometer data and could have an error of around 15 min. Future studies could apply the same methodologies as Newell and Gjerloev (2011) or Forsyth et al. (2015) to the local magnetometer data in order to better identify onset times. Considering this error, the results from the local onset epoch time and SuperMAG onset epoch time are similar, and that is that the electron density is higher for the short response events than for the long response events.

The electron density profiles in the SEA show strong F-region enhancements of electron density for the short response events. While substorm precipitation typically occurs in the 557.0 nm green-line emission region (E-region), several studies show precipitation in the 630.0 nm red-line emission region (F-region) as well. A case study done by Liu et al. (2008) used the NORSTAR multispectral imager (MSI) and found equatorward moving streamers in the 630.0 nm emission line prior to substorm onset. Kepko et al. (2009) observed an equatorward moving diffuse auroral patch in the 630.0 nm emission line just before

substorm onset. Gillies et al. (2017) used a REGO ASI and the Resolute Bay Incoherent Scatter Radar-Canadian (RISR-C) to study 630.0 nm auroral emissions and found that at the 220–240 km altitude range, electron density increased within red discrete arcs and in the region of diffuse aurora. This study also showed electron density enhancement in this altitude range, which produces more ion-neutral collisions and therefore a faster response time. Future work could include comparing the F-region density enhancements of our events to an ASI capable of observing the 630.0 nm emissions to see if the enhancements coincide with F-region auroral features.

It is important to note that the superposed epoch analyses are not a perfect representation of each short or long response event, but rather an average of the conditions of each group. Even though one event may share IMF characteristics with the short response group, it may share electron densities characteristics with the long response group, and *vice versa*. This result indicates that there is not one distinct controlling factor of the neutral wind response time. Neutral wind behavior is incredibly complex and, like the momentum equation shows, have many controlling factors. Even if neutral wind behavior were dependent on a single force, such as ion-drag, this force alone is dependent on plasma velocity, wind velocity, electron density, neutral density, and, to a lesser degree, ion and neutral temperatures. Because of this, a general characterization of the controlling factors of the neutral wind response time is difficult, and on a case by case basis more careful consideration should be used in order to pinpoint the controlling factors. However, this superposed epoch analysis is beneficial in a 'more often than not' approach. Because the SEA provides the average conditions of the short and long response events, we are able to say that more often than not, short and long neutral wind responses occur under those conditions.

3.6 Discussion of other controlling factors

Other controlling factors of the neutral wind response time have also been considered, such as the substorm onset time. Some events occur near magnetic midnight (0 MLT), which is around 11:00 UT for central Alaska. While this onset time falls within the typical MLT range of substorm onsets (Frey et al., 2004; Liou, 2010), winds in this region could also be subjected to strong anti-sunward forcing over the polar cap (Conde et al., 2001; Smith et al., 1998; Meriwether Jr. et al., 1988), potentially limiting it is response time to zonal forcing. Additionally, for earlier UT onset times, the central Alaska region could be spatially located further away from the typical near midnight substorm onset. For example, at 8:00 UT, central Alaska is around 20 MLT. This spatial separation could additionally hinder the neutral wind response time. However, Figure 6A shows the response time compared to UT onset time, and no clear dependence of UT is present. We also consider any seasonal dependence of the neutral wind response time. Dhadly et al. (2017) used 34 years of observational data to perform a climatological study of the large-scale neutral winds and found that mean neutral wind circulation increases from winter (Nov - Feb) to equinox (Mar, Apr, Sep, Oct) to summer (May - Aug) months. While this study has significantly less events than use in their study, we observe no seasonal dependence of the neutral wind response time, but no definitive conclusion can be made without a more robust data set. Consideration was also made for the SDI station used for each event. Since the study used both the Toolik Lake (68.6°N, −149.6°E) and Poker Flat (65.1°N, −147.5°E) SDIs, it is a possibility that the SDI location can influence the calculated neutral wind response times. Toolik Lake is about 2° in longitude away from Poker Flat, where our plasma measurements are, meaning there could exist a spatial delay in the neutral wind response time, instead of a temporal delay. However, the SDI station used has little impact on the neutral wind response time, with 60% of short response events using TLK and 50% of long response events using TLK.

Additional controlling factors include the presence of other thermospheric forces, such as pressure-gradient and advection forces. For example, the neutral winds may respond more slowly to ion-drag forcing if there exists a counteracting pressure-gradient force. Without more robust measurements of the high-latitude F-region thermosphere, it is difficult to estimate the influence of these forces. However, Davidson et al. (2025) showed that during active geomagnetic periods, ion-drag is a dominant zonal wind driver. Therefore, the addition of other forces may not have as strong of an influence on the neutral wind response time as the results of our SEA showed.

4 Summary

This study presented for the first time a statistical analysis of the neutral wind response time. The neutral wind response time is not well understood, and previous response time estimations range on the order of tens of minutes to hours, and are typically presented on a case by case basis. Using 23 substorm events, it was shown that statistically, F-region neutral wind response times are on the order of tens of minutes, with an average response time of ~16 min. This result is similar to recent studies that have shown response times on the order of tens of minutes (Aruliah and Griffin, 2001; Anderson et al., 2011; Conde et al., 2018; Zou et al., 2018). A response time of this scale can quickly alter the mass distribution of the upper atmosphere, which is crucial for estimating the damaging effects of space weather such as satellite drag. Based on the average response time, events were split into short (≤15 min) and long (≥20 min) and a case study was shown for each category, including the geomagnetic and ionospheric conditions for each event. The short response case showed a southward turning of the IMF 1 h and 15 min before onset time, quiet SYM-H index conditions (>−15 nT) throughout the duration of the event, quiet AE index conditions (<200 nT) until substorm onset time, and electron density enhancement at substorm onset time. The long response event occurred during a period of heightened geomagnetic activity, with a slightly enhanced SYM-H index (between −20 and −40 nT) and AE index fluctuating around 200–300 nT for around 4 h before substorm onset time. The long response event also showed sustained southward IMF for around 5 h before substorm onset, but turned northward by onset time. Additionally, electron density enhancements were more sporadic for the long response event as compared to the short response event.

The case study analysis shows clear differences between short and long neutral wind response times, and a superposed epoch

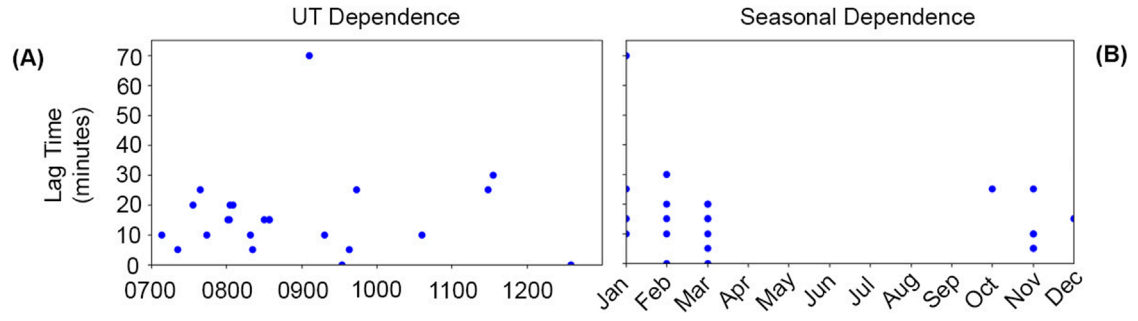

FIGURE 6
Neutral wind response time vs. **(A)** UT and **(B)** month.

analysis was performed to observe whether or not these trends continued on a statistical scale. This analysis showed that more often than not, quiet-time conditions (the SYM/H index greater than −15 nT and the AE index of less than 200 nT with little variations) and a southward turning of IMF 82.5 min before substorm onset result in fast neutral wind response times. Alternatively, substorms that occur during more active periods (the SYM/H index between −20 and −40 nT and variations in the AE index up to 400 nT prior to substorm onset) are more likely to result in longer response times. These results suggest that geomagnetic pre-conditioning can affect the neutral atmosphere's response to geomagnetic disturbances. For example, the southward turning of IMF around 1.5 h before substorm onset time for the short response cases would allow enough time for energy to be loaded into the magnetotail and released at onset time, whereas the sustained southward IMF of the long response events suggests multiple loading and unloading cycles, releasing less energy during the studied onset time. The effects of this pre-conditioning can be seen in the SEA of the electron density, which had higher amounts of precipitation for the short response events than for the long response events. The results of the electron density SEA indicate that larger ionospheric densities lead to a shorter neutral wind response time, due to the increased number of collisions and therefore stronger ion-drag forcing. These results also raise the question of the role of thermospheric pre-conditioning. The active geomagnetic conditions of the long response events could result in faster initial wind speeds and higher thermospheric densities, leading to longer response times. Further analysis is needed to investigate the role of thermospheric pre-conditioning, and this work is left for future studies.

In addition to the geomagnetic and ionospheric conditions, the neutral wind response time's dependence on other controlling factors was investigated. The response time showed no dependence on UT, season, or SDI station being used for analysis. This study has shown that the controlling factors of the neutral wind response time are dynamic and dependent on the geomagnetic, ionospheric, and potentially thermospheric, pre-conditioning of disturbed times. While these factors may vary on a case to case basis, this study provides an average of the geomagnetic and ionospheric conditions of neutral wind responses.

Data availability statement

The datasets presented in this study can be found in online repositories. The names of the repository/repositories and accession number(s) can be found below: Data was made using a new package, which is now uploaded on https://zenodo.org/records/10892410. SDI data are available at http://sdi_server.gi.alaska.edu/sdiweb/index.asp. The THEMIS mission data are available from http://themis.ssl.berkeley.edu/index.shtml. PFISR operations data are available from http://amisr.com/database.

Author contributions

KD: Methodology, Conceptualization, Investigation, Writing – review and editing, Validation, Formal Analysis, Writing – original draft, Visualization, Funding acquisition. YZ: Supervision, Conceptualization, Writing – review and editing. LL: Writing – review and editing, Data curation, Writing – original draft. AB: Writing – review and editing, Data curation. MC: Data curation, Writing – review and editing.

Funding

The author(s) declare that financial support was received for the research and/or publication of this article. This work was supported by NASA grant 80NSSC21K1859. Publication fees were supported by the Department of Space Science, University of Alabama in Huntsville.

Acknowledgments

We acknowledge the SuperMAG collaborators (https://supermag.jhuapl.edu/info/?page%3Dacknowledgement). We acknowledge NASA contract NAS5-02099 and V. Angelopoulos for use of data from the THEMIS Mission. Specifically: S. Mende and E. Donovan for use of the ASI data, the CSA for logistical support in fielding and data retrieval from the GBO stations, and NSF for support of GIMNAST through grant AGS-1004736 and

data provided by the Geophysical Institute Magnetometer Array operated by the Geophysical Institute, University of Alaska. More information about this dataset is available at http://magnet.asf.alaska.edu/. We acknowledge Poker Flat Incoherent Scatter Radar which is a major facility funded by the National Science Foundation through cooperative agreement AGS 1840962 to SRI International.

Conflict of interest

The authors declare that the research was conducted in the absence of any commercial or financial relationships that could be construed as a potential conflict of interest.

Generative AI statement

The author(s) declare that no Generative AI was used in the creation of this manuscript.

Publisher's note

All claims expressed in this article are solely those of the authors and do not necessarily represent those of their affiliated organizations, or those of the publisher, the editors and the reviewers. Any product that may be evaluated in this article, or claim that may be made by its manufacturer, is not guaranteed or endorsed by the publisher.

References

Akasofu, S.-I. (1964). The development of the auroral substorm. *Planet. Space Sci.* 12, 273–282. doi:10.1016/0032-0633(64)90151-5

Akasofu, S.-I. (2013). Where is the magnetic energy for the expansion phase of auroral substorms accumulated? *J. Geophys. Res. Space Phys.* 118, 7219–7225. doi:10.1002/2013JA019042

Anderson, C., Conde, M., and McHarg, M. G. (2012a). Neutral thermospheric dynamics observed with two scanning Doppler imagers: 1. monostatic and bistatic winds. *J. Geophys. Res. Space Phys.* 117. doi:10.1029/2011JA017041

Anderson, C., Conde, M., and McHarg, M. G. (2012b). Neutral thermospheric dynamics observed with two scanning Doppler imagers: 3. horizontal wind gradients. *J. Geophys. Res. Space Phys.* 117. doi:10.1029/2011JA017471

Anderson, C., Davies, T., Conde, M., Dyson, P., and Kosch, M. J. (2011). Spatial sampling of the thermospheric vertical wind field at auroral latitudes. *J. Geophys. Res. Space Phys.* 116. doi:10.1029/.2011JA016485

Aruliah, A. L., and Griffin, E. (2001). Evidence of meso-scale structure in the high-latitude thermosphere. *Ann. Geophys.* 19, 37–46. doi:10.5194/angeo-19-37-2001

Bargatze, L. F., Ogino, T., McPherron, R. L., and Walker, R. J. (1999). Solar wind magnetic field control of magnetospheric response delay and expansion phase onset timing. *J. Geophys. Res. Space Phys.* 104, 14583–14599. doi:10.1029/1999JA900013

Baron, M. J., and Wand, R. H. (1983). F region ion temperature enhancements resulting from joule heating. *J. Geophys. Res. Space Phys.* 88, 4114–4118. doi:10.1029/JA088iA05p04114

Billett, D. D., McWilliams, K. A., and Conde, M. G. (2020). Colocated observations of the e and f region thermosphere during a substorm. *J. Geophys. Res. Space Phys.* 125, e2020JA028165. doi:10.1029/2020JA028165

Cai, H. T., Ma, S. Y., Fan, Y., Liu, Y. C., and Schlegel, K. (2007). Climatological features of electron density in the polar ionosphere from long-term observations of eiscat/esr radar. *Ann. Geophys.* 25, 2561–2569. doi:10.5194/.angeo-25-2561-2007

Cai, L., Oyama, S., Aikio, A., Vanhamäki, H., and Virtanen, I. (2019). Fabry-perot interferometer observations of thermospheric horizontal winds during magnetospheric substorms. *J. Geophys. Res. Space Phys.* 124, 3709–3728. doi:10.1029/2018JA026241

Conde, M., Craven, J. D., Immel, T., Hoch, E., Stenbaek-Nielsen, H., Hallinan, T., et al. (2001). Assimilated observations of thermospheric winds, the aurora, and ionospheric currents over Alaska. *J. Geophys. Res. Space Phys.* 106, 10493–10508. doi:10.1029/2000JA000135

Conde, M., and Smith, R. W. (1995). Mapping thermospheric winds in the auroral zone. *Geophys. Res. Lett.* 22, 3019–3022. doi:10.1029/95GL02437

Conde, M., and Smith, R. W. (1997). Phase compensation of a separation scanned, all-sky imaging fabry–perot spectrometer for auroral studies. *Appl. Opt.* 36, 5441–5450. doi:10.1364/AO.36.005441

Conde, M., and Smith, R. W. (1998). Spatial structure in the thermospheric horizontal wind above poker flat, Alaska, during solar minimum. *J. Geophys. Res. Space Phys.* 103, 9449–9471. doi:10.1029/.97JA03331

Conde, M. G., Bristow, W. A., Hampton, D. L., and Elliott, J. (2018). Multiinstrument studies of thermospheric weather above Alaska. *J. Geophys. Res. Space Phys.* 123, 9836–9861. doi:10.1029/2018JA025806

Conde, M. G., and Nicolls, M. J. (2010). Thermospheric temperatures above poker flat, Alaska, during the stratospheric warming event of january and february 2009. *J. Geophys. Res. Atmos.* 115. doi:10.1029/2010JD014280

Cousins, E. D. P., and Shepherd, S. G. (2010). A dynamical model of high-latitude convection derived from superdarn plasma drift measurements. *J. Geophys. Res. Space Phys.* 115. doi:10.1029/2010JA016017

Davidson, K., Lu, G., and Conde, M. (2025). Effects of high-latitude input on neutral wind structure and forcing during the 17 march 2013 storm. *J. Geophys. Res. Space Phys.* 130, e2024JA033366. doi:10.1029/2024JA033366

Davidson, K., Zou, Y., Conde, M., and Bhatt, A. (2024). A new method for analyzing f-region neutral wind response to ion convection in the nightside auroral oval. *J. Geophys. Res. Space Phys.* 129, e2024JA032415. doi:10.1029/2024JA032415

Dhadly, M., Emmert, J., Drob, D., Conde, M., Doornbos, E., Shepherd, G., et al. (2017). Seasonal dependence of northern high-latitude upper thermospheric winds: a quiet time climatological study based on ground-based and space-based measurements. *J. Geophys. Res. Space Phys.* 122, 2619–2644. doi:10.1002/.2016JA023688

Dhadly, M. S., Meriwether, J., Conde, M., and Hampton, D. (2015). First ever cross comparison of thermospheric wind measured by narrow- and wide-field optical Doppler spectroscopy. *J. Geophys. Res. Space Phys.* 120, 9683–9705. doi:10.1002/2015JA021316

Forsyth, C., Rae, I. J., Coxon, J. C., Freeman, M. P., Jackman, C. M., Gjerloev, J., et al. (2015). A new technique for determining substorm onsets and phases from indices of the electrojet (sophie). *J. Geophys. Res. Space Phys.* 120 (10), 10592–10606. doi:10.1002/2015JA021343

Frey, H. U., Mende, S. B., Angelopoulos, V., and Donovan, E. F. (2004). Substorm onset observations by image-fuv. *J. Geophys. Res. Space Phys.* 109. doi:10.1029/2004JA010607

Fukizawa, M., Sakanoi, T., Ogawa, Y., Tsuda, T. T., and Hosokawa, K. (2021). Statistical study of electron density enhancements in the ionospheric f region associated with pulsating auroras. *J. Geophys. Res. Space Phys.* 126, e2021JA029601. doi:10.1029/.2021JA029601

Gillies, M., Knudsen, D., Donovan, E., Jackel, B., Gillies, R., and Spanswick, E. (2017). Identifying the 630 nm auroral arc emission height: a comparison of the triangulation, fac profile, and electron density methods. *J. Geophys. Res. Space Phys.* 122, 8181–8197. doi:10.1002/2016JA023758

Gjerloev, J. W., and Hoffman, R. A. (2001). The convection electric field in auroral substorms. *J. Geophys. Res. Space Phys.* 106, 12919–12931. doi:10.1029/1999JA000240

Grandin, M., Partamies, N., and Virtanen, I. I. (2024). Statistical comparison of electron precipitation during auroral breakups occurring either near the open–closed field line boundary or in the central part of the auroral oval. *Ann. Geophys.* 42, 355–369. doi:10.5194/angeo-42-355-2024

Heinselman, C. J., and Nicolls, M. J. (2008). A bayesian approach to electric field and e-region neutral wind estimation with the poker flat advanced modular incoherent scatter radar. *Radio Sci.* 43. doi:10.1029/.2007RS003805

Huang, C.-S., Reeves, G. D., Borovsky, J. E., Skoug, R. M., Pu, Z. Y., and Le, G. (2003). Periodic magnetospheric substorms and their relationship with solar wind variations. *J. Geophys. Res. Space Phys.* 108. doi:10.1029/2002JA009704

Hutchinson, J. A., Wright, D. M., and Milan, S. E. (2011). Geomagnetic storms over the last solar cycle: a superposed epoch analysis. *J. Geophys. Res. Space Phys.* 116. doi:10.1029/2011JA016463

Jones, S. L., Lessard, M. R., Rychert, K., Spanswick, E., and Donovan, E. (2011). Large-scale aspects and temporal evolution of pulsating aurora. *J. Geophys. Res. Space Phys.* 116. doi:10.1029/.2010JA015840

Kaeppler, S. R., Sanchez, E., Varney, R. H., Irvin, R. J., Marshall, R. A., Bortnik, J., et al. (2020). "Chapter 6 - incoherent scatter radar observations of 10–100kev precipitation: review and outlook," in *The dynamic loss of Earth's radiation belts*. Editors A. N. Jaynes, and M. E. Usanova (Elsevier), 145–197. doi:10.1016/.B978-0-12-813371-2.00006-8

Kepko, L., Spanswick, E., Angelopoulos, V., Donovan, E., McFadden, J., Glassmeier, K.-H., et al. (2009). Equatorward moving auroral signatures of a flow burst observed prior to auroral onset. *Geophys. Res. Lett.* 36. doi:10.1029/2009GL041476

Killeen, T. L., and Roble, R. G. (1984). An analysis of the high-latitude thermospheric wind pattern calculated by a thermospheric general circulation model: 1. momentum forcing. *J. Geophys. Res. Space Phys.* 89, 7509–7522. doi:10.1029/JA089iA09p07509

Killeen, T. L., Won, Y.-I., Niciejewski, R. J., and Burns, A. G. (1995). Upper thermosphere winds and temperatures in the geomagnetic polar cap: solar cycle, geomagnetic activity, and interplanetary magnetic field dependencies. *J. Geophys. Res. Space Phys.* 100, 21327–21342. doi:10.1029/95JA01208

Kim, E., Jee, G., Ji, E.-Y., Kim, Y., Lee, C., Kwak, Y.-S., et al. (2020). Climatology of polar ionospheric density profile in comparison with mid-latitude ionosphere from long-term observations of incoherent scatter radars: a review. *J. Atmos. Solar-Terrestrial Phys.* 211, 105449. doi:10.1016/j.jastp.2020.105449

Kosch, M. J., Cierpka, K., Rietveld, M. T., Hagfors, T., and Schlegel, K. (2001). High-latitude ground-based observations of the thermospheric ion-drag time constant. *Geophys. Res. Lett.* 28, 1395–1398. doi:10.1029/.2000GL012380

Lamarche, L. (2024). amisr/resolvedvelocities: v1.0.0-beta (v1.0.0-beta). doi:10.5281/zenodo.10892410

Laundal, K. M., and Richmond, A. D. (2017). Magnetic coordinate systems. *Space Sci. Rev.* 206, 27–59. doi:10.1007/s11214-016-0275-y

Liou, K. (2010). Polar ultraviolet imager observation of auroral breakup. *J. Geophys. Res. Space Phys.* 115. doi:10.1029/2010JA015578

Liu, W. W., Liang, J., Donovan, E. F., Trondsen, T., Baker, G., Sofko, G., et al. (2008). Observation of isolated high-speed auroral streamers and their interpretation as optical signatures of Alfvén waves generated by bursty bulk flows. *Geophys. Res. Lett.* 35. doi:10.1029/2007GL032722

Lovati, G., De Michelis, P., Alberti, T., and Consolini, G. (2023). Unveiling the core patterns of high-latitude electron density distribution at swarm altitude. *Remote Sens.* 15, 4550. doi:10.3390/rs15184550

McPherron, R. L., Terasawa, T., and Nishida, A. (1986). Solar wind triggering of substorm expansion onset. *J. geomagnetism Geoelectr.* 38, 1089–1108. doi:10.5636/jgg.38.1089

Mende, S. B., Harris, S. E., Frey, H. U., Angelopoulos, V., Russell, C. T., Donovan, E., et al. (2008). The themis array of ground-based observatories for the study of auroral substorms. *Space Sci. Rev.* 141, 357–387. doi:10.1007/s11214-008-9380-x

Meriwether, Jr. J. W., Killeen, T. L., McCormac, F. G., Burns, A. G., and Roble, R. G. (1988). Thermospheric winds in the geomagnetic polar cap for solar minimum conditions. *J. Geophys. Res. Space Phys.* 93, 7478–7492. doi:10.1029/JA093iA07p07478

Murr, D. L., and Hughes, W. J. (2001). Reconfiguration timescales of ionospheric convection. *Geophys. Res. Lett.* 28, 2145–2148. doi:10.1029/2000GL012765

Nagai, T., Nakamura, R., Hori, T., and Kokubun, S. (2005). "The loading-unloading process in the magnetotail during a prolonged steady southward imf bz period,". *Frontiers in magnetospheric plasma Physics*. Editors M. Hoshohino, Y. Omura, and L. Lanzerotti (Pergamon), 16, 190–193. doi:10.1016/S0964-2749(05)80029-0

Newell, P. T., and Gjerloev, J. W. (2011). Evaluation of supermag auroral electrojet indices as indicators of substorms and auroral power. *J. Geophys. Res. Space Phys.* 116. doi:10.1029/2011JA016779

Nishimura, Y., and Lyons, L. R. (2021). "*The active magnetosphere*,". American Geophysical Union AGU, 277–291. chap. 18. doi:10.1002/9781119815624.ch18

Omaya, S., Aikio, A., Sakanoi, T., Hosokawa, K., Vanhamaki, H., Cai, L., et al. (2023). Geomagnetic activity dependence and dawn-dusk asymmetry of thermospheric winds from 9-year measurements with a Fabry–Perot interferometer in Tromsø, Norway. *Earth, Planets Space* 75, 70. doi:10.1186/s40623-023-01829-0

Oyama, S., Miyoshi, Y., Shiokawa, K., Kurihara, J., Tsuda, T. T., and Watkins, B. J. (2014). Height-dependent ionospheric variations in the vicinity of nightside poleward expanding aurora after substorm onset. *J. Geophys. Res. Space Phys.* 119, 4146–4156. doi:10.1002/2013JA019704

Partamies, N., Tesema, F., Bland, E., Heino, E., Nesse Tyssøy, H., and Kallelid, E. (2021). Electron precipitation characteristics during isolated, compound, and multi-night substorm events. *Ann. Geophys.* 39, 69–83. doi:10.5194/angeo-39-69-2021

Ponthieu, J.-J., Killeen, T. L., Lee, K. M., Carignan, G. R., Hoegy, W. R., and Brace, L. H. (1988). Ionosphere-thermosphere momentum coupling at solar maximum and solar minimum from de-2 and ae-c data. *Phys. Scr.* 37, 447–453. doi:10.1088/0031-8949/37/3/028

Richmond, A. D. (1995). Ionospheric electrodynamics using magnetic apex coordinates. *J. geomagnetism Geoelectr.* 47, 191–212. doi:10.5636/jgg.47.191

Richmond, A. D., Lathuillère, C., and Vennerstroem, S. (2003). Winds in the high-latitude lower thermosphere: dependence on the interplanetary magnetic field. *J. Geophys. Res. Space Phys.* 108. doi:10.1029/2002JA009493

Rostoker, G., Akasofu, S.-I., Foster, J., Greenwald, R., Kamide, Y., Kawasaki, K., et al. (1980). Magnetospheric substorms—definition and signatures. *J. Geophys. Res. Space Phys.* 85, 1663–1668. doi:10.1029/JA085iA04p01663

Russell, C. T., Chi, P. J., Dearborn, D. J., Ge, Y. S., Kuo-Tiong, B., Means, J. D., et al. (2009). *THEMIS ground-based magnetometers*. New York: Springer, 389–412. doi:10.1007/.978-0-387-89820-9_17

Sánchez, E. R., Ruohoniemi, J. M., Meng, C.-I., and Friis-Christensen, E. (1996). Toward an observational synthesis of substorm models: precipitation regions and high-latitude convection reversals observed in the nightside auroral oval by dmsp satellites and hf radars. *J. Geophys. Res. Space Phys.* 101, 19801–19837. doi:10.1029/96JA00363

Sangalli, L., Knudsen, D. J., Larsen, M. F., Zhan, T., Pfaff, R. F., and Rowland, D. (2009). Rocket-based measurements of ion velocity, neutral wind, and electric field in the collisional transition region of the auroral ionosphere. *J. Geophys. Res. Space Phys.* 114. doi:10.1029/2008JA013757

Shumko, M., Chaddock, D., Gallardo-Lacourt, B., Donovan, E., Spanswick, E. L., Halford, A. J., et al. (2022). Aurorax, pyaurorax, and aurora-asi-lib: a user-friendly auroral all-sky imager analysis framework. *Front. Astronomy Space Sci.* 9. doi:10.3389/fspas.2022.1009450

Smith, R. W., Hernandez, G., Roble, R. G., Dyson, P. L., Conde, M., Crickmore, R., et al. (1998). Observation and simulations of winds and temperatures in the antarctic thermosphere for august 2–10, 1992. *J. Geophys. Res. Space Phys.* 103, 9473–9480. doi:10.1029/97JA03336

Sobral, J. H. A., Takahashi, H., Abdu, M. A., Muralikrishna, P., Sahai, Y., Zamlutti, C. J., et al. (1993). Determination of the quenching rate of the $o(^1d)$ by $o(^3p)$ from rocket-borne optical (630 nm) and electron density data. *J. Geophys. Res. Space Phys.* 98, 7791–7798. doi:10.1029/92JA01839

Spencer, E., Srinivas, P., and Vadepu, S. K. (2019). Global energy dynamics during substorms on 9 march 2008 and 26 february 2008 using satellite observations and the windmi model. *J. Geophys. Res. Space Phys.* 124, 1698–1710. doi:10.1029/2018JA025582

Tanskanen, E., Pulkkinen, T. I., Koskinen, H. E. J., and Slavin, J. A. (2002). Substorm energy budget during low and high solar activity: 1997 and 1999 compared. *J. Geophys. Res. Space Phys.* 107, 15–11. doi:10.1029/2001JA900153

Tanskanen, E. I. (2009). A comprehensive high-throughput analysis of substorms observed by image magnetometer network: years 1993–2003 examined. *J. Geophys. Res. Space Phys.* 114. doi:10.1029/.2008JA013682

Wing, S., Gkioulidou, M., Johnson, J. R., Newell, P. T., and Wang, C.-P. (2013). Auroral particle precipitation characterized by the substorm cycle. *J. Geophys. Res. Space Phys.* 118, 1022–1039. doi:10.1002/jgra.50160

Wing, S., Sibeck, D. G., Wiltberger, M., and Singer, H. (2002). Geosynchronous magnetic field temporal response to solar wind and imf variations. *J. Geophys. Res. Space Phys.* 107, 32–10. doi:10.1029/2001JA009156

Yin, P., Mitchell, C., and Bust, G. (2006). Observations of the f region height redistribution in the storm-time ionosphere over europe and the USA using gps imaging. *Geophys. Res. Lett.* 33. doi:10.1029/2006GL027125

Yu, Y., and Ridley, A. J. (2009). Response of the magnetosphere-ionosphere system to a sudden southward turning of interplanetary magnetic field. *J. Geophys. Res. Space Phys.* 114. doi:10.1029/2008JA013292

Zou, Y., Lyons, L., Conde, M., Varney, R., Angelopoulos, V., and Mende, S. (2021). Effects of substorms on high-latitude upper thermospheric winds. *J. Geophys. Res. Space Phys.* 126, e2020JA028193. doi:10.1029/2020JA028193

Zou, Y., Nishimura, Y., Lyons, L., Conde, M., Varney, R., Angelopoulos, V., et al. (2018). Mesoscale f region neutral winds associated with quasi-steady and transient nightside auroral forms. *J. Geophys. Res. Space Phys.* 123, 7968–7984. doi:10.1029/.2018JA025457

frontiers | Frontiers in Astronomy and Space Sciences

TYPE Original Research
PUBLISHED 20 May 2025
DOI 10.3389/fspas.2025.1574577

Check for updates

OPEN ACCESS

EDITED BY
Guram Kervalishvili,
GFZ German Research Centre for Geosciences, Germany

REVIEWED BY
Shan Wang,
Peking University, China
Masaru Nakanotani,
University of Alabama in Huntsville, United States

*CORRESPONDENCE
H. Madanian,
hadi@epexsci.com

†PRESENT ADDRESS
H. Madanian, Epex Scientific, Richmond, VA, United States

RECEIVED 11 February 2025
ACCEPTED 16 April 2025
PUBLISHED 20 May 2025

CITATION
Madanian H, Pfau-Kempf Y, Rice R, Liu T, Karlsson T, Raptis S, Turner D and Beedle J (2025) Sunward flows in the magnetosheath associated with the magnetic pressure gradient and magnetosheath expansion. *Front. Astron. Space Sci.* 12:1574577. doi: 10.3389/fspas.2025.1574577

COPYRIGHT
© 2025 Madanian, Pfau-Kempf, Rice, Liu, Karlsson, Raptis, Turner and Beedle. This is an open-access article distributed under the terms of the Creative Commons Attribution License (CC BY). The use, distribution or reproduction in other forums is permitted, provided the original author(s) and the copyright owner(s) are credited and that the original publication in this journal is cited, in accordance with accepted academic practice. No use, distribution or reproduction is permitted which does not comply with these terms.

Sunward flows in the magnetosheath associated with the magnetic pressure gradient and magnetosheath expansion

H. Madanian[1,2*†], Y. Pfau-Kempf[3], R. Rice[1,4], T. Liu[5], T. Karlsson[6], S. Raptis[7], D. Turner[8] and J. Beedle[8]

[1]Heliophysics Division, NASA Goddard Space Flight Center, Greenbelt, MD, United States, [2]Department of Physics, The Catholic University of America, Washington, DC, United States, [3]Department of Physics, University of Helsinki, Helsinki, Finland, [4]Department of Astronomy, University of Maryland, College Park, MD, United States, [5]Department of Earth, Planetary, and Space Sciences, University of California Los Angeles, Los Angeles, CA, United States, [6]School of Electrical Engineering and Computer Science, KTH Royal Institute of Technology, Stockholm, Sweden, [7]Applied Physics Laboratory, Johns Hopkins University, Laurel, MD, United States, [8]Department of Physics and Astronomy, University of New Hampshire, Durham, NH, United States

A density structure within the magnetic cloud of an interplanetary coronal mass ejection impacted Earth and caused significant perturbations in plasma boundaries. Using spacecraft data, we describe the effects of this structure on the magnetosheath plasma downstream of the bow shock. During this event, the bow shock breathing motion is evident due to changes in the upstream dynamic pressure. A magnetic enhancement forms in the inner magnetosheath and ahead of a plasma compression region. The structure exhibits characteristics of a fast magnetosonic shock wave, propagating earthward and perpendicular to the background magnetic field and further accelerating the already heated magnetosheath plasma. Following these events, a sunward motion of the magnetosheath plasma is observed. Ion distributions show that both the high-density core population and the high-energy tail of the distribution of the distribution propagate sunward, indicating that the sunward flows are caused by magnetic field line expansion in the very low β magnetosheath plasma. Rarefaction effects and enhancement of the magnetic pressure in the magnetosheath result in magnetic pressure gradient forcing, which drives the expansion of magnetosheath magnetic field lines. This picture is supported by a reasonable agreement between the estimated plasma accelerations and the magnetic pressure gradient force.

KEYWORDS

shocks, magnetosheath, space weather, solar wind, space plasmas, bow shock, interplanetary coronal mass ejection

1 Introduction

The magnetosheath region at Earth and other planetary systems lies between the upstream solar wind and the downstream magnetic obstacle (e.g., the magnetosphere or the magnetic pileup boundary). The magnetosheath region contains heated and compressed solar wind plasma that has been scattered and slowed down to subsonic speeds. Solar wind heating involves a variety of microphysical processes that are

largely dependent on upstream plasma and shock parameters (Krasnoselskikh et al., 2013; Burgess et al., 2016). These include the bow shock inclination angle (θ_{Bn}) with respect to the interplanetary magnetic field (IMF) and the upstream Mach number. The magnetosheath plasma downstream of quasi-parallel shocks, where $\theta_{Bn} < \sim 45°$ is more turbulent than that in the quasi-perpendicular side of the bow shock. Such asymmetries can continue through the magnetosheath and be imposed on the magnetopause (Madanian et al., 2022; Gurchumelia et al., 2022). At supercritical shocks, heating and energy dissipation occur partly through ion reflection (Schwartz et al., 2022), the rate of which is dependent on the magnetic amplification at the shock and the magnetization (Madanian et al., 2024b). Hot upstream ion populations with larger pitch angles are reflected more easily upon encountering a magnetic boundary (Burgess, 1989). Heavy ions, such as alpha particles and singly charged helium ions in proton-dominated solar wind plasma, interact differently with the bow shock, resulting in an unstable shock layer (Broll et al., 2018; Madanian et al., 2024a).

In addition to upstream effects, the magnetosheath plasma is driven by factors including the deflection pattern around Earth at the point of measurement and transient effects generated locally or transported from downstream, such as surface waves (Plaschke et al., 2013; Burkholder et al., 2023). The energy density of the magnetosheath plasma drives the magnetopause boundary stand-off distance, an important parameter in space physics that determines the state of the magnetosphere and the magnetosphere–solar wind coupling rate. Empirical models relate the location of the magnetopause boundary to the dynamic pressure in the solar wind using the hydrodynamic theory and assuming that flow pressure is entirely converted to thermal pressure in the magnetosheath (Chapman and Ferraro, 1931). Other models also include the IMF B_z component as a proxy to consider the reconnection effects (Shue et al., 1998). The bow shock boundary distance in these models is simply scaled from the magnetopause based on the upstream Mach number in the solar wind (Farris and Russell, 1994).

Magnetosheath plasma jets are periods of high dynamic pressure caused by either increases in density or earthward flow velocity of the magnetosheath plasma (Krämer et al., 2025). Magnetosheath jets are typically localized, constrained in size (Fatemi et al., 2024), and are formed due to a variety of processes, including foreshock effects, upstream discontinuities, and microphysical effects at the bow shock (Plaschke et al., 2018). Discontinuities in the solar wind can also rattle the boundaries. The interaction of a tangential discontinuity (e.g., a density structure) with the bow shock and magnetosphere launches a fast-mode magnetosonic shock wave through the magnetosheath (Maynard et al., 2008; Wu et al., 1993). Another form of magnetic enhancement in the magnetosheath, known as paramagnetic plasmoids, can also form during the passage of upstream discontinuities (Karlsson et al., 2015). Both the fast shocks and paramagnetic plasmoids are compressive structures. Upon encountering the magnetopause, the magnetosheath plasma is typically either deflected around the magnetosphere or enters the magnetosphere through reconnection. The ion plasma β difference and the magnetic shear angle between the magnetosphere and magnetosheath plasmas influence the reconnection rate at the magnetopause (Phan et al., 2010).

Sunward flows in the magnetosheath are rare. Some observational studies associate sunward flows with the magnetopause boundary motion in response to either a change in the upstream dynamic pressure or due to indentation of the magnetopause boundary (Siscoe et al., 1980; Shue et al., 2009; Archer et al., 2014; Zhou et al., 2024; Farrugia et al., 2018). As the magnetopause moves outward, it drives the magnetosheath plasma with different β and magnetic Reynolds numbers, creating sunward flows. In spacecraft observations, this process is followed by a full or partial magnetopause crossing or the presence of the boundary layer plasma. The specific properties of the magnetosheath plasma have direct consequences on the reconnection rate and the amount of energy transfer at the magnetopause. As such, characterizing the properties and dynamics of the magnetosheath is important in understanding the connected Sun–Earth system. In this paper, we investigate the properties and the underlying cause of sunward flows observed in the Earth's magnetosheath during a period of very low β solar wind flow. The remainder of this paper is organized as follows: analysis of *in situ* observations of the solitary magnetic enhancement and sunward flows are described in Section 3, discussion and interpretation of results are provided in Section 4, and conclusions are provided in Section 5. Links to data sources are also provided in Section 5.

2 Data and methods

In this study, we use data from the Time History of Events and Macroscale Interactions during Substorms (THEMIS) (Angelopoulos, 2008), Cluster (Escoubet et al., 2001), Magnetospheric Multiscale (MMS) (Burch et al., 2016), and Wind (Harten and Clark, 1995) missions. The fortuitous configuration of these spacecraft on the dayside geospace allows for a multi-point study of this event. The magnetic field data are obtained from the fluxgate magnetometer (FGM) instruments onboard the spacecraft. For THEMIS and MMS, we use 16 Hz magnetic field data products, while for Cluster, the data cadence is 5 Hz. The THEMIS ion data are taken from the reduced distributions of the electrostatic analyzer (ESA). All plasma moments from the THEMIS spacecraft are recalculated from the returned distributions. The solar wind dynamic pressure is calculated from measurements by the Wind Three-Dimension Plasma (3DP) instrument (Lin et al., 1995).

3 Observations and analysis results

In this section, we describe the impact of a density structure in the solar wind on the magnetosheath. The density structure is observed within the magnetic cloud of an interplanetary coronal mass ejection (ICME) observed on 24 April 2023. The upstream solar wind plasma conditions and the interaction of the structure with the Earth's bow shock have been characterized in earlier studies (Madanian et al., 2024a), and it has been shown that high abundances of protons, alpha particles, and singly charged helium ions exist within the density enhancement. This event caused significant geomagnetic activity and displacement of the bow shock and magnetopause from their nominal positions (Liu et al., 2024). Prior to the onset of the

density peak, the solar wind plasma is dominated by the high magnetic pressure in the strong magnetic fields of the magnetic cloud (very low β plasma). Figure 1 shows different pressure terms in the solar wind as measured by the solar wind monitor at Lagrange point 1 and shifted to the Earth's bow shock by a 42-min lag time. The second panel in this figure shows that in the density structure, high dynamic pressures ($P_{Dyn.} = \rho \cdot |V_{SW}|^2$, where ρ is the mass density and $|V_{SW}|$ is the solar wind speed) are superimposed on top of the relatively high magnetic pressure solar wind flow.

We analyze data from three constellations of spacecraft, namely, THEMIS, Cluster, and MMS, positioned across the dayside magnetosheath during this event. Figure 2 shows the spacecraft positions with respect to the nominal bow shock and magnetopause boundaries. The conic section parameters are selected to match the MMS1 and THEMIS-E (TH-E) crossings of the bow shock and magnetopause, respectively. The MMS spacecraft are initially inside the magnetosheath and close to the bow shock. We only show data from MMS1 since the four MMS spacecraft are in a close tetrahedron formation and make similar observations. TH-D, TH-A, and TH-E spacecraft are inside the magnetosheath and closer to the nose of the magnetopause, while Cluster 2 (CL2) and CL4 spacecraft are in the magnetosheath, with CL2 positioned above the ecliptic plane and separated from CL4 by 4.3 R_E.

The magnetic field measurements by each spacecraft are shown on the right panels in Figure 2. The Earth's bow shock recedes inward upon encountering the high dynamic pressure structure in the solar wind, placing different spacecraft in the solar wind until it bounces back out. The durations of solar wind segments (the gray shaded areas) are consistent with the spacecraft distances to the bow shock and the bow shock breathing motion. In the solar wind, a rotation in the magnetic field is evident in MMS and CL2 data where the B_z component approaches 0. This magnetic perturbation also coincides with the second density peak of the double-peak density structure. The inward motion of the bow shock stops below the TH-A spacecraft as TH-E never crosses the bow shock or encounters the solar wind. Before the end of the period, the TH-E magnetic field data in Figure 2g show a magnetopause crossing at ~ 04:03:00 UT where B_z changes sign from negative in the magnetosheath to positive in the magnetosphere. The magnetic field strength, however, remains roughly similar or slightly decreases from the magnetosheath to the magnetosphere. With the exception of the beginning and ending intervals when TH-E is in the magnetosphere, the spacecraft is in the magnetosheath region. Other spacecraft (MMS, CL2, CL4, TH-D, and TH-A) also observe the magnetosheath plasma, except when excursions into the solar wind occur.

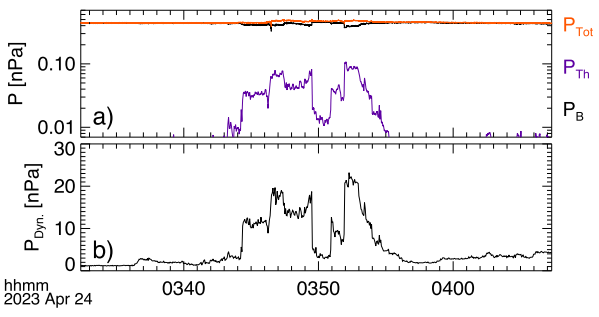

FIGURE 1
Pressure terms associated with the density structure in the solar wind, as observed by the solar wind monitor. The data have been time-shifted to account for the travel time to Earth's bow shock. **(a)** Thermal pressure (blue), magnetic pressure (black), and the total pressure (red). **(b)** Dynamic pressure.

We determine the normal vector direction during contraction and expansion motions (each side of the gray shaded areas in Figure 2) using the minimum variance analysis (MVA) (Sonnerup and Cahill, 1967). The solid vectors at each spacecraft in Figure 2a show the normal vectors during the inward motion, while the dashed vectors are determined for the expanding bow shock. Based on the orientation of the normal vectors, it appears that the bow shock is more curved during the expansion motion than during the receding motion. The sequence of bow shock crossings also indicates that the bow shock contraction occurs faster than its expansion at Cluster and MMS orbits, while it expands faster near the nose region where the THEMIS spacecraft are positioned. We compared MVA estimates of the normal vector with estimates from the mixed coplanarity method. For several crossings, the two estimates are consistent and within a few degrees (< 10°), while a few other estimates, particularly during the contraction phase, show larger discrepancies. Details of the MVA and mixed coplanarity analyses and spacecraft positions are listed in Supplementary Table S1. Normal vectors in Figure 2 are from the MVA analysis.

3.1 Magnetic enhancement in the magnetosheath

An interesting feature observed inside the magnetosheath and ahead of the receding bow shock is the magnetic enhancement observed by all THEMIS and Cluster spacecraft in Figure 2. This structure is marked with purple boxes in the magnetic field time series data. The sequence of observations in the time series data begins with TH-D at 03:51:26 UT. The CL2 spacecraft observes the enhancement 4 s after TH-D, and TH-A and TH-E observe the onset of the enhancement within 9 and 12 s, respectively, after TH-D. The initial magnetic jump ratio (enhancement from the ambient magnetosheath field) is ~1.3 in all spacecraft that observe the enhancement. The magnetic field continues to grow, and the ratio increases to 1.4 and 1.5 at TH-E and TH-A, respectively, and ~1.6 at CL4. The MMS spacecraft does not show any increase in $|\mathbf{B}|$ other than the jump associated with the bow shock crossing.

Figure 3 shows the plasma and field measurements by TH-E around the magnetic peak identified by vertical dashed lines. The magnetic field components in panel (b) indicate that the field increases along the background magnetic field, while the normal vector to the shock front is mostly along the Sun–Earth line. The ion energy flux spectrogram within the magnetic enhancement in panel (c) shows higher ion energy fluxes across all energies. The flow velocity downstream of the shock is also more anti-sunward. Plasma densities in panel (e) during the magnetic enhancement also increase (both electrons and ions) by roughly similar ratios as those observed for the magnetic field enhancements. Such a correlation

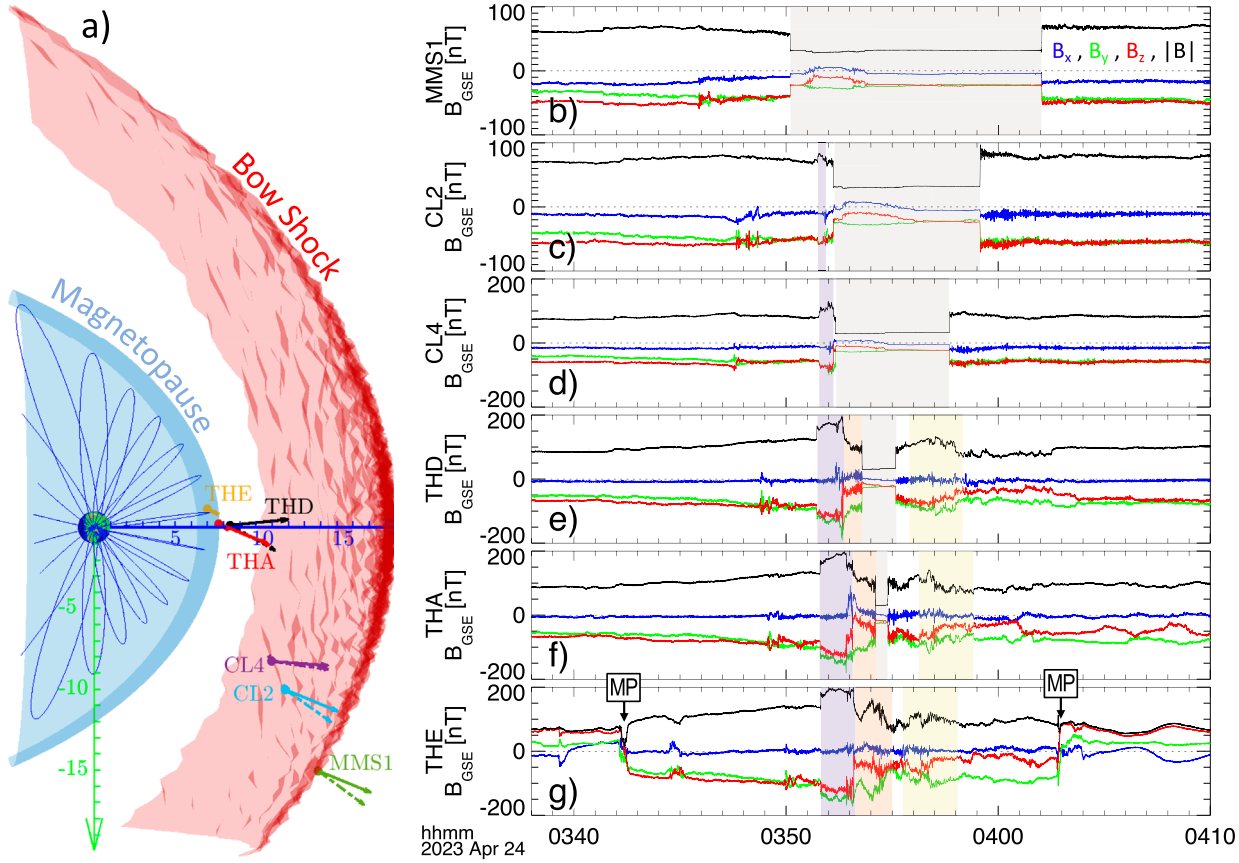

FIGURE 2
Spacecraft positions and magnetic field measurements. The schematic on the left (panel **(a)**) shows the projection of spacecraft positions on the *xy* plane. The axes are in units of Earth radii (R_E). Vector quantities in this figure and throughout the text are given in the geocentric solar ecliptic (GSE) coordinates, where +*x* points toward the sun, +*y* is opposite to the planetary orbital motion, and +*z* completes the right-hand triple. The solid and dashed vectors originating from each spacecraft show the normal vector to the bow shock during its receding and expanding motion, respectively. Panels **(b)** through **(g)** show the magnetic field components and magnitude measured by MMS1, CL2, CL4, TH-D, TH-A, and TH-E spacecraft. Shaded areas highlight the following: gray for the solar wind, purple for the fast magnetosonic shock, pink for the density pileup, and yellow for the sunward flow periods. Instances of magnetopause crossing by the TH-E spacecraft are marked by "MP" on the last panel.

in density and magnetic field variations is indicative of the compressional nature of the structure. Using the mixed coplanarity method, we obtain the shock normal vector $n = [-0.90, 0.09, 0.43]$ at TH-E and $n = [-0.86, -0.27, 0.43]$ at TH-D. The shock normal is almost exactly perpendicular to the upstream magnetic field at TH-D, while it becomes less oblique at TH-E. The propagation direction, flow velocity pattern, and compressional feature indicate that the magnetic enhancement is consistent with an FMSW propagating in the magnetosheath.

The magnetic enhancement ends with a sudden decrease in the absolute value of the $|B_z|$ component of the magnetic field. High ion-flux intensities at approximately 800 eV in panel (c) after the second vertical dashed line are reminiscent of the density peak in the solar wind downstream of the bow shock. A significant plasma pileup in the magnetosheath between the magnetic structure and the receding bow shock is evident in plasma densities in the last panel of Figure 3. The density pileup is associated with the compressed solar wind during the density peak and likely includes protons, alpha particles, and He^+ ions. The ion energy spectra upstream of the receding bow shock in the solar wind (approximately 03:54:30 UT) show the cold proton beam and additional populations of alpha particles and He^+ at higher energies within the density structure. It is also worth noting that prior to the arrival of the fast magnetosonic shock wave, the magnetic field strength in the magnetosheath exhibits a gradual increase, which is most noticeably visible in TH-E data in Figure 2g. This magnetic field enhancement could be associated with the precursor particles from the upstream density structure entering the magnetosheath before the main density enhancement occurs. However, the sharp jump in the magnetic field corresponding to the fast shock is clearly noticeable in all THEMIS spacecraft. Such a structure not only pushes the magnetopause to move further inward but also increases and adds to the magnetic energy density of the magnetosheath plasma near the magnetopause.

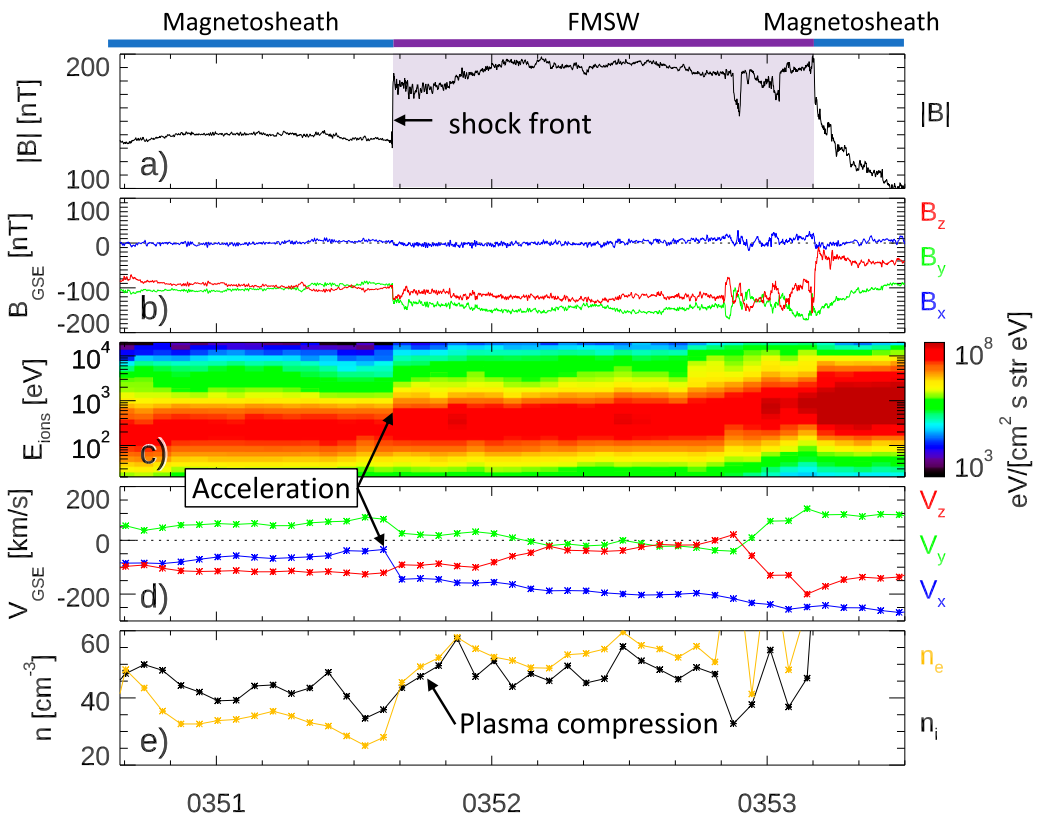

FIGURE 3
Magnetic field and plasma measurements around the magnetic enhancement structure measured by the TH-E spacecraft. **(a,b)** Magnetic field magnitude and components, **(c)** ion energy flux spectrogram, and **(d,e)** plasma velocity and density, respectively. The fast magnetosonic shock wave (FMSW) and signatures of acceleration and compression by the shock are annotated in the figure.

3.2 Sunward flows

The passage of the density structure through the magnetosheath and the breathing motion of the bow shock are followed by sunward plasma flows in the magnetosheath. These flows are observed by TH-D, TH-A, and TH-E spacecraft and are shown in Figure 4. Measurements of the proton plasma from CL4 (not shown) do not indicate any signs of sunward flows, while the MMS spacecraft near the bow shock measures anti-sunward flows (Madanian et al., 2024a). Therefore, the extent of sunward flows is limited to the inner magnetosheath. The periods of sunward flows ($+V_x$) are highlighted with yellow in the velocity panels (b), (e), and (h) in Figure 4. TH-D and TH-A measurements are also interrupted by an excursion into the solar wind.

The flow reversal from anti-sunward to sunward directions begins with flow becoming less anti-sunward, and the initial part of the flow reversal can be due to the reduction in flux or slow-down of the anti-sunward flow (i.e., transition to the fully heated solar wind plasma). As the magnetosheath plasma flow becomes sunward, the plasma densities decrease to values comparable to those observed during the fast magnetosonic shock structure (i.e., at the beginning of each interval in panels (c), (f), and (i)). The maximum sunward plasma speed (V_x) at TH-E, TH-A, and TH-D reaches as high as 94, 113, and 107 km/s, respectively. We estimate the plasma expansion acceleration rate along the Sun–Earth line in time-series data using the V_x component changes, between the black arrows, and obtain sunward plasma accelerations of $dv_x/dt = 6.7$, 5.8, and 4.2 km/s^2 for TH-D, TH-A and TH-E, respectively.

The distribution cut in Figure 4j in the BV plane is produced from TH-E ion distribution data (at the vertical dashed line in panel h) and shows ions at different energies in both sunward and anti-sunward directions and both parallel and anti-parallel to the magnetic field. Higher-energy ions are more abundant in the perpendicular direction to the magnetic field. Determining which segment of the ion distribution constitutes the sunward flow helps in identifying the source and the underlying plasma mechanism(s). In Figure 5, we calculate partial moments of ions at different energy ranges from TH-D ion distributions. Panels (a) and (b) show the magnetic field and energy spectra downstream of the bow shock and when sunward flows are observed. The bow shock is quasi-perpendicular. In the next two panels, the plasma velocity and density of all ions are shown (similar to Figures 4b,c). The flow reversal period is evident at approximately 03:55:50 UT. In panels (e) and (f), we show the velocity vectors and densities of 3 keV–10 keV ions. These ions include mostly alpha particles and singly charged helium ions that are present during this event, in addition to the high-energy tail of the proton distributions. Abundances of heavy, helium group ions and protons in the solar wind decrease near the end of the density structure (see panels f and h). Typically, in the downstream region of a quasi-perpendicular shock, ions

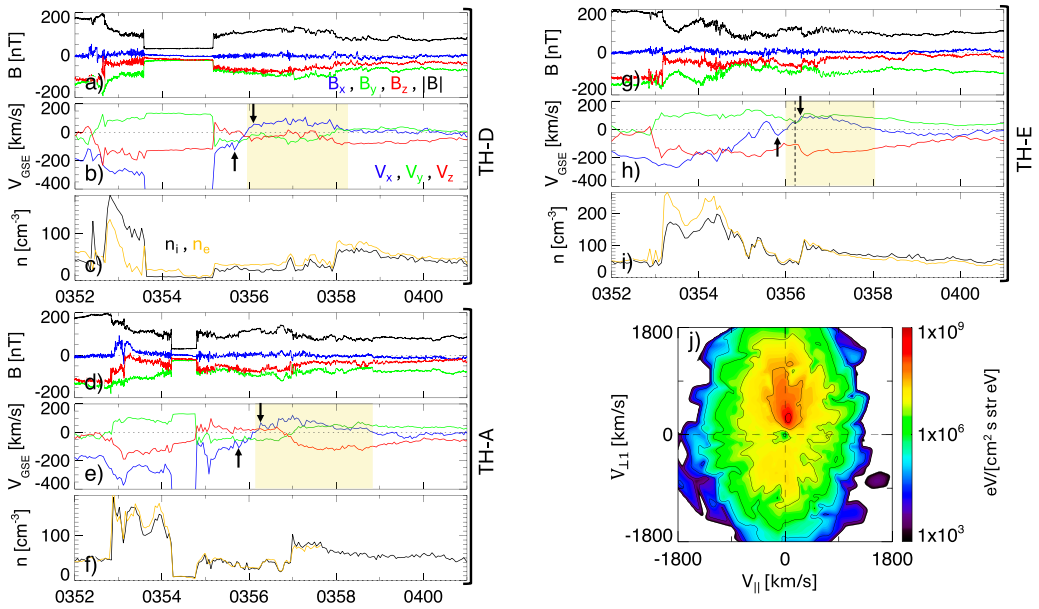

FIGURE 4
Sunward flows in the magnetosheath plasma. Magnetic field, the plasma velocity, and ion (black) and electron (gold) densities are shown from TH-D in panels **(a–c)**, TH-A in panels **(d–f)**, and TH-E in panels **(g–i)**. Panel j shows a cut-through ion distributions in the $V_{||} - V_{\perp 1}$ plane at the time of the vertical dashed line in TH-E data. $V_{||}$ is parallel to the magnetic field, and $V_{\perp 1}$ is perpendicular to the field and along the flow velocity. The yellow shaded areas highlight the periods of sunward flows. The black arrows on the velocity panels indicate data points used in linear fits to estimate the expansion rates.

begin to gyrate and have a velocity component perpendicular to the background magnetic field, and their guiding center is pointed downstream. However, after the initial earthward motion at the beginning of the interval, high-energy ions begin to propagate sunward. Similar behavior is observed at lower energy ranges. Thus, the plasma as a whole moves sunward, while ions gyrate around the background magnetic field.

4 Discussion

4.1 Solitary magnetic structure in the magnetosheath

Unlike the observation sequence of the receding bow shock that follows the spacecraft distances from the bow shock, the first observation of the magnetosonic shock wave in the magnetosheath is by the TH-D probe, which is downstream of the Cluster spacecraft. The MMS spacecraft positioned immediately downstream of the bow shock does not show such a magnetic enhancement. Therefore, it appears that certain conditions in the magnetosheath must be present for the fast magnetosonic shock to form, rather than being launched immediately at the bow shock. The high abundances of alpha particles and singly charged helium ions during this event result in these ion populations (and also protons, but to a lesser degree) traveling at super-Alfvénic speeds in the magnetosheath upon crossing the bow shock (Madanian et al., 2024a). If a fraction of ions crossing the bow shock remain super-Alfvénic, they can cause perturbations in the magnetosheath to generate additional heating. Alpha particles and He^+ ions can change the accuracy of the reported plasma moments. These ions can also modify the underlying assumptions used for the fluid approximation of a planar shock (Lin et al., 2006).

While the magnetic field enhancement across the fast shock wave is along the background magnetic field, the wavefront propagates perpendicular or at highly oblique angles to the background magnetic field. The timing analysis of the shock front observations indicates that the shock wave traveled the 0.7 R_E distance along the Sun–Earth line between TH-D and TH-A spacecraft at a speed of ~440 km/s, which is comparable to the fast mode wave speed in the magnetosheath (V_f = 453 km/s). V_f increases to ~550 km/s downstream of the shock. The conservation of mass flux ($[\rho v_n] = 0$) across the shock at TH-D results in a shock speed of v_n = 241 km/s. If we assume that the difference in density between the upstream and downstream of the shock is due to helium group ions, v_n increases to ~413 km/s. However, doing so increases the divergence in the tangent component of the electric field across the shock. It is also worth noting that the TH-D spacecraft observes the magnetosheath shock before the spacecraft upstream and downstream of it (e.g., TH-A and CL2), indicating that the Earthward propagating shock structure does not necessarily originate at the bow shock. Instead, it develops inside the magnetosheath when certain conditions are met. The shock front remains fairly unperturbed as it propagates through the inner magnetosheath, which is rare for any plasma structure in the typically turbulent magnetosheath plasma. The unperturbed nonlinear propagation pattern is suggestive of a soliton-like shock formation process. Regardless of the formation mechanism, such a magnetic enhancement increases the magnetic energy density near the magnetopause.

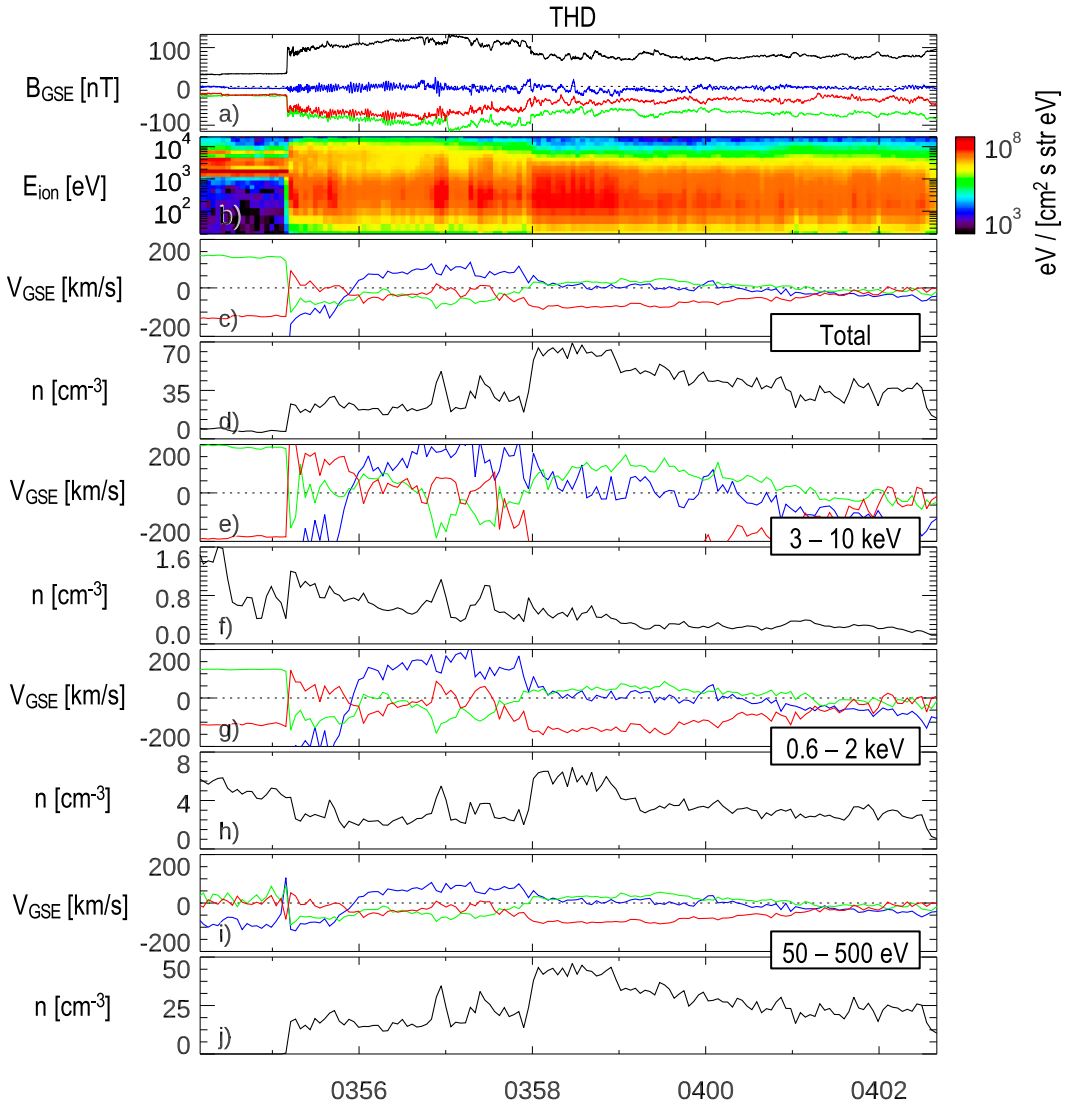

FIGURE 5
Partial moment analysis of sunward flows observed by the THD spacecraft. **(a)** Magnetic field data, **(b)** ion energy flux spectrogram, and **(c,d)** ion velocity and density, respectively, for all ions (of all measured energies); **(e,f)** 3–10 keV ions, **(g,h)** 0.6–2 keV ions, and **(i,j)** 50 eV–500 eV ions. The flow velocity and magnetic field components along *x*, *y*, and *z* are shown in blue, green, and red colors, respectively.

4.2 Cause of sunward flows

Observations of sunward flows thus far have been associated with the sunward motion of the magnetopause boundary and pressure gradient forces driving the plasma (Archer et al., 2015; Shue et al., 2009). During the event discussed in this study, due to strong magnetic fields within the magnetic cloud flux rope, the ion β in the solar wind is extremely low ($\beta \ll 1$), and it remains low even inside the magnetosheath (e.g., β is ~0.2 at TH-D during the sunward flows). Thus, the plasma dynamics in the magnetosheath are dominated by the magnetic field, and a thermal plasma pressure gradient cannot drive the sunward flows in the magnetosheath. Instead, the enhanced magnetic field pressure in the inner magnetosheath responds to the upstream pressure changes by creating a magnetic pressure gradient force perpendicular to the background magnetic field. Given that the magnetic fields in the inner magnetosheath are dominated by B_y and B_z components, such a gradient force would drive the magnetosheath magnetic field lines along x to expand toward rarefied upstream regions. This picture is consistent with the observations in Figures 4a,d,g, where higher magnetic field strengths emerge with sunward flows. In addition, the higher expansion rate observed at TH-D than at TH-A and TH-E is in agreement with a magnetosheath expansion in response to an upstream pressure decrease. During the magnetosheath sunward flows shown in Figure 4, the magnetic field lines in the magnetosheath are almost entirely perpendicular to the Sun–Earth line ($B_x \sim 0$). As such, ions cannot stream along the magnetic field line to travel sunward. In addition, Figure 5 shows that ions in all energies have a net sunward flow, including high-energy ions in the 3–10 keV energy range. In strong magnetic fields of ~ 120 nT, these ions are bound to the field lines with rather small gyroradii of ~65 – 120 km, and their dynamics (e.g., through reflection) cannot

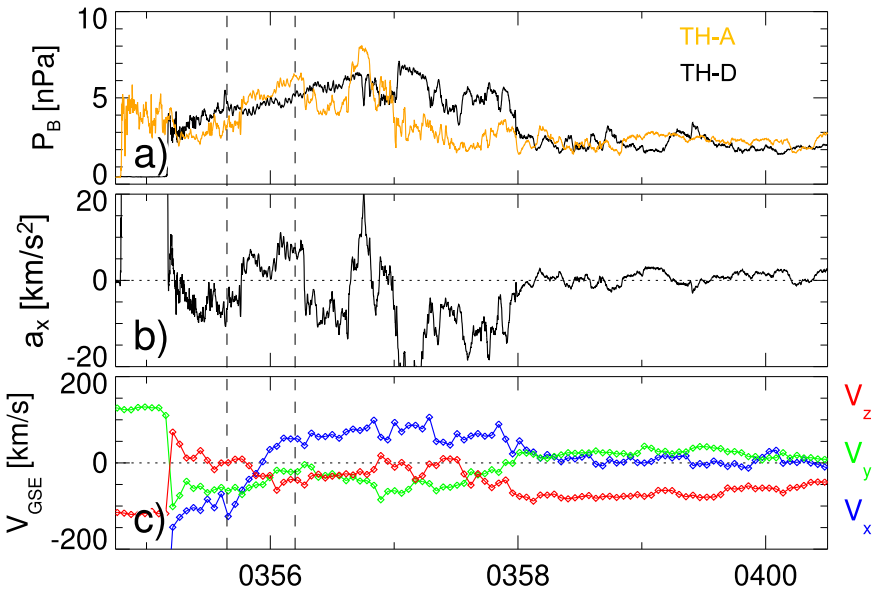

FIGURE 6
Magnetic pressure gradient observed by the THEMIS spacecraft. **(a)** Magnetic pressures from TH-D and TH-A, **(b)** plasma acceleration along the Sun–Earth line, and **(c)** ion velocities at TH-D.

explain the observed sunward plasma flows in the magnetosheath (Fuselier et al., 1991; Farrugia et al., 2018). It seems, however, that the sunward plasma flows are the result of the sunward motion of the magnetic flux tubes and field lines.

As discussed in Section 3.1, the earthward propagating shock causes enhancement of the magnetic pressure in the magnetosheath. Figure 6a shows magnetic pressure terms from TH-A and TH-D spacecraft. In panel (b), we estimate instantaneous acceleration rates projected along the Sun–Earth line using $a_x = \frac{1}{\rho}\nabla_x P_B$, where ρ is the proton mass density at TH-D. The average of instantaneous acceleration rates between vertical dashed lines results in an average acceleration rate of 2.9 km/s^2, which is comparable to the acceleration rate of 6.7 km/s^2 obtained from plasma velocities in panel (c) in the same period. This agreement between plasma acceleration and pressure gradient forcing indicates that magnetosheath sunward flows are caused by magnetosheath expansion. Data in Figure 6 also indicate that after 03:58:00 UT, magnetic pressure variations in both spacecraft decrease, and the estimated acceleration rates reduce to very small values. At this time, MMS is still in the solar wind (Figure 2b), and the magnetic pressure gradient effects have already subsided due to a short temporal scale before MMS returns to the magnetosheath, which could explain why it did not measure sunward plasma flows.

Our observations further indicate that the sunward flows are unrelated to the magnetopause boundary motion. Magnetic field measurements during the magnetopause boundary crossing at 04:03:00 UT by the TH-E spacecraft in Figure 2g indicate that the magnetic pressure in the magnetosheath is slightly higher than the magnetospheric magnetic pressure. Thus, the magnetopause motion is limited by the high magnetic pressure in the magnetosheath, and the magnetopause is controlled by the strong magnetic fields within the magnetosheath. In addition, a sunward magnetopause boundary motion leads to a more consistent flow pattern across different THEMIS spacecraft. In Figure 4, when the sunward flows at TH-E begin to slow down at ~ 03:57:00 UT, sunward flows at TH-D continue at the same rate and even increase at times. The observed sunward plasma flows are rather smooth and even plateau at certain velocities and are unlikely to originate at a distant reconnection zone as we see no signs of the boundary layer plasma.

5 Conclusion

In this study, we characterize a series of events in the magnetosheath caused by the interaction of an upstream density structure embedded within a strong flux rope of an ICME. Strong magnetic fields within the magnetic cloud of the ICME dominate the plasma interactions within the magnetosheath and magnetopause. We show evidence for the formation of a magnetic enhancement in the inner magnetosheath associated with a fast magnetosonic shock wave caused by the sudden surge of upstream charged particles and the associated dynamic pressure pulse. We find that the sunward flows are formed due to magnetosheath expansion and the sunward motion of the flux tubes driven by the magnetic pressure gradient force in the inner magnetosheath, with sunward expansion rates as high as 6.7 km/s^2. The rarefaction effects following the density structure cause sunward flows in the magnetosheath, which responds to the upstream dynamic pressure decrease caused by expanding sunward. These events cause significant geomagnetic activity and are significant in space weather.

Data availability statement

Publicly available datasets were analyzed in this study. These data can be found at https://cdaweb.gsfc.nasa.gov/.

Author contributions

HM: Conceptualization, Methodology, Formal analysis, Investigation, Validation, Writing – original draft, Writing – review and editing. YP: Validation, Visualization, Writing – review and editing. RR: Investigation, Writing – review and editing. TL: Investigation, Writing – review and editing. TK: Investigation, Visualization, Writing – review and editing. SR: Investigation, Data curation, Writing – review and editing. DT: Validation, Visualization, Writing – review and editing. JB: Investigation, Writing – review and editing.

Funding

The author(s) declare that financial support was received for the research and/or publication of this article. This work was supported by the NASA MMS project through the Partnership for Heliophysics and Space Environment Research (PHaSER) cooperative agreement. YP-K acknowledges the Research Council of Finland grant number 339756. SR acknowledges funding from the MMS Early Career Award 80NSSC25K7353. RR was supported by the MMS Early Career Grant 80NSSC23K1601.

Acknowledgments

The authors thank the THEMIS, MMS, and Cluster operation teams for making the data available. They acknowledge the THEMIS magnetometer team at the Technical University of Braunschweig for the use of FGM data, provided with the financial support of the German Federal Ministry for Economic Affairs and Climate Action (BMWK) and the German Aerospace Center (DLR) under contract 50 OC 2201.

Conflict of interest

The authors declare that the research was conducted in the absence of any commercial or financial relationships that could be construed as a potential conflict of interest.

Generative AI statement

The author(s) declare that no Gen AI was used in the creation of this manuscript.

Publisher's note

All claims expressed in this article are solely those of the authors and do not necessarily represent those of their affiliated organizations, or those of the publisher, the editors and the reviewers. Any product that may be evaluated in this article, or claim that may be made by its manufacturer, is not guaranteed or endorsed by the publisher.

Supplementary material

The Supplementary Material for this article can be found online at: https://www.frontiersin.org/articles/10.3389/fspas.2025.1574577/full#supplementary-material

References

Angelopoulos, V. (2008). The THEMIS mission. *Space Sci. Rev.* 141, 5–34. doi:10.1007/s11214-008-9336-1

Archer, M., Turner, D., Eastwood, J., Schwartz, S., and Horbury, T. (2015). Global impacts of a Foreshock Bubble: magnetosheath, magnetopause and ground-based observations. *Planet. Space Sci.* 106, 56–66. doi:10.1016/j.pss.2014.11.026

Archer, M. O., Turner, D. L., Eastwood, J. P., Horbury, T. S., and Schwartz, S. J. (2014). The role of pressure gradients in driving sunward magnetosheath flows and magnetopause motion. *J. Geophys. Res. Space Phys.* 119, 8117–8125. doi:10.1002/2014JA020342

Broll, J. M., Fuselier, S. A., Trattner, K. J., Schwartz, S. J., Burch, J. L., Giles, B. L., et al. (2018). MMS observation of shock-reflected He^{++} at Earth's quasi-perpendicular bow shock. *Geophys. Res. Lett.* 45, 49–55. doi:10.1002/2017GL075411

Burch, J. L., Moore, T. E., Torbert, R. B., and Giles, B. L. (2016). Magnetospheric Multiscale overview and science objectives. *Space Sci. Rev.* 199, 5–21. doi:10.1007/s11214-015-0164-9

Burgess, D. (1989). Alpha particles in field-aligned beams upstream of the bow shock: simulations. *Geophys. Res. Lett.* 16, 163–166. doi:10.1029/GL016i002p00163

Burgess, D., Hellinger, P., Gingell, I., and Trávníček, P. M. (2016). Microstructure in two- and three-dimensional hybrid simulations of perpendicular collisionless shocks. *J. Plasma Phys.* 82, 905820401. doi:10.1017/S0022377816000660

Burkholder, B. L., Chen, L.-J., Sorathia, K., Sciola, A., Merkin, S., Trattner, K. J., et al. (2023). The complexity of the day-side X-line during southward interplanetary magnetic field. *Front. Astronomy Space Sci.* 10, 1175697. doi:10.3389/fspas.2023.1175697

Chapman, S., and Ferraro, V. C. A. (1931). A new theory of magnetic storms. *Terr. Magnetism Atmos. Electr.* 36, 77–97. doi:10.1029/TE036i002p00077

Escoubet, C. P., Fehringer, M., and Goldstein, M. (2001). *Introduction*The cluster mission. *Ann. Geophys.* 19, 1197–1200. doi:10.5194/angeo-19-1197-2001

Farris, M. H., and Russell, C. T. (1994). Determining the standoff distance of the bow shock: Mach number dependence and use of models. *J. Geophys. Res.* 99, 17681–17689. doi:10.1029/94JA01020

Farrugia, C. J., Cohen, I. J., Vasquez, B. J., Lugaz, N., Alm, L., Torbert, R. B., et al. (2018). Effects in the near-magnetopause magnetosheath elicited by large-amplitude alfvénic fluctuations terminating in a field and flow discontinuity. *J. Geophys. Res. Space Phys.* 123, 8983–9004. doi:10.1029/2018JA025724

Fatemi, S., Hamrin, M., Krämer, E., Gunell, H., Nordin, G., Karlsson, T., et al. (2024). Unveiling the 3D structure of magnetosheath jets. *Mon. Notices R. Astronomical Soc.* 531, 4692–4713. doi:10.1093/mnras/stae1456

Fuselier, S. A., Klumpar, D. M., and Shelley, E. G. (1991). Ion Reflection and transmission during reconnection at the Earth's subsolar magnetopause. *Geophys. Res. Lett.* 18, 139–142. doi:10.1029/90GL02676

Gurchumelia, A., Sorriso-Valvo, L., Burgess, D., Yordanova, E., Elbakidze, K., Kharshiladze, O., et al. (2022). Comparing quasi-parallel and quasi-perpendicular configuration in the terrestrial magnetosheath: multifractal analysis. *Front. Phys.* 10, 903632. doi:10.3389/fphy.2022.903632

Harten, R., and Clark, K. (1995). The design features of the GGS wind and polar spacecraft. *Space Sci. Rev.* 71, 23–40. doi:10.1007/BF00751324

Karlsson, T., Kullen, A., Liljeblad, E., Brenning, N., Nilsson, H., Gunell, H., et al. (2015). On the origin of magnetosheath plasmoids and their relation to magnetosheath jets: on the origin of magnetosheath plasmoids. *J. Geophys. Res. Space Phys.* 120, 7390–7403. doi:10.1002/2015JA021487

Krämer, E., Koller, F., Suni, J., LaMoury, A. T., Pöppelwerth, A., Glebe, G., et al. (2025). Jets downstream of collisionless shocks: recent discoveries and challenges. *Space Sci. Rev.* 221, 4. doi:10.1007/s11214-024-01129-3

Krasnoselskikh, V., Balikhin, M., Walker, S. N., Schwartz, S., Sundkvist, D., Lobzin, V., et al. (2013). The dynamic quasiperpendicular shock: Cluster discoveries. *Space Sci. Rev.* 178, 535–598. doi:10.1007/s11214-013-9972-y

Lin, C. C., Chao, J. K., Lee, L. C., Lyu, L. H., and Wu, D. J. (2006). A new shock fitting procedure for the MHD Rankine-Hugoniot relations for the case of small He^{2+} slippage. *J. Geophys. Res. Space Phys.* 111, 2005JA011449. doi:10.1029/2005JA011449

Lin, R. P., Anderson, K. A., Ashford, S., Carlson, C., Curtis, D., Ergun, R., et al. (1995). A three-dimensional plasma and energetic particle investigation for the wind spacecraft. *Space Sci. Rev.* 71, 125–153. doi:10.1007/BF00751328

Liu, T. Z., Shi, X., Hartinger, M. D., Angelopoulos, V., Rodger, C. J., Viljanen, A., et al. (2024). Global observations of geomagnetically induced currents caused by an extremely intense density pulse during a coronal mass ejection. *Space weather.* 22, e2024SW003993. doi:10.1029/2024SW003993

Madanian, H., Chen, L.-J., Ng, J., Starkey, M. J., Fuselier, S. A., Bessho, N., et al. (2024a). Interaction of the prominence plasma within the magnetic cloud of an interplanetary coronal mass ejection with the Earth's bow shock. *Astrophysical J.* 976, 219. doi:10.3847/1538-4357/ad8579

Madanian, H., Gingell, I., Chen, L.-J., and Monyek, E. (2024b). Drivers of magnetic field amplification at oblique shocks: *in situ* observations. *Astrophysical J. Lett.* 965, L12. doi:10.3847/2041-8213/ad3073

Madanian, H., Liu, T. Z., Phan, T. D., Trattner, K. J., Karlsson, T., and Liemohn, M. W. (2022). Asymmetric interaction of a solar wind reconnecting current sheet and its magnetic hole with Earth's bow shock and magnetopause. *J. Geophys. Res. Space Phys.* 127. doi:10.1029/2021JA030079

Maynard, N. C., Farrugia, C. J., Ober, D. M., Burke, W. J., Dunlop, M., Mozer, F. S., et al. (2008). Cluster observations of fast shocks in the magnetosheath launched as a tangential discontinuity with a pressure increase crossed the bow shock: fast shocks in the magnetosheath. *J. Geophys. Res. Space Phys.* 113. doi:10.1029/2008JA013121

Phan, T. D., Gosling, J. T., Paschmann, G., Pasma, C., Drake, J. F., Øieroset, M., et al. (2010). The dependence of magnetic reconnection on plasma β and magnetic shear: evidence from solar wind observations. *Astrophysical J.* 719, L199–L203. doi:10.1088/2041-8205/719/2/L199

Plaschke, F., Angelopoulos, V., and Glassmeier, K. (2013). Magnetopause surface waves: THEMIS observations compared to MHD theory. *J. Geophys. Res. Space Phys.* 118, 1483–1499. doi:10.1002/jgra.50147

Plaschke, F., Hietala, H., Archer, M., Blanco-Cano, X., Kajdič, P., Karlsson, T., et al. (2018). Jets downstream of collisionless shocks. *Space Sci. Rev.* 214, 81. doi:10.1007/s11214-018-0516-3

Schwartz, S. J., Goodrich, K. A., Wilson, L. B., Turner, D. L., Trattner, K. J., Kucharek, H., et al. (2022). Energy partition at collisionless supercritical quasi-perpendicular shocks. *J. Geophys. Res. Space Phys.* 127, e2022JA030637. doi:10.1029/2022JA030637

Shue, J., Chao, J., Song, P., McFadden, J. P., Suvorova, A., Angelopoulos, V., et al. (2009). Anomalous magnetosheath flows and distorted subsolar magnetopause for radial interplanetary magnetic fields. *Geophys. Res. Lett.* 36, 2009GL039842. doi:10.1029/2009GL039842

Shue, J.-H., Song, P., Russell, C. T., Steinberg, J. T., Chao, J. K., Zastenker, G., et al. (1998). Magnetopause location under extreme solar wind conditions. *J. Geophys. Res. Space Phys.* 103, 17691–17700. doi:10.1029/98JA01103

Siscoe, G. L., Crooker, N. U., and Belcher, J. W. (1980). Sunward flow in Jupiter's magnetosheath. *Geophys. Res. Lett.* 7, 25–28. doi:10.1029/GL007i001p00025

Sonnerup, B. U., and Cahill, L. J. (1967). Magnetopause structure and attitude from Explorer 12 observations. *J. Geophys. Res.* 72, 171. doi:10.1029/JZ072i001p00171

Wu, B. H., Mandt, M. E., Lee, L. C., and Chao, J. K. (1993). Magnetospheric response to solar wind dynamic pressure variations: interaction of interplanetary tangential discontinuities with the bow shock. *J. Geophys. Res.* 98, 21297–21311. doi:10.1029/93JA01013

Zhou, Y., Raptis, S., Wang, S., Shen, C., Ren, N., and Ma, L. (2024). Magnetosheath jets at Jupiter and across the solar system. *Nat. Commun.* 15, 4. doi:10.1038/s41467-023-43942-4

frontiers | Frontiers in Astronomy and Space Sciences

TYPE Perspective
PUBLISHED 06 June 2025
DOI 10.3389/fspas.2025.1553076

Check for updates

OPEN ACCESS

EDITED BY
Jiansen He,
Peking University, China

REVIEWED BY
Xi Luo,
Shandong Institute of Advanced Technology, China

*CORRESPONDENCE
Y. Wang,
wy@hit.edu.cn,
wingwy@mail.ustc.edu.cn

RECEIVED 30 December 2024
ACCEPTED 26 May 2025
PUBLISHED 06 June 2025

CITATION
Wang Y, Luo RD, Wei FS, Feng XS, Wang BY, Zuo PB, Jiang CW, Xu XJ and Zhou ZL (2025) Space weather impacts on aviation: bridging scientific understanding and operational implications.
Front. Astron. Space Sci. 12:1553076.
doi: 10.3389/fspas.2025.1553076

COPYRIGHT
© 2025 Wang, Luo, Wei, Feng, Wang, Zuo, Jiang, Xu and Zhou. This is an open-access article distributed under the terms of the Creative Commons Attribution License (CC BY). The use, distribution or reproduction in other forums is permitted, provided the original author(s) and the copyright owner(s) are credited and that the original publication in this journal is cited, in accordance with accepted academic practice. No use, distribution or reproduction is permitted which does not comply with these terms.

Space weather impacts on aviation: bridging scientific understanding and operational implications

Y. Wang[1,2]*, R. D. Luo[1], F. S. Wei[1,2], X. S. Feng[1,2], B. Y. Wang[1,2], P. B. Zuo[1,2], C. W. Jiang[1,2], X. J. Xu[3] and Z. L. Zhou[3]

[1]State Key Laboratory of Solar Activity and Space Weather, School of Aerospace, Harbin Institute of Technology, Shenzhen, China, [2]Shenzhen Key Laboratory of Numerical Prediction for Space Storm, School of Aerospace, Harbin Institute of Technology, Shenzhen, China, [3]State Key Laboratory of Lunar and Planetary Sciences, Macau University of Science and Technology, Macao, China

Space weather, long considered a peripheral concern for aviation, is increasingly recognized as a significant systemic factor influencing global flight operations. While its impact on communication, navigation, and power systems is well-documented, the broader contribution of space weather to flight delays and cancellations has been historically underestimated, with attention largely confined to polar route disruptions. This perspective calls for a paradigm shift, highlighting the systemic effects of space weather on flight delays and cancellations worldwide and stressing the urgent need to integrate space weather considerations into aviation research, operational frameworks, and strategic planning. Building on recent analyses of U.S. airline data (2024) and prior investigations of Chinese hub airports (2015–2019), we reveal how understanding these impacts can transform aviation operations, improving efficiency and resilience in an interconnected global network. By moving beyond a traditionally siloed approach, this perspective uncovers a previously underappreciated global challenge with profound implications for the future of air travel. We advocate for interdisciplinary collaboration, advanced real-time monitoring, and predictive analytics to enhance aviation resilience and operational efficiency amidst escalating space weather activity.

KEYWORDS

space weather, aviation, flight delays, flight cancellation, solar storm

1 Introduction

The term 'Space Weather' appeared in the 1960s and 1970s, and became widely used after the United States proposed the 'National Space Weather Program' in the mid-1990s (Schwenn, 2006). Early research efforts understandably concentrated on the most immediately apparent and high-consequence risks associated with space weather (Pulkkinen, 2007; Hapgood, 2012). In the realm of aviation, particular focuses are put on the unique challenges posed to aviation operations on polar region and specified routes. These initial investigations primarily addressed concerns radiation exposure for flight crews and passengers at high latitudes and the potential for high frequency (HF) communication outages in regions with limited satellite coverage (Jones et al., 2005; Fisher, 2009; Authority, 2020; Zou and Hansen, 2014; Fiori et al., 2022). This focused approach fostered crucial international collaborations, such as the establishment of the China-Russia Consortium

space weather center under the auspices of the International Civil Aviation Organization (ICAO) in 2019 (Aleshin et al., 2021).

However, the broader implications of space weather for general flight operations, including its potential impacts on flight delays, remained largely speculative and outside the primary scope of these investigations (Lyakhov and Kozlov, 2012; Polishchuk et al., 2012; Tobiska et al., 2011). Traditional research on flight delays has predominantly concentrated on factors such as meteorological conditions within the Earth's atmosphere, inefficiencies in air traffic managements, and various airline-specific operational challenges (Chakrabarty et al., 2019; Lambelho et al., 2020; Gui et al., 2020; Gultepe et al., 2019; Borsky and Unterberger, 2019). While these terrestrial factors undoubtedly play a significant role in flight disruptions, the exclusion of space weather from comprehensive delay models has created a significant disciplinary isolation, severely limiting our holistic understanding of the complex dynamics that contribute to them. This limitation is further exacerbated by the inherently difficulty and complexity of space weather's impacts on the Earth's Magnetosphere-Ionosphere-Thermosphere system, which makes it even more challenging to establish a clear logical chain connecting space weather and flight delays (Schwenn, 2006; Pulkkinen, 2007; Wang et al., 2023).

The influence of space weather on flight delays is not a simple, direct relationship, but rather a complex interplay of nonlinear and multi-coupled effects propagating through various technological systems (Wang et al., 2023; Xu et al., 2023). Space weather, manifested through Solar Flares (SFs), Interplanetary Coronal Mass Ejections (ICMEs), and Solar Energetic Particles (SEPs), arising from the dynamic interaction of solar activity with Earth's magnetosphere and ionosphere, can induce global-scale disturbances, including HF radio blackouts, significant errors in Global Navigation Satellite System (GNSS) positioning, and elevated radiation levels at flight altitudes (Cander, 2019; Kauristie and Team, 2020; Bust et al., 2021). The potential for these disruptions to exacerbate flight delays, a systemic and globally interconnected challenge for the aviation industry, has been consistently neglected in mainstream research and policy.

Unlike terrestrial weather, space weather phenomena are not directly perceptible, leading to limited public awareness of their potential effects on aviation. Within the aviation industry, attention has primarily centered on safety concerns, with research focusing on links to accidents, radiation exposure for crew and passengers, and impacts on avionics (Lyakhov and Kozlov, 2012; Polishchuk et al., 2012; Bust et al., 2021; Meier and Matthia, 2014; Meier et al., 2020). For example, studies have demonstrated that solar particle events (SPEs) can increase polar radiation levels and disrupt HF communications. Such disruptions occasionally necessitate route diversions for polar flights, resulting in longer flight times and delays (Bland et al., 2018; Zaalov et al., 2015). However, the relatively small number of affected flights, even with the rise in polar routes, has reinforced the perception that space weather's impact on flight delays is negligible or non-systemic.

Public and scientific awareness of space weather's impact on aviation, particularly on flight delays beyond polar routes, remains limited due to a lack of robust quantitative studies exploring this complex relationship. Within the space weather research community, this gap has led some researchers, perhaps prioritizing scientific rigor, to conclude that no significant relationship exists, while others, relying on conventional understandings of space weather effects on communication and navigation systems (Kauristie and Team, 2020; Bust et al., 2021; Meier and Matthia, 2014), speculate that while impacts might be present in specific regions, the systemic influence on modern commercial flights is negligible. However, these perspectives remain largely conjectural, as peer-reviewed quantitative analyses are scarce (Wang, 2022). In fact, beyond our own work (Wang et al., 2023; Xu et al., 2023), no published journal article has comprehensively investigated the systemic effects of space weather events on flight delays and cancellations, leaving a critical gap in understanding.

Recent studies are providing compelling evidence for the systemic impact of space weather on flight delays, challenging the long-held notion that its effects are primarily confined to polar routes and specific regions. Wang et al. (2023) analyzed comprehensive arrival and departure data (~4×10^6 records) from five major hub airports in China spanning 2015–2019. Examining flight delays during 103 space weather events, and employing the Kolmogorov-Smirnov non-parametric hypothesis test, the study provided the first statistical evidence demonstrating a systemic increase in flight delays (~7.41 min) during these periods. Further strengthening the causal link, Xu et al. (2023) identified a distinct spatiotemporal signature in departure delays during 52 solar flare events. Dayside flares resulted in an additional 8.12-min delay compared with nightside flares, with a latitudinal gradient showing delays decreasing by 0.35 min per degree of latitude. Remarkably, Wang et al. (2023) also discovered a correlation between long-term flight punctuality trends and the 11-year solar cycle, suggesting a pervasive, cyclical influence of solar activities on aviation performance.

These findings also demonstrate a monotonic increase in flight delay time and rate with increasing geomagnetic field fluctuations and ionospheric disturbances. This correlation suggests that disruptions to communication and navigation systems during space weather events are a likely primary driver of the observed increase in flight delays (Wang et al., 2023; Xu et al., 2023). Robust communication and navigation are integral to the civil aviation CNS (communications, navigation, and surveillance) system; consequently, such disruptions directly impact both the safety and efficiency of air travel. These emerging evidences indicate that the influence of space weather on flight delays may be mediated through its effects on communication and navigation infrastructure, as well as on air traffic management system efficiency. Collectively, these studies are prompting a critical re-evaluation of the factors influencing flight delays and highlighting the previously underappreciated role of space weather as a significant driver of systemic disruptions.

2 Preliminary evidence from U.S. data

Flight delays often exhibit localized characteristics, whereas space weather events can produce widespread, even global, impacts on Earth's systems. Consequently, investigating the relationship between space weather and flight delays requires a broad geographical scope and a selection of airports distributed across a wide area (Wang et al., 2023; Campanelli et al., 2016). To ensure data homogeneity, such studies are best conducted within

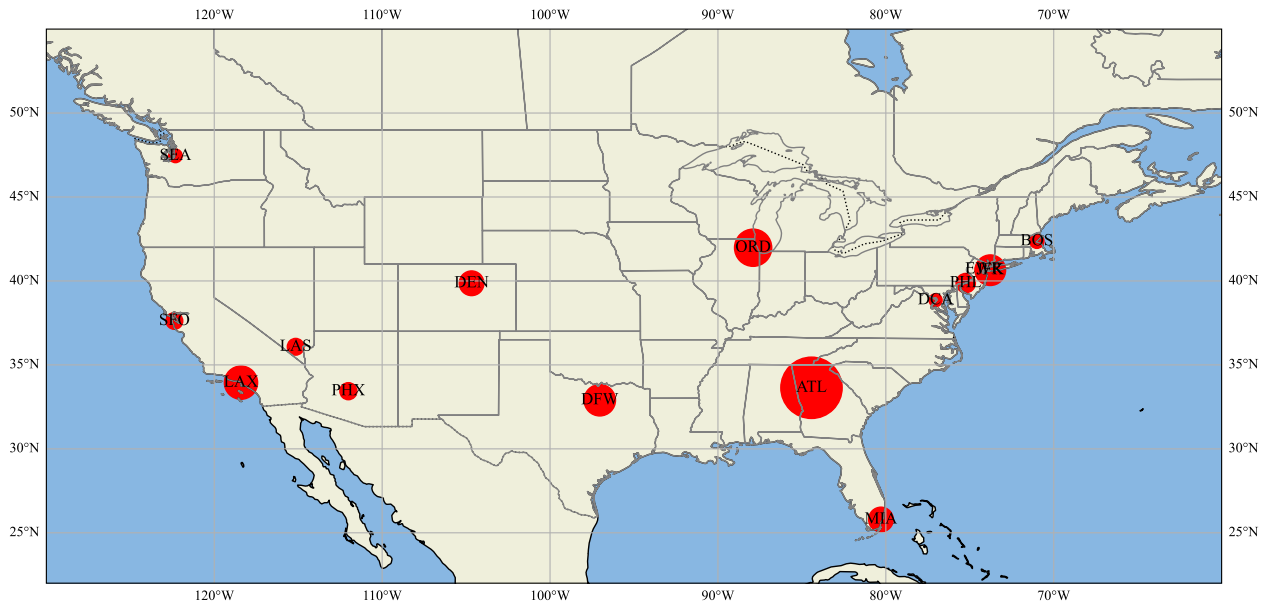

FIGURE 1
The distribution of airports used in this study.

a single country. Among the nations capable of meeting these criteria, China, the United States, Russia, and Canada. While Russia and Canada are less ideal due to lower population density and commercial aviation activity. Prior research has focused on Chinese hub airport data, primarily comparing flight delays during space weather events to those in quiet periods. In this perspective, we extend the scope by presenting a preliminary investigation into the impact of space weather events on flight cancellation rates in the United States. Using superposed epoch analysis, we examine the temporal response of cancellations to space weather events and explore potential differences arising from varying aviation policies.

Flight delays exhibit non-linear propagation across airline networks, with performance in managing delays and cancellations varying significantly among airlines of different scales (AhmadBeygi et al., 2008). These differences are primarily driven by variations in operational models, route network structures, and resource allocation capacities for disruption management. Consistent with established research practices (Bitzan and Peoples, 2016; Avogadro et al., 2021; Bombelli and Sallan, 2023), we categorize airlines into two groups: full-service carriers (FSCs) and low-cost carriers (LCCs). FSCs generally maintain extensive route networks and larger resource reserves, while LCCs, operating under strict cost constraints, are more vulnerable to cascading disruptions. Recognizing these distinctions, our study explicitly incorporates this factor. Among the top ten U.S. airlines by passenger volume in 2024, we selected United Airlines (UA), American Airlines (AA), and Delta Air Lines (DL) as representative FSCs (Group 1) and Frontier Airlines (F9), Southwest Airlines (WN), and Spirit Airlines (NK) as representative LCCs (Group 2). Additionally, we included data from 15 major hub airports distributed across the eastern, central, and western United States, which also include the middle and lower latitude regions, to account for the large-scale impacts of space weather events as shown in Figure 1.

Data for this study were sourced from the U.S. Bureau of Transportation Statistics (BTS) online database, covering the first 8 months of 2024. To minimize confounding factors unrelated to space weather, we excluded data from two major events: the January 2024 North American winter storm and the late July 2024 Microsoft aviation system outage. Our primary focus was the compound Space Weather Event (SWE) period from May 25 to 7 June 2024 (14 days; flight data volume: 238,793), during which no other significant disruptions occurred. Most crucially, the 3 days before and after this period were free of space weather events, allowing us to analyze the temporal evolution of flight cancellation rates in direct response to the space weather activities.

Given the extremely high solar activity in 2024, characterized by frequent events occurring at intervals of only a few days or even hours for SFs, extended quiet periods were scarce. For baseline comparisons, we identified 'Quiet Time Periods 1' (QTP1) with no significant space weather events or major disruptions affecting national flight operations: January 29 to 11 February 2024 (14 days; flight data volume: 221,622), and August 11 to 24 August 2024 (14 days; flight data volume: 247,510) (Bombelli and Sallan, 2023). To further address the scarcity of quiet periods and enhance comparison robustness, we incorporated 'Quiet Time Period 2' (QTP2), which consisted of geomagnetically quiet days (Q1, the quietest days of each month in 2024), as identified from data provided by the Helmholtz Centre Potsdam, GFZ German Research Centre for Geosciences (Matzka et al., 2021) (7 days; flight data volume: 112,815). This dual-baseline approach offers a comprehensive framework for assessing flight delays during space weather events, facilitating a deeper understanding of their systemic impacts.

Figures 2a,b present the solar soft X-ray flux from the GOES satellite and the solar wind magnetic field components from the ACE satellite, respectively. Figure 2c illustrates the temporal evolution

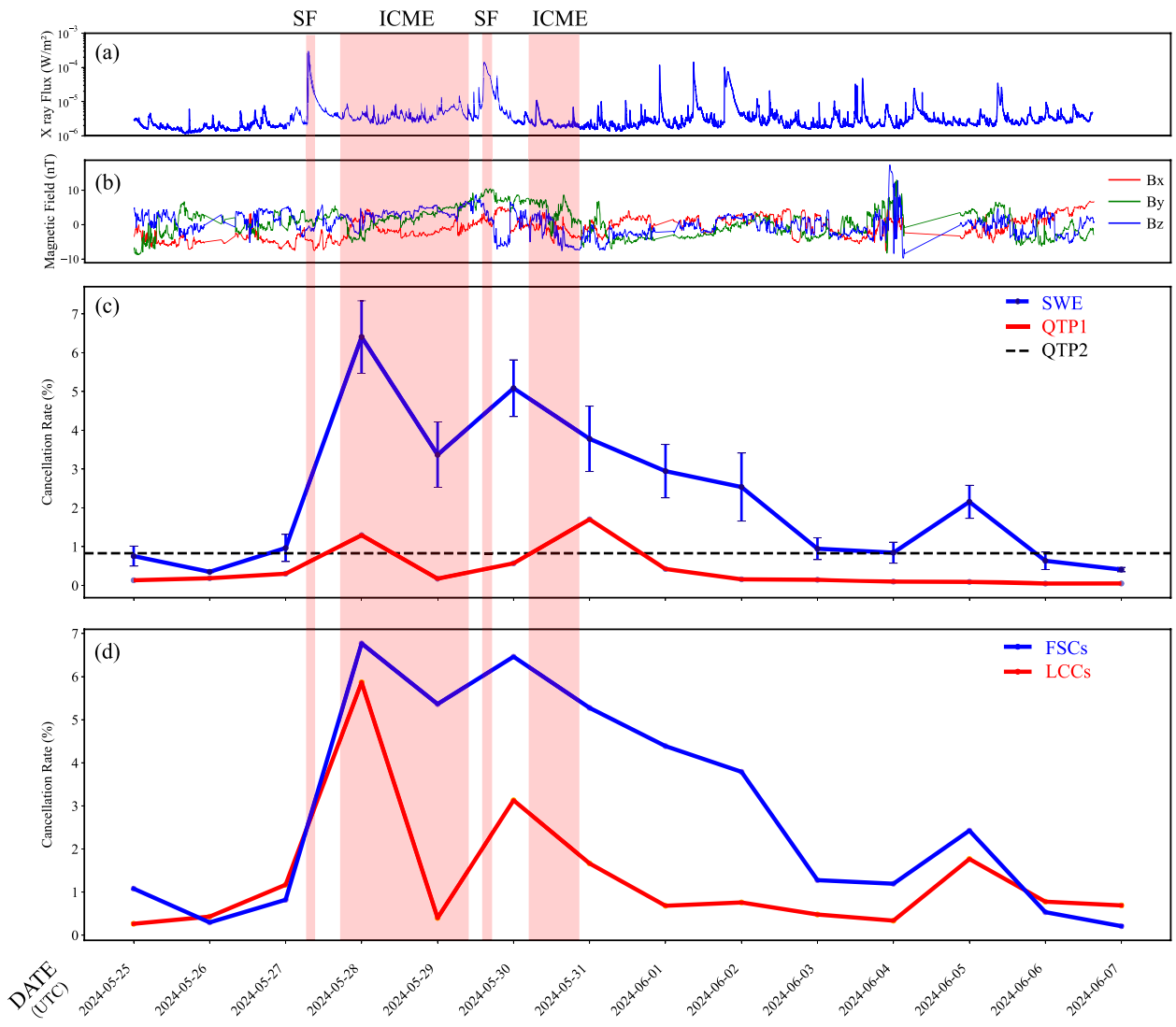

FIGURE 2
(a) Solar soft X-ray flux from the GOES satellite. **(b)** Solar magnetic component flux from the ACE satellite. **(c)** The superposed epoch analysis of flight cancellation rates in response to SWEs (blue), QTP1 (red), and QTP2 (black). **(d)** The superposed epoch analysis of flight cancellation rates for Group 1 (blue) and Group 2 (red) airlines. The light red rectangles mark the durations of space weather events.

of flight cancellation rate in response to space weather events. In the 3 days preceding the onset of the SWE, the cancellation rate remains low and stable at approximately 1%. Following the first SF at 07:14 UTC on May 27, the cancellation rate rises sharply, escalating further with the arrival of an ICME, which significantly perturbs the Earth's magnetosphere-ionosphere system. This disruption causes cancellation rate to surge from approximately 1%–6%. Although cancellation rate begins to decline on May 30, a second X-class SF around 14:23 UTC, significant southward B_z, together with the ICME, contribute another spike, with cancellation rate eventually returning to baseline levels after 3–4 days. Notably, as shown in Figure 2d, the fluctuation of the cancellation rate of Group 2 (LCCs) is more pronounced. This observation seems to align well with previous findings that low-cost carriers are more vulnerable to cascading disruptions due to their strict cost constraints and limited resource buffers (Bitzan and Peoples, 2016; Avogadro et al., 2021). In contrast, during quiet time periods, when no major solar activity is present, the cancellation rate of QTP1 remains relatively constant over time. This stability is also consistent with the rate calculated during the geomagnetically quiet days (QTP2). The high consistency between the two further confirms the systemic impact of solar activity on flight cancellations. Finally, given that previous studies indicate that low-intensity, nighttime, or short-duration SFs are unlikely to significantly impact flight delays (Xu et al., 2023), the minor increase in flight cancellations observed on June 5th is more likely to be attributed to other factors rather than space weather events.

3 Conclusion and discussion

As mentioned before, the influence of space weather on flight delays is not a simple cause-and-effect relationship but rather

a complex, multi-faceted interaction mediated through various technological and atmospheric systems. Although challenging to conceptualize intuitively, our prior research utilizing Chinese aviation data (Wang et al., 2023; Xu et al., 2023), alongside the findings presented here based on U.S. data, provides compelling evidence of increased flight disruptions during space weather events. Together, these studies establish a robust foundation supporting a causal framework for understanding the impact of space weather on flight delays and cancellations.

The most likely primary mechanisms through which space weather affects aviation operations involve geomagnetic-ionospheric perturbations caused by space weather events. These disturbances can disrupt communication systems, leading to increased noise, signal degradation, or even complete outages. Similarly, navigation systems may experience delays in satellite signal transmission and heightened positioning errors. As foundational components of the civil aviation CNS framework, reliable communication and navigation are critical for ensuring safe and efficient air travel. Regulatory frameworks in both the U.S. (e-CFR, 2022) (e-CFR, 2022) and China (CCAR-93TM-R5, 2017) (CCAR-93TM-R5, 2017) mandate continuous two-way communication and provide protocols for addressing communication failures. Consequently, space weather-induced disruptions can necessitate flight diversions, impose ground delays for additional inspections, and ultimately lead to significant delays and cancellations. Moreover, interruptions in communication between Air Traffic Control (ATC) and flight crews can cascade operationally, causing delays in takeoff and landing clearances and inaccuracies in flight planning due to disrupted information flow to dispatch centers. These effects can compound, amplifying minor delays into widespread disruptions across the aviation network. Similarly, even small increases in time required to manage navigation interference can accumulate, further exacerbating delays and cancellations (Wang et al., 2023).

Our ongoing analysis of U.S. flight data aims to examine the influence of space weather events on flight operations over an extended timeframe, encompassing an entire solar cycle. This research accounts for geographical variations, temporal dynamics, and event categorizations and is being compared with findings from Chinese aviation data to construct a comprehensive causal chain linking space weather events to operational disruptions. Although our preliminary findings provide new insights, the broader implications of space weather on aviation remain a complex and expansive field, with many unresolved questions and limited theoretical frameworks (Schwenn, 2006; Pulkkinen, 2007; Authority, 2020; Aleshin et al., 2021; Baker, 2002). Addressing these gaps will require sustained, multidisciplinary research efforts over decades, supported by significant resources. This perspective explores only a subset of these issues, presenting preliminary findings and encouraging further exploration to deepen our understanding of the mechanisms linking space weather and aviation operations. Comprehensive insights will require extensive collaboration across disciplines, leveraging global datasets and innovative analytical approaches.

Whether or not one assumes the two are intrinsically connected, the seemingly counterintuitive systemic phenomenon demands rigorous investigation grounded in both inductive and deductive reasoning, supported by robust quantitative analysis. Refusing to acknowledge this emerging phenomenon based on personal experience or intuition is scientifically untenable. Recognizing space weather as a significant systemic contributor to flight delays has profound strategic implications, requiring a paradigm shift in aviation operations and planning. Current delay models must be revisited, as the ambiguous 'other' category often used for unexplained delays likely obscures significant impacts from space weather. Operationally, proactive measures are essential, including integrating space weather forecasts and nowcasts into air traffic management systems beyond the polar regions, developing adaptive routing and scheduling strategies informed by space weather predictions, and enhancing the resilience of critical aviation technologies. For example, the Civil Aviation Administration of China's (CAAC) 2024 revision of the 'Regulations on the Release and Exchange of Civil Aviation Flight Meteorological Information,' which significantly expanded the inclusion of space weather information, exemplifies progress in embedding space weather considerations into operational decision-making frameworks.

Beyond operational efficiency, these findings have broader implications for governments and international organizations, which must develop robust contingency plans to safeguard essential services. Future research should prioritize interdisciplinary collaborations to unravel the intricate interactions between space weather and aviation (Jones et al., 2005; Fisher, 2009), as well as the associated economic impacts (Eastwood et al., 2017; Xue et al., 2023). Additionally, the aviation insurance industry should integrate space weather risk assessments into its frameworks. Bridging the gap between space weather science and aviation operations presents opportunities to enhance efficiency, improve safety, and strengthen the resilience of the global air transportation network.

In conclusion, prioritizing space weather in aviation strategy, research, and planning is critical, particularly as aviation continues to expand. A proactive, integrated approach to understanding and mitigating space weather effects is vital for addressing the challenges of our interconnected world. The future of aviation is inherently linked to space weather dynamics, necessitating coordinated and forward-thinking strategies to ensure safety, efficiency, and predictability in global air travel.

Data availability statement

The original contributions presented in the study are included in the article/supplementary material, further inquiries can be directed to the corresponding author.

Author contributions

YW: Conceptualization, Formal Analysis, Funding acquisition, Investigation, Project administration, Resources, Validation, Writing – original draft, Writing – review and editing. RL: Data curation, Formal Analysis, Investigation, Methodology, Resources, Software, Validation, Visualization, Writing – review and editing, Conceptualization. FS: Conceptualization, Writing – review and editing. XF: Conceptualization, Writing – review and editing. BW: Writing – review and editing. PZ: Writing – review and editing. CJ:

Writing – review and editing. XX: Writing – review and editing. ZZ: Writing – review and editing.

Funding

The author(s) declare that financial support was received for the research and/or publication of this article. This work is jointly supported by the National Key R & D Program of China (Grant No. 2022YFF0503900), the National Natural Science Foundation of China 42030204 and 42174199, the Specialized Research Fund for State Key Laboratory of Solar Activity and Space Weather, Guangdong Basic and Applied Basic Research Foundation 2023B1515040021, Shenzhen Technology Project (GXWD20220817152453003 and RCJC20210609104422048), and Shenzhen Key Laboratory Launching Project (No. ZDSYS20210702140800001).

Acknowledgments

We thank the Bureau of Transportation Statistics for providing the U.S. flight records, NASA CDAWeb for providing the GOES soft X-ray flux and ACE solar wind magnetic field data, and the GFZ German Research Centre for Geosciences for providing the geomagnetic Kp index data.

Conflict of interest

The authors declare that the research was conducted in the absence of any commercial or financial relationships that could be construed as a potential conflict of interest.

Generative AI statement

The author(s) declare that no Generative AI was used in the creation of this manuscript.

Publisher's note

All claims expressed in this article are solely those of the authors and do not necessarily represent those of their affiliated organizations, or those of the publisher, the editors and the reviewers. Any product that may be evaluated in this article, or claim that may be made by its manufacturer, is not guaranteed or endorsed by the publisher.

References

AhmadBeygi, S., Cohn, A., Guan, Y., and Belobaba, P. (2008). Analysis of the potential for delay propagation in passenger airline networks. *J. Air Transp. Manag.* 14 (5), 221–236. doi:10.1016/j.jairtraman.2008.04.010

Aleshin, I. M., Arakelov, A. S., Burov, V. A., Ivanov, S. D., Ochelkov, Y. P., Repin, A. Y., et al. (2021). Space weather center to support international air navigation: infrastructure and software. *Russ. Meteorol. Hydrol.* 46 (3), 200–204. doi:10.3103/s1068373921030092

Authority, C. A. (2020). Impacts of space weather on aviation.

Avogadro, N., Malighetti, P., Redondi, R., and Salanti, A. (2021). A tale of airline competition: when full-service carriers undercut low-cost carriers fares. *J. Air Transp. Manag.* 92, 102027. doi:10.1016/j.jairtraman.2021.102027

Baker, D. N. (2002). How to cope with space weather. *Science* 297 (5586), 1486–1487. doi:10.1126/science.1074956

Bitzan, J., and Peoples, J. (2016). A comparative analysis of cost change for low-cost, full-service, and other carriers in the US airline industry. *Res. Transp. Econ.* 56, 25–41. doi:10.1016/j.retrec.2016.07.003

Bland, E. C., Heino, E., Kosch, M. J., and Partamies, N. (2018). SuperDARN radar-derived HF radio attenuation during the september 2017 solar proton events. *Space Weather.* 16 (10), 1455–1469. doi:10.1029/2018SW001916

Bombelli, A., and Sallan, J. M. (2023). Analysis of the effect of extreme weather on the US domestic air network. A delay and cancellation propagation network approach. *J. Transp. Geogr.* 107, 103541. doi:10.1016/j.jtrangeo.2023.103541

Borsky, S., and Unterberger, C. (2019). Bad weather and flight delays: the impact of sudden and slow onset weather events. *Econ. Transp.* 18, 10–26. doi:10.1016/j.ecotra.2019.02.002

Bust, G. S., Liles, W., and Mitchell, C. (2021). Space weather influences on HF, UHF, and VHF radio propagation. *Space Weather Eff. Appl.* 153–163. doi:10.1002/9781119815570.ch7

Campanelli, B., Fleurquin, P., Arranz, A., Etxebarria, I., Ciruelos, C., Eguíluz, V. M., et al. (2016). Comparing the modeling of delay propagation in the US and European air traffic networks. *J. Air Transp. Manag.* 56, 12–18. doi:10.1016/j.jairtraman.2016.03.017

Cander, L. R. (2019). *Ionospheric space weather. Springer geophysics*. Springer International Publishing.

CCAR-93TM-R5 (2017). China civil aviation regulation. *Civ. Aviat. Adm. China*. Available online at: https://www.caac.gov.cn/XXGK/XXGK/MHGZ/201712/P020171221370496163543.pdf

Chakrabarty, N., Kundu, T., Dandapat, S., Sarkar, A., and Kole, D. K. (2019). "Flight arrival delay prediction using gradient boosting classifier," *Emerging technologies in data mining and information security* (Singapore: Springer Singapore).

Eastwood, J. P., Biffis, E., Hapgood, M. A., Green, L., Bisi, M. M., Bentley, R. D., et al. (2017). The economic impact of space weather: where do we stand? *Risk Anal.* 37 (2), 206–218. doi:10.1111/risa.12765

e-CFR. (2022). Electronic code of federal regulations e-CFR, 14-121.992022.

Fiori, R. A. D., Kumar, V. V., Boteler, D. H., and Terkildsen, M. B. (2022). Occurrence rate and duration of space weather impacts on high-frequency radio communication used by aviation. *J. Space Weather Space Clim.* 12, 21. doi:10.1051/swsc/2022017

Fisher, G. (2009). Lessons from aviation: linking space weather science to decision making. *Space Weather.* 7, 3. doi:10.1029/2008sw000432

Gui, G., Liu, F., Sun, J., Yang, J., Zhou, Z., and Zhao, D. (2020). Flight delay prediction based on aviation big data and machine learning. *IEEE Trans. Veh. Technol.* 69 (1), 140–150. doi:10.1109/TVT.2019.2954094

Gultepe, I., Sharman, R., Williams, P. D., Zhou, B., Ellrod, G., Minnis, P., et al. (2019). A review of high impact weather for aviation meteorology. *Pure Appl. Geophys.* 176 (5), 1869–1921. doi:10.1007/s00024-019-02168-6

Hapgood, M. (2012). Prepare for the coming space weather storm. *Nature* 484 (7394), 311–313. doi:10.1038/484311a

Jones, J. B. L., Bentley, R. D., Hunter, R., Iles, R. H. A., Taylor, G. C., and Thomas, D. J. (2005). Space weather and commercial airlines. *Adv. Space Res.* 36 (12), 2258–2267. doi:10.1016/j.asr.2004.04.017

Kauristie, K., and Team, P. (2020). "Global navigation satellite systems contributing to space weather services for civil aviation," in *European navigation conference (ENC); 2020 nov 23-24; electr network* (New York, NY: IEEE).

Lambelho, M., Mitici, M., Pickup, S., and Marsden, A. (2020). Assessing strategic flight schedules at an airport using machine learning-based flight delay and cancellation predictions. *J. Air Transp. Manag.* 82, 101737. doi:10.1016/j.jairtraman.2019.101737

Lyakhov, A. N., and Kozlov, S. L. (2012). Whether space weather factors affect the occurrence of aviation accidents. *Geomagn. Aeron.* 52 (1), 129–134. doi:10.1134/s0016793212010069

Matzka, J., Stolle, C., Yamazaki, Y., Bronkalla, O., and Morschhauser, A. (2021). The geomagnetic Kp index and derived indices of geomagnetic activity. *Space Weather.* 19 (5), e2020SW002641. doi:10.1029/2020SW002641

Meier, M. M., Copeland, K., Kloble, K. E. J., Matthia, D., Plettenberg, M. C., Schennetten, K., et al. (2020). Radiation in the atmosphere-A hazard to aviation safety? *Atmosphere* 11 (12), 1358. doi:10.3390/atmos11121358

Meier, M. M., and Matthia, D. (2014). A space weather index for the radiation field at aviation altitudes. *J. Space Weather Space Clim.* 4, A13. doi:10.1051/swsc/2014010

Polishchuk, S., Chynchenko, Y., and Shishkov, F. (2012). Aviation accidents and incidents in USA during 23rd solar cycle. *Adv. Aerosp. Technol.* 51 (2), 30–34. doi:10.18372/2306-1472.51.2153

Pulkkinen, T. (2007). Space weather: terrestrial perspective. *Living Rev. Sol. Phys.* 4 (1). doi:10.12942/lrsp-2007-1

Schwenn, R. (2006). Space weather: the solar perspective. *Living Rev. Sol. Phys.* 3 (1), 2. doi:10.12942/lrsp-2006-2

Tobiska, W. K., Bouwer, D., Shelley, R., Mertens, C., Gersey, B., Atwell, W., et al. (2011). "Demonstration of operational real-time space weather prototypes for aviation radiation and magnetospheric sub-storms," in *49th AIAA aerospace sciences meeting including the new horizons forum and aerospace exposition*.

Wang, Y. (2022). "Private Communications with some scholars, experts and reviewers," in *As their options have not been formally published in any academic journal, formal citations cannot be provided*. Private Communications.

Wang, Y., Xu, X. H., Wei, F. S., Feng, X. S., Bo, M. H., Tang, H. W., et al. (2023). Additional flight delays and magnetospheric–ionospheric disturbances during solar storms. *Sci. Rep.* 13 (1), 3246. doi:10.1038/s41598-023-30424-2

Xu, X. H., Wang, Y., Wei, F. S., Feng, X. S., Bo, M. H., Tang, H. W., et al. (2023). Characteristics of flight delays during solar flares. *Sci. Rep.* 13 (1), 6101. doi:10.1038/s41598-023-33306-9

Xue, D., Yang, J., Liu, Z., and Yu, S. (2023). Examining the economic costs of the 2003 halloween storm effects on the North hemisphere aviation using flight data in 2019. *Space Weather.* 21 (3), e2022SW003381. doi:10.1029/2022SW003381

Zaalov, N. Y., Moskaleva, E. V., Rogov, D. D., and Zernov, N. N. (2015). Influence of X-ray and polar cap absorptions on vertical and oblique sounding ionograms on different latitudes. *Adv. Space Res.* 56 (11), 2527–2541. doi:10.1016/j.asr.2015.09.008

Zou, B., and Hansen, M. (2014). Flight delay impact on airfare and flight frequency: a comprehensive assessment. *Transp. Res. Part E-Logistics Transp. Rev.* 69, 54–74. doi:10.1016/j.tre.2014.05.016

Frontiers in
Astronomy and Space Sciences

Explores planetary science and extragalactic astronomy in all wavelengths

Advances the understanding of our universe - from planetary science to extragalactic astronomy, to high-energy and astroparticle physics.

Discover the latest Research Topics

See more →

Frontiers

Avenue du Tribunal-Fédéral 34
1005 Lausanne, Switzerland
frontiersin.org

Contact us

+41 (0)21 510 17 00
frontiersin.org/about/contact